Propagation of Laminar Premixed Flames with Equivalence Ratio Gradient across the Flame Front

February 2022

Takuya Tomidokoro

Propagation of Laminar Premixed Flames with

Equivalence Ratio Gradient across the Flame Front

by

Takuya Tomidokoro

A dissertation submitted in partial fulfillment
of the requirements for the degree of
Doctor of Philosophy (Engineering)
in the Graduate School of Science and Technology,
Keio University
February 2022

Acknowledgments

First, I would like to express my utmost gratitude to my research advisor Professor Takeshi Yokomori, who has passionately guided me and strongly encouraged me throughout my study. Not only has he taught me to think logically and critically, especially to always imagine the underlying physical phenomena, he has shown me how to be a professional mentor who is willing to tackle challenges alongside his students and guide them step by step. Also, I enjoyed our occasional conversations on recent and future combustion studies, ranging from the political and economic background to technical details. I wish to have many more of them in the coming days.

I would also like to deeply thank the members of my preliminary review committee, Professor Akiko Matsuo, Associate Professor Keita Ando, and Assistant Professor Satoko Fujioka, for carefully reviewing and critiquing this dissertation and providing fruitful comments to improve its quality. Their advice has greatly helped clarify the contribution of this dissertation and make the description of the research method more rigorous from the aspect of fluid dynamics and numerical analysis.

This work would have never been possible without my co-researcher, Professor Hong G. Im in King Abdullah University of Science and Technology (KAUST), Saudi Arabia, who has generously allowed me to use the OPUS code. I am also grateful for him providing me with many critical and fruitful suggestions when I was working on research papers or struggling to make a rebuttal to reviewers' comments. As a leading combustion scientist in the world, he has been an inspiring figure for me. It is a pity that I could not visit KAUST due to the pandemic, but I hope it becomes possible in the future.

I would like to thank Professor Toshihisa Ueda, my undergraduate and master's course supervisor, for guiding me to this field of research. Without his encouragement, I would never have chosen this path. He has also taught me to think and act independently, which has always been a valuable skill in my doctoral studies.

Many others require my gratitude. The members of the Yokomori Laboratory were always pleasant to be around. Especially, I would like to thank Dr. Masaki Yamaguchi and Mr. Masayoshi Matsuda, who have inspired me to continue my study in the doctoral course. Only after they have left, I had realized how precious it was to have fellow doctoral students in the same laboratory. Also, I had a good time discussing and working with my research partners, Mr. Taiga Hosoda and Mr. Yo Mikami. I wish them the best in their future studies and careers. Outside the laboratory, I would like to thank Professor Makoto Asai for providing me with great opportunities to view the academic world outside Keio University and Japan through the GESL program. He has always been kind to advise me and has enlightened me as a researcher who can think and act outside the conventional academic sense in Japan. I also owe the alumni of the GESL program, Dr. Ami Ogawa, Dr. Chikahiro Imashiro, Dr. Ryoko Tatsumi, and Dr.

Abstract

New combustion technologies for efficient and low-emission internal combustion engines sometimes result in stratified flames, i.e., premixed flames propagating in inhomogeneous mixtures of fuel and air, and understanding their behavior is crucial for numerical modeling and improving combustor designs. This dissertation aims to elucidate fundamental properties and mechanisms of laminar premixed flame propagation toward richer or leaner mixtures.

Chapter 1 provides the background and basic concepts of stratified flames, followed by motivations and an outline of this dissertation.

Chapter 2 provides the physical model and numerical method of the OPUS code used in the following studies.

Chapter 3 analyzes the response of methane/air premixed flames to oscillating equivalence ratios to investigate the mechanism of the "back-support" effect, where the stratified flame speed is modified from the flame speed in homogeneous mixtures. It is shown that the back-support effect is caused by preferential diffusion of light reactive species, i.e., H/O radicals and hydrogen molecules, from the burned gas toward the reaction zone.

Chapter 4 analyzes rich-to-lean stratified methane/air flames under different flow strain rates to investigate their influence on the back-support effect. It was shown that a larger flow strain increases the local equivalence ratio gradient in the flame zone, which magnifies the back-support effect.

Chapter 5 studies the effect of the back-support effect in rich-to-lean stratified methane/air flames with hydrogen blended up to 40% in the fuel mixture. It is shown that the effect is mitigated due to hydrogen molecules preferentially diffusing out of the flame zone into the unburned mixture.

Chapter 6 analyzes stratified ammonia/air flame propagation and shows that the back-support effect occurs similarly to methane/air mixtures. It is also shown that additional reduction of nitrogen monoxides, a major pollutant of ammonia combustion, occurs in the stoichiometric region of the burned gas.

Chapter 7 summarizes the conclusions and suggests future research topics.

Contents

List of Figures

List of Tables

Nomenclature

Abbreviations

BECCS   Bioenergy equipped with CCUS

BDF   Backward-differentiation formula

CCUS   Carbon capture, utilization, and storage

CFD   Computational fluid dynamics

DAE   Differential algebraic equations

DI   Direct injection

DNS   Direct numerical simulation

HCCI   Homogeneous-charge compression-ignition

HF   Homogeneous flame

LES   Large Eddy Simulation

LP   Lean premixed

LPP   Lean premixed prevaporized

LSL   Local stratification level

MOFs   Metal-organic frameworks

NOx   Nitrogen oxides

RANS   Reynolds-Averaged Navier-Stokes equation

RTP   Reactant-to-product

RTR   Reactant-to-reactant

ODE   Ordinary differential equations

OPUS   Opposed-flow unsteady strained flames

SCCI   Stratified-charge compression-ignition

SDGs   Sustainable Development Goals

SDS   Sustainable Development Scenario

SF	Stratified flame
SI	Spark ignition
SOFC	Solid-oxide fuel cells
SOx	Sulfur oxides
STEPS	Stated Policies Scenario
TPED	Total primary energy demand
PAFC	Phosphoric acid fuel cells
PEMFC	Polymer electrolyte membrane fuel cells
PM	Particulate matter

Greek symbols

α	Mixture thermal diffusivity
β	Conserved scalar
$\beta_{f,i}$	Arrhenius parameter of ith forward reaction
Δ	System eigenvalue
$\Delta\phi$	Equivalence ratio variation at the inlet
ΔT	Temperature variation in the flame
δ_s	Stratification thickness
δ_T	Thermal flame thickness
Θ_k	Thermal diffusion ratio of kth species
λ	Mixture-averaged thermal conductivity
μ	Mixture viscosity
$v'_{k,i}$	Stoichiometric coefficient of kth reactant in ith reaction
$v''_{k,i}$	Stoichiometric coefficient of kth product in ith reaction
ρ	Mixture density
ρ_b	Burned mixture density
ρ_u	Unburned mixture density
σ_d	Damping coefficient
τ_f	Flame timescale
τ_{ptcl}	Travel time of a fluid particle under consideration
$\tau_{ptcl,c}$	The beginning travel time τ_{ptcl} of NO consumption reaction

$\tau_{ptcl,n}$	Travel time of an nth fluid particle
τ_s	Stratification timescale
ϕ	Equivalence ratio
ϕ_a	Amplitude of equivalence ratio oscillation
$\phi_{e,element}$	Element-based effective equivalence ratio
$\phi_{e,species}$	Species-based effective equivalence ratio
$\phi_{element}$	Element-based equivalence ratio
ϕ_{in}	Inlet equivalence ratio
ϕ_{init}	Initial equivalence ratio of a fluid particle under consideration
$\phi_{init,n}$	Initial equivalence ratio of an nth fluid particle
ϕ_m	Center of equivalence ratio oscillation
$\phi_{o,element}$	Element-based overall equivalence ratio
$\phi_{o,species}$	Species-based overall equivalence ratio
ϕ_R	Equivalence ratio at the reaction zone
$\phi_{R,h}$	Equivalence ratio at the reaction zone of a homogeneous flame
$\phi_{R,s}$	Equivalence ratio at the reaction zone of a stratified flame
$\phi_{species}$	Species-based equivalence ratio
$\dot{\Psi}_{j \to k}$	Total integrated production rate of kth species in a reaction path $M_j \to M_k$ $(j \neq k)$
$\dot{\Psi}_{j \to k,h}$	$\dot{\Psi}_k$ in a homogeneous flame
$\dot{\Psi}_{j \to k,s}$	$\dot{\Psi}_k$ in a stratified flame
ψ	Stream function
$\dot{\Omega}_{k,i}$	Integrated production rate of kth species in ith reaction
$\dot{\omega}_f$	Mole reaction rate of fuel species
$\widehat{\omega}_i$	Net rate of progress of ith reaction
$\widehat{\omega}_{i,b}$	Rate of progress of ith backward reaction
$\widehat{\omega}_{i,f}$	Rate of progress of ith forward reaction
$\dot{\omega}_k$	Mole reaction rate of kth species
$\dot{\omega}_{k,i}$	Rate of production of kth species in ith reaction

Latin symbols

a	Flow strain rate
a_G	Global strain rate
a_R	Local strain rate at the reaction zone
$B_{f,i}$	Arrhenius parameter of ith forward reaction
C_k	Mole concentration of kth species
$c_{p.k}$	Specific heat capacity of kth species
$\bar{c}_p$	Mixture-averaged specific heat capacity
D	Mass diffusion coefficient
D_k	(Mixture-averaged) diffusion coefficient of kth species
D_{jk}	Binary diffusion coefficient between jth and kth species
D_{km}	Mixture-averaged diffusion coefficient of kth species
$E_{f,i}$	Activation energy of ith forward reaction
f	Oscillation frequency
G	Field scalar in the level-set approach
h	Mixture specific enthalpy
h_k	Specific enthalpy of kth species
h_k^0	Standard enthalpy of formation
h_k^s	Sensible heat of kth species
K	Total number of species
K_i	Equilibrium constant of ith reaction
$k_{b,i}$	Backward reaction rate constant of ith reaction
$k_{f,i}$	Forward reaction rate constant of ith reaction
Le_k	Lewis number of kth species
l_K	Kolmogorov scale
l_L	Laminar flame thickness
l_o	Integral length scale
l_R	Reaction zone thickness
M_k	Chemical symbol of kth species
$n'_{k,i}$	Reaction order of kth species in ith forward reaction
$n''_{k,i}$	Reaction order of kth species in ith backward reaction

N	Total number of reactions or total number of tracked fluid particles
p	Hydrodynamic pressure
p_0	Thermodynamic pressure
p_{tot}	Total pressure
q_r	Radial heat flux
q_x	Axial heat flux
R	Universal gas constant
$R_{j \to k,i}$	Contribution of ith reaction in a reaction path $M_j \to M_k$ $(j \neq k)$
Re_o	Turbulent Reynolds number
r	Radial coordinate
S_c	Fuel consumption speed
S_d	Displacement speed
$S_{c,h}$	Homogeneous fuel consumption speed
$S_{c,s}$	Stratified fuel consumption speed
S_L	Laminar flame speed
S_T	Turbulent flame speed
T	Temperature
T_{ad}	Adiabatic temperature
T^0	Reference temperature for standard enthalpy of formation
t	Time
t_n	Starting time of tracking nth particle in a stratified flame
U	Arbitrary function
u	General flow velocity or axial flow velocity
u_b	Flow velocity of burned mixture
u_{in}	Inlet flow velocity
$u_{in,p}$	Inlet flow velocity at the product nozzle
$u_{in,r}$	Inlet flow velocity at the reactant nozzle
u_u	Flow velocity of unburned mixture
u_o'	Turbulent velocity fluctuation
V	Normalized radial velocity $(\equiv v/r)$
V_c	Correction term for diffusion velocity

V_k	Diffusion velocity of kth species
$V_{r,k}$	Radial diffusion velocity of kth species
$V_{x,k}$	Axial diffusion velocity of kth species
v	Radial flow velocity
$\boldsymbol{v}$	Velocity vector
W_f	Molecular weight of fuel species
W_k	Molecular weight of kth species
$\overline{W}$	Mixture-averaged molecular weight
X_{air}	Mole fraction of air
X_f	Mole fraction of fuel species
X_k	Mole fraction of kth species
x	General spatial coordinate or axial coordinate
$\boldsymbol{x}$	Coordinate vector
x_{in}	Inlet location
x_P	Location of upstream edge of the preheat zone
$x_{ptcl,s}$	Location of a fluid particle in a stratified flame
x_R	Reaction zone location
$x_{R,s}$	Reaction zone location of a stratified flame
Y_f	Mass fraction of fuel species
Y_k	Mass fraction of kth species
$Y_{f,b}$	Mass fraction of fuel species in burned mixture
$Y_{f,u}$	Mass fraction of fuel species in unburned mixture
Z	Mixture fraction
Z_k	Atomic mole fractions of kth element

Subscripts

max	Indicates a maximum value of the parameter
min	Indicates a minimum value of the parameter
P	Indicates a parameter evaluated at the upstream edge of the preheat zone
R	Indicates a parameter evaluated at the reaction zone
st	Indicates a parameter under stoichiometric condition

Mathematical Operators

∇ Differential operator

$\sum_i$ Summation over i

$\prod_i$ Product of a sequence over i

Chapter 1
Introduction

1.1 Motivations

Combustion technology, especially the technology of extracting and using thermal energy from combustible substances, has played a pivotal role in the development of human civilization since the primitive ages. In particular, the Industrial Revolution in the late 18th and early 19th centuries has seen a rapid increase in the combustion of fossil fuels such as coal and oil for steam engines, power generation, and internal combustion engines [1]. Since then, our understanding of combustion phenomena has been boosted by the industrial need to increase the output and efficiency of combustion devices. In addition, mitigation of pollutant emissions such as oxides of nitrogen and sulfur (NOx, SOx) and particulate matter (PM) has also become an important part of combustion research since the late 1900s. Currently, combustion is used to supply energy in a wide range of fields such as land, marine and air transportation, power generation, heat processing, and heating for buildings. In 2019, 80% of the total primary energy demand (TPED) of the world was met by fossil fuels [2], most of which are used for some form of combustion. In the power sector, fossil fuels shared 72% of the energy demand. In addition, the ratio of energy consumption through the combustion of fossil fuels was 61% for industry and 91% for transport [2]. While the TPED is estimated to have declined more than 5% in 2020 due to slowed economic activities caused by the Covid-19 pandemic, it is expected to return to the pre-pandemic growth rates in the 2020s [2]. This is led by rising economic growth in the Asia Pacific region, e.g., China and India, and emerging market and developing economies in Africa and Central and South America [2]. Such an extensive dependence on fossil fuels has led to an emergence of global issues including energy security risks, health risks due to air pollution, and global warming. In particular, the third issue has been more urgent than ever.

Global warming is considered to be caused by increased emission of greenhouse gas, primarily CO_2, CH_4, and N_2O, into the atmosphere. Therefore, it is highly likely that human activities associated with the combustion of fossil fuels have contributed to the increase in CO_2.

Changes in global surface temperature relative to 1850-1900

a) Change in global surface temperature (decadal average)
as reconstructed (1-2000) and observed (1850-2020)

b) Change in global surface temperature (annual average) as **observed** and
simulated using **human & natural** and **only natural** factors (both 1850-2020)
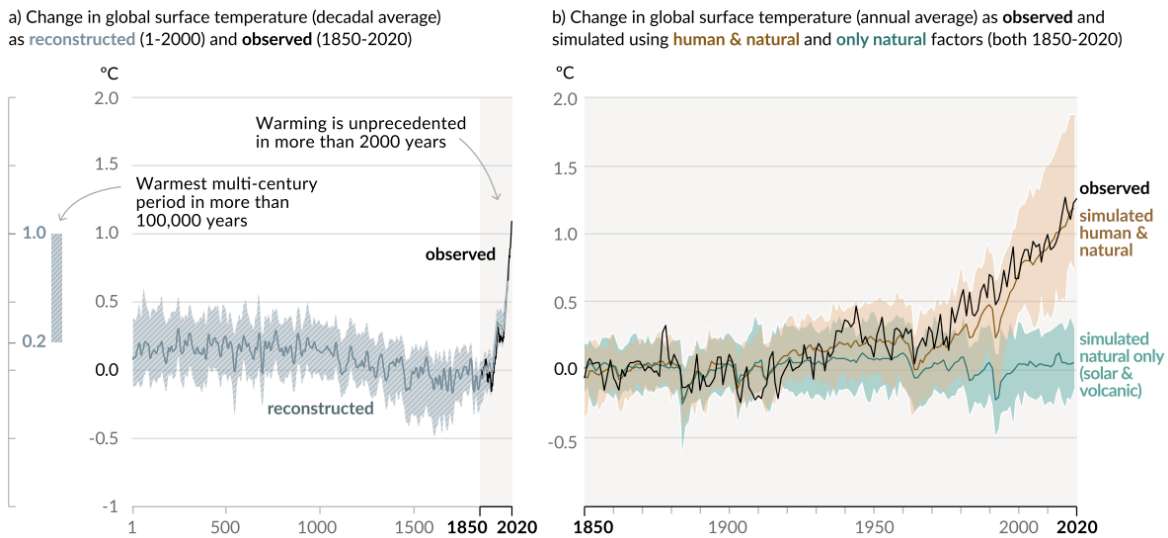
Fig. 1.1: History of reconstructed, observed, and simulated global surface temperature change. (Reproduced from Figure SPM.1 on page SPM-7 of Ref. [3].)

In fact, the atmospheric CO_2 concentrations in 2019 were higher than at any time in at least 2 million years [3]. This has led to a successive increase in the global surface temperature. As shown in **Fig. 1.1**, it was about 1.09℃ warmer in 2011-2020 than in 1850-1900 primarily due to human activities. The effect of global warming is already tangible through the increased occurrence of weather and climate extremes such as heatwaves, heavy precipitation, droughts, and tropical cyclones [3]. Therefore, every additional increase in the temperature will result in an even higher frequency and intensity of the weather and climate extremes. Without any reduction in the consumption of fossil fuels, it is estimated that the temperature increase will be up to 4.4℃ in 2081-2100 [3], which would seriously threaten the future of human society. Unfortunately, the human activities associated with fossil fuels are so vast that even with a deep reduction in CO_2 and other greenhouse gas emissions, it is estimated that the temperature will continue to rise until at least the mid-century. The international communities became increasingly aware of the crisis in recent years. In 2015, the Paris Agreement was adopted, where 196 parties agreed to contribute to limiting global warming to well below 2℃, if possible 1.5℃, compared to pre-industrial levels [4]. The ambitious 1.5℃ goal is associated with the estimate that, by achieving net-zero CO_2 emissions by 2050, the temperature increase will peak out around 1.5℃ and would likely decline back to below 1.5℃ toward the end of the 21st century [3]. The Agreement entered into force in 2016 and has been a strong motivation for the world to make a move for achieving net zero emissions. Meanwhile, very recently, the 2021 Nobel Prize in Physics was awarded to Dr. Syukuro Manabe and Dr. Klaus Hasselmann "for the physical modelling of Earth's climate, quantifying variability and reliably predicting global

warming" [5]. This is a first time that the Prize was awarded to the contribution in the climate science, which signifies the international attention toward the current crisis the humans face.

The International Energy Agency (IEA) estimates future energy mix based on several scenarios. With the Stated Policies Scenario (STEPS), the total share of the fossil fuels in the TPED is estimated to increase to 82%, which is estimated to result in a temperature rise of 2.7℃ in 2100 [2]. On the other hand, the Sustainable Development Scenario (SDS) shows a future course that needs to be taken to achieve energy- or climate-related United Nations Sustainable Development Goals (SDGs), including the Paris Agreement. It is estimated that with the SDS, global net-zero emission is achieved by 2070 and the temperature rise is limited to 1.65℃ with a 50% probability [2]. With this scenario, the fossil fuel share is reduced to 56% in 2040. One way to compensate for the decline in fossil fuel consumption is expanding the use of bioenergy such as solid biomass, biofuels, and biogas which is estimated to share 13% of TPED in 2040 [2]. In particular, when bioenergy is fitted with carbon capture utilization and storage (CCUS), negative emissions can be achieved. Such an approach is known as BECCS (Bioenergy Equipped with CCUS) and is expected to offset unabated emissions from remaining fossil-fuel-powered plants and vehicles. As most of the bioenergy will be burned similarly to fossil fuels, it can be said that up to 69% of the primary energy demand will still be relevant to combustion technologies in 2040. Another solution for compensating for reduced fossil-fuel consumption is decreasing the TPED itself by 10% in 2040, which is achieved through increased efficiency and electrification [2]. Therefore, the above estimates show that a continued effort on developing more efficient and environmentally friendly combustion technologies is necessary for achieving a sustainable society in the future.

In addition, rapid deployment of renewable energy is critical for meeting the Paris Agreement goals. The SDS estimates that renewable energies, i.e., hydropower, geothermal, solar photovoltaic, concentrating solar power, wind, and marine, make up 22% of the TPED in 2040 [2]. Especially, in the power sector, they make up 46% of the energy demand [2]. However, the power output of the renewable energy sources fluctuates over diurnal to seasonal timescales and has different levels of intensity from one place to another. Therefore, to increase the share of their generation capacity, their power output must be managed effectively. One solution is to store the electrical energy in some form so that it can then be used to fulfill peak demand or compensate for the lack of primary energy supplies when needed [6–8]. Currently, various methods of energy storage including mechanical, electrical, thermal, and chemical approaches are available [6,8]. However, chemical energy storage is virtually the only choice that allows for large energy storage capacity over long periods at any location, which makes it applicable to long-distance energy trade, remote power generation, and powering heavy-duty machinery [6,8]. Batteries are one of the most common chemical storage methods, and improvements in battery efficiency and production cost are expected to further drive elec-

trification in the transport sector [7]. Meanwhile, the existing rechargeable secondary batteries have volumetric and gravimetric densities that are much lower than those of fossil fuels [8,9], making them impractical for systems that require large power sources. In addition, the sustainability of secondary batteries is still debated [8].

On the other hand, there has been a growing interest in storing renewable electrical energy in terms of fuels, which are sometimes called *electrofuels* or *e-fuels*. Generally speaking, e-fuels store energy as the oxidation potential of materials that are reduced by renewable electrical energies [8]. Therefore, the energy can be extracted by burning or oxidizing the fuel using oxygen in the air. This is the reason why the e-fuels generally have higher specific energies than other chemical storage methods, such as batteries, as they do not require an oxidizer with them on board [8]. Hydrogen (H_2) has long been considered as a potential e-fuel, as it can be produced by electrolyzing water (H_2O), and do not produce CO_2 when burned or oxidized in fuel cells. In addition, non-hydrocarbon fuels such as methanol and ammonia that are derived from sustainable hydrogen are attracting attention as "hydrogen carriers" [7], as will be explained in the following chapters. Therefore, in addition to the conventional challenges including improvement of combustion efficiency and emission characteristics, the above trends regarding emerging e-fuels pose a number of new research questions to combustion scientists; to utilize them in commercial combustion devices, investigation of their fundamental combustion characteristics as well as development of new strategies to burn them in a stable and clean manner are highly anticipated.

In most cases, combustion accompanies a non-equilibrium, self-organized distribution of temperature and concentration known as flames. Therefore, understanding the physics behind flames is crucial for controlling and optimizing the combustion process in practical devices. In particular, numerical simulations are extremely useful for designing, developing, and testing combustion devices with much less time, labor, and expenses than experiment-based approaches. Thanks to advancements in physical modeling, computational power, and numerical algorithms, computational fluid dynamics (CFD)-based tools for combustion simulation have dramatically improved over the last decades. However, they are still quantitatively unreliable primarily due to uncertainties in the turbulent combustion modeling [10]. Such modeling is needed because directly solving the fundamental equations with required resolutions in space and time, i.e., direct numerical simulation (DNS), is unpractically costly for simulating turbulent reacting flows in commercial combustors. For instance, for a DNS of a turbulent reacting flow in a jet engine, it is estimated that years of calculation and millions of dollars are required even with the use of the latest supercomputers [11]. Therefore, to bring down the computational cost to a practical level by reducing the degree of freedom, the governing equations are solved in averaged schemes such as Reynolds-Averaged Navier-Stokes (RANS) modeling

and Large Eddy Simulation (LES). Here, turbulent combustion modeling is necessary for proposing a closure model for unknown quantities that appear in the averaged governing equations [12]. This has been one of the prominent pillars of combustion studies in the last decades and is still a vastly broad area of active research. To develop physically reasonable models, fundamental properties and mechanisms of flames must be elucidated through asymptotic analysis, simplified experiments and numerical simulations of laminar flames, and DNS of reference turbulent flames. Especially, laminar flames are useful for clarifying local elementary processes that occur in turbulent flames for reasons explained in the following section.

1.2 Basic concepts

In this section, some fundamental concepts associated with premixed flames are explained. The following ideas are crucial for understanding the phenomena of stratified combustion discussed in the following part.

1.2.1 Equivalence ratio

When the molar ratio of reactants in a mixture equals the stoichiometric coefficients of their global reaction, the mixture is said to be stoichiometric. The equivalence ratio is evaluated by dividing the fuel-air ratio of the mixture by the stoichiometric fuel-air ratio:

$$\phi = \frac{X_f/X_{\text{air}}}{\left(X_f/X_{\text{air}}\right)_{st}} \tag{1.1}$$

where X_f and X_{air} is the mole fractions of fuel and air, respectively, and $\left(X_f/X_{\text{air}}\right)_{st}$ is the stoichiometric fuel-air molar ratio. In the above definition, $\phi = 1$ in a stoichiometric mixture, $0 < \phi < 1$ in a fuel-lean mixture, and $\phi > 1$ in a fuel-rich mixture. In combustion reactions, the temperature and the product composition of a fuel-air mixture depend strongly on ϕ.

1.2.2 Premixed flame propagation

Flames are localized regions of self-sustaining combustion reactions. In general, flames can be classified into two main categories: premixed and non-premixed. In premixed flames, fuel and the oxidizer (usually air) streams are mixed in advance and a reaction zone is formed in the mixture. Meanwhile, in non-premixed flames, a reaction occurs at the interface of the fuel and air streams. A critical difference in the characteristics of these flames is that premixed flames propagate into and consume the unburned mixture, while non-premixed flames do not. As such, a premixed flame is a wave phenomenon [13]. To understand the mechanism of premixed flame propagation, the flame structure needs to be considered.

Figure 1.2 shows distributions of some important scalars in a premixed flame, namely the heat release rate, temperature, and reactant and radical concentrations. The flame zone
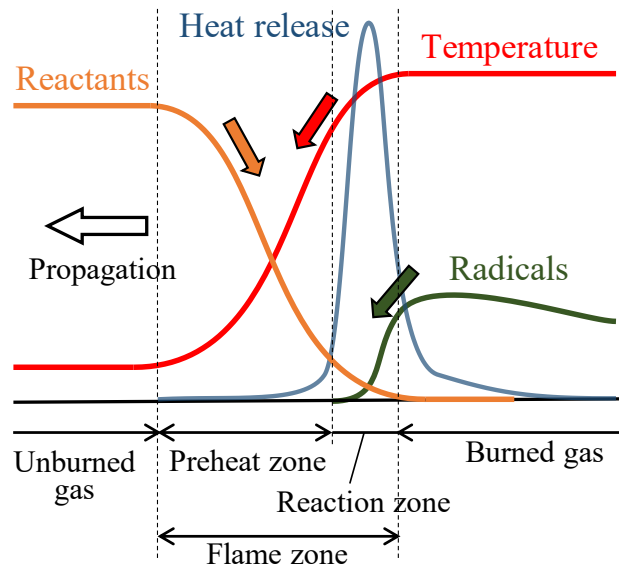
Fig. 1.2: Schematic of a premixed flame structure.

consists of the preheat and the reaction zones. In the preheat zone, heat conduction from the reaction zone toward the unburned gas and mass diffusion from the unburned gas to the reaction zone occurs. The reactants and temperature profiles in the preheat zone are dominated by a convective-diffusive balance of heat and mass transport. Consequently, under faster flame propagation, the gradient of the profiles becomes larger to balance the increase in convective heat and mass transport. When the temperature becomes sufficiently high, the activation energy is overcome and combustion initiates in the reaction zone. In addition to the temperature rise, radicals that diffused from the burned gas into the reaction zone play major roles in triggering fuel decomposition, which leads to a series of chain reactions. Therefore, with a higher temperature or radical concentration in the reaction zone, the reaction rate increases, and the flame propagates faster. The profiles in the reaction zone are dominated by reactive-diffusive balance, thus it indirectly depends on the flame speed through diffusive interaction with the preheat zone. Since the reaction proceeds at a finite rate, the burned gas composition gradually approaches chemical equilibrium downstream of the reaction zone. As the upstream reactants are continuously depleted in the reaction zone, the reaction zone continuously relocates itself toward the unburned mixture. The above mechanism shows that premixed flame propagation is fundamentally a diffusive process balanced by the relative convection of the unburned mixture.

The relative speed of flame propagation toward the unburned mixture is called the flame speed S_L, which is the most important property of premixed flames. While there are various methods to experimentally measure the flame speed as a global propagation speed of the flame zone [14], in numerical simulations, the flame speed can be calculated through profiles

of certain scalars across the flame such as temperature and species [13]. Consider a one-dimensional planar premixed flame propagating into a quiescent fuel/air mixture with velocity u_u, as shown in **Fig. 1.3**. Note that the coordinate is in a wave-stationary frame. In the figure, $Y_{f,u}$ and $Y_{f,b}$ are respectively unburned and residual fuel mass fraction, while ρ_u and ρ_b are respectively unburned and burned mixture densities. Assuming steady propagation, the continuity equation and the species mass conservation equation are written as [15]

$$\frac{d}{dx}(\rho u) = 0, \qquad \rho u = \rho_u u_u = \rho_b u_b = \text{const.} \tag{1.2}$$

$$\rho u \frac{dY_f}{dx} = \frac{d}{dx}\left(\rho D \frac{dY_f}{dx}\right) + W_f \dot{\omega}_f \tag{1.3}$$

where ρ and u are respectively density, velocity; Y_f, W_f, $\dot{\omega}_f$, and D are respectively mass fraction, molecular weight, reaction rate, and mass diffusion coefficient of the fuel. Considering Eq. (1.2) and integrating Eq. (1.3) from the unburned mixture side ($x = -\infty$) to burned mixture side ($x = +\infty$),

$$\rho_u u_u \left(Y_{f,b} - Y_{f,u}\right) = \rho D \frac{dY_f}{dx}\bigg|_{-\infty}^{+\infty} + \int_{-\infty}^{+\infty} W_f \dot{\omega}_f dx \tag{1.4}$$

In the above, the first term on the RHS vanishes because the mass fraction gradient approaches zero toward unburned or burned mixtures [15]. Therefore, solving Eq. (1.4) for u_u yields

$$u_u = \frac{1}{\rho_u \left(Y_{f,u} - Y_{f,b}\right)} \int_{-\infty}^{+\infty} \left(-W_f \dot{\omega}_f\right) dx \tag{1.5}$$

It is seen that u_u is expressed in terms of the integrated fuel consumption rate divided by the fuel mass flux into the reaction zone. As u_u is equivalent to the flame speed, it is known as the *fuel consumption speed* S_c [13,16] of the propagating flame;
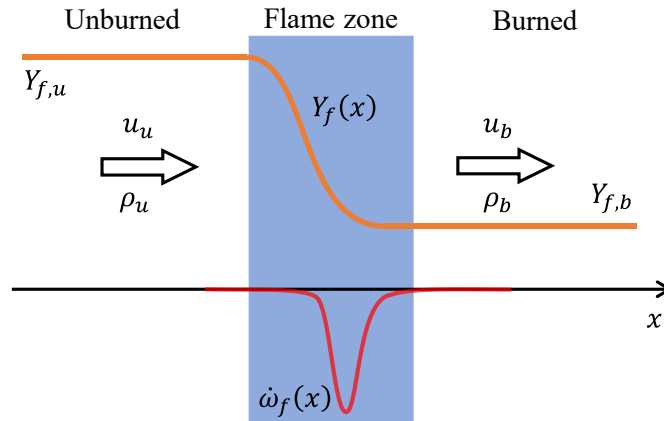
Fig. 1.3: Schematic of steady premixed flame propagation and its fuel mass fraction and reaction rate profiles.

$$S_c = \frac{1}{\rho_u (Y_{f,u} - Y_{f,b})} \int_{-\infty}^{+\infty} (-W_f \dot{\omega}_f) dx \qquad (1.6)$$

In the following studies, the flame speed is evaluated in terms of S_c. However, modifications in Eq. (1.6) are needed to appropriately represent the flame speed in each case, as will be explained.

Another common definition of flame speed is the displacement speed S_d [17], which represents the propagation of a characteristic iso-surface in the flame zone. While S_d is useful for analyzing contributions of reactive and diffusive factors on the flame speed [18–20], it is not used in this study for the following reasons. First, it is known that S_d depends on the definition of the iso-surface under flow divergence [21,22], which is not favorable for the counterflow configuration used in this study. In addition, in a highly transient flow, S_d may fail to characterize the unsteady burning rate as S_d is affected by local variation in the flow velocity [23]. As will be explained, this study is interested in the chemical aspects of the flame propagation speed, i.e., the fuel consumption rate, and thus such a hydrodynamic effect on the flame speed is not desirable. Therefore, only the fuel consumption speed S_c will be used as a measure of the flame speed in this study.

Figure 1.4 shows the experimentally measured flame speed of methane/air laminar premixed flames under different mixture equivalence ratios. It is seen that the flame speed peaks around stoichiometry ($\phi = 1$) and decreases toward leaner or richer mixtures. When the flame speed becomes too low with decreasing or increasing equivalence ratio, it becomes impossible to sustain chain reactions in the reaction zone and the flame extinguishes. Such lean and rich limits of the equivalence ratios are called lean/rich or upper/lower flammable limits.
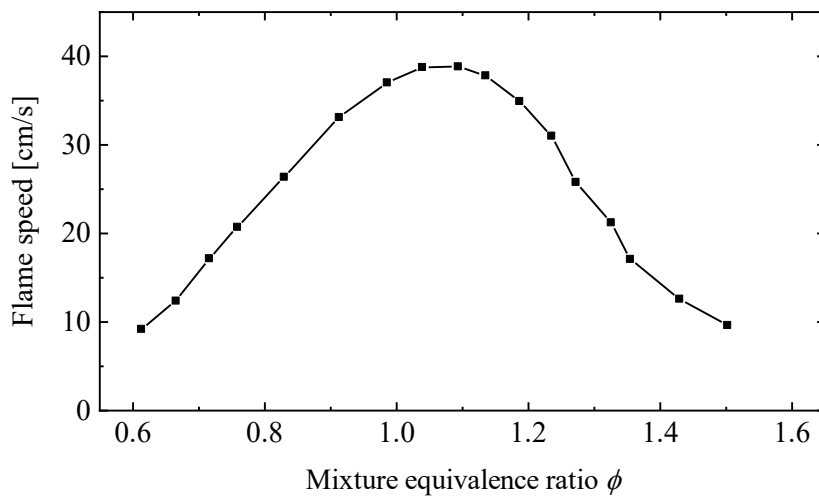
Fig. 1.4: Measured flame speed of a methane/air premixed flame under different equivalence ratios. (Redrawn from Ref. [24].)

The turbulent flame speed S_T, which is a *global* propagation speed of a turbulent flame toward the unburned mixture, is known to depend on the laminar flame speed, expressed as S_L in general. However, predicting S_T from S_L is a highly challenging task as S_T also depends on the turbulent characteristics of the flow and the turbulence-flame interaction, as will be explained in the next part. In terms of turbulent combustion modeling, the laminar flame speed is directly relevant to a popular model using the level set approach. In this method, the turbulent flame is modeled as an iso-surface G_0 of a field scalar $G(\boldsymbol{x}, t)$ and is tracked by solving the transport equation, known as the *G-equation*, which is expressed in the simplest form as

$$\frac{\partial G}{\partial t} + \boldsymbol{v} \cdot \nabla G = S_L |\nabla G| \tag{1.7}$$

where $\boldsymbol{v}$ is the velocity field. It is seen that S_L describes the propagation speed normal to the iso-surface, i.e., the flame front. Equation (1.7) can be modified to account for local diffusive and hydrodynamic effects that influence the flame speed [25]. The parameter S_L also appears indirectly in other turbulent combustion models to close the averaged reaction rate term [13].

1.2.3   Laminar flamelet concept

Other than the above premixed/non-premixed classification, flames can be categorized into laminar and turbulent flames. A common approach to modeling the premixed turbulent flame structure is through the *regime diagram*. The version most commonly used today, which was originally developed by Borghi [26] and later modified by Peters [25], is shown in **Fig. 1.5**. In this diagram, the ordinate is the ratio of the velocity fluctuation u_o' to the laminar flame speed S_L, and the abscissa is the ratio of the integral length scale l_o to the laminar flame thickness l_L. On the lower left corner, the laminar flame regime is represented by the area where the turbulent Reynolds number Re_o is smaller than unity; other regions represent turbulent flame regimes. In particular, the shaded area on the lower right corner is relevant to modelling the turbulent flame structure in terms of the *flamelet* concept [25]. The key assumption of the flamelet concept is that the turbulent flame locally consists of laminar flames, i.e., flamelets. Such a concept has been widely utilized because it enables the modeling of turbulent flames in terms of corresponding laminar flame properties. While the range over which the flamelet concept is valid is still lively debated [27], it is commonly believed that the relevant condition is $l_K > l_L$, where l_L is the thickness of the flame zone and l_K is the smallest turbulent length scale, i.e., the Kolmogorov scale [13]. This is because, when there are turbulent eddies that are smaller than the flame thickness, they can penetrate into the flame zone and disrupt the laminar flame structure, which invalidates the flamelet assumption. The flamelet regime can be further classified into two regimes [13,25]. One is the *wrinkled flamelet* regime, where $u_o' < S_L$. In this regime, the laminar flame structure is hardly affected by the presence of turbulent eddies and the flame surface is only slightly wrinkled. The other is the *corrugated flamelet* regime, where
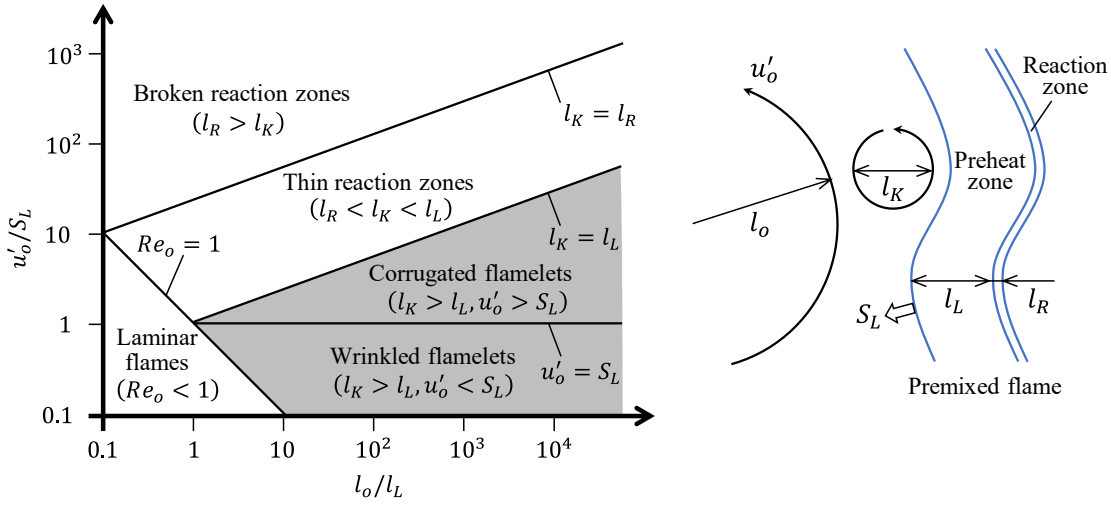
Fig. 1.5: (Left) Turbulent flame regime diagram; (Right) Schematic of interaction between a propagating flame front and turbulent eddies. l_o: Integral length scale, u'_o: Velocity fluctuation, l_K: Kolmogorov length scale, l_L: Laminar flame thickness, l_R: Reaction zone thickness, and S_L: Laminar flame speed.

$u'_o > S_L$. In this regime, while the local laminar flame structure is retained, the flamelet becomes highly convoluted by turbulent eddies and may lead to formations of pockets of unburned and burned mixtures.

In most practical combustors, combustion occurs in turbulent flows. Since detailed studies on the properties of turbulent flames are challenging, the laminar flamelet concept has been widely used as a basis for explaining and predicting the behavior of turbulent flames. However, it should be noted that in many practical combustors, the flamelet assumption may not be justified due to highly turbulent flows where the eddies become small enough to penetrate the flame zone. As shown in **Fig. 1.5**, when $l_R < l_K < l_L$, where l_R is the reaction zone thickness, the turbulent eddies penetrate and broaden the preheat zone while leaving the reaction zone unperturbed. This regime is called the *thin reaction zone* regime or the *broadened preheat–thin reaction* zone regime. Moreover, when $l_R > l_K$, it is expected that the eddies further penetrate the reaction zone, though the local flame structure in this regime is still unclear; Peters suggested that local extinction occurs due to enhanced heat loss to the preheat zone, while later studies claimed that the local extinction is not solely due to turbulence-flame interactions and the reaction zone remains unperturbed [27]. Either way, it is known that in practical devices with high Reynolds numbers, e.g., aeronautical engines, combustion occurs in the above non-flamelet regimes [28]. Nevertheless, many studies report that flamelet models are capable of reproducing turbulent flame properties even when the flamelet assumption does not hold [29–31]. Therefore, it is expected that many behaviors of laminar flames apply to practical turbulent flames.

One of the common laminar flame configurations used for flamelet modeling is a laminar strained flame. Unlike the simplest, one-dimensional laminar flames, strained flames are capable of simulating the effect of a non-uniform flow across the flame zone. In addition, when flow strain is imposed on a flame, the flame surface is said to be "stretched". It can be mathematically shown that flame stretch is also induced by other hydrodynamic effects associated with non-uniform flame curvature and unsteady propagation of a curved flame [13]. Therefore, studying the influence of flow strain on a laminar flame leads to understanding the flame response to a variety of hydrodynamic effects that occur in turbulent flames. Because of these advantages, the strained flame configuration has been a common tool for investigating the behavior of flamelets under various conditions.

1.3   Stratified combustion

1.3.1   Partially premixed combustion

The classification of flames into two regimes, premixed and non-premixed, has been useful especially for analytical purposes. By assuming a homogeneous fuel/air mixture or two separate streams of pure fuel and air, it becomes possible to analytically derive basic flame properties such as the flame speed and the asymptotic flame structure [13]. However, in actual piston engines or gas turbine combustors, the mixture can be locally rich, stoichiometric, or lean at different locations at the same time [32,33]. This trend is accelerated by the development and implementation of unconventional modes of combustion in modern engines [33]. For example, in gas turbine combustors used for power generation and propulsion, lean premixed (LP) or lean premixed prevaporized (LPP) combustion is expected to achieve significantly low NOx emissions due to its low combustion temperature [34]. However, in typical LP or LPP combustors, the mixing time of fuel and air is too short and the flame is fed with a mixture with compositional inhomogeneity [32,33]. It is well-known that such equivalence ratio perturbations are associated with the occurrence of thermoacoustic instability [34–36] or combustion noise [37] in the combustors. In addition, when liquid fuels are used, localized pockets of a rich mixture may exist as the rates of fuel evaporation is limited [38]. Meanwhile, unlike conventional spark-ignition (SI) engines where the fuel is premixed with air, direct injection (DI) of liquid fuel into the combustion chamber is considered to achieve higher efficiency [39]. In DI SI engines, insufficient mixing of fuel and air leads to flame propagation in a highly inhomogeneous mixture; the local composition may be beyond the flammability limits that combustion occurs both in premixed and non-premixed modes [33,40]. Another strategy under development for piston engines is homogeneous-charge compression-ignition (HCCI) technology, where high efficiency and low emissions are achieved through low-temperature combustion of a lean mixture [40]. However, the development of HCCI is prohibited by the occurrence of combustion noise and knocking due to volumetric combustion and

difficulties in controlling auto-ignition [40]. Therefore, HCCI has been modified by introducing some levels of mixture inhomogeneities to mitigate rapid pressure rise and enhance combustion control at wider operating conditions [41,42]. One of such strategies include stratified-charge compression-ignition (SCCI), where compositional inhomogeneity is utilized to smooth the combustion process. With this method, the ratio between auto-ignition and flame propagation can be regulated by controlling fuel stratification [43].

As seen above, the actual combustion process is much more complex than the canonical premixed/non-premixed combustion modes; in the combustion chamber, premixed, non-premixed, and combustion modes that fall in between those modes can co-exist due to mixture inhomogeneity. Such a mode of combustion is called "partially premixed" combustion [32], as shown in **Fig. 1.6**. In partially premixed combustion, the compositional inhomogeneity covers a wide range of fuel concentrations including flammable and non- flammable mixtures.
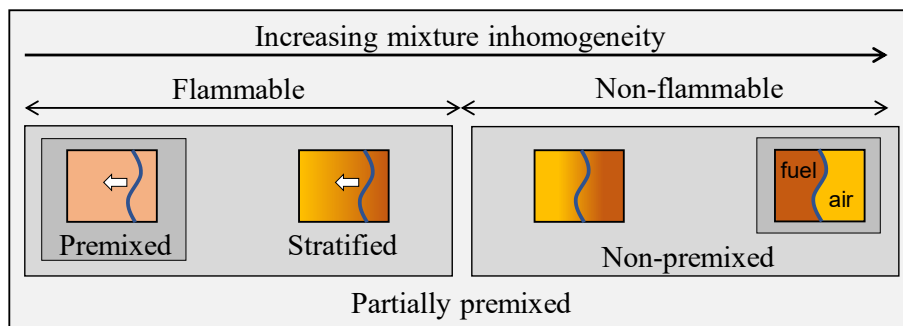
Fig. 1.6: Classification of combustion modes in terms of mixture inhomogeneity.

In locally flammable regions, two modes of flame propagation exist. One is the premixed flame propagation in a locally homogeneous mixture. Another is premixed flame propagation in a locally inhomogeneous mixture whose compositional variation is within the flammable limits. The latter mode is often referred to as "stratified" combustion and the corresponding premixed flame a "stratified flame". On the other hand, in locally non-flammable regions, non-premixed combustion can occur in two modes. One is canonical non-premixed combustion, where two streams of pure air and fuel mix and react at their interface. Another is a reaction between fuel-rich and fuel-lean mixtures whose concentrations are outside of the flammable limits. All of these modes can co-exist in partially premixed combustion; thus, the subject of analytical approaches is limited to steady and simple flame structures. One of the well-known cases is the tribrachial (triple) flames, i.e., edge flames [44]. As shown in **Fig. 1.7**, a tribrachial flame consists of a non-premixed flame branch surrounded by fuel-rich and fuel-lean premixed flame branches. Such a configuration is known to play a crucial role in the stabilization of non-premixed jet flames [33]. However, to study the flame response to various

perturbations in the equivalence ratio, numerical and experimental approaches have played major roles in clarifying the fundamental characteristics.
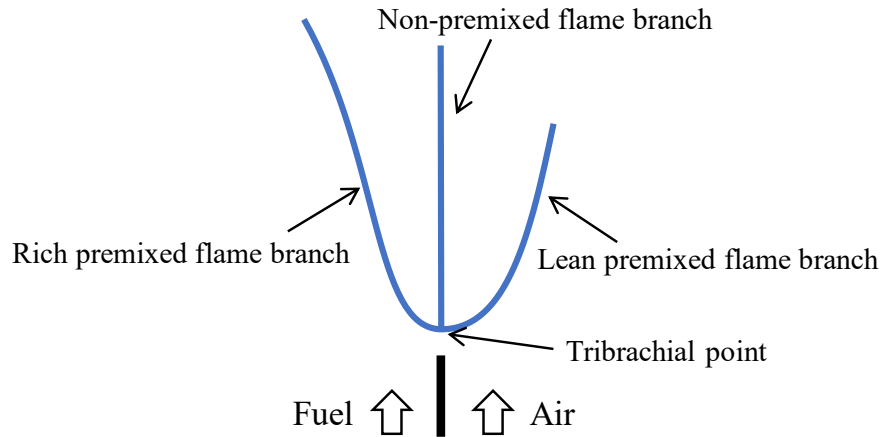
Fig. 1.7: Schematic showing the structure of a tribrachial flame.

1.3.2   Local effects on stratified flames

The focus of this dissertation is solely restricted to premixed flame propagation in inhomogeneous mixtures, i.e., stratified flame propagation. It should be noted that while the term "stratified combustion" sometimes assumes the combustion process in DI SI engines, here it is used to refer to a general combustion phenomenon that does not limit itself to any specific applications. A comprehensive review by Lipatnikov [33] provides a detailed overview of laminar and turbulent stratified combustion. In particular, two basic local effects that are unique to stratified combustion are known [32,33]. One of them is the flame surface generation, which occurs when the mixture equivalence ratio varies along the flame surface, as shown in **Fig. 1.8**(a). The consequence of this effect is straightforward; as different elements of the flame surface propagate at different speeds, the flame surface becomes wrinkled, which results in an increased flame surface area. This effect is expected to be pronounced only in laminar or weakly turbulent flames, as the generation of the flame surface is controlled by turbulent stretching with increasing turbulence intensity. The other effect is known as the "back support" effect, which is associated with flame propagation parallel to the direction of equivalence ratio gradient, as shown in **Fig. 1.8**(b). For example, consider a stratified flame propagating from a stoichiometric region ($\phi = 1$) to a fuel-lean region ($\phi < 1$). This is schematically illustrated in **Fig. 1.9**. When compared with a homogeneous premixed flame (broken lines) that has the same equivalence ratio at the reaction zone ϕ_R, the stratified flame (solid lines) has higher temperature and radical concentration in the burned gas downstream of the reaction zone. Therefore, the reaction rate of the stratified flame is thermally and chemically enhanced by extra heat and mass flux from the burned gas into the reaction zone, resulting in a faster

flame propagation than the corresponding homogeneous premixed flame. This is a typical description of a back-supported flame propagation in a lean stratified mixture, though the detailed mechanism is still debated as will be explained in the following chapters.

While it was conventionally thought that the flame speed in an inhomogeneous mixture is determined by the local composition at the flame location, the presence of the back-support effect contradicts such an assumption. Therefore, understanding how and to what extent the back-support effect occurs is crucial for revealing the fundamental combustion process in the partially premixed regime. In terms of practical significance, accurate prediction of stratified

(a) Flame surface generation   (b) Back support effect
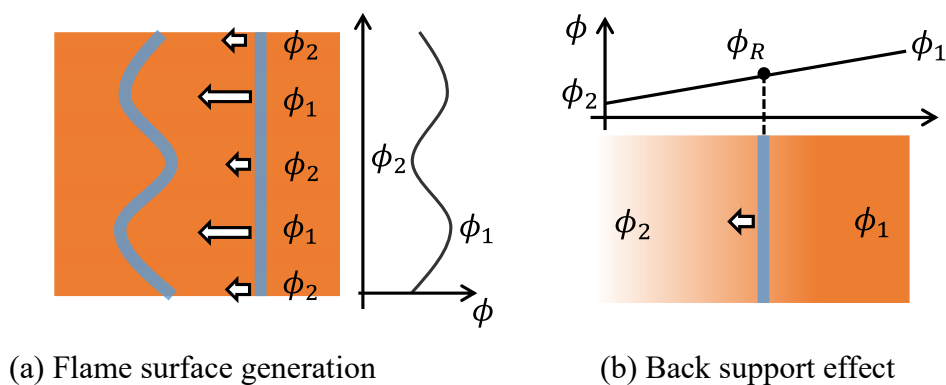
Fig. 1.8: Basic local effects due to mixture stratification: (a) flame surface generation and (b) back-support effect. The arrows represent the local flame speed.
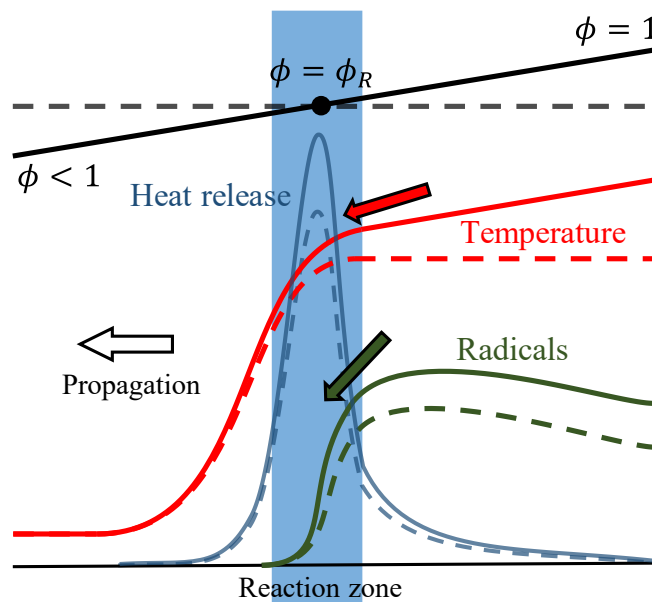
Fig. 1.9: Schematic of equivalence ratio, temperature, radicals, and heat release rate profiles of the stratified flame propagating in a stoichiometric-to-lean mixture (solid lines) and those of the corresponding homogeneously premixed flames (dashed lines).

flame propagation is critical for optimizing the performance of combustion devices. For turbulent combustion modeling in stratified mixtures, the modeling process is further complicated by interactions between flame propagation and mixture concentration. Though there have been a number of continued efforts to develop turbulent combustion models for stratified [45–47] and partially premixed [48–50] flames, small-scale phenomena such as flame surface generation and the back-support effect have been generally neglected in the modeling process [33]. This necessitates further study on the mechanism and significance of such effects. This dissertation will focus on stratified flame propagation parallel to the mixture composition gradient, including the back-support effect.

The local effects on stratified flames, including the back-support effect, have been studied extensively. For turbulent stratified flames, there have been studies on characterizing local phenomena and validating stratified turbulent combustion models. Recent experimental efforts include studies on V-flames [51,52], swirl flames [53,54], bluff-body stabilized flames [55,56], and piloted flames [57,58] with inhomogeneous inlets for studying stratified flames under weak and strong turbulence. Stahler et al. [56] measured temperature and species concentration in a radially stratified turbulent flame. They found that H_2 concentration was increased on the product side of the flame, while the temperature gradient on the product side was only slightly affected by stratification. While these experimental studies confirm the existence of the local stratification effect on the flame, it is difficult to estimate the extent of the effect of stratification on flame properties. Meanwhile, three-dimensional direct numerical simulations (DNS) of stratified turbulent flames with detailed kinetics [59–61] are beginning to provide fundamental insights into local effects of stratification in detail. Richardson and Chen [61] conducted DNS of turbulent slot-Bunsen flame with mixture stratification at the nozzle outlet. They reported that the local flame speed is enhanced in the region where the flame experiences an equivalence ratio gradient, confirming the existence of the back-support effect in turbulent stratified flames. While such DNS studies are capable of elucidating local stratification effects in turbulent flames, they are in general too costly for investigating the effect of stratification under various conditions.

On the other hand, laminar stratified flames are more suitable for precisely controlling mixture stratification and evaluating the local flame speed. As will be reviewed in Chapter 3, there are a number of experimental and numerical studies on laminar stratified flames. Especially, numerical simulations are preferred over experimental approaches as they are capable of imposing large equivalence ratio variation on the flame and extracting detailed chemical and transport processes that drive the local effects. Therefore, the following studies conduct numerical simulations of stratified flame propagation in a laminar flow. In particular, a laminar counterflow configuration is used for the reasons explained in Chapter 2.

1.4   Outline

This dissertation aims to elucidate the local effects of mixture stratification on laminar flame propagation. Numerical simulations of laminar strained flames are conducted to evaluate detailed kinetics and transport phenomena in the stratified flames.

The contents are organized in the following order:

- Chapter 1: Introduction
  First, the roles of combustion technology in the coming decades, especially in terms of mitigating global warming, are discussed. Then, basic concepts regarding premixed flame propagation including the flame speed and the laminar flamelet concept are introduced, and the concept of stratified combustion and the current understanding of local effects are explained. The outline of this dissertation is provided at the end.

- Chapter 2: Numerical Details
  First, the laminar counterflow premixed flame configuration used in the following studies is introduced. Then, the rest of the chapter describes details of the OPUS code including derivation of the one-dimensional governing equations and explanation of numerical schemes and methods.

- Chapter 3: Fundamental Mechanism of Stratified Flame Propagation
  A literature review of the flame speed of laminar stratified flame propagation, especially regarding the mechanism of the back-support effect, is given and strategies to fill the gaps in the previous studies are discussed. The numerical setup and the method of characterizing the stratified flames are explained. The mechanism of the back-support effect on methane/air stratified flames is elucidated by comparing the response of the flame speed and the flame structure to compositional oscillation under different conditions.

- Chapter 4: Strained Flame Propagation in Stratified Mixtures
  The concept of *self-back-support* and *forced-back-support* are proposed and their significance in stratified turbulent flames are discussed. Then, a novel method is devised to characterize strained self-back-supported flames is described, followed by the results that illustrate the effect of flow strain on the magnitude of the back-support effect.

- Chapter 5: Stratified Combustion of Alternative Fuels – Hydrogen-blended Methane
  Based on the mechanism of the back-support effect elucidated in Chapter 3, hydrogen (H_2) addition in the methane/air mixture is proposed as a unique situation where the

back-support effect may be suppressed. In addition, the practical significance of blending hydrogen as an alternative fuel is explained. The effect of hydrogen blending on the back-support effect of methane/air flame is elucidated by comparing the results of two methods to impose stratification.

- Chapter 6: Stratified Combustion of Alternative Fuels – Ammonia
The disadvantages of hydrogen as an alternative fuel are clarified and the potential of ammonia (NH_3) as a fuel for combustion is introduced, followed by a discussion of the significance of studying stratified ammonia/air flames in overcoming the challenges associated with ammonia combustion. The characteristics of the stratified ammonia/air flames are reported for the first time in terms of the response of the flame speed and the NOx emission characteristics.

- Chapter 7: Concluding Remarks
Key findings from Chapters 3-6 are summarized and comments on some topics for future work are provided.

Chapter 2
Numerical Details

In this chapter, details of the OPUS code used for the following numerical analyses are explained. First, characteristics of the counterflow premixed flames are discussed. Secondly, the governing equations solved in OPUS are derived from the general axisymmetric equations and the numerical schemes and methods used for solving the governing equations are introduced.

2.1   Laminar counterflow premixed flames

As explained in Chapter 1, a premixed flame is fundamentally a one-dimensional phenomenon. Therefore, a planar flame is suitable for investigating basic heat and mass transport phenomena in the flame zone. In addition, as turbulent flames in practical combustors experience highly strained flows, a strained flame is used to investigate the effect of flow strain on stratified flame propagation. A common method to analyze a planar strained flame is to utilize counterflow configurations, as shown in **Fig. 2.1**. It is illustrated that planar flames are stabilized in a stagnation flow formed by impinging two streams of reacting mixtures supplied from the opposing nozzles. Toward the stagnation point, the flame experiences compressive flow strain, whose magnitude is controlled by the nozzle velocity or the distance between the opposed nozzles. There are two approaches to stabilize a counterflow premixed flame. One way is to supply an identical mixture of reactants, such as fuel and air, from both nozzles and ignite to create twin planar flames, as shown in **Fig. 2.1**(a). This is called a reactant-to-reactant (RTR) configuration; here, both flames propagate toward the respective nozzles. Another way is to supply a reactant stream from one nozzle and its hot combustion product stream from another, as shown in **Fig. 2.1**(b). This is called a reactant-to-product (RTP) configuration; here, one premixed planar flame is formed and propagates toward the reactant nozzle.

In both counterflow configurations, a planar flame surface is achieved despite the curved streamlines. This is because the governing equations of a stagnation flow can be reduced to a one-dimensional form in the axial direction by a similarity formulation, as will be shown later.

Therefore, in this study, a radial plane that intersects perpendicularly at the stagnation point will be referred to as a "stagnation plane". In both configurations, the axial velocity continuously increases from zero at the stagnation plane to the velocity at the nozzle. Therefore, the flame stabilizes itself at a location where its flame speed and the local axial velocity balance. Specifically, with increasing flame speed, the flame locates itself closer to the nozzle. On the other hand, with increasing nozzle velocity, the flame moves further away from the nozzle. This is an important characteristic of a counterflow premixed flame.

There are additional advantages to the counterflow flame configuration. First, unlike other flame stabilization methods, the flame is detached from the nozzle with an appropriate nozzle velocity, which prevents heat loss from the flame to the nozzle. Secondly, as the flow is dominated by forced convection, buoyancy effects are negligible. In this study, the RTR and RTP configurations are used for different purposes. In particular, the reactant mixture equivalence ratio is transiently varied in the RTR configuration to simulate stratified flames. For details, please refer to the numerical setup of each study in the following chapters.
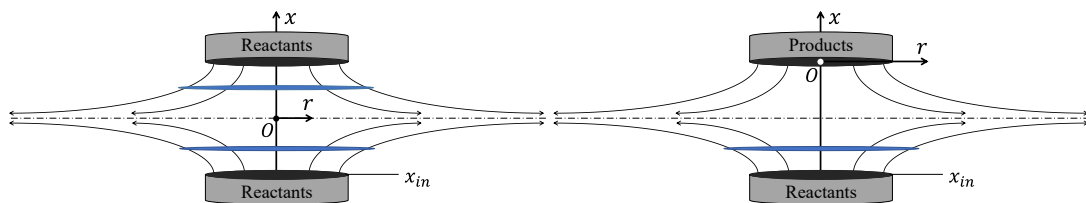
Fig. 2.1: Schematic representation of counterflow premixed flames in the reactant-to-reactant (RTR) configuration (left) and the reactant-product (RTP) configuration (right).

2.2   OPUS

For the numerical analysis of counterflow premixed flames, unsteady one-dimensional conservation equations for mass, momentum, energy, and species mass fractions are solved using the *OPUS* (OPposed Unsteady Strained flames) code [62,63]. OPUS is an unsteady extension of a classic steady counterflow flame code OPPDIF [64], except that the constant-pressure approximation in the original code is relaxed to account for acoustic waves in highly transient problems. Due to its ability to handle a variety of transient problems, it has been used for a number of numerical studies on ignition [63,65,66], extinction under oscillating equivalence ratio [67–69], flame response to oscillating flow [70–72], and stratified flames [20]. OPUS is interfaced with CHEMKIN [73] and Transport [74] libraries for the calculation of chemical kinetics and thermodynamic transport properties, where reaction mechanism with element, species, and reaction constant information, thermodynamic properties, and transport properties are supplied by the user. The following is a description of the governing equations and the numerical schemes and methods implemented in OPUS.

2.2.1 Governing equations

(a) Strain-rate-based vs. velocity-based formulations

The continuity equation of a steady axisymmetric flow with x in the axial direction and r in the radial direction is expressed as follows:

$$\frac{\partial}{\partial x}(r\rho u) + \frac{\partial}{\partial r}(r\rho v) = 0 \tag{2.1}$$

where u and v are the axial and the radial flow velocities, respectively, and ρ is the density. Here, the stream function $\psi(x, r)$, defined as follows, satisfies the continuity equation:

$$\begin{cases} \dfrac{\partial \psi}{\partial r} = r\rho u \\ -\dfrac{\partial \psi}{\partial x} = r\rho v \end{cases} \tag{2.2}$$

When the stream function is expressed as $\psi = r^2 U(x)$ where $U(x)$ is an arbitrary function of x, the following relations are obtained from the above definition:

$$\begin{cases} \rho u = 2U(x) \\ \rho v = -r\dfrac{\partial U(x)}{\partial x} \equiv \rho r V(x) \end{cases} \tag{2.3}$$

This shows that both the axial velocity u and the normalized radial velocity $V(x) \equiv v/r$ depend at most on x. Therefore, using u and V, the Navier-Stokes equation can be transformed into a one-dimensional form. Similarly, the equations for energy and species conservations are also expressed one-dimensionally [75,76]. One such example that satisfies the above relations is the stagnation flow.

When $U(x) = ax$ where a is a constant, Eq. (2.3) is expressed as

$$\begin{cases} \rho u = 2ax \\ \rho v = -ar \end{cases} \tag{2.4}$$

Thus, $2a$ is the axial strain rate of the flow. This is a potential stagnation flow under constant density. Dixon-Lewis et al. [77] extended the above formulation using boundary-layer assumptions and conducted a numerical calculation of counterflow diffusion flames in a stagnating flow. This has been one of the standard one-dimensional formulations of governing equations for counterflow flames [78,79]. As the flow field is specified by the strain rate $2a$, it will be called the strain-rate-based formulation. Note that in this formulation, the nozzle velocity is obtained as a solution and is not given in advance. In addition, as it is based on a potential flow formulation, it assumes a semi-infinite domain, where a point-source of the flow, i.e., the inlet nozzle, is located infinitely far from the stagnation surface [80].

Meanwhile, Kee et al. [80] developed a velocity-based formulation, where the flow is specified by a purely axial nozzle velocity and the distance between the nozzle and the stagnation plane is finite. Instead, the strain rate varies locally in the axial direction and is obtained as a

solution. This formulation is based on the relations Eq. (2.3), in which the stream function is defined in a more general form without the potential flow assumption. OPUS solves an unsteady version of this velocity-based formulation, which is derived in the next part.

(b) Formulation of the governing equations

Overall Continuity

The continuity equation in an axisymmetric, cylindrical coordinate is expressed as

$$\frac{\partial \rho}{\partial t} + \frac{\partial}{\partial x}(\rho u) + \frac{1}{r}\frac{\partial}{\partial r}(r\rho v) = 0 \tag{2.5}$$

where ρ is mixture density. Assuming $\rho(x)$ and substituting V in Eq. (2.3) into the above equation, the one-dimensional form

$$\frac{\partial \rho}{\partial t} + \frac{\partial}{\partial x}(\rho u) + 2\rho V = 0 \tag{2.6}$$

is obtained.

Meanwhile, the equation of state for an ideal gas is expressed as

$$\rho = \frac{p_{tot}\overline{W}}{RT} \tag{2.7}$$

Here, the static pressure p_{tot} is the sum of thermodynamic pressure p_0 and hydrodynamic pressure $p(t, x, r)$; $\overline{W}$ is the mixture-averaged molecular weight; R is the universal gas constant; T is the temperature. In the current formulation, Eq. (2.7) is substituted into Eq. (2.6). First, the time-derivative of the above equation results in the following equation:

$$\frac{\partial \rho}{\partial t} = \frac{\rho}{p_{tot}}\frac{\partial p}{\partial t} - \rho\overline{W}\sum\left(\frac{1}{W_k}\frac{\partial Y_k}{\partial t}\right) - \frac{\rho}{T}\frac{\partial T}{\partial t} \tag{2.8}$$

where Y_k and W_k are mass fraction and molecular weight of kth species, respectively. Substituting the above into Eq. (2.6) yields

$$\frac{\rho}{p_{tot}}\frac{\partial p}{\partial t} - \frac{\rho}{T}\frac{\partial T}{\partial t} - \rho\overline{W}\sum_k\left(\frac{1}{W_k}\frac{\partial Y_k}{\partial t}\right) + \frac{\partial}{\partial x}(\rho u) + 2\rho V = 0 \tag{2.9}$$

Conservation of axial momentum

Conservation of axial momentum in an axisymmetric, cylindrical coordinate is expressed as

$$\begin{aligned}\rho&\left(\frac{\partial u}{\partial t} + v\frac{\partial u}{\partial r} + u\frac{\partial u}{\partial x}\right) \\ &= -\frac{\partial p}{\partial x} + \frac{\partial}{\partial r}\left[\mu\left(\frac{\partial u}{\partial r} + \frac{\partial v}{\partial x}\right)\right] - \frac{\partial}{\partial x}\left[\mu\left(\frac{2}{3}\frac{\partial v}{\partial r} + \frac{2}{3}\frac{v}{r} - \frac{4}{3}\frac{\partial u}{\partial x}\right)\right] + \frac{\mu}{r}\left(\frac{\partial v}{\partial x} + \frac{\partial u}{\partial r}\right)\end{aligned} \tag{2.10}$$

where the mixture viscosity μ is constant in the r direction. The Stokes hypothesis [81] is applied in the above and the following radial momentum equation. The buoyant force is neglect-

ed as the flow is dominated by forced convection [13,80]. In addition, the baroclinic torque that arises from axial density gradient and radial pressure gradient is neglected in the current formulation as the latter is sufficiently small [82]. Substituting the relations in Eq. (2.3), the above equation is transformed into a one-dimensional form:

$$\rho \frac{\partial u}{\partial t} + \rho u \frac{\partial u}{\partial x} + \frac{\partial p}{\partial x} - 2\mu \frac{\partial V}{\partial x} - \frac{4}{3} \frac{\partial}{\partial x} \left(\mu \frac{\partial u}{\partial x} \right) + \frac{4}{3} \frac{\partial}{\partial x} (\mu V) = 0 \qquad (2.11)$$

In the above, the mixture viscosity μ is evaluated by Wilke's formula [74]. As the flow is quasi-one-dimensional, the role of viscous force is limited. The reason to include viscosity in the current formulation is discussed in Appendix B.

Conservation of radial momentum

Conservation of axial momentum in an axisymmetric, cylindrical coordinate is expressed as

$$\rho \left(\frac{\partial v}{\partial t} + v \frac{\partial v}{\partial r} + u \frac{\partial v}{\partial x} \right)$$
$$= -\frac{\partial p}{\partial r} + \frac{\partial}{\partial r} \left[\mu \left(\frac{4}{3} \frac{\partial v}{\partial r} - \frac{2}{3} \frac{v}{r} - \frac{2}{3} \frac{\partial u}{\partial x} \right) \right] + \frac{\partial}{\partial x} \left[\mu \left(\frac{\partial u}{\partial r} + \frac{\partial v}{\partial x} \right) \right] + \frac{2\mu}{r} \left(\frac{\partial v}{\partial r} - \frac{v}{r} \right) \qquad (2.12)$$

Substituting the relations in Eq. (2.3), the above equation is transformed into a one-dimensional form:

$$\rho \frac{\partial V}{\partial t} + \rho u \frac{\partial V}{\partial x} + \rho V^2 - \frac{\partial}{\partial x} \left(\mu \frac{\partial V}{\partial x} \right) + \frac{1}{r} \frac{\partial p}{\partial r} = 0 \qquad (2.13)$$

Meanwhile, from Eq. (2.11), it is seen that $\partial p / \partial x$ is at most a function of t and x. Therefore, the term $(\partial p / \partial r)/r$ in Eq. (2.13) satisfies the following condition:

$$\frac{\partial}{\partial x} \left(\frac{1}{r} \frac{\partial p}{\partial r} \right) = \frac{1}{r} \frac{\partial}{\partial r} \left(\frac{\partial p}{\partial x} \right) = 0 \qquad (2.14)$$

As such, the term $(\partial p / \partial r)/r$ in Eq. (2.14) is a function of t only. Therefore, by expressing it as $\Delta(t)$, Eq. (2.13) is written as follows:

$$\rho \frac{\partial V}{\partial t} + \rho u \frac{\partial V}{\partial x} + \rho V^2 - \frac{\partial}{\partial x} \left(\mu \frac{\partial V}{\partial x} \right) + \Delta = 0 \qquad (2.15)$$

Here, $\Delta(t)$ is an eigenvalue of the flow field and is a part of the solution. Specifically, Δ corresponds to the strain rate in the strain-rate-based formulation [80]. To maintain the banded structure of the iteration matrix, the following trivial equation is introduced:

$$\frac{\partial \Delta}{\partial x} = 0 \qquad (2.16)$$

Conservation of species

Conservation of species mass in an axisymmetric, cylindrical coordinate is expressed as

$$\rho\left(\frac{\partial Y_k}{\partial t} + v\frac{\partial Y_k}{\partial r} + u\frac{\partial Y_k}{\partial x}\right) = \dot{\omega}_k W_k - \left[\frac{1}{r}\frac{\partial}{\partial r}\left(r\rho Y_k V_{r,k}\right) + \frac{\partial}{\partial x}\left(\rho Y_k V_{x,k}\right)\right] \qquad (2.17)$$

where $\dot{\omega}_k$ is mole reaction rate of kth species, while $V_{r,k}$ and $V_{x,k}$ are diffusion velocities of kth species in r and x directions. Under the similarity assumption, $Y_k(t,x)$, $V_{x,k}(t,x)$ and $V_{r,k} = 0$. Therefore, $V_{x,k}$ will be written as V_k in the following part. Eq. (2.17) is thus written in a one-dimensional form as

$$\rho\frac{\partial Y_k}{\partial t} + \rho u\frac{\partial Y_k}{\partial x} + \frac{\partial}{\partial x}\left(\rho Y_k V_k\right) - W_k\dot{\omega}_k = 0 \qquad (2.18)$$

Here, the diffusion velocity V_k is modeled by the mixture-averaged formulation as

$$V_k = -D_{km}\frac{1}{X_k}\frac{\partial X_k}{\partial x} - \frac{D_{km}\Theta_k}{X_k}\frac{1}{T}\frac{\partial T}{\partial x} - V_c \qquad (2.19)$$

where D_{km}, X_k, and Θ_k are mixture-averaged diffusion coefficient, mole fraction, and thermal diffusion ratio of kth species, while V_c is the correction velocity. Here, D_{km} is computed as [83]

$$D_{km} = \frac{\sum_{j\neq k}^{K} X_j W_j}{\overline{W}\sum_{j\neq k}^{K} X_j/D_{jk}} \qquad (2.20)$$

where K is the total number of species. Meanwhile, Θ_k is associated with the thermal diffusion, i.e., Soret effect [84], on light species such as H_2 and H. In the current mixture-averaged formulation, the extent of thermal diffusion is expressed in terms of the ratio Θ_k to the ordinary Fickian diffusion [83]. The correction velocity V_c is introduced artificially to ensure net mass conservation:

$$\sum_k Y_k V_k = 0 \qquad (2.21)$$

Lastly, a system of elementary reactions consisting of K species and N reactions can be written in a general form as

$$\sum_{k=1}^{K} v'_{k,i} M_k \underset{k_{b,i}}{\overset{k_{f,i}}{\rightleftarrows}} \sum_{k=1}^{K} v''_{k,i} M_k , \qquad (i = 1,2,\dots,N) \qquad (2.22)$$
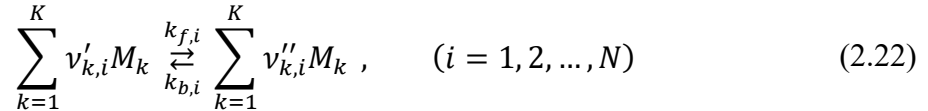
where M_k is the chemical symbol of kth species; $v'_{k,i}$ and $v''_{k,i}$ are stoichiometric coefficients of kth reactant and product species, respectively, in the ith reaction; and $k_{f,i}$ and $k_{b,i}$ are reaction rate constants of forward and backward reactions in the ith reaction. The forward reaction constant $k_{f,i}$ is evaluated by the Arrhenius equation [13]:

$$k_{f,i} = B_{f,i} T^{\beta_{f,i}} \exp\left(-\frac{E_{f,i}}{RT}\right) \qquad (2.23)$$

where $B_{f,i}$ and $\beta_{f,i}$ are Arrhenius parameters; $E_{f,i}$ is the activation energy. On the other hand, the backward reaction constant $k_{b,i}$ is evaluated through the equilibrium constant K_i of the ith

reaction, if not specified otherwise:

$$k_{b,i} = \frac{k_{f,i}}{K_i} \tag{2.24}$$

Using the above constants, the mole reaction rate $\dot{\omega}_k$ in Eq. (2.18) is calculated by

$$\dot{\omega}_k = \sum_i \left(v''_{k,i} - v'_{k,i}\right) \left(k_{f,i} \prod_k C_k^{n'_{k,i}} - k_{b,i} \prod_k C_k^{n''_{k,i}}\right) \tag{2.25}$$

where $n'_{k,i}$ and $n''_{k,i}$ are reaction orders of kth species in the ith forward and backward reactions; and C_k is the mole concentration of kth species.

Conservation of energy

In terms of specific enthalpy h and heat flux q_x and q_r in the x and the r directions, respectively, conservation of energy in an axisymmetric, cylindrical coordinate is expressed as

$$\rho\left(\frac{\partial h}{\partial t} + v\frac{\partial h}{\partial r} + u\frac{\partial h}{\partial x}\right) - \left(\frac{\partial p}{\partial t} + v\frac{\partial p}{\partial r} + u\frac{\partial p}{\partial x}\right) = -\left[\frac{1}{r}\frac{\partial}{\partial r}(rq_r) + \frac{\partial q_x}{\partial x}\right] \tag{2.26}$$

In the above, viscous dissipation and thermal radiation were neglected. The exclusion of thermal radiation is justified as soot production in the flames studied here is negligible [13]. Based on the similarity assumption, the above equation is written in a one-dimensional form as follows:

$$\rho\left(\frac{\partial h}{\partial t} + u\frac{\partial h}{\partial x}\right) - \left(\frac{\partial p}{\partial t} + u\frac{\partial p}{\partial x}\right) + \frac{\partial q_x}{\partial x} = 0 \tag{2.27}$$

Here, the pressure work in the r direction was neglected. The heat flux q_x is modeled by the following expression:

$$q_x = -\lambda\frac{\partial T}{\partial x} + \rho\sum_k h_k Y_k V_k \tag{2.28}$$

where the first and the second term represents heat conduction and heat transport through species mass diffusion, respectively; λ is the mixture-averaged thermal conductivity and h_k is the specific enthalpy of kth species. Here, λ is calculated by averaging species thermal conductivities λ_k [74]:

$$\lambda = \frac{1}{2}\left(\sum_k X_k\lambda_k + \frac{1}{\sum_k X_k\lambda_k}\right) \tag{2.29}$$

Substituting Eq. (2.28) into Eq. (2.27) yields the following equation:

$$\rho\left(\frac{\partial h}{\partial t} + u\frac{\partial h}{\partial x}\right) - \left(\frac{\partial p}{\partial t} + u\frac{\partial p}{\partial x}\right) - \frac{\partial}{\partial x}\left(\lambda\frac{\partial T}{\partial x}\right) + \frac{\partial}{\partial x}\left(\rho\sum_k h_k Y_k V_k\right) = 0 \tag{2.30}$$

In OPUS, the energy equation is solved in terms of temperature. Therefore, in the following, Eq. (2.30) is rearranged into a temperature equation. In terms of the specific heat of kth species h_k, the mixture specific heat is expressed as

$$h = \sum_k h_k Y_k \tag{2.31}$$

Here, the calorific equation of state is

$$h_k = h_k^0 + h_k^S \tag{2.32}$$

where h_k^0 and h_k^S are standard enthalpy of formation and sensible heat of kth species, respectively. The sensible heat h_k^S is determined by the specific heat capacity $c_{p,k}$ and temperature T as

$$h_k^S = \int_{T^0}^{T} c_{p,k} dT \tag{2.33}$$

In addition, the mixture-averaged specific heat capacity is calculated as

$$\bar{c}_p = \sum_k c_{p.k} Y_k \tag{2.34}$$

First, substituting Eqs. (2.31) into Eq. (2.30) yields

$$\rho \frac{\partial}{\partial t}\left(\sum_k h_k Y_k\right) + \rho u \frac{\partial}{\partial x}\left(\sum_k h_k Y_k\right)$$
$$-\frac{\partial p}{\partial t} - u\frac{\partial p}{\partial x} - \frac{\partial}{\partial x}\left(\lambda\frac{\partial T}{\partial x}\right) + \frac{\partial}{\partial x}\left(\rho \sum_k h_k Y_k V_k\right) = 0 \tag{2.35}$$

Calculating the partial derivatives of enthalpy yields

$$\rho\left(\sum_k \frac{\partial h_k}{\partial t}Y_k + \sum_k h_k\frac{\partial Y_k}{\partial t}\right) + \rho u\left(\sum_k \frac{\partial h_k}{\partial x}Y_k + \sum_k h_k\frac{\partial Y_k}{\partial x}\right)$$
$$-\frac{\partial p}{\partial t} - u\frac{\partial p}{\partial x} - \frac{\partial}{\partial x}\left(\lambda\frac{\partial T}{\partial x}\right) + \left[\rho\sum_k \frac{\partial h_k}{\partial x}Y_k V_k + \sum_k h_k\frac{\partial}{\partial x}(\rho Y_k V_k)\right] = 0 \tag{2.36}$$

Rearranging,

$$\rho\sum_k \frac{\partial h_k}{\partial t}Y_k + \rho u\sum_k \frac{\partial h_k}{\partial x}Y_k - \frac{\partial p}{\partial t} - u\frac{\partial p}{\partial x} - \frac{\partial}{\partial x}\left(\lambda\frac{\partial T}{\partial x}\right) + \rho\sum_k \frac{\partial h_k}{\partial x}Y_k V_k$$
$$+\rho\sum_k h_k\frac{\partial Y_k}{\partial t} + \rho u\sum_k h_k\frac{\partial Y_k}{\partial x} + \sum_k h_k\frac{\partial}{\partial x}(\rho Y_k V_k) = 0 \tag{2.37}$$

Using the species conservation in Eq. (2.18) multiplied by h_k and taken the sum over k, the last three terms on the LHS can be substituted by a reaction term to yield

$$\rho \sum_k \frac{\partial h_k}{\partial t} Y_k + \rho u \sum_k \frac{\partial h_k}{\partial x} Y_k - \frac{\partial p}{\partial t} - u \frac{\partial p}{\partial x} - \frac{\partial}{\partial x}\left(\lambda \frac{\partial T}{\partial x}\right) + \rho \sum_k \frac{\partial h_k}{\partial x} Y_k V_k$$
$$+ \sum_k h_k W_k \dot{\omega}_k = 0 \tag{2.38}$$

From Eqs. (2.32) and (2.33), the partial derivative of species enthalpy h_k is expressed as

$$\frac{\partial h_k}{\partial \phi} = c_{p,k} \frac{\partial T}{\partial \phi}, \qquad \phi = t \text{ or } x \tag{2.39}$$

Therefore, using Eqs. (2.39) and (2.34), the energy equation Eq. (2.38) is re-written in terms of temperature as

$$\rho \bar{c}_p \frac{\partial T}{\partial t} + \rho u \bar{c}_p \frac{\partial T}{\partial x}$$
$$- \frac{\partial p}{\partial t} - u \frac{\partial p}{\partial x} - \frac{\partial}{\partial x}\left(\lambda \frac{\partial T}{\partial x}\right) + \rho \left(\sum_k c_{p,k} Y_k V_k\right) \frac{\partial T}{\partial x} + \sum_k h_k W_k \dot{\omega}_k = 0 \tag{2.40}$$

Summary

The governing equations solved in OPUS are summarized as follows.

Overall Continuity:

$$\frac{\rho}{p_{tot}} \frac{\partial p}{\partial t} - \frac{\rho}{T} \frac{\partial T}{\partial t} - \rho \bar{W} \sum_k \left(\frac{1}{W_k} \frac{\partial Y_k}{\partial t}\right) + \frac{\partial}{\partial x}(\rho u) + 2\rho V = 0 \tag{2.41}$$

Conservation of axial momentum:

$$\rho \frac{\partial u}{\partial t} + \rho u \frac{\partial u}{\partial x} + \frac{\partial p}{\partial x} - 2\mu \frac{\partial V}{\partial x} - \frac{4}{3} \frac{\partial}{\partial x}\left(\mu \frac{\partial u}{\partial x}\right) + \frac{4}{3} \frac{\partial}{\partial x}(\mu V) = 0 \tag{2.42}$$

Conservation of radial momentum:

$$\rho \frac{\partial V}{\partial t} + \rho u \frac{\partial V}{\partial x} + \rho V^2 - \frac{\partial}{\partial x}\left(\mu \frac{\partial V}{\partial x}\right) + \Delta = 0 \tag{2.43}$$

Conservation of species:

$$\rho \frac{\partial Y_k}{\partial t} + \rho u \frac{\partial Y_k}{\partial x} + \frac{\partial}{\partial x}(\rho Y_k V_k) - W_k \dot{\omega}_k = 0 \tag{2.44}$$

Conservation of energy

$$\rho \bar{c}_p \frac{\partial T}{\partial t} + \rho u \bar{c}_p \frac{\partial T}{\partial x}$$
$$- \frac{\partial p}{\partial t} - u \frac{\partial p}{\partial x} - \frac{\partial}{\partial x}\left(\lambda \frac{\partial T}{\partial x}\right) + \rho \left(\sum_k c_{p,k} Y_k V_k\right) \frac{\partial T}{\partial x} + \sum_k h_k W_k \dot{\omega}_k = 0 \tag{2.45}$$

Eigenvalue (trivial)

$$\frac{\partial \Delta}{\partial x} = 0 \tag{2.46}$$

2.2.2 Numerical schemes and methods

(a) Calculation domain and boundary conditions

Due to the inherent symmetry, only half of the counterflow flame domain is calculated in the RTR configuration, while the whole reacting flow is calculated in the RTP configuration. The distance between the nozzle is specified for each study. For the reactant stream in the RTR and the RTP configurations, a mixture of fuel and air is supplied. In this study, the temperature and the pressure of the reactant mixture are always kept at 300 K and 0.1013 MPa, respectively. The inlet velocity is kept constant at a specific value for each calculation run. For unsteady calculations, the mixture equivalence ratio is transiently varied to impose compositional stratification on the premixed flame. At the stagnation boundary of the RTR configuration, a symmetric boundary condition is applied, except for the axial velocity where $u = 0 \text{ cm/s}$. For the product stream in the RTP configuration, a hot adiabatic combustion product of the corresponding reactant stream, whose composition is obtained from the equilibrium calculation code EQUIL [85], is supplied. For detailed specifications, please refer to the numerical setup of each study in the following chapters.

(b) Discretization

The governing equations are solved by a finite difference method. OPUS employs a staggered grid system; all dependent variables are represented at the control-volume center nodes, except the axial velocity is represented at the control-volume interfaces. For the species, energy, and momentum equations, a second-order central differencing is used for diffusive terms, while first-order upwind differencing is used for the convective terms. It should be noted that the current discretization scheme is employed with a sufficiently fine grid. For large-scale multi-dimensional combustion fields, more efficient methods such as high-order discretization schemes and adaptive mesh refinement are required. The pressure gradient term $\partial p / \partial x$ in the axial momentum equation and the axial mass flux term $\partial (\rho u) / \partial x$ in the continuity equation are both first-order central differencing due to the staggered-grid system. A uniform grid of 10 μm was applied for all calculations, if not specified otherwise. **Fig. 2.2** shows the grid dependence of the flame speed of a stoichiometric methane/air flame. The true flame speed is estimated from the y-intercept of the second-order fitting curve. It is seen that at 10 μm, the relative error in the flame speed is less than 2%.
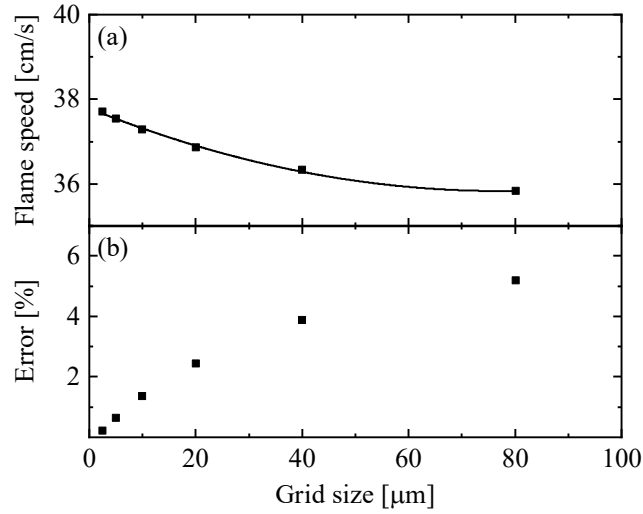
Fig. 2.2: (a) Flame speed of a stoichiometric methane/air flame in an RTR counterflow configuration with different grid sizes. The solid line is a second-order fitting curve. (b) The relative error in the flame speed in comparison to the fitted flame speed at the y-intercept.

(c) Damping term

The term $2\rho V$ in the continuity equation, Eq. (2.9), is discretized by central differencing. This makes the equation only neutrally stable [62,86], thus the iteration process tends to diverge under highly transient variation in the flow field. Therefore, to maintain numerical stability, OPUS introduces a damping term $\sigma_d(\partial^2 p/\partial x^2)$ [87] in Eq. (2.9) so that

$$\frac{\rho}{p_{tot}}\frac{\partial p}{\partial t} - \frac{\rho}{T}\frac{\partial T}{\partial t} - \rho\overline{W}\sum_k\left(\frac{1}{W_k}\frac{\partial Y_k}{\partial t}\right) + \frac{\partial}{\partial x}(\rho u) + 2\rho V - \sigma_d\frac{\partial^2 p}{\partial x^2} = 0 \qquad (2.47)$$

Here, σ_d is the damping coefficient. In this study, σ_d was determined as the smallest value that achieves a stable calculation. For all cases, a typical value of σ_d was about $5 \times 10^{-3} \pm 3 \times 10^{-3}$, which is in the same order as in a previous study [86].

(d) Solution algorithms

By discretizing the governing equations, a system of differential-algebraic equations (DAE), which consists of ordinary differential equations (ODE) and algebraic equations, arises [88,89]. The algebraic equations consist of equations that do not have a time derivative term, such as boundary conditions. DAE is expressed in the form $\boldsymbol{F}(t, \boldsymbol{y}, \boldsymbol{y}') = \boldsymbol{0}$, with the solution vector as $\boldsymbol{y}(t)$ and its first derivative as $\boldsymbol{y}'(t)$. OPUS incorporates a DAE solver DASPK [88,90] which employs a variable-step, variable-order backward-differentiation formula (BDF) to approximate the time derivative $\boldsymbol{y}'(t)$. At each time step, DASPK solves the resulting non-linear equation by a modified Newton's method, where the iteration matrix is reused for as many time steps as possible until convergence fails. When the iteration has converged,

DASPK performs a local error test. If the error test is satisfied, the code takes another time step. If not, the step size and/or integration order are modified and the iteration is attempted again. A typical condition during transient flame propagation was a step size of $O(10^{-6})$ s and an integration order of 3. The relative and absolute convergence criteria for DASPK were set at 1×10^{-6} and 1×10^{-9}, respectively.

DASPK requires a consistent initial condition, meaning that the initial condition must satisfy all the equations in the DAE system. Therefore, a fully converged steady solution is supplied as the initial condition. Here, the steady version of the governing equations Eqs. (2.42) – (2.47) are solved by OPPST, which is a steady counterpart of OPUS. OPPST is implemented with a two-point boundary value problem solver Twopnt [91]. The relative and absolute convergence criteria for Twopnt were set at 1×10^{-6} and 1×10^{-9}, respectively. Twopnt searches for steady-state solutions with a combination of the modified Newton's method and a time marching method. In the latter, time derivatives are included in the governing equations for slow but stable convergence. Such a combination is known to be effective for numerically stiff problems, like combustion problems, where Newton's method tends to be unstable especially at the initial stage of the iteration [92]. OPPST is also used for obtaining solutions of steady flames that are used as references for the unsteady results.

Chapter 3
Fundamental Mechanism of Stratified Flame Propagation

In this chapter, the mechanism of the back-supporting phenomena in methane/air counterflow stratified flames under low-frequency compositional oscillations is numerically studied. First, previous studies on stratified flame propagation are reviewed and the objective of the current study is discussed. Then, the numerical setup specific to the current study is explained and some important parameters to characterize the flame are explained. Lastly, the calculation results of flame response in lean and rich mixtures are presented and discussed in detail. Important findings are summarized at the end.

3.1 Introduction

It was explained in Chapter 1, Section 1.3 that one of the two basic local effects on stratified flames is the *back-support* effect, where the flame speed of a premixed flame propagating into a learner or a richer mixture is modified from the flame speed in a homogeneous mixture at each equivalence ratio. The term was first coined by the research group of the Massachusetts Institute of Technology [93–95] in 1999. However, the idea of a modified flame speed in stratified mixtures has been studied since the 1960s. The initial motivations of such studies were to investigate flame propagation through stratified methane gas in coal mines [96] or to investigate the rate of fire spread in case of an accidental fuel leakage [97,98]. Karim and Tsang [97] developed an experimental apparatus in which a lean premixed flame propagates upward into richer or leaner mixtures. They reported that the flame propagates faster than the corresponding flame speed of the local mixture under stoichiometric-to-lean stratification because of larger buoyancy induced by hotter burned gas. On the other hand, they found that under lean-to-stoichiometric stratification, the flame propagates mostly as fast as the predicted flame speed. However, using a similar apparatus, Karim and Lam [98] reported that the flame speed is increased from the corresponding flame speed at the local equivalence ratio for both rich-to-lean or lean-to-rich stratified mixtures. It is seen that the buoyancy of the burned gas heavi-

ly affects flame propagation in these experimental configurations. Another motivation for the initial studies on the flame propagation in stratified mixtures was the development of stratified charge combustion methods in internal combustion engines, which resulted in several theoretical [99,100], numerical [101], and experimental [102] studies.

Despite the above early efforts, it was not until around 2000 that a direct numerical simulation with detailed kinetics became available to control mixture stratification precisely and to investigate the mechanism of stratified flame propagation in detail. In fact, in the 28th International Symposium on Combustion in 2000, three research groups [95,103,104] presented the results of a numerical study of laminar flame propagation in stratified mixtures. The first group, Marzouk et al. [95], studied the response of a methane/air counterflow flame in the reactant-to-product configuration, where the unburned mixture is supplied from one nozzle and combustion products are supplied from another. In fuel-lean mixtures, when the unburned equivalence ratio is decreased faster than the flame timescale, the flame exhibited a higher flame speed and a wider flammability range. By investigating the flame structure, they concluded that additional fuel consumption reactions continue to occur in the burned gas of stratified flames, as it has higher temperature and concentrations of CO and OH than that in homogeneous mixtures. As such, they called this effect the "back-support" effect, though their explanation was different from the studies that followed. This is probably because their numerical setup was uncommon, and the results were difficult to interpret straightforwardly.

Meanwhile, the second group, Lauvergne and Egolfopoulos [103], conducted numerical studies on strained propane/air flame response to oscillating equivalence ratios. They found that there exists a cut-off frequency in the response of maximum temperature and fuel consumption rate variations, where the amplitude of the response rapidly attenuates with increasing frequency. They developed a method to predict the cut-off frequency based on the thickness of a relevant zone in the flame. Later, similar studies on the extinction limits of strained flames under compositional oscillations were conducted by another research group [68,69]. However, these studies were focused on the global flame characteristics rather than detailed diffusive phenomena inside the flame.

Lastly, the third group, da Cruz et al. [104], conducted numerical simulations of a one-dimensional methane/air premixed flame propagating in a step-stratified mixture. They showed that the flame speed of the stratified flame is increased from that in homogeneous mixtures when the flame propagates into leaner mixtures, while it is decreased when it propagates from stoichiometric to rich mixtures. Observing variations in the temperature and species mole fraction profiles, they concluded that an increased diffusive flux of heat from the burned gas into the reaction zone is the cause of the increased flame speed in the lean mixture. Meanwhile, it was concluded that an increased mass flux of H_2 from the burned gas into the reaction zone is the cause for rich mixtures. After this study, it became common to interpret

the back-supporting phenomena of stratified flames from the aspect of variations in the heat or mass flux from the burned gas.

Motivated by the above study, Kang and Kyritsis [105–108] conducted a series of experimental studies on methane/air stratified flame propagation by developing an apparatus that can control and retain the equivalence ratio gradient using a convective-diffusive balance of fuel concentration in a very slow flow. It was found that under stoichiometric-to-lean stratification, the flame speed was increased. With a simple theoretical analysis, they explained the results in terms of increased heat flux from the burned gas. On the other hand, under stoichiometric-to-rich stratification, the flame speed was temporarily increased and decreased. They concluded that, in addition to the thermal effect, propagation in the rich mixture is influenced by product species in the burned gas.

It is important to study methane/air stratified flame propagation since methane is the simplest hydrocarbon fuel and the conclusions are expected to apply to heavier hydrocarbons. As seen above, early studies by da Cruz et al. and Kang and Kyritsis attributed the cause of the back-support in lean stratified mixtures to an increase in the heat flux from the burned gas. Several studies that followed explained their results in the same manner: Zhou and Hochgreb [78] numerically compared the response of a methane/air counterflow flame in a reactant-to-product configuration under equivalence ratio and temperature gradients and concluded that the flame is back-supported by heat flux in lean mixtures. In a numerical study by Tomita et al [109], the unsteady response of a methane/air counterflow flame location under compositional oscillation was explained by variations in the heat flux from the burned gas. Later, Abdul Rahman [110] analytically confirmed the results. Experimentally, Balusamy et al. [111] developed a novel apparatus to study propane/air laminar stratified flame propagation in a confined chamber, in which a unique injection setup enables the formation of a stratified mixture in a controlled manner. They showed that the flame propagation under rich-to-lean stratification was back-supported, which was explained as a consequence of increased heat flux induced by excess fuel consumed in the burned gas.

On the other hand, Richardson et al. [20] mentioned a chemical effect as the cause of the back-support in a numerical study of lean stratified methane/air counterflow flames. When the flame was back-supported, they noticed that increase in the temperature around the reaction zone was small compared to the increase in the reactive species such as H_2, H, and O. They claimed that these species were increased by the higher temperature of the burned gas and diffused into the reaction zone to increase the flame speed. As reviewed above, the cause of the back-support is disputed in *methane/air* lean mixtures; whether it is driven by thermal or species diffusion is unclear. Interestingly, for *hydrogen/air* stratified mixtures, several recent studies have attributed species diffusion from the burned gas as the dominant driving force of the back-support effect: Zhang and Abraham [112] numerically compared the results of one-

dimensional hydrogen/air stratified flame propagation under normal diffusion model and equal-diffusivity transport model. They concluded that preferential diffusion of H atoms is more important than heat conduction as a cause of the back-support. A similar conclusion was reached by Wei et al. [19] and Shi et al. [113] in numerical studies on stratified hydrogen/air flames.

Meanwhile, in rich methane/air mixtures, da Cruz et al. [104] and Zhou and Hochgreb [78] have all claimed that it is driven by diffusion of H_2 abundant in the rich burned gas. This is also suggested by numerical studies by Shi et al. [114], where propagation of methane/air flames in a rich-to-lean stratified mixture was investigated with artificially modified diffusion coefficients of reactive species, particularly H_2. They showed that preferential diffusion of H_2 from the burned gas is the key driving factor of the back-support effect and developed a Local Stratification Level (LSL) model based on the amount of H_2 accumulated in the flame, which successfully predicted the magnitude of the back-support on the flame speed. A similar conclusion was reached for heavier hydrocarbon/air stratified flames [115].

The following points can be made from the above review of previous efforts to elucidate the mechanism of back-supporting phenomena:

1. Although experimental studies are important for validating the numerical results, the obtained results are often influenced by external factors such as buoyancy effects [97,98], distortion of the flame surface [108], and a non-uniform flow field [111]. More importantly, measurements of detailed heat and mass transport and chemical process in a transiently propagating flame, which are crucial for investigating the mechanism of back-support, are very challenging and rarely conducted.

2. Especially in lean mixtures, both heat and mass flux exist as possible causes of the back-support. Therefore, it is difficult to evaluate the roles of heat and mass diffusion independently. While artificial modification of species diffusion coefficients has been found useful to evaluate the roles of preferential diffusion of species in the back-support effect [112–114], it has not been conducted specifically for lean and rich methane/air stratified flames, which are relevant to practical hydrocarbon fuels.

3. Many of the previous studies on stratified flame propagation have been conducted under a monotonically varying equivalence ratio. This is for the sake of simplicity or to imitate flame propagation in practical applications such as stratified charge engines. However, there are cases where compositional fluctuations occur in the combustion fields, as mentioned in Chapter 1, Section 1.1. While there are studies on flame response under equivalence ratio oscillations [68,69,103], they are more concerned about high-frequency os-

cillations where the flame ceases to respond to variation in the equivalence ratio. Thus, the influence of the back-support effect under compositional oscillation is not sufficient-ly studied.

This chapter focuses on elucidating the mechanism behind the back-support effect of me-thane/air stratified flames. To address the issues mentioned above, the study in this chapter

1. uses OPUS to perform numerical simulation of laminar stratified flames with detailed reaction kinetics to resolve the heat and mass transfer and the chemical process in the flame.

2. investigates the response of methane/air flames with modified diffusion coefficients to elucidate the roles of species diffusion. In addition, global kinetics is also used to further investigate the roles of specific species in the back-support effect.

3. imposes low-frequency, large-amplitude compositional oscillations on the flame so that the flame is influenced by the back-support effect.

3.2   Numerical setup

OPUS was used for steady and unsteady calculations of counterflow premixed flames in reac-tant-to-reactant configuration, as shown in **Fig. 3.1**. The distance between the nozzle and the stagnation plane was set to 21 mm. A mixture of methane and air (mole fractions: 21% O_2 and 79% N_2) was supplied from the nozzle at 300 K and 0.1013 MPa. Considering the flame speed in methane/air mixtures, the nozzle flow velocity u_{in} was set to 50 cm/s so that the flame is sufficiently detached from the nozzle ($x = x_{in}$) and the stagnation plane ($x = 0$ mm).
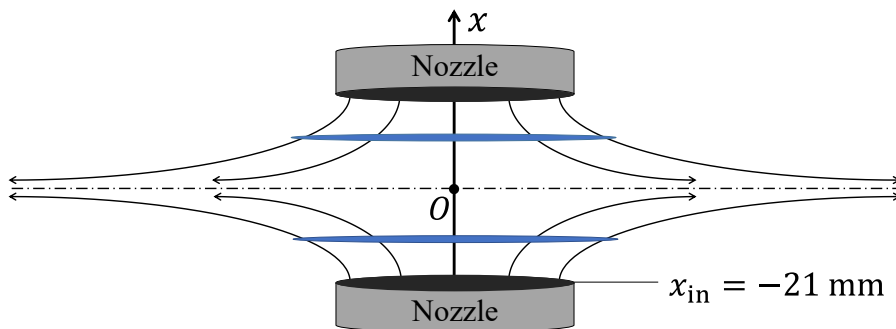
Fig. 3.1: Schematic representation of counterflow premixed flames in the reactant-to-reactant configuration and the computational domain $[x_{in}, 0 \text{ mm}]$, where the inlet is at $x = x_{in} = -21$ mm.

A uniform grid of 10 μm was applied to ensure grid independence. GRI_Mech 3.0 [116], which is an established detailed methane/air reaction model with 53 species and 325 reactions, was used. In this study, the elementary reactions in GRI_Mech 3.0 will be referred to as (GRI #), where # is the number of the elementary reactions compiled in **Table A.1** in Appendix A.

Steady calculations were conducted for premixed flames propagating in homogenous mixtures with equivalence ratios ϕ_{in} ranging from 0.6 to 1.4. As will be explained later, these flames are used as references for evaluating the characteristics of stratified flames. On the other hand, unsteady calculations were conducted for flames propagating under compositional oscillations. At the nozzle, the mixture equivalence ratio $\phi_{in}(t)$ was oscillated in a sinusoidal manner as expressed by

$$\phi_{in}(t) = \phi_m + \phi_a \cos(2\pi f t) \tag{3.1}$$

where ϕ_m, ϕ_a, and f are oscillation center, amplitude, and frequency. The values of the oscillation parameters are shown in **Table 3.1**. The frequencies were chosen so that the oscillation timescale $1/f$ is sufficiently longer than the flame timescale τ_f. Specifically, when τ_f is calculated as the thermal flame thickness $\delta_T = \Delta T/(dT/dx)_{max}$ divided by the flame speed S_c, the resulting τ_f at $\phi_{in} = 0.8$ and 1.2 are approximately 2 ms, which is 500 Hz in frequency.

Table 3.1: Oscillation parameters for the stratified flames with normal diffusion coefficients and detailed kinetics.

ϕ_m		ϕ_a	f [Hz]
Lean	Rich		
0.80	1.20	0.20	10
0.80	1.20	0.50	80

Profiles of temperature, heat release rate, local equivalence ratio, and reactants mole fractions at the moment of stoichiometric-to-lean propagation are shown in **Fig. 3.2**. The definition of the local equivalence ratio is given in Section 3.3. It is seen that the oscillation amplitude of the equivalence ratio attenuates as it is convected toward the flame front. Therefore, as shown in **Table 3.1**, the amplitudes of the oscillation ϕ_a were adjusted so that the range of the equivalence ratio oscillation in lean and rich mixtures are 0.6-1.0 and 1.0-1.4 at the flame location, respectively. Defining the stratification thickness δ_s as $(\phi_{max} - \phi_{min})/(d\phi/dx)_{max}$ at the upstream edge of the preheat zone ($T = 300.1$ K), the resulting non-dimensional stratification thickness δ_s/δ_T under 80-Hz oscillation is respectively 14 and 18 for lean and rich oscillations, where δ_T is the thermal flame thickness in homogeneous mixtures of $\phi_{in} = 0.8$ and 1.2, respectively. Although the current values of δ_s/δ_T are larger than those in previous studies [18,112,114], meaning that the level stratification is moderate due to intense attenuation in the oscillation amplitude, it was large enough for the back-support effect to occur. The
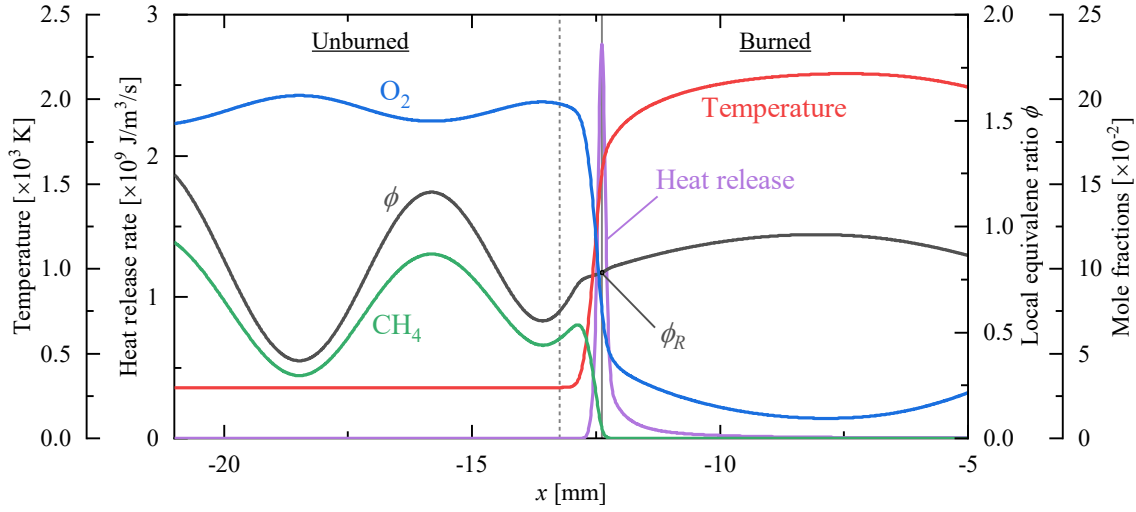
Fig. 3.2: Profiles of temperature, heat release rate, local equivalence ratio, O_2 and CH_4 mole fractions during stoichiometric-to-lean propagation under equivalence ratio oscillation in a lean mixture. The solid and broken vertical lines represent the flame location, i.e., the location of the peak heat release rate, and the upstream edge of the preheat zone, respectively.

results of the unsteady calculations are presented for one cycle of the flame response after it reached a limit cycle.

In addition to the above conditions, calculations with modified diffusion coefficients or with global kinetics are conducted to investigate the roles of species diffusion in stratified flames. Steady and unsteady calculations with 80-Hz oscillation were conducted similarly as explained above. However, the nozzle velocity and the oscillation amplitude were modified for some cases as the flame speed varies depending on the modifications. The oscillation parameters are shown in **Table 3.2**. The reference case (a) is the same as the above numerical conditions, except for the smaller oscillation amplitude. Cases (b) to (e) involves modified diffusion coefficients D_k and Lewis number Le_k of kth species. The global kinetics in case (f) is a four-step reaction mechanism developed by Jones and Lindstedt [117], whose Arrhenius

Table 3.2: Oscillation parameters for stratified flames with modified diffusion coefficients or global kinetics.

Case	u_{in} [cm/s]	ϕ_m		ϕ_a	
		Lean	Rich	Lean	Rich
(a) Reference	50	0.80	1.20	0.40	0.40
(b) $Le_{H2} = 1$	50	0.80	1.20	0.35	0.40
(c) $Le_{H,OH,O} = 1$	40	0.80	1.20	0.60	0.60
(d) $Le_{H2,H,OH,O} = 1$	40	0.80	1.20	0.50	0.50
(e) $D_{H2} = 0$	50	0.80	1.20	0.35	0.40
(f) Global kinetics	50	0.80	1.35	0.40	0.40

parameters and reaction orders were derived by Andersen et al. [118]. For the calculation with global kinetics, a smaller grid size of 5 μm was applied because the reaction zone thickness tends to be narrower than that with the detailed kinetics. In this study, the elementary reactions in the mechanism by Jones and Lindstedt [117] will be referred to as (JL #), where # is the number of the reaction given in Section 3.4. For the specific description of the modifications, please refer to the following results and discussions in Section 3.4.

3.3   Method of flame characterization

3.3.1   Flame location and local equivalence ratio

To evaluate the difference in the characteristics of the unsteady flame propagating under compositional oscillation (*stratified flame*) and those of the steady homogeneous flame propagating in a homogeneous mixture (*homogeneous flame*), they must be compared under the same local mixture characteristics, that is, the local equivalence ratio ϕ. However, as the premixed flames have a finite thickness, a characteristic location in a flame needs to be defined. Conventionally, it has been defined as the peak location of heat release rate x_R [18–20,78,104,112,114,115,119–121], as it is well-defined for a variety of flames regardless of mixture inhomogeneity. In addition, as the reaction zone is usually thinner than the thermal flame thickness by a factor of ten [13] and the minimum length scale of mixture stratification in this study is larger than the flame thickness, the local equivalence ratio ϕ_R at x_R can be considered as the characteristic local equivalence ratio of the reaction zone. The profile of the local equivalence ratio ϕ and the location of ϕ_R is illustrated in **Fig. 3.2**.

Meanwhile, the conventional species-based definition of the equivalence ratio is written as [13]

$$\phi_{\text{species}} = \frac{X_{\text{CH4}}/X_{\text{air}}}{(X_{\text{CH4}}/X_{\text{air}})_{st}} \tag{3.2}$$

where X_k is the mole fraction of a mixture component k, and $(X_{\text{CH4}}/X_{\text{air}})_{st}$ is the stoichiometric fuel-air molar ratio. Based on the definition of the fuel-air ratio, the above expression can be written as

$$\phi_{\text{species}} = \frac{2X_{\text{CH4}}}{X_{\text{O2}}} \tag{3.3}$$

Considering the global reaction $CH_4 + 2O_2 \rightarrow CO_2 + 2H_2O$, the above expression can be interpreted that the numerator represents the minimum moles of O_2 required for complete combustion of CH_4 in the mixture, while the denominator represents the actual moles of O_2 present in the mixture. Therefore, the mixture is stoichiometric when $\phi_{\text{species}} = 1$, is rich when $\phi_{\text{species}} > 1$, and is lean when $\phi_{\text{species}} < 1$.

However, the equivalence ratio defined by Eq. (3.3) cannot represent the local equivalence

ratio at x_R, where the fuel or the oxidizer is mostly depleted. Therefore, extending the above definition, an element-based equivalence ratio ϕ_{element} has been previously adopted [78,113–115]:

$$\phi_{\text{element}} = \frac{2Z_C}{Z_O} + \frac{0.5Z_H}{Z_O} = \frac{2Z_C + 0.5Z_H}{Z_O} \tag{3.4}$$

where Z_C, Z_H, and Z_O are mole fractions of C, H, and O atoms in the mixture, respectively. It is seen that ϕ_{element} is defined as the ratio of the minimum number of O atoms required to oxidize C and H atoms to the actual number of O atoms. As shown in **Fig. 3.3,** the conventional species-based equivalence ratio for $\phi_{in} = 0.60$ and 1.00 decreases rapidly near the reaction zone ($x - x_R = 0$ mm) because the fuel is depleted faster than the oxidizer, while that for $\phi_{in} = 1.40$ increases rapidly near the reaction zone because the oxidizer is depleted. On the other hand, the element-based equivalence ratio is well-defined throughout the reacting mixture, where $x - x_R > 0$ mm is the downstream side of the flame. Therefore, the local equivalence ratio is defined by Eq. (3.4) in this study. In the following part, ϕ_{element} will be written as ϕ.

However, as shown in **Fig. 3.3,** the local values of element-based equivalences ratio at the reaction zone ϕ_R fluctuate from their unburned values ϕ_{in}. This is because of preferential diffusion of light species over heavier species, which disrupts the local atomic composition of the mixture [20,114,115]. Therefore, even for homogeneous flames, the unburned mixture
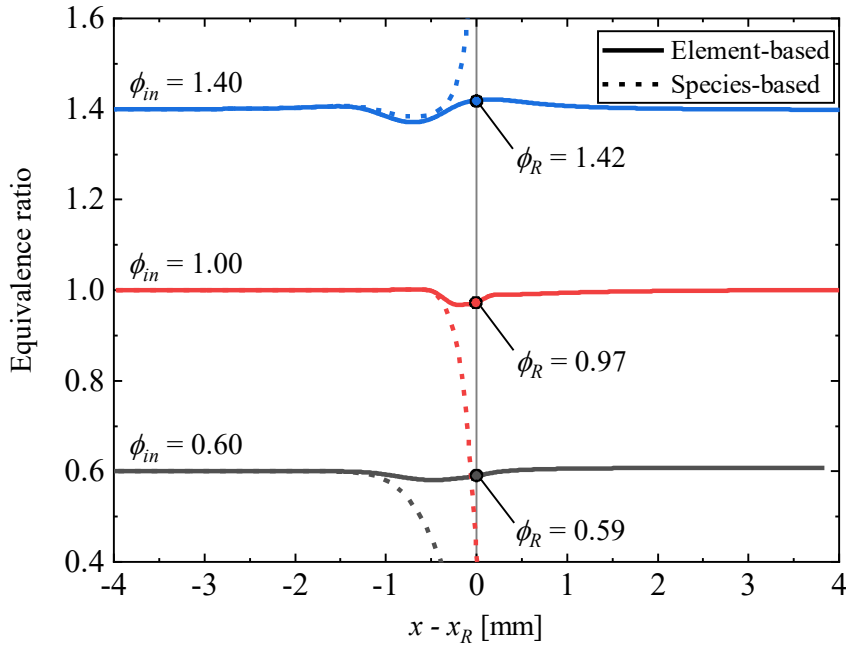
Fig. 3.3: Profiles of element-based (solid lines) and species-based (broken lines) equivalence ratio in methane/air homogeneous flames with the inlet equivalence ratio 0.6, 1.0, and 1.4. The x-axes are shifted so that the reaction zone is at $x - x_R = 0$ mm for all cases.

equivalence ratio at the inlet ϕ_{in} is different from the local equivalence ratio ϕ_R at the reaction zone. To minimize the influence of such fluctuation in ϕ_R on the accuracy of the comparison between the stratified and homogeneous flames, ϕ_R instead of ϕ_{in} was defined as the characteristic equivalence ratio for both stratified and homogeneous flames.

3.3.2 Flame speed

As discussed in Chapter 1, Section 1.2, the flame speed of stratified and homogeneous flames is evaluated as the fuel consumption speed:

$$S_c = \frac{1}{\rho_u Y_{f,u}} \int_{x_{in}}^{x=0\ mm} (-W_f \dot{\omega}_f) dx \tag{3.5}$$

where ρ_u is the unburned gas density; $Y_{f,u}$ is the fuel mass fraction in the unburned gas; W_f and $\dot{\omega}_f$ are respectively the molecular weight and the molar reaction rate of the fuel. Unburned mixture properties ρ_u and $Y_{f,u}$ are calculated from ϕ_R and the temperature at x_R. The integration range is the entire calculation domain. In the above expression, the denominator $Y_{f,u}$ is originally $Y_{f,u} - Y_{f,b}$ in the theoretical derivation [16], where $Y_{f,b}$ is the fuel mass fraction on the burned side. However, especially in rich stratified mixtures, $Y_{f,b}$ cannot be evaluated unambiguously in the burned gas where the mixture composition continuously varies in the downstream direction [104,113–115]. Therefore, following the convention adopted in previous studies [104,113–115], $Y_{f,u} - Y_{f,b}$ is replaced by $Y_{f,u}$. Such simplification is reasonable in this study because $Y_{f,b}$ is negligibly small even in rich mixtures considered in this chapter, as will be shown in the following results.

3.3.3 Effect of flow strain on the flame speed

Unlike in previous studies of transient one-dimensional flame propagation [19,104,112–115], the flame is *stretched* in the present counterflow configuration. For planar flames, the stretch rate is equivalent to the local strain rate a_R tangent to the flame surface [13]. In the axisymmetric counterflow configuration considered in this study, a_R is equivalent to the local tangential flow divergence at x_R, which is twice the value of the radial strain rate:

$$a_R = [(\nabla \cdot \boldsymbol{v})_t]_R = \left[\frac{1}{r}\frac{\partial}{\partial r}(rv)\right]_R = (2V)_R \tag{3.6}$$

It is well-known that the flame speed is increased or decreased with increasing stretch rate when an unbalance exists between the diffusive flux of heat and mass in the preheat zone [13]. The sensitivity of the flame speed to the stretch rate depends on the extent of the unbalance in the heat and mass diffusion. **Figure 3.4** shows the response of the flame speed of steady counterflow flames in homogeneous mixtures to different local strain rates a_R evaluated from the local radial velocity gradient at x_R. The response is qualitatively similar behavior to previous

reports [122,123]; although not shown here in a full range, with increasing strain rate the flame speed decreases linearly for both lean and rich cases.

Although the inlet velocity is fixed in the unsteady calculation of stratified flames, a_R fluctuates due to variation in the flow expansion ratio, which is caused by a variation in the heat release rate. The shaded area in the figure corresponds to the maximum range of a_R fluctuation for the stratified flames under compositional oscillations. It can be seen that the variation in the flame speed caused by the stretch effect is less than 1 % for both rich and lean mixtures, which is small enough as compared to the maximum magnitude of the modification of the stratified flame speed considered in this chapter. Therefore, when comparing the characteristics of the stratified and the homogeneous flames, the influence of the differences in a_R on the flame speed is ignored in the current analysis. The effect of flow strain on the stratified flame propagation is investigated in Chapter 4.
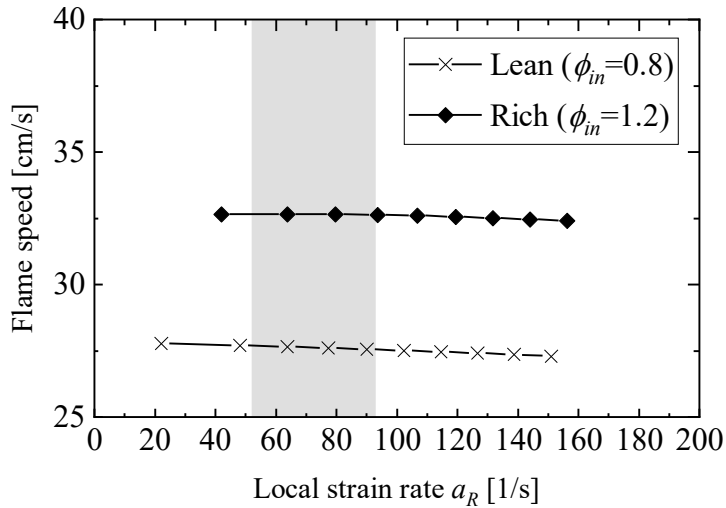
Fig. 3.4: Response of the flame speed of counterflow premixed flames with detailed kinetics in lean ($\phi_{in} = 0.8$) and rich ($\phi_{in} = 1.2$) mixtures. The shaded area represents the maximum range of local strain rate fluctuation in the following analysis.

3.4 Results and discussions

3.4.1 Burned gas characteristics

As the previous studies suggest that the back-support effect is driven by variations in the heat or mass flux from the burned gas, it is beneficial to clarify the temperature and the chemical composition of the burned gas under different equivalence ratios. In many cases, the state of the burned gas of a premixed flame can be approximated to be in thermodynamic equilibrium [13]. Therefore, using the numerical code EQUIL [85], equilibrium calculations were performed for methane/air mixtures at various equivalence ratios ranging from $\phi = 0.5$ to 1.6

under the temperature and the pressure conditions of this study. The results are shown in **Fig. 3.5**.

In **Fig. 3.5**(a), it is seen that the adiabatic temperature T_{ad}, which can be interpreted as the approximate burned gas temperature of the corresponding premixed flame, peaks around stoichiometry ($\phi = 1.0$) and decreases toward leaner ($\phi < 1$) or richer ($\phi > 1$) mixtures. As the rate of combustion is strongly influenced by the reaction temperature, the flame speed also peaks around stoichiometry and decreases in leaner or richer mixtures, as will be shown later. Therefore, in stratified flames, it is expected that the heat flux from the burned gas is increased when propagating from stoichiometric to leaner or richer mixtures. Mole fractions of the major product species, H_2O and CO_2, also peak around stoichiometry. However, as they are relatively stable, they are usually not considered as the driving factors of the back-support effect. In **Fig. 3.5**(b), the mole fractions of the residual oxidizer, O_2, is negligible in the rich mixtures and increases in lean mixtures with decreasing ϕ. Meanwhile, in **Fig. 3.5**(d), the mole fractions of the unburned fuel, CH_4, is extremely small regardless of ϕ, which contradicts the expectation based on the global reaction $CH_4 + 2O_2 \rightarrow 2H_2O + CO_2$. The reason for this trend is because, with detailed kinetics, most of the CH_4 is decomposed into CO
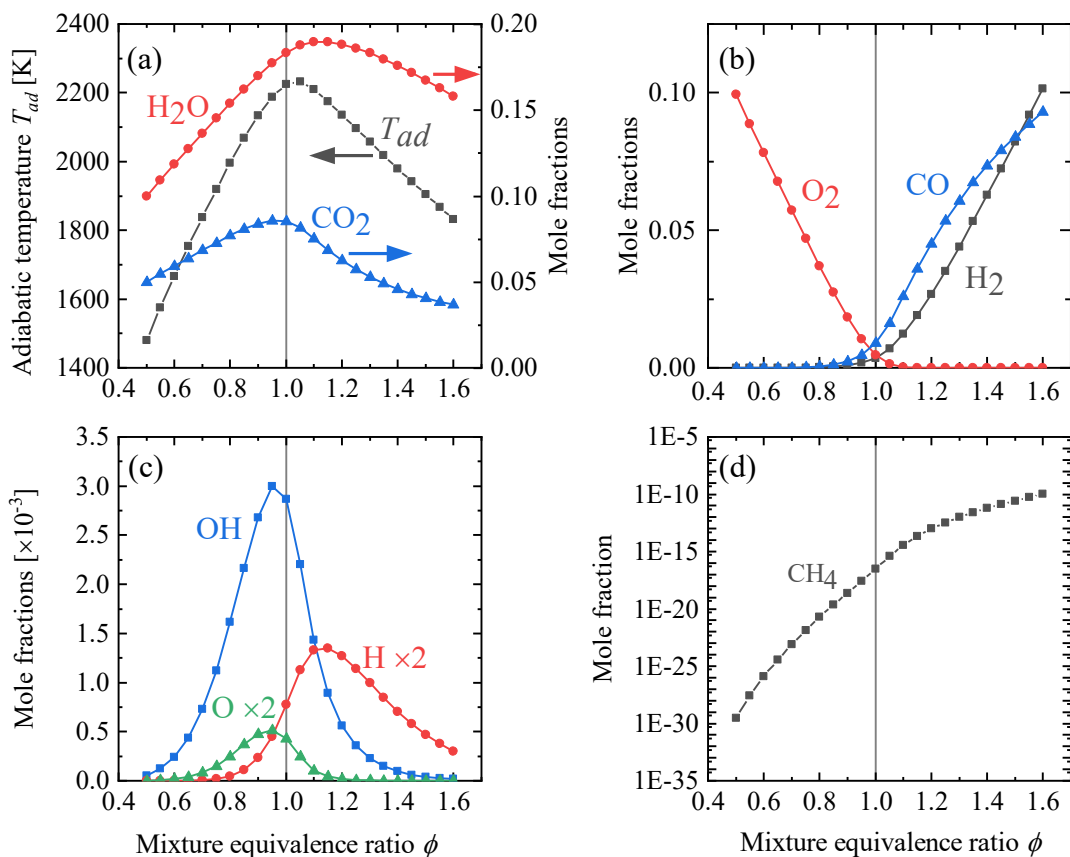
Fig. 3.5: Adiabatic temperature T_{ad} and major species mole fractions of equilibrium composition for methane/air mixtures under different equivalence ratios ϕ.

and H_2 in rich mixtures. This can be seen in **Fig. 3.5**(b), where the mole fractions of CO and H_2 is negligible in lean mixtures but increases in rich mixtures with increasing ϕ. Other important species are OH radicals and H/O atoms shown in **Fig. 3.5**(c). In methane and other hydrocarbon premixed flames, these highly reactive species diffuse from the burned gas toward the unburned mixture and drive initial fuel decomposition reactions

$$CH_4 + OH \rightarrow CH_3 + H_2O \qquad \qquad \text{(GRI 98)}$$
$$CH_4 + H \rightarrow CH_3 + H_2 \qquad \qquad \text{(GRI 53)}$$
$$CH_4 + O \rightarrow CH_3 + OH \qquad \qquad \text{(GRI 11)}$$
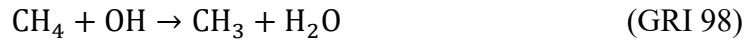
and many chain-branching reactions in the reaction zone of the flame [13]. It is seen that they all peak around stoichiometry, which is similar to the trend of the adiabatic temperature T_{ad}. As will be shown later, this is one of the reasons that makes elucidation of the cause of the back-support effect in lean mixtures difficult, as both heat flux and mass flux of reactive species from the burned gas is increased when the flame propagates from stoichiometric to lean mixtures. The above trends will be revisited for interpreting the results discussed in the following sections.

3.4.2 Flame response in a lean mixture

Responses of the flame speed $S_{c,s}$ of stratified flames under oscillating equivalence ratio and the homogeneous flame speed $S_{c,h}$ at each local mixture equivalence ratio ϕ_R at the reaction zone are shown in **Fig. 3.6**. As the laminar flame speed of methane/air flames peaks around stoichiometry [13], $S_{c,h}$ decreases with decreasing ϕ_R. Under oscillating equivalence ratio, $S_{c,s}$ increases from $S_{c,h}$ with decreasing ϕ_R and decreases from $S_{c,h}$ with increasing ϕ_R. These trends are consistent with previous numerical and experimental studies on the back-support effect of methane/air stratified flames [20,78,104,105,114,115]. With a higher frequency, the deviation of $S_{c,s}$ from $S_{c,h}$ becomes larger. This is because the spatial gradient of the equivalence ratio variation increases, which leads to a larger gradient of temperature and species mole fractions on the downstream side of the flame.

It has been considered that when the time scale of the compositional oscillation is sufficiently long as compared to that of the flame time scale, the stratified flame responds in a quasi-steady manner, meaning that the flame structure and the global flame characteristics such as the flame speed will be the same as those of the homogeneous flames at each local equivalence ratio. However, the current results demonstrate that when the amplitude of the oscillation is sufficiently large, the flame speed deviates from that of homogeneous flames due to the back-support effect, even under low-frequency oscillations. Therefore, the response of the flame speed under compositional oscillations should be classified from another
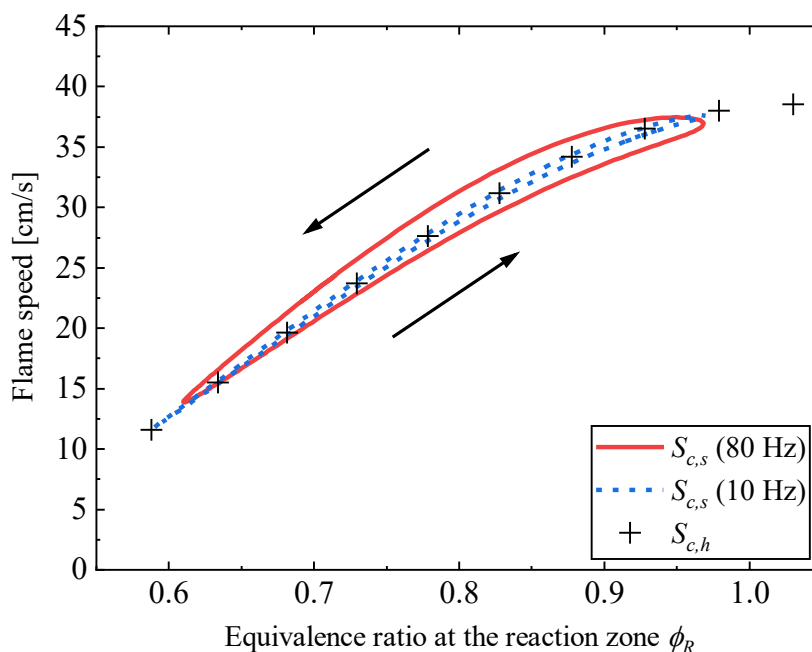
Fig. 3.6: Response of the flame speed $S_{c,s}$ of stratified flames in lean mixtures under 80 Hz and 10 Hz oscillations and the flame speed $S_{c,h}$ of homogeneous flames with the same local equivalence ratio at the reaction zone ϕ_R.

perspective. When the spatial gradient of mixture composition is sufficiently large, the stratified flame speed $S_{c,s}$ deviates from the homogeneous flame speed $S_{c,h}$, regardless of the time scale of the oscillation. On the other hand, when the spatial gradient is sufficiently small, the stratified flame speed $S_{c,s}$ will be the same as the homogeneous flame speed $S_{c,h}$. In the experimental studies of stratified flames propagating under monotonically decreasing equivalence ratio, Kang and Kyritsis [105] named the latter situation as "quasi-homogeneous". The current results show that when dealing with the flame response under large compositional oscillations, the quasi-homogeneous assumption may not be justified even when the quasi-steady assumption holds.

To elucidate the mechanism of the back-support effect in lean mixtures, the variation in the flame structure is investigated. In the following discussion, the moment when $S_{c,s}$ is increased from $S_{c,h}$ under decreasing equivalence ratio is considered, as the flame response is symmetric around the center of the oscillation. **Figure 3.7** shows the profiles of heat release rate, temperature, and species mole fractions of a stratified flame (80 Hz) at $\phi_R = 0.78$ under decreasing equivalence ratio along with the profiles of the corresponding homogeneous flame.

In **Fig. 3.7**(a), it is shown that the heat release rate of the stratified flame is increased, as expected from the increased flame speed. Moreover, the thermal thickness of the stratified flame is thinner, as indicated by the steeper temperature gradient in the preheat zone
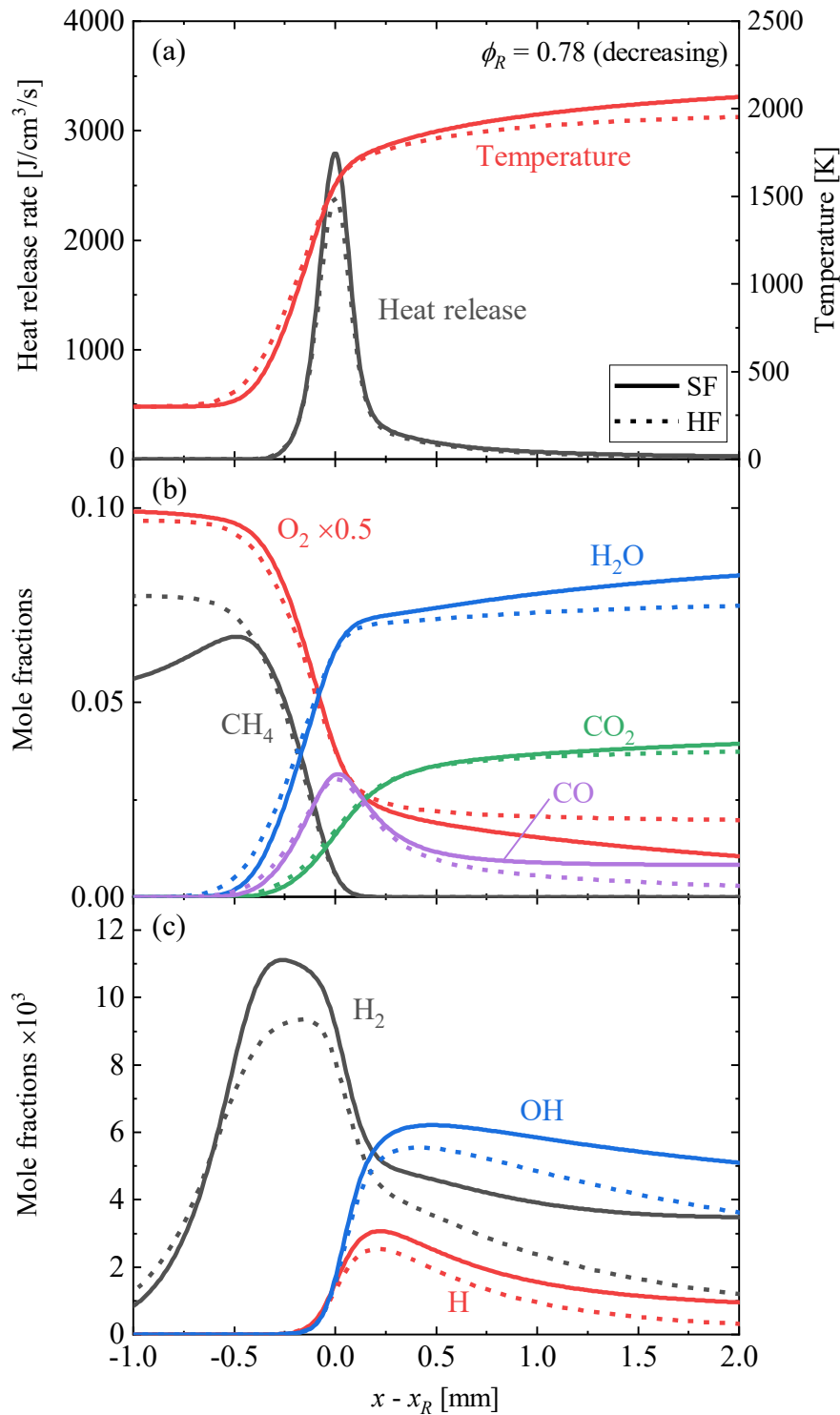
Fig. 3.7: Profiles of heat release rate, temperature, and major species mole fractions of the stratified flame (SF, 80 Hz) in a lean mixture at $\phi_R = 0.78$ under decreasing local equivalence ratio and those of the homogeneous flame (HF) with the same ϕ_R. The x-axes are shifted so that the reaction zone is at $x - x_R = 0$ mm for both flames.

(-0.5 mm $< x - x_R < 0$ mm), which is also a sign of the increased flame speed. On the other hand, the temperature on the downstream side of the flame ($x - x_R > 0$ mm) is higher for the stratified flame. This is because the burned gas on the downstream side of the stratified flame is richer, i.e., closer to stoichiometry, than that of the homogeneous flame, which results in a higher temperature as explained previously in **Fig. 3.5**. Therefore, the heat flux from the burned gas is increased for the stratified flame. Although, the temperature around the reaction zone ($x - x_R = 0$ mm) is only slightly varied, as also mentioned by Richardson et al. [20].

Figure 3.7(b) shows the profiles of major species mole fractions. Since the flame is propagating in a lean mixture, the excess oxidizer O_2 exists and the fuel CH_4 is depleted in the burned gas. Meanwhile, O_2 and CH_4 respectively increases and decreases toward the unburned mixture ($x - x_R > 0$ mm), as it is leaner compared to that of the homogeneous flame. It should be mentioned that the spatial gradient of CH_4 is slightly increased in the preheat zone (-0.5 mm $< x - x_R < 0$ mm) of the stratified flame, despite the decreasing trend toward the upstream region of the preheat zone ($x - x_R < -0.5$ mm). This is due to the increased fuel consumption of the stratified flame, which implies that the back-support effect is not driven by the spatial gradient in the unburned mixture. The influence of species diffusion on the upstream side of the flame will be further investigated in Chapter 5. Other major species such as H_2O, CO_2, and CO are all increased in the burned gas, as expected from the equilibrium composition in **Fig. 3.5**. As these species are more stable compared to others, they are not expected as the driving factor of the back-support effect.

Mole fractions of the more reactive species, H_2, OH, and H, are shown in **Fig. 3.7**(c). Although not shown in the figure, mole fractions of the O atom were similar to that of the OH radicals. On the downstream side, the mole fractions of these species are increased from those of the stratified flame, as expected from the equilibrium composition in **Fig. 3.5**. This results in increased mole fractions around the reaction zone of the stratified flame due to the increased diffusive flux from the downstream region. In addition to the downstream distribution, a pool of H_2 exists on the upstream side of the reaction zone ($x - x_R < 0$ mm). Along with the H_2 composition in the burned gas, this H_2 pool increases with increasing equivalence ratio. Therefore, it is seen that the H_2 pool of the stratified flame is larger as compared to that of the homogeneous flame. This results in an increased H_2 consumption, which occurs around $x - x_R = 0.1$ mm.

From the above observations, it is shown that both temperature and the reactive species mole fraction profiles in the burned gas are increased for the stratified flame under decreasing equivalence ratio, and it is difficult to conclude which is the dominant factor that drives the back-support effect. Therefore, the response of stratified flames with modified diffusion coefficients and global kinetics are investigated in the following discussion.

3.4.3 Lean flame response with modified diffusion and kinetics

The roles of species diffusion were investigated by (A) modifying their diffusion coefficients or (B) using a global reaction model for the calculation of the response of stratified and homogeneous flames. For approach (A), the Lewis number $Le_k = \alpha/D_k$ of kth species was modified. Here, α is the mixture thermal diffusivity and D_k is the mixture-averaged diffusion coefficient of kth species. The reactive species such as H_2, H, OH, and O usually have Lewis numbers less than unity, e.g., $Le_{H2} = 0.28$, $Le_H = 0.16$, $Le_{OH} = 0.70$, and $Le_O = 0.69$ [124], which means that they diffuse preferentially over heat conduction. Therefore, imposing $Le_k = 1$ for those species would weaken their diffusivity. If the back-support is driven by species diffusion rather than heat, it is expected to weaken the increase in the stratified flame speed. Numerical studies on the back-support effect with modified Le_k has been conducted recently on hydrogen/air stratified flames [112,113] and methane/air stratified flames [114], but this is the first effort to investigate the flame response in lean and rich mixtures separately. This is important as the composition of burned gas varies asymmetrically around stoichiometry, as shown in **Fig. 3.5**, and it has been considered that the cause of the back-support is different in lean and rich mixtures. In addition, approach (A) includes a case where the diffusivity of H_2 is neglected, i.e., $D_{H2} = 0 \text{ m}^2/\text{s}$, to further clarify differences in the roles of H_2 and other species H, OH, and O.

On the other hand, approach (B) is a more explicit method in that the reaction kinetics used for calculation does not include H, OH, and O. Instead, it consists of the four-step global reactions by Jones and Lindstedt [117],

$$CH_4 + 0.5O_2 \rightarrow CO + H_2 \qquad\qquad \text{(JL 1)}$$
$$CH_4 + H_2O \rightarrow CO + 3H_2 \qquad\qquad \text{(JL 2)}$$
$$H_2 + 0.5O_2 \leftrightarrow H_2O \qquad\qquad \text{(JL 3)}$$
$$CO + H_2O \leftrightarrow CO_2 + H_2 \qquad\qquad \text{(JL 4)}$$

which include only H_2 and CO as intermediate species. With this kinetics, CH_4 is primarily consumed by O_2 in (JL 1), and H_2 only plays a role as an intermediate species between CH_4 and H_2O. Therefore, the contribution of the diffusion of reactive species from the burned gas on flame propagation is practically eliminated.

Figure 3.8 shows the response of the flame speed of stratified flames under 80-Hz oscillation and those of homogeneous flames calculated with approaches (A) and (B). The modified calculation parameters are shown in **Table 3.2**. Here, the oscillation amplitude ϕ_a and the inlet velocity was adjusted for cases (b-f) so that the variation in the equivalence ratio gradient at the reaction zone is comparable to case (a). In **Fig. 3.8**(a), the response of the flame speed calculated with mixture-averaged diffusion coefficients and detailed kinetics is shown as a

reference. **Figures 3.8**(b) and (c) respectively show the response of the flame speed with (b) $Le_{\text{H2}} = 1$ and (c) $Le_{\text{H,OH,O}} = 1$. It is seen that in both cases, the deviation of $S_{c,s}$ from $S_{c,h}$ is smaller than the case (a) with mixture-averaged diffusion coefficients, implying that preferential diffusion of both H_2 and other reactive species H, OH, and O take part in modifying the stratified flame speed. In fact, when the Lewis numbers for all reactive species are set to unity in **Fig. 3.8**(d), the difference between $S_{c,s}$ and $S_{c,h}$ becomes negligibly small, i.e., the back-support effect disappears. Considering that the heat conduction from the burned gas still exists in case (d), it seems that preferential diffusion of reactive species such as H_2, H, OH, and O play a dominant role in driving the back-support effect. Also, the flame speed is overall smaller in cases (b) with $Le_{\text{H,OH,O}} = 1$ and (d) with $Le_{\text{H2,H,OH,O}} = 1$ by up to 10 cm/s as compared to the reference case. This shows that the preferential diffusion of H, OH, and O is important for driving flame propagation even in homogeneous flames [125]. **Figure 3.8**(e) with $D_{H2} = 0$ m^2/s shows the flame response with the diffusion of H_2 eliminated. It is seen that the deviation of $S_{c,s}$ from $S_{c,h}$ is on a similar magnitude as that in case (b) $Le_{H2} = 1$, which implies that diffusion of H_2 without preferential diffusion ($Le_{H2} = 1$) has negligible contribution on the flame propagation. Therefore, similar to case (b), the back-support effect observed in case (e) is primarily driven by preferential diffusion of H, OH, and O. **Figure 3.8**(f) corresponds to approach (B) with the global kinetics. It is seen that, similar to case (d) with $Le_{\text{H2,H,OH,O}} = 1$, the deviation of $S_{c,s}$ from $S_{c,h}$ is negligibly small. Since only heat conduction from the burned gas takes place in this case, it also shows that heat conduction alone cannot cause the back-support effect.

Contrary to the previous conclusions [78,95,104,107] that the back-support effect in a lean mixture is driven by heat conduction from the higher burned gas temperature, the above results show that the influence of burned gas temperature on stratified flame propagation is negligibly small and preferential diffusion of reactive species such as H_2, H, OH, and O is the driving factor of the back-support effect. A similar conclusion was reached by Shi et al. [113] in a numerical study on hydrogen/air stratified flame propagating from rich to lean mixtures. They concluded that only fast-diffusing species from the burned gas influences the reaction rate of the stratified flame as they must diffuse faster than the flame speed to "catch up" the propagation of the reaction zone. To the best of the author's knowledge, Richardson et al. [20] is the only previous report that associated the cause of the back-support in a lean methane/air mixture to species diffusion rather than heat conduction. However, their report was based only on the observation of the temperature and species mole fraction profiles of the stratified flame. As already mentioned, the study in this chapter is the first effort to clarify the influence of preferential diffusion of reactive species in a lean mixture using modified diffusion coefficients and global kinetics.
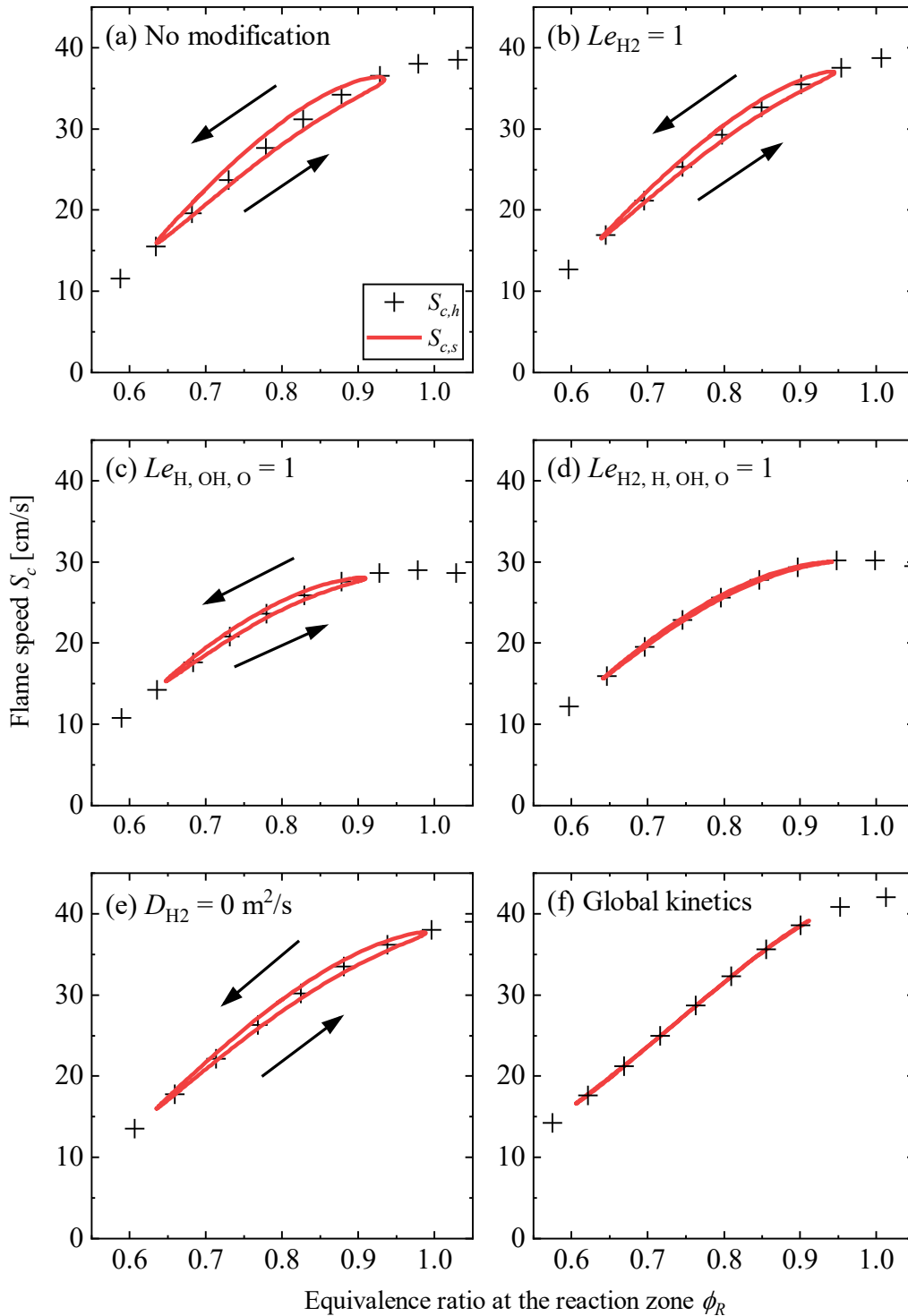
Fig. 3.8: Solid lines: Responses of the flame speed $S_{c,s}$ of stratified flames (80 Hz) in a lean mixture with (a) mixture-averaged diffusion coefficients; (b-e) modified diffusion coefficients: (b) $Le_{H2} = 1$, (c) $Le_{H,OH,O} = 1$, (d) $Le_{H2,H,OH,O} = 1$, and (e) $D_{H2} = 0$ m²/s; and (f) global kinetics. Symbols: The flame speed $S_{c,h}$ of homogeneous flames with the same local equivalence ratio at the reaction zone ϕ_R.

3.4.4 Flame response in a rich mixture

Response of the flame speed $S_{c,s}$ of stratified flames under oscillating equivalence ratio and the homogeneous flame sped $S_{c,h}$ at each local mixture equivalence ratio ϕ_R at the reaction zone are shown in **Fig. 3.9**. It is seen that $S_{c,h}$ decreases with increasing ϕ_R. Similar to the flame response in the lean mixture, $S_{c,s}$ increases from $S_{c,h}$ with decreasing ϕ_R and decreases from $S_{c,h}$ with increasing ϕ_R. These trends are consistent with previous numerical studies on methane/air stratified flames [104,114,115]. As expected, the deviation of $S_{c,s}$ from $S_{c,h}$ becomes larger with increasing oscillation frequency, indicating that the quasi-homogeneous assumption does not hold for the current case even though the oscillation frequencies are sufficiently small. Compared to the flame response in a lean mixture, it is seen that the deviation of $S_{c,s}$ from $S_{c,h}$ is larger. Moreover, at the richest and the leanest turning points, $S_{c,s}$ does not equal $S_{c,h}$ even though the spatial gradient of the equivalence ratio is expected to be zero at those points. This is due to the "memory effect" of the back-supporting phenomenon [107,111,114], which is a hysteresis of the back-support effect under transient variation in the equivalence ratio at the reaction zone ϕ_R. This effect is observed because the burned gas composition is not homogeneous yet at the moment when the equivalence ratio gradient becomes zero.
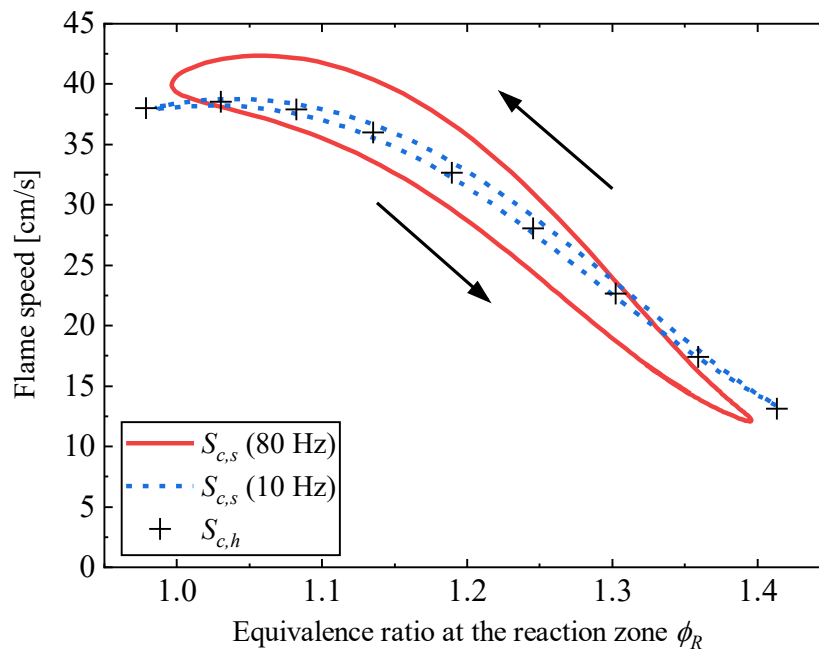
Fig. 3.9: Response of the flame speed $S_{c,s}$ of stratified flames in lean mixtures under 80 Hz and 10 Hz oscillations and the flame speed $S_{c,h}$ of homogeneous flames with the same local equivalence ratio at the reaction zone ϕ_R.

To elucidate the mechanism of the back-support effect in rich mixtures, the variation in the flame structure is investigated. In the following discussion, again, the moment when $S_{c,s}$ is increased from $S_{c,h}$ under decreasing equivalence ratio is considered, considering the symmetry of the flame response. **Figure 3.10** shows the profiles of heat release rate, temperature, and species mole fractions of a stratified flame (80 Hz) at $\phi_R = 1.14$ under decreasing equivalence ratio along with the profiles of the corresponding homogeneous flame.

In **Fig. 3.10**(a), similar to the profiles seen in **Fig. 3.7**, it is shown that the heat release rate is increased and the thermal thickness is thinner, which are signs of the increased flame speed. Meanwhile, contrarily to the profile in the lean mixture, the temperature on the downstream side of the stratified flame is mostly the same as that of the homogeneous flame until around $x - x_R = 1.0$ mm, where the downstream temperature gradually becomes lower than the homogeneous case. This is because the burned gas on the downstream side of the stratified flame is richer, i.e., further from stoichiometry than that of the homogeneous flame, which results in a lower temperature as explained previously in **Fig. 3.5**. It seems that the temperature of stratified flames is slightly increased just downstream of their reaction zones (0 mm $< x - x_R < 1.0$ mm) due to the larger heat release rate, compensating the decrease in the burned gas temperature. From these observations, it is shown that heat conduction from the burned gas is not the cause of the back-support effect in a rich mixture.

Figure 3.10(b) shows the mole fractions of major species. Since the flame is propagating in a rich mixture, the oxidizer O_2 is depleted in the burned gas. In addition, the fuel CH_4 is also depleted because of the reasons explained in **Fig. 3.5**. Meanwhile, O_2 and CH_4 respectively increases and decreases toward the unburned mixture ($x - x_R > 0$ mm), as it is leaner compared to that of the homogeneous flame. Other major species such as H_2O and CO are increased in the burned gas, while CO_2 is decreased in the burned gas, as expected from the equilibrium composition in **Fig. 3.5**.

Mole fractions of the more reactive species, H_2, OH, and H, are shown in **Fig. 3.10**(c). Although not shown in the figure, mole fractions of the O atom were similar to that of the OH radicals. Similar to the lean mixture, H_2 is increased in the burned gas of the stratified flame, resulting in an increase in the H_2 mole fraction around the reaction zone due to increased back-diffusion. This is expected from the equilibrium composition in **Fig. 3.5**. Meanwhile, based on the equilibrium composition shown in **Fig. 3.5**, mole fractions of OH and H should be decreased in the burned gas, which is richer than that of the homogeneous flame. Nevertheless, they are both increased around the reaction zone. For the H mole fraction, it is still larger than the homogeneous case further downstream of the reaction zone, while for the OH mole fraction, it becomes smaller than the homogeneous case for $x - x_R > 0.7$ mm. The increase in the mole fractions of OH and H around the reaction zone is because of the increased H_2 mole fraction enhances the following major chain-branching cycle [78]:
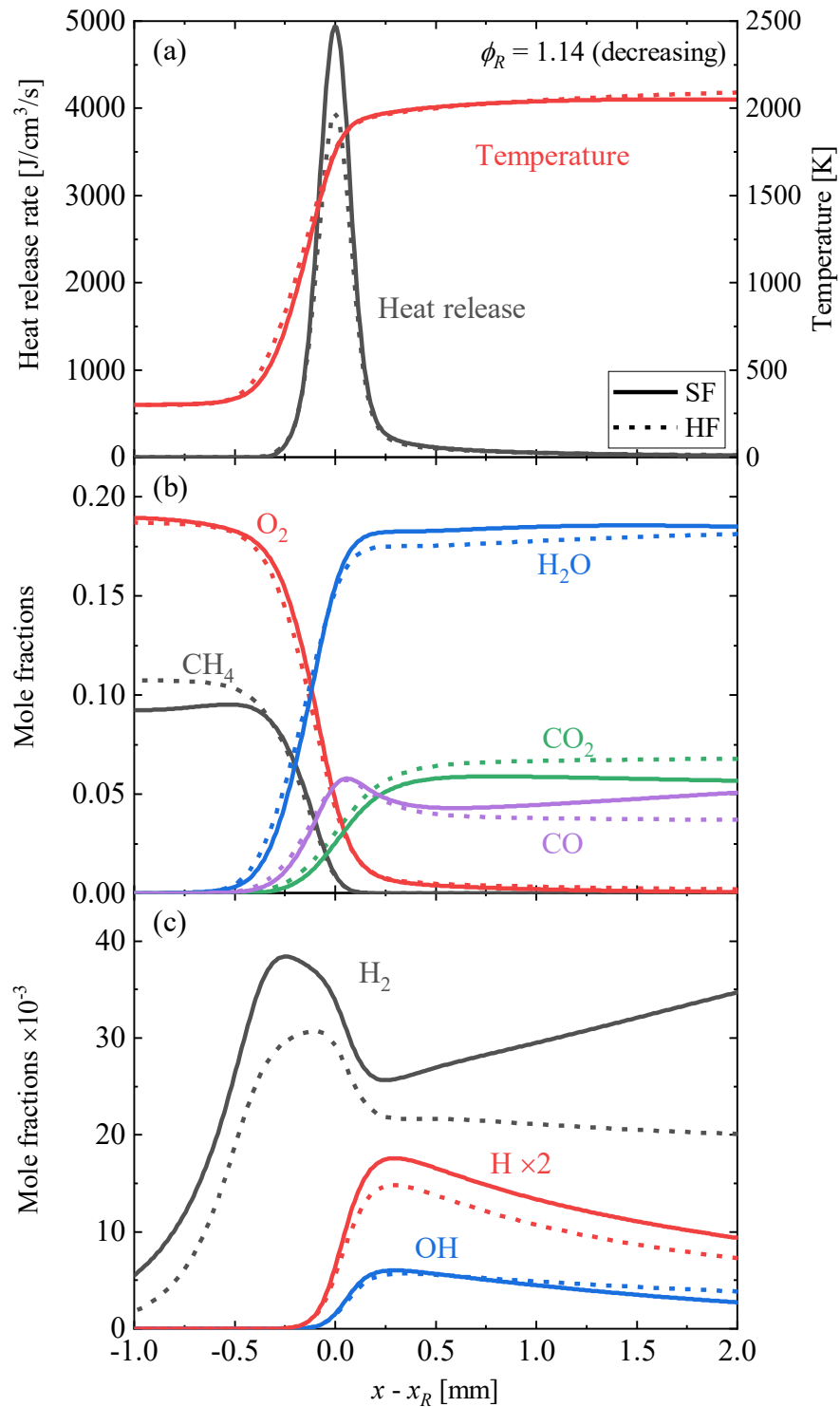
Fig. 3.10: Profiles of heat release rate, temperature, and major species mole fractions of the stratified flame (80 Hz) in a rich mixture at $\phi_R = 1.14$ under decreasing local equivalence ratio and those of the homogeneous flame with the same ϕ_R. The x-axes are shifted so that the reaction zone is at $x - x_R = 0$ mm for both flames.

$$H + O_2 \rightarrow O + OH \qquad\qquad\qquad \text{(GRI 38)}$$
$$O + H_2 \rightarrow H + OH \qquad\qquad\qquad \text{(GRI 3)}$$
$$OH + H_2 \rightarrow H + H_2O \qquad\qquad\qquad \text{(GRI 84)}$$
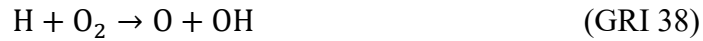
The above observations show that the back-support in a rich mixture is primarily driven by species diffusion from the burned gas and not by heat conduction. However, unlike in lean mixtures, the mole fractions of H_2 and other reactive species such as OH, H, and O do not respond in the same manner, as H_2 increases monotonically with increasing mixture equivalence ratio and others peak out around stoichiometry. Such trends require the roles of species diffusion to be investigated separately for H_2 and other species. Therefore, in the same manner as in **Fig. 3.8**, the response of stratified flames with modified diffusion coefficients and global kinetics are investigated in the following discussion.

3.4.5 Rich flame response with modified diffusion and kinetics

Figure 3.11 shows the response of the flame speed of stratified flames under 80-Hz oscillation and those of homogeneous flames calculated with approaches (A) modified diffusion coefficients and (B) global kinetics. The modified calculation parameters are shown in **Table 3.2**. In the same manner as the lean case, the oscillation amplitude ϕ_a and the inlet velocity was adjusted for cases (b-f) so that the variation in the equivalence ratio gradient at the reaction zone is comparable to case (a). In addition, the center of oscillation ϕ_m for case (f) with the detailed kinetics was shifted to $\phi_m = 1.35$ to keep the flame away from the nozzle, as the global kinetics results in higher flame speeds than others in rich mixtures. In **Fig. 3.11**(a), the response of the flame speed calculated with mixture-averaged diffusion coefficients and detailed kinetics is shown as a reference. **Figure 3.11**(b) and (c) respectively show the response of the flame speed with (b) $Le_{H2} = 1$ and (c) $Le_{H,OH,O} = 1$. It is seen that in both cases, the deviation of $S_{c,s}$ from $S_{c,h}$ is attenuated from case (a). Meanwhile, case (c) results in a larger deviation than case (b), which implies that the influence of preferential diffusion on the back-support is larger for H_2 than for H, OH, and O. This is in contrast to the lean case, where the magnitude of deviation was similar for cases (b) and (c). When the Lewis numbers for all reactive species are set to unity in **Fig. 3.11**(d), the difference between $S_{c,s}$ and $S_{c,h}$ becomes insignificantly small, showing that the preferential diffusion of reactive species H_2, H, OH, and O play primary roles in modifying the stratified flame speed.

Figure 3.11(e) with $D_{H2} = 0$ m^2/s shows the flame response with the diffusion of H_2 eliminated, where a distinctly different flame response is observed. In this case, the limit cycle of $S_{c,s}$ results in a clockwise direction, in contrast to the counterclockwise direction in other cases. This means that the back-supporting phenomenon takes place in opposite ways. To
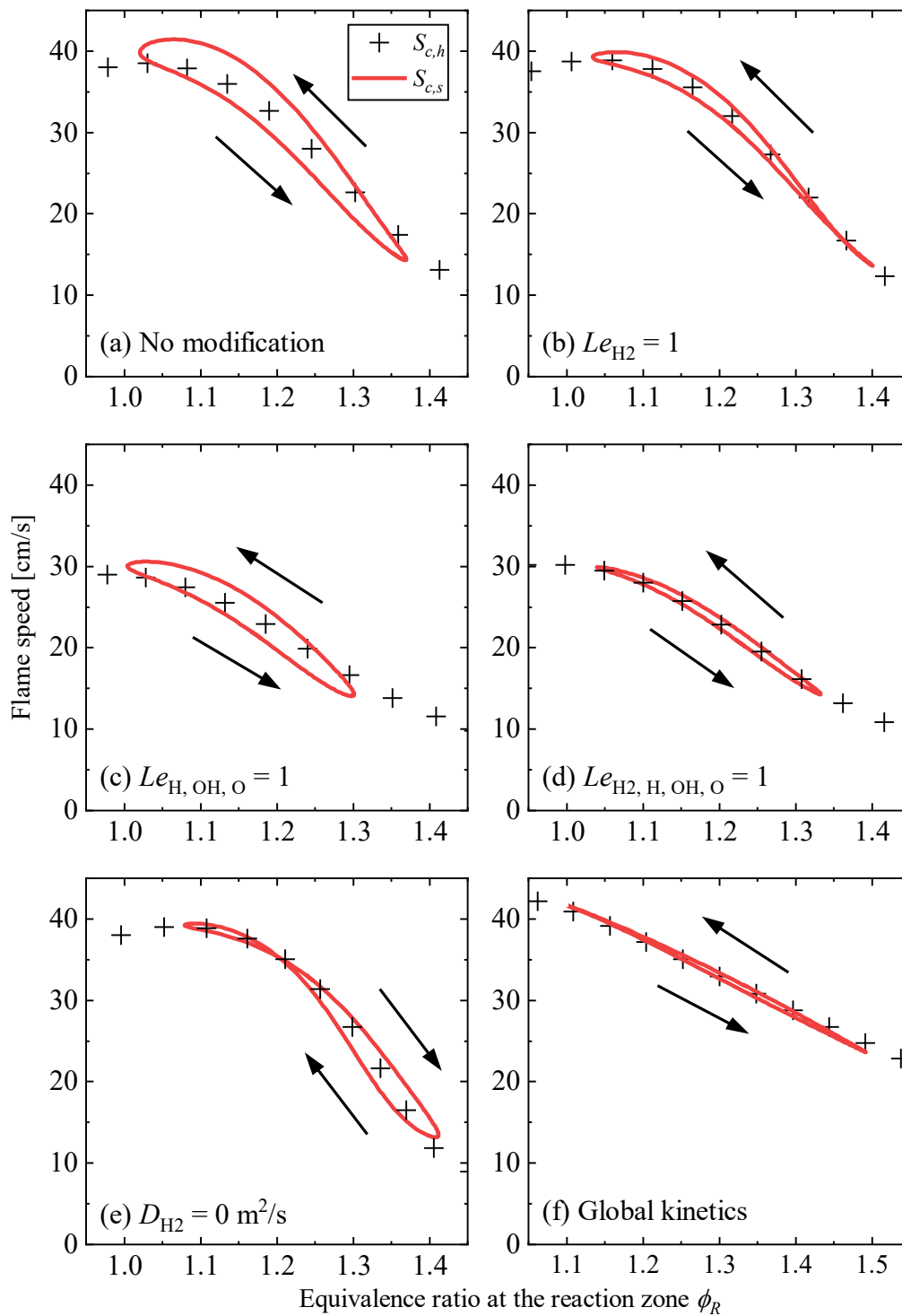
Fig. 3.11: Solid lines: Responses of the flame speed $S_{c,s}$ of stratified flames (80 Hz) in a rich mixture with (a) mixture-averaged diffusion coefficients; (b-e) modified diffusion coefficients: (b) $Le_{H2} = 1$, (c) $Le_{H,OH,O} = 1$, (d) $Le_{H2,H,OH,O} = 1$, and (e) $D_{H2} = 0$ m^2/s; and (f) global kinetics. Symbols: The flame speed $S_{c,h}$ of homogeneous flames with the same local equivalence ratio at the reaction zone ϕ_R.

elucidate the mechanism behind this behavior, **Fig. 3.12** shows the profiles of heat release rate, temperature, and H_2, H, and OH mole fractions of a stratified flame in case (e) at $\phi_R = 1.34$ under decreasing equivalence ratio along with the profiles of the corresponding homogeneous flame. Although not shown, the mole fractions of the O atom were similar to that of the OH radicals. The lower heat release rate and the broadened thermal thickness in **Fig. 3.12**(a) indicate that the flame speed is decreased for the stratified flame.

Meanwhile, the temperature profile downstream of the reaction zone is only slightly decreased from that of the homogeneous flame, implying that a decrease in the heat flux from the burned gas is not the cause of the decrease in the heat release rate. The mole fractions in **Fig. 3.12**(b) show interesting trends in contrast to those in **Fig. 3.10**(c). Following the
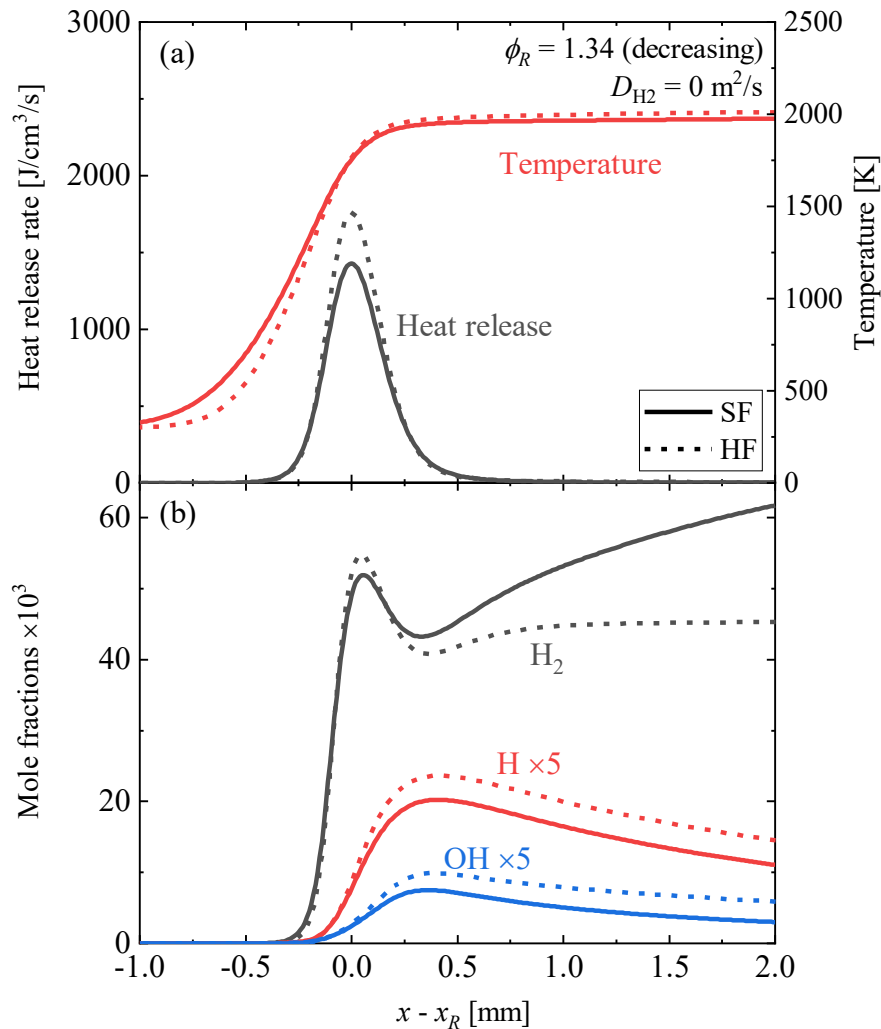
Fig. 3.12: Profiles of heat release rate, temperature, and H_2, H, and OH mole fractions of the stratified flame (80 Hz) with $D_{H2} = 0$ m^2/s in a rich mixture at $\phi_R = 1.34$ under decreasing local equivalence ratio and those of the homogeneous flame with the same ϕ_R. The x-axes are shifted so that the reaction zone is at $x - x_R = 0$ mm for both flames.

equilibrium composition in **Fig. 3.5**, H_2 is increased and H/OH are decreased in the burned gas. However, while increased H_2 diffusion in **Fig. 3.10**(c) resulted in an increase in the H and OH mole fractions around the reaction zone through the chain-branching cycle (GRI 38, 3, 84), such production of H and OH radicals are not observed in **Fig. 3.12**(b). This is because, as $D_{H2} = 0 \ \mathrm{m^2/s}$ in the current case, the increased H_2 in the burned gas cannot diffuse into the reaction zone and enhance the chain-branching cycle. Consequently, the decreased H and OH radicals in the burned gas directly decrease their mole fractions around the reaction zone, suppressing fuel consumption reactions and resulting in a lower heat release rate. From the observations in cases (b) and (e), it can be said that the diffusion of H_2 is crucial for causing the back-support effect, and its influence is enhanced by preferential diffusion. This conclusion conforms to the report by Shi and Chen [114], who had conducted a numerical study on a one-dimensional flame propagating in a rich-to-lean stratified mixture. Therefore, it can be said that the stratified flame propagation in a rich-to-lean mixture is governed by the back-supporting mechanism in rich mixtures, since the abundant H_2 in the rich burned gas is carried into the lean mixture as the flame propagates. Lastly, **Fig. 3.11**(f) shows the flame response with the global kinetics, in which the reactive species H, OH, and O are not included. It is seen that the deviation of $S_{c,s}$ from $S_{c,h}$ is negligibly small, which again shows that the temperature variation in the burned gas alone is not sufficient to modify the stratified flame speed.

3.5 Summary

A numerical study on methane/air counterflow premixed flames under compositional oscillations is conducted. The flame response to low-frequency oscillations, where the oscillation timescale is longer than the flame timescale, is investigated under large equivalence ratio amplitudes. In addition, the analyses are conducted for lean and rich mixtures respectively to clarify differences in the stratified flame response and its mechanism. The response of the flame speed and the profiles of temperature and species mole fraction of the flame under compositional oscillation (*stratified flame*) is contrasted with those of steady premixed flames propagating in homogeneous mixtures (*homogeneous flames*) whose equivalence ratio corresponds to the local equivalence ratio at the reaction zone of the stratified flame. In addition, the response of flames with modified diffusion coefficients or with global kinetics was investigated to clarify the roles of species diffusion in stratified flames. The following specific conclusions have been reached from the observations and analysis:

- The stratified flame speed $S_{c,s}$ deviates increasingly from the corresponding homogeneous flame speed $S_{c,h}$ with increasing oscillation frequency due to the so-called "back-

support" effect. In both lean and rich mixtures, $S_{c,s} > S_{c,h}$ under decreasing equivalence ratio and $S_{c,s} < S_{c,h}$ under increasing equivalence ratio. It is shown that even when the oscillation frequency is sufficiently low that the flame is expected to respond in a quasi-steady manner, a sufficiently large variation in the equivalence ratio gradient may cause the stratified flame to behave differently from the corresponding homogeneous flames. Therefore, in addition to the oscillation timescale, the flame response under compositional oscillation should be considered in terms of amplitudes of variations in the equivalence ratio gradient.

- When $S_{c,s} > S_{c,h}$ in lean mixtures, both temperature and mole fractions of major reactive species H_2, H, OH, and O in the burned gas are increased. In the responses of stratified flames with modified diffusion coefficients for the reactive species, the back-support effect is not observed. This shows that the preferential diffusion of the reactive species is the driving factor of the effect. Contrary to the previous reports, it is shown that variations in the burned gas temperature of stratified flames do not contribute to the increase or decrease in the stratified flame speed. This is also confirmed by the absence of the back-support effect in the response of the stratified flame with global kinetics.

- When $S_{c,s} > S_{c,h}$ in rich mixtures, the temperature and the mole fractions of H, OH, and O in the burned gas are decreased, while the mole fraction of H_2 in the burned gas is increased. The responses of the stratified flames with modified diffusion coefficients indicate that the abundance of H_2 in the burned gas leads to increased diffusion of H_2 into the reaction zone. It is also shown that the above mechanism is enhanced by the preferential diffusion of H_2. This enhances the chain-branching cycle and increases radical production, which overrides the decrease in the diffusive flux of radical species from the burned gas.

Chapter 4

Strained Flame Propagation in Stratified Mixtures

In this chapter, the influence of flow strain rates on flame propagation in rich-to-lean stratified mixtures is numerically investigated. Especially, the stratified flames supported by their own combustion products, or the *self-back-supported* flames, are studied. First, different modes of the back-support effect on stratified flames are explained and a gap in previous literature is discussed. Then the numerical setup and a novel method to characterize stratified flame propagation in a strained flow are introduced. Lastly, the calculation results are presented and discussed.

4.1   Introduction

It was seen in Chapter 3 that when a flame propagates into gradually richer or leaner mixtures, the flame speed is modified from the corresponding flame speed in homogeneous mixtures at each local equivalence ratio. This phenomenon has been called the *back-support* effect, as it is caused by variations in the diffusive flux from the burned gas into the reaction zone. In Chapter 3, it was shown that the preferential diffusion of reactive species from the burned gas was the dominant factor in driving the back-supporting phenomenon.

Laminar flame propagation in stratified mixtures has been conventionally studied in two major configurations: an unsteady one-dimensional flame propagating into a quiescent stratified mixture [19,97,104,105,112,113,119,126], and a steady counterflow flame in a reactant-to-product (RTP) configuration [20,78,95,121,127] in which the product stream is richer or leaner than the reactant stream. The former represents a flame propagating into richer or leaner mixtures and being influenced by its own burned gas (**Fig. 4.1**(a)), while the latter represents a part of a flame influenced by entrained burned gas from richer or leaner neighbors (**Fig. 4.1**(b)). In this study, these two situations are distinguished as *self-back-support* and *forced-back-support*, respectively. In practical situations, the former is relevant to stratified charge combustion in IC engines [43,128,129] and partially-premixed gas-turbine model

combustors [130,131], where the flame propagates into compositionally inhomogeneous mixtures. Meanwhile, the latter is relevant to piloted burners [59], swirl burners [132,133], trapped vortex combustors [134,135], and radially stratified burners [54,136], where a recirculation zone is created in the flow to entrain downstream hot burned gas toward the unburned mixture to support the flames. In highly turbulent reacting flows, these two situations are expected to co-exist.

(a) Self-back-support

(b) Forced-back-support
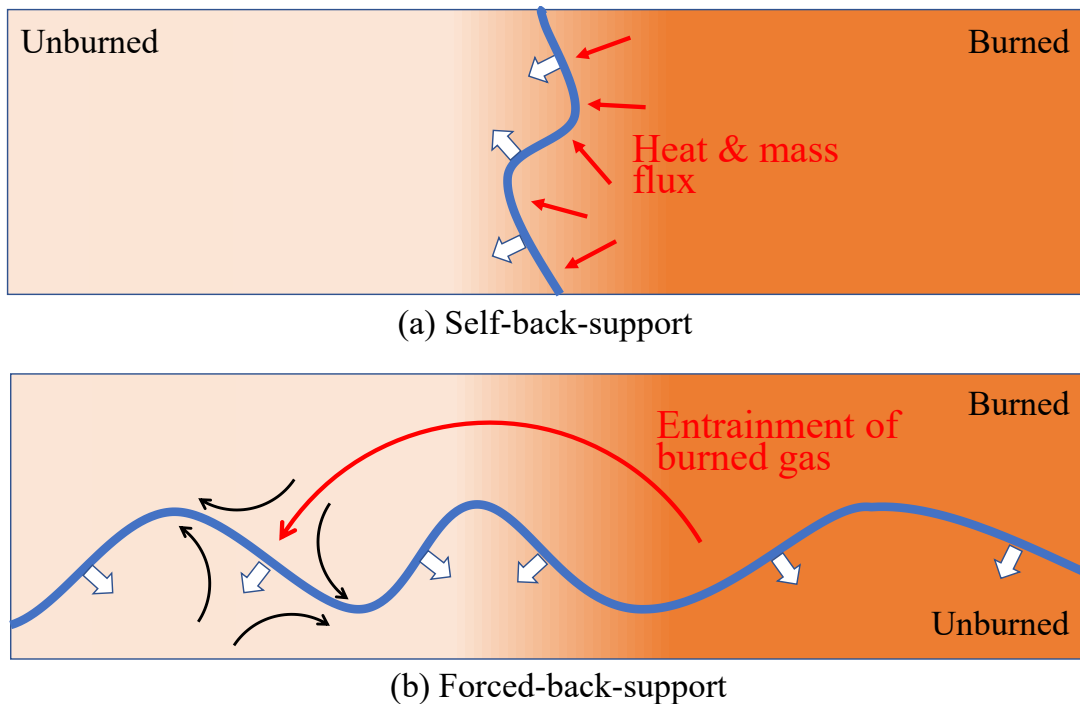
Fig. 4.1: Schematic representation of (a) self-back-supported and (b) forced-back-supported flames. The background color represents variations in the local equivalence ratio.

In the forced-back-support case, the flame inevitably propagates under a flow strain since a stagnation plane is formed. Therefore, several previous studies investigated the effect of flow strain on laminar stratified flames using the RTP configuration. Coriton et al. [121] numerically studied the influence of the product stream equivalence ratio on flame extinction with increasing strain rate. They reported that the extinction behavior depends on the stoichiometry of the product stream. Later, they extended the results by a series of experimental studies on turbulent RTP counterflow flames [137–139]. Richardson et al. [20] conducted a numerical simulation of lean RTP stratified flames under a transient variation in the strain rate, which emulates a collision of a turbulent vortex on the flame. They found that the increased flow strain pushes the reaction zone onto the product stream, which strengthens the back-support effect. Zhou and Hochgreb [78] numerically studied the back-support effect in an RTP configuration under three different strain rates, which led to a similar conclusion as Richardson et

al.

Meanwhile, to the best of the author's knowledge, there are no studies that investigated the effect of flow strain on self-back-supported flames. It should be noted that the above conclusions on strained forced-back-supported flames cannot be generalized to strained self-back-supported flames because, for the self-back-supported flame, the flame is always free-standing, i.e., the flame is always detached from the stagnation plane. Therefore, the idea of the strained flame being "pushed onto the product stream" cannot be applied directly to the self-back-supported flames. In practical situations, the turbulent flame constantly experiences flow strain due to interactions with turbulent vortices. Therefore, it is beneficial to investigate the characteristics of strained flame propagation in self-back-supported situations.

To address the above gap in the literature, we investigate the propagation of a strained self-back-supported flame under different flow strain rates. For this purpose, a reactant-to-reactant (RTR) configuration was used for the calculation of strained stratified flames. By imposing transient equivalence ratio variations at the nozzle, the flame was supported by its own combustion products similarly to the conventional studies on self-back-supported flames using a one-dimensional setup. A novel method was devised to characterize transient flame propagation under varying local equivalence ratios and the local strain rate.

4.2   Numerical setup

Numerical simulations of unsteady premixed flames propagating in a rich-to-lean stratified mixture (*stratified flames*) and steady premixed flames propagating in homogeneous mixtures (*homogeneous flames*) were conducted using OPUS. For the reasons explained in Section 4.3, the stratified flames were calculated in a reactant-to-reactant (RTR) configuration, while the homogeneous flames were calculated in a reactant-to-product (RTP) configuration, as shown in **Fig. 4.2**. For all cases, a uniform grid of 10 μm was applied. In the same manner as in Chapter 3, a mixture of methane and air (mole fraction: 21% O_2 and 79% N_2) was supplied from the reactant nozzle at 300 K and 0.1013 MPa. GRI_Mech 3.0 [116] was used as a detailed methane/air chemical kinetic model.

For the RTR configuration in **Fig. 4.2**, the calculation domain is only one side of the stagnating flow $[x_{in}, 0 \text{ mm}]$, considering symmetry. The distance between the nozzle and the stagnation plane was set to 10 mm. At the nozzle, the equivalence ratio $\phi_{in}(t)$ was decreased linearly from $\phi_1 = 1.2$ to $\phi_2 = 0.6$ over the duration of the stratification time τ_s, defined based on the tangent lines shown in **Fig. 4.3**. To avoid numerical difficulty, the beginning and the end of the linear variation are smoothed by sinusoidal curves whose amplitudes are $0.1\Delta\phi$. The low strain and the high strain cases, with the initial local strain rate a_R of 150 s^{-1} and 450 s^{-1}, respectively, were analyzed. The definition of a_R will be given in Section 4.3. The
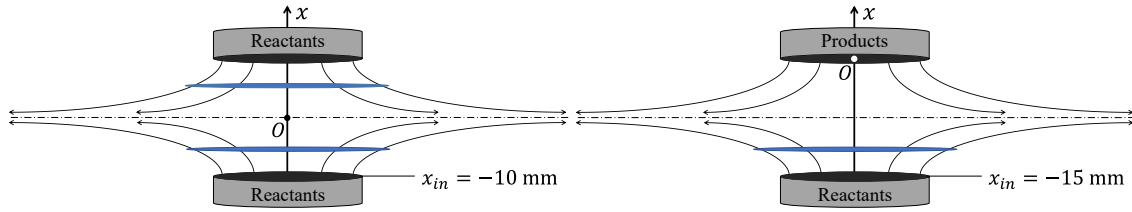
Fig. 4.2: Schematic representation of counterflow premixed flames in the reactant-to-reactant (RTR) configuration (left) and in in the reactant-to-product (RTP) configuration (right).

nozzle velocities were set at 50 cm/s and 147 cm/s for the former and the latter cases. The range of the strain rate and the equivalence ratio variation were determined so that the stratified flames are sufficiently detached from the stagnation plane during their propagation. The stratification time τ_s in **Fig. 4.3** was determined for each case so that the resulting peak values of the equivalence ratio gradient in the unburned mixture at the upstream edge of the flame zone, $(\partial\phi/\partial x)_P$, was approximately 0.6 mm^{-1} for both the high strain and the low strain cases, as shown in **Fig. 4.4**. This corresponds to a non-dimensional stratification thickness of $\delta_s/\delta_T = 2.1$ at $\phi = 0.9$, where δ_s is the stratification thickness $\delta_s = \Delta\phi/(d\phi/dx)_{P,max}$ [18,114] and δ_T is the thermal flame thickness $\delta_T = \Delta T/(dT/dx)_{max}$. The current value of δ_s/δ_T is comparable to previous numerical studies on laminar stratified flames [18,112,114]. The definition of $(\partial\phi/\partial x)_P$ will be given in Section 4.3.

For the RTP configuration in **Fig. 4.2**, the calculation domain is the entire opposing reacting flow, $[x_{in}, 0 \text{ mm}]$. The distance between the opposing nozzles was set to 30 mm. An unburned methane/air mixture was supplied from the nozzle at $x = -15$ mm, while hot adiabatic combustion products of the corresponding reactant mixture was supplied from the opposite nozzle at $x = 0$ mm. The composition and the temperature of the combustion products
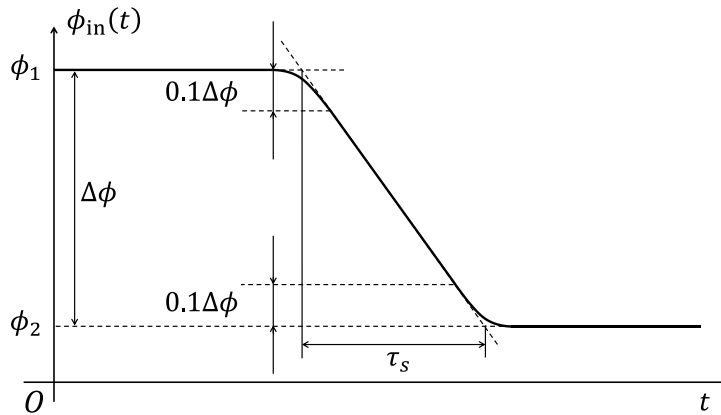
Fig. 4.3: Time variation of the inlet equivalence ratio $\phi_{in}(t)$ for the analysis of stratified flames, where $(\phi_1, \phi_2) = (1.2, 0.8)$. The stratification time τ_s is modified to adjust the magnitude of the equivalence ratio gradient.
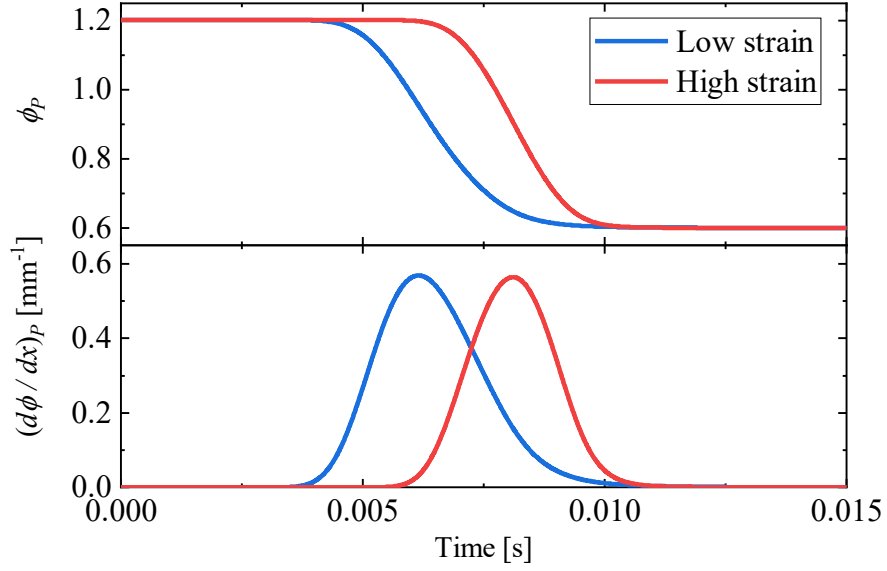
Fig. 4.4: Time variation of local equivalence ratio at the upstream edge of the preheat zone ϕ_P (first low) and its spatial gradient $(d\phi/dx)_P$ (second low) for the high and low strain flames.

were obtained from equilibrium calculations using EQUIL [85]. As will be explained in Section 3.4, the equivalence ratio ϕ_{in} and the inlet velocity $u_{in,r}$ of the reactant stream were varied to generate a library of homogeneous flames. Specifically, ϕ_{in} was varied from 0.65 to 1.20, while $u_{in,r}$ was varied from 30 cm/s to 350 cm/s depending on the equivalence ratio. Meanwhile, the inlet velocity of the product stream $u_{in,p}$ at $x = 0$ mm was determined in the following manner so that the flame is stabilized sufficiently far from both nozzles. First, assuming an RTR configuration, the global strain rate a_G was calculated as follows:

$$a_G = \frac{u_{in,r}}{-x_{in}/2} \tag{4.1}$$

Then, to reproduce the above global strain rate in the RTP configuration, $u_{in,p}$ was determined using the following expression derived for the global strain rate in the RTP configuration [23]:

$$a_G = \frac{u_{in,r}}{-x_{in}}\left(1 + \frac{u_{in,p}\sqrt{\rho_p}}{u_{in,r}\sqrt{\rho_r}}\right) \tag{4.2}$$

where ρ_r and ρ_p are the density of the reactant and the product streams, respectively. With the above procedure, the flame will be stabilized approximately at the location where it will be stabilized in a corresponding RTR configuration.

4.3 Method of flame characterization

4.3.1 Definitions

The flame speed S_c was calculated in the same manner as in Eq. (3.5) of Chapter 3:

$$S_c = \frac{1}{\rho_u Y_{f,u}} \int_{x_{in}}^{x=0\ \text{mm}} (-W_f \dot{\omega}_f) dx \tag{4.3}$$

where ρ_u is the unburned gas density; $Y_{f,u}$ is the fuel mass fraction in the unburned gas; W_f and $\dot{\omega}_f$ are respectively molecular weight and molar reaction rate of the fuel.

Meanwhile, two characteristic locations in the flame were defined. First, the reaction zone location x_R was defined as the location of peak heat release rate. In addition, the location of the upstream edge of the preheat zone x_P was defined as the location at which the temperature rises to 300.1 K. x_P represents the location of a portion of the unburned mixture that is about to enter the flame zone. The example locations of x_R and x_P are marked in **Fig. 4.5**.

The local equivalence ratio ϕ was defined as the element-based equivalence ratio, as explained in Chapter 3. Moreover, as the magnitude of the back-support depends on the spatial gradient of the equivalence ratio, a local equivalence ratio gradient was evaluated at the characteristic locations defined above. As mentioned in Chapter 3, the local equivalence ratio fluctuates around the reaction zone even for homogeneous flames, as also shown in **Fig. 4.5**. Therefore, the local spatial derivative of the equivalence ratio profile does not appropriately represent the equivalence ratio gradient experienced by the entire flame. Instead, the equivalence ratio gradient was defined as the time derivative of ϕ divided by the displacement speed $S_{d,i}$ at the characteristic location x_i in the flame:

$$\left(\frac{\partial \phi}{\partial x}\right)_i = -\frac{1}{S_{d,i}}\left(\frac{\partial \phi}{\partial t}\right)_i, \quad i = R \text{ or } P \tag{4.4}$$

where $(\partial \phi / \partial t)_i$ is the time derivative of ϕ at x_R ($i = R$) or x_P ($i = P$). In the above, $S_{d,i}$ is calculated as follows:

$$S_{d,i} = u_i - \frac{dx_i}{dt}, \quad i = R \text{ or } P \tag{4.5}$$

where u_i is the axial velocity at x_R ($i = R$) or x_P ($i = P$). The displacement speed $S_{d,i}$ represents propagation velocity of the characteristic location relative to the axial flow, thus it can be understood as a kind of flame speed. Therefore, as $S_{d,i}$ is always positive, a negative time derivative corresponds to a positive spatial gradient. In the current configuration, the flame is propagating toward a negative direction on the x-axis. Thus, the positive spatial gradient corresponds to flame propagation into a leaner mixture under rich-to-lean stratification.

Lastly, in the current counterflow model, the strain rate continuously increases toward the stagnation plane, as shown in **Fig. 4.5**. Therefore, the local strain rate a_R at the reaction zone

x_R was defined as the characteristic strain rate of the flame.
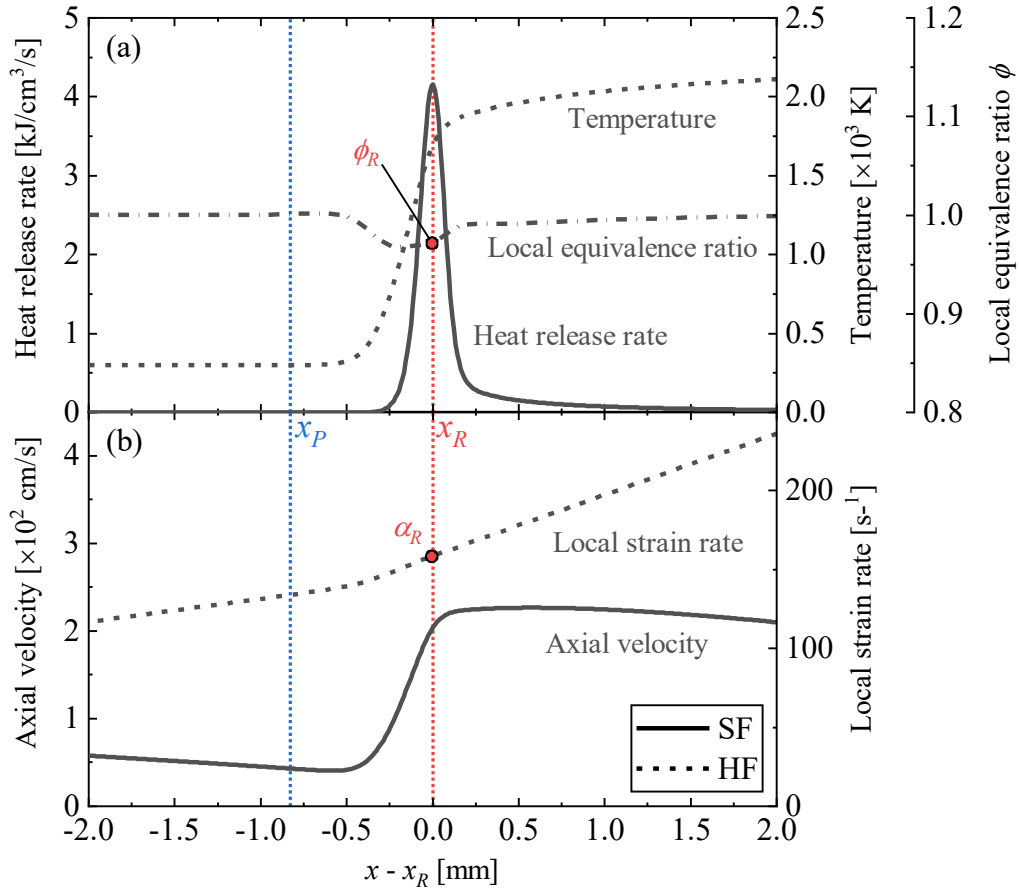
Fig. 4.5: Profiles of heat release rate, temperature, local equivalence ratio, axial velocity, and local strain rate of a counterflow premixed flame in a stoichiometric methane/air mixture. The dotted vertical lines represent the locations of the upstream edge of the preheat zone x_P and the location of the reaction zone x_R. The x-axes are shifted to so that the reaction zone is at $x - x_R = 0$ mm for all cases

4.3.2 Evaluation of the stratified flame speed in a strained flow

In this analysis, the temperature and the pressure of the unburned mixture are kept constant, which means that the homogeneous flame speed $S_{c,h}$ is a function of the local equivalence ratio ϕ_R and the local strain rate a_R. Therefore, to evaluate the effect of mixture stratification of stratified flames, the stratified flame speed $S_{c,s}(\phi_R(t), a_R(t))$ and the homogeneous flame speed $S_{c,s}(\phi_R, a_R)$ need to be compared under the same values of ϕ_R and a_R. Note that in Chapter 3, the difference in a_R of the stratified and the homogeneous cases were ignored. However, as the purpose of this study is to investigate the influence of different a_R, both ϕ_R and a_R need to be considered. As discussed in Section 4.1, the stratified flames were analyzed

in the RTR configuration since it is suitable for analyzing the stratified flames supported by their own combustion products.

In the high strain case, the flame locates closer to the stagnation plane. In the RTR configuration, when the flame is too close to the stagnation plane such that the downstream profiles of the twin flames begin to interfere with each other, the flame cannot be considered free-standing anymore. This is especially a concern for flames with low flame speeds. In **Fig. 4.6**, the distance of the reaction zone x_R from the stagnation plane for the stratified and the homogeneous flames are shown. For the homogeneous flames, it is seen that with decreasing equivalence ratio, the flame speed decreases, and the flame is closer to the stagnation plane. For $\phi_R < 0.7$, the distance becomes less than 2 mm, which is on the order of the flame thickness. On the other hand, for the stratified flame, the distance of more than 2 mm is retained until around $\phi_R = 0.65$, which means that the flame is free-standing for most of its propagation in the stratified mixture. This is because a finite time is required for the flame to relocate itself based on the balance between its flame speed and the local flow velocity. As the variation in the mixture equivalence ratio occurs much faster than the timescale of the flame relocation, the flame retains its initial location despite the decreasing flame speed.

As a remedy for evaluating the effect of mixture stratification on strained stratified flames under a high strain rate, the stratified and the homogeneous flames were calculated and compared as follows: For the stratified flames, the RTR configuration with transient equivalence ratio variation at the nozzle $\phi_{in}(t)$ is used because it is necessary for analyzing the stratified
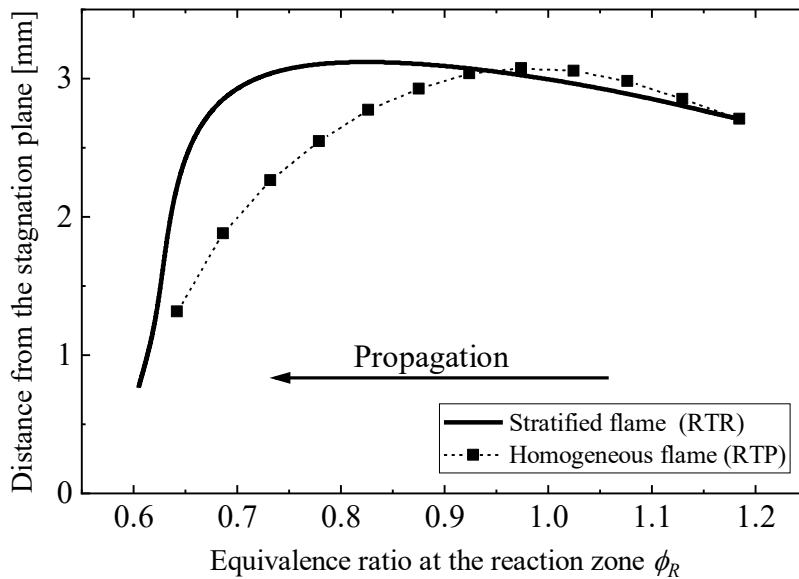
Fig. 4.6: Distance between the reaction zone location x_R and the stagnation plane for the high strain stratified flame and the corresponding homogeneous flames at each local equivalence ratio ϕ_R.

flames supported by their own combustion products. In addition, the flame is expected to locate far enough from the stagnation plane, as the initial location is retained for most of its propagation in the stratified mixture. On the other hand, for the homogeneous flames used as references, the RTP configuration is used as it is reported to better represent the steady flame response under high strain rates [70]. This is because, with the RTP configuration, the flame structure is not disturbed even when the flame is pushed onto the stagnation plane, as the combustion products are supplied from the downstream side. It was confirmed that the response of $S_{c,h}$ to the strain rate was identical in the RTR and the RTP configurations as long as the flame was sufficiently detached from the stagnation plane.

To obtain reference homogeneous flames that have the same values of ϕ_R and a_R as the stratified flame, a library of homogeneous flames with different values of ϕ_R and a_R was generated by varying the inlet equivalence ratio ϕ_{in} and velocity for the calculation of homogeneous flames in the RTP configuration. The symbols in **Fig. 4.7** represent the combinations of ϕ_R and a_R in the homogeneous flame library; the number of symbols was reduced for better visualization. Meanwhile, the solid lines represent the transient variation in ϕ_R and a_R of the stratified flame. Using this figure, the homogeneous flames which have the closest values of ϕ_R and a_R to the stratified flame were chosen as the reference homogeneous flames. The relative error in ϕ_R and a_R between the stratified and the corresponding homogeneous flames were less than 1%.
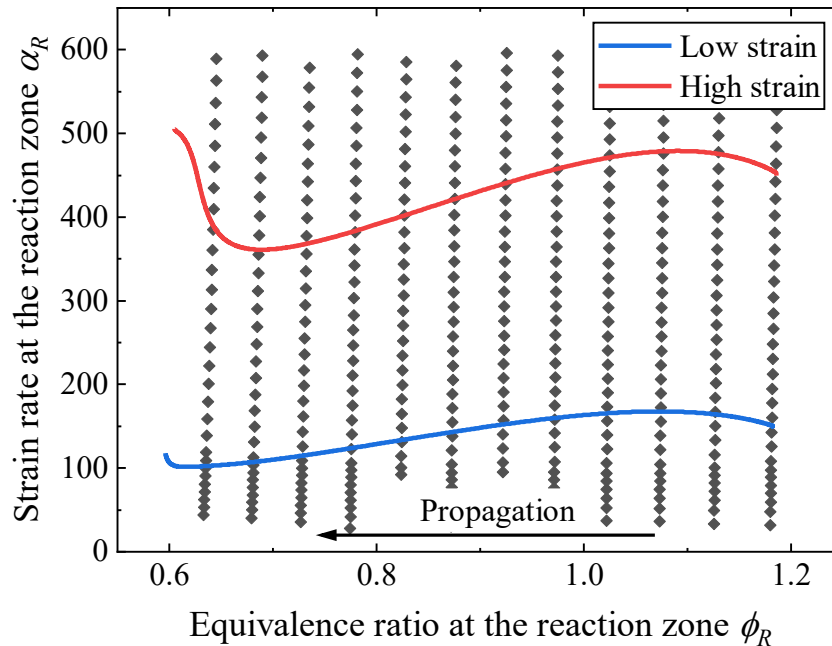
Fig. 4.7: The local equivalence ratio ϕ_R and the local strain rate a_R at the reaction zone of high and low strain stratified flames (solid lines) and a library of homogeneous flames (symbols). Note that the number of symbols was reduced for better visibility.

4.4 Results and discussions

4.4.1 Response of the flame speed

Response of the flame speed $S_{c,s}$ of stratified flames under high and low flow strain and the corresponding homogeneous flame speed $S_{c,h}$ at each local equivalence ratio ϕ_R are shown in **Fig. 4.8**(a). It is seen that, with decreasing equivalence ratio, the homogeneous flame speeds $S_{c,h}$ first increases and peaks out at around stoichiometry. In addition, $S_{c,h}$ of the high strain case is lower than $S_{c,h}$ of the low strain case. This is due to the larger stretch effect induced by the higher flow strain rate. It is known that for methane/air counterflow flames, an increasing stretch rate always reduces S_c [123]. In addition, the sensitivity of variation in $S_{c,h}$ to the stretch rate is larger for richer mixtures [123], as also observed in the slightly larger difference between $S_{c,h}$ of high strain and low strain cases in richer mixtures in **Fig. 4.8**(a). Meanwhile, $S_{c,s}$ is larger than $S_{c,h}$ for both low strain and high strain cases. The result is consistent with that discussed in Chapter 3 and previous studies [78,104,114,115]. Moreover, for $\phi_R < 0.95$,
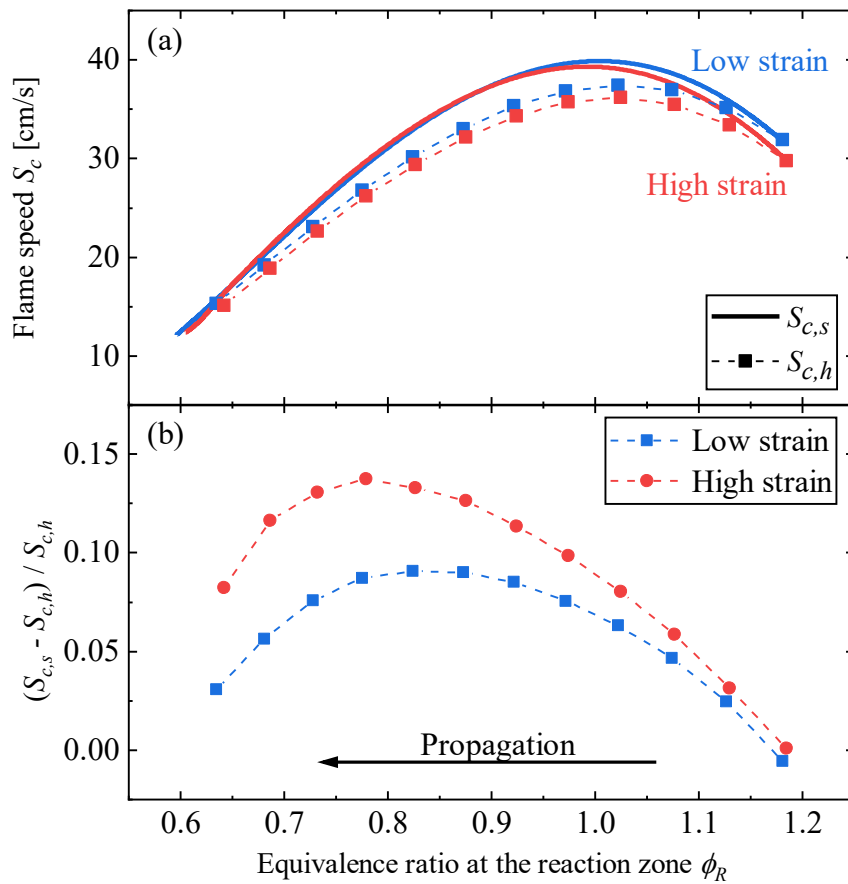
Fig. 4.8: Response of the flame speed $S_{c,s}$ of the stratified flames, the flame speed $S_{c,h}$ of homogeneous flames with the same ϕ_R, and the relative increase in $S_{c,s}$ as compared to $S_{c,h}$ for the high strain and the low strain cases.

$S_{c,s}$ of the high and the low strain cases are the same. This means that the increase of $S_{c,s}$ from $S_{c,h}$ is larger for the high strain case.

Figure 4.8(b) shows a relative increase of $S_{c,s}$ from $S_{c,h}$ for the high and the low strain cases at each ϕ_R. It is seen that the maximum relative increase peaks around $\phi_R = 0.80$, even though the maximum equivalence ratio gradient is at around $\phi_R = 0.90$ as seen in **Fig. 4.4**. This is due to the memory effect of the back-supporting phenomena [114], in which the response of the variation in $S_{c,s}$ is delayed from the variation in the equivalence ratio gradient. A clear example of this effect was observed in the rich stratified flame speed response in Chapter 3, Section 3.4. The maximum relative increase in $S_{c,s}$ for the high strain and the low strain cases are 14% and 9%, respectively. Therefore, the magnitude of the back-support effect is larger for the high strain stratified flame, even though the equivalence ratio gradient in the unburned mixture is the same for both cases. In the following discussion, the chemical, thermal, and hydrodynamic structures of both flames are investigated to elucidate the difference in the flame speed response.

4.4.2 Flame structures

Profiles of axial velocity, local strain rate, heat release rate, temperature, local equivalence ratio, and H_2 mole fraction of the high strain and the low strain stratified flames at $\phi_R = 0.92$ along with those of the corresponding homogeneous flames are shown in **Fig. 4.9**. In **Fig. 4.9**(a), for all cases, the axial velocities decrease toward the reaction zone ($x - x_R = 0$ mm) due to the stagnating flow. In the preheat zone (-0.5 mm $< x - x_R < 0$ mm), they increase rapidly due to thermal expansion. In the burned gas ($x - x_R > 0$ mm), they decrease again toward the stagnation plane. For the high strain cases (red lines), it is seen that the velocity gradients and the local strain rate profiles are larger than the low strain cases (blue lines). For the stratified flames (solid lines), the downstream velocity gradient and the local strain rate profiles are larger than those of the homogeneous flames (broken lines). This is due to the increased $S_{c,s}$. In **Fig. 4.9**(b) and (c), the heat release rate, temperature, local equivalence ratio and H_2 mole fraction profiles of the homogeneous flame are minimally affected by the difference in the flow strain. This is because variations in the homogeneous flame structure due to the stretch effect are very small under the moderate strain rate imposed in this study [140]. Meanwhile, in **Fig. 4.9**(b), the heat release rate profiles of the stratified flames (solid lines) are noticeably larger than those of the homogeneous flames (broken lines), as expected from the increased $S_{c,s}$. On the other hand, the temperature profiles of the stratified flames are only slightly larger than those of the homogeneous flames. This is because, as the downstream side of the stratified flames is close to stoichiometry, variations in the burned gas temperature are small. Contrarily, in **Fig. 4.9**(c) the H_2 mole fractions in the burned gas are larger for the
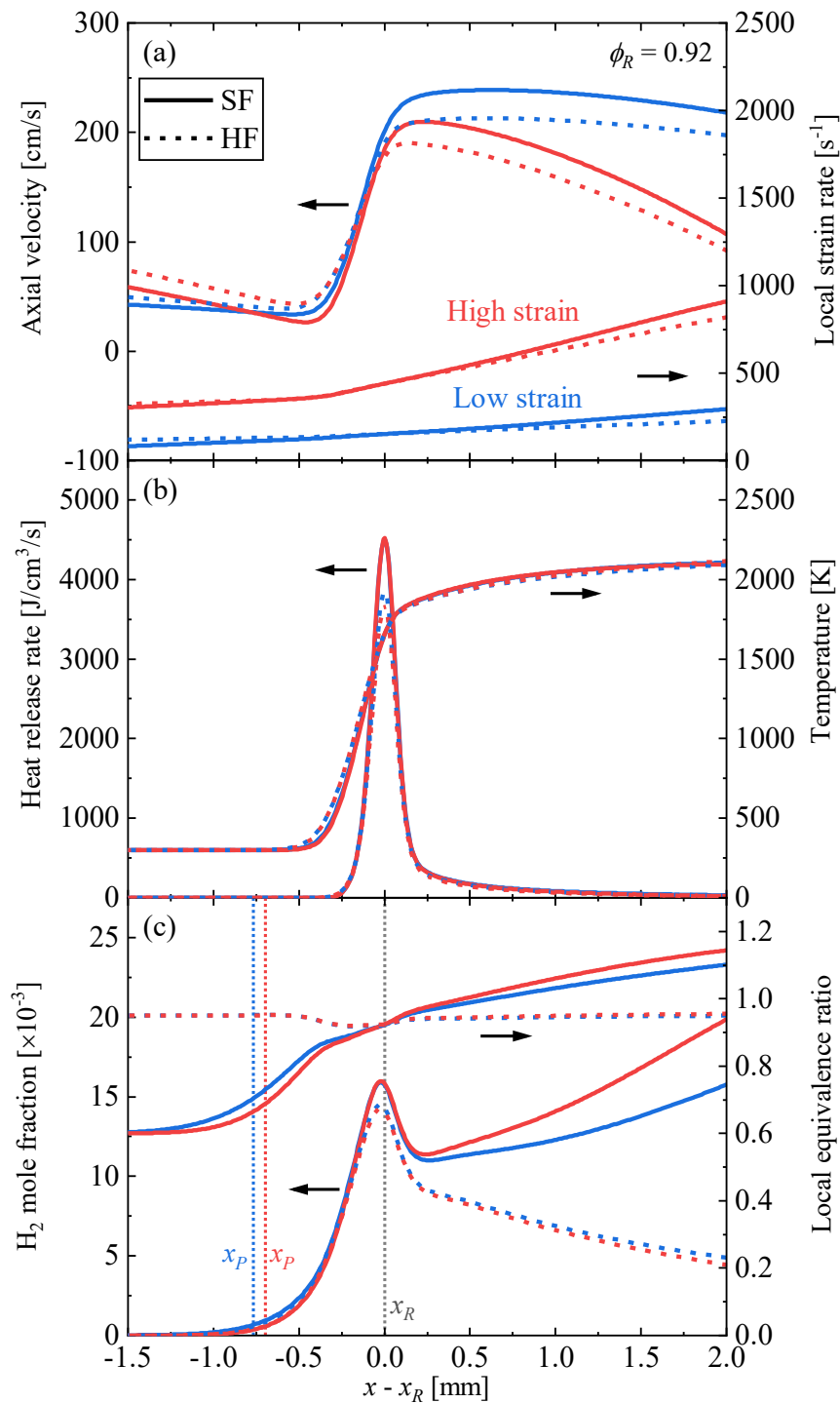
Fig. 4.9: Profiles of axial velocity, local strain rate, heat release rate, temperature, local equivalence ratio, and H_2 mole fraction of the high strain and the low strain stratified flames (SF) at $\phi_R = 0.92$ under rich-to-lean propagation and those of homogeneous flames (HF) with the same ϕ_R. The dotted vertical lines represent the locations of the upstream edge of the preheat zone x_P and the location of the reaction zone x_R. The x-axes are shifted to so that the reaction zone is at $x - x_R = 0$ mm for all cases.

stratified flames. In addition, the increase in the H_2 mole fraction is larger for the high strain stratified flame (red solid line) than for the low strain stratified flame (blue solid line). Considering the fundamental mechanism of the back-support effect investigated in Chapter 3, the increased diffusive flux of H_2 from the burned gas into the reaction zone is the cause of the larger increase in $S_{c,s}$ of the high strain case in **Fig. 4.8**.

The local equivalence ratio profiles of the stratified flames in **Fig. 4.9**(c) indicate that the larger equivalence ratio gradient on the downstream side of the reaction zone resulted in a richer burned gas for the high strain stratified flames, which led to the larger mole fraction of H_2 in the burned gas. This means that the equivalence ratio gradient $(\partial \phi / \partial x)_R$ at the reaction zone x_R is larger for the high strain case. Meanwhile, the equivalence ratio gradient $(\partial \phi / \partial x)_P$ at the upstream edge of the preheat zone x_P was adjusted to be the same for both the high strain and the low strain cases. The difference in $(\partial \phi / \partial x)_P$ and $(\partial \phi / \partial x)_R$ for the high strain and the low strain cases are shown in **Fig. 4.10**. First, it is observed that the magnitude of $(\partial \phi / \partial x)_R$ is attenuated to around one third of $(\partial \phi / \partial x)_P$ for both high strain and low strain cases. This is due to the rapid thermal expansion in the preheat zone, as seen in **Fig. 4.9**(a). In addition, as the temperature profiles of the high strain and the low strain stratified flames were identical in **Fig. 4.9**(a), the extent of the attenuation of $(\partial \phi / \partial x)_R$ from $(\partial \phi / \partial x)_P$ should be the same for both cases. However, as expected from the observation of the local equivalence ratio profiles in the burned gas, $(\partial \phi / \partial x)_R$ for the high strain case is larger
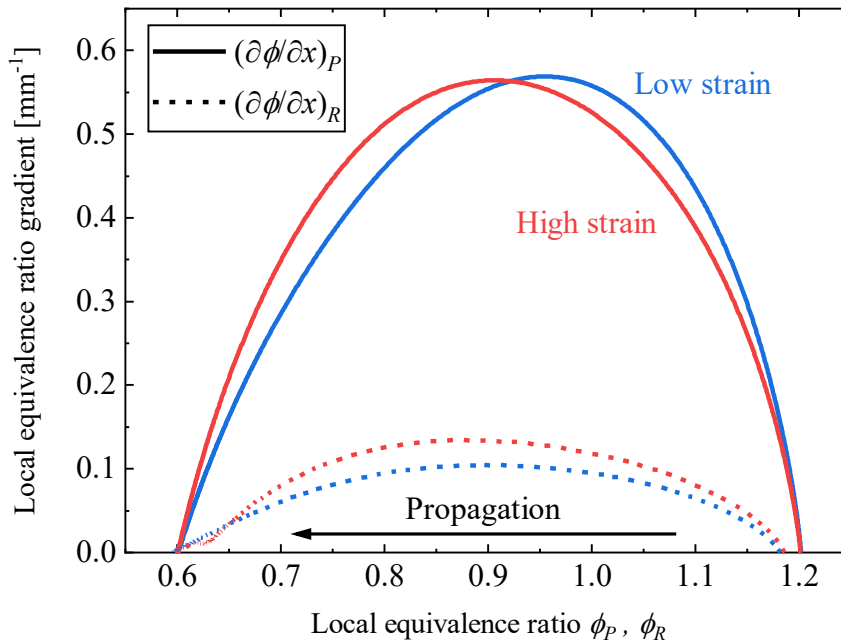
Fig. 4.10: Equivalence ratio gradients at the upstream edge of the preheat zone $(\partial \phi / \partial x)_P$ (solid lines) and at the reaction zone $(\partial \phi / \partial x)_R$ (broken lines) at the respective local equivalence ratio ϕ_P and ϕ_R for the high strain and the low strain flames.

than that for the low strain case. This trend can be explained by the larger axial velocity gradient for the high strain case, as seen in **Fig. 4.9**(a). Because of the higher strain rate, the axial velocity decreases more rapidly toward the downstream side, which decelerates the thermal expansion of the flow. Consequently, the attenuation of the local equivalence ratio gradient is mitigated in high strain stratified flames.

From the above results, it can be said that $(\partial\phi/\partial x)_R$ is a more appropriate parameter to characterize the effect of stratification on the chemical process in the reaction zone than $(\partial\phi/\partial x)_P$. Meanwhile, it should be noted that in general, $(\partial\phi/\partial x)_R$ alone is not sufficient to predict the magnitude of the back-support effect due to the memory effect; the response of the back-support to variation in $(\partial\phi/\partial x)_R$ will be affected by its history. However, the important implication here is that, while it is common to characterize the equivalence ratio gradient of an unburned mixture in a one-dimensional manner [18,104,105,114], it would be insufficient to estimate the actual equivalence ratio on the downstream side of the flame in a strained flow. For instance, in experiments in multi-dimensional flow [111] and engine-relevant apparatus [43], evaluation and control of mixture stratification may need to consider the influence of flow non-uniformity.

4.5   Summary

A numerical study of methane/air counterflow premixed flames under rich-to-lean mixture stratification is conducted. To investigate the effect of flow strain on the back-support effect of stratified flames, high strain ($450\ s^{-1}$) and low strain ($150\ s^{-1}$) cases are considered. A new method is devised to characterize the flame speed of unsteady strained flame propagating under a gradually decreasing mixture equivalence ratio. Unlike previous studies on strained flames supported by combustion products supplied from other flames, this method can study strained flames supported by their own combustion products. The results show that a higher strain rate decelerates the attenuation of the equivalence ratio gradient in the flame zone, which enhances the influence of the back-support effect on stratified flames. It is suggested that evaluation and control of mixture stratification in practical applications may need to consider the influence of flow non-uniformity.

Chapter 5

Stratified Combustion of Alternative Fuels – Hydrogen-blended Methane

In this chapter, stratified flame propagation in a hydrogen-blended methane/air mixture is numerically investigated. First, the significance of the presence of hydrogen on the upstream side of the stratified flame and its practical relevance is discussed. Then, modifications on the numerical setup from Chapter 4 and extensions of the definitions of the flame speed and the local equivalence ratio are explained. Lastly, the calculation results are presented, and their implications are discussed.

5.1   Introduction

It was shown in Chapter 3 that when a methane/air flame propagates under a gradually decreasing equivalence ratio, diffusion of H_2 from the richer burned gas on the downstream side increases because H_2 mole fraction is higher for the products of richer mixtures. In particular, preferential diffusion of H_2, i.e., H_2 diffusing faster than heat conduction, was found to be a crucial factor in the above so-called "back-support" effect. Meanwhile, when the flame propagates under decreasing equivalence ratio, the mole fraction of CH_4 in the unburned mixture gradually decreases toward the upstream side, as shown in **Fig. 5.1**(a), because the mixture becomes leaner. The mole fraction gradient could cause CH_4 in the unburned mixture to diffuse away from the preheat zone and suppress its consumption in the reaction zone, as shown by the arrow on the upstream side in **Fig. 5.1**(a). However, as seen in Chapter 3, Section 3.4, CH_4 mole fraction in the preheat zone slightly increases in a stratified flame under decreasing equivalence ratio due to the increased stratified flame speed. Therefore, it is seen that the influence of CH_4 diffusing away from the flame zone is overridden by the influence of H_2 diffusing into the reaction zone. This is because the Lewis number of CH_4 is much closer to unity than that of H_2, i.e., $Le_{CH4} = 0.97$ and $Le_{H2} = 0.28$ [124]. In other words, the upstream
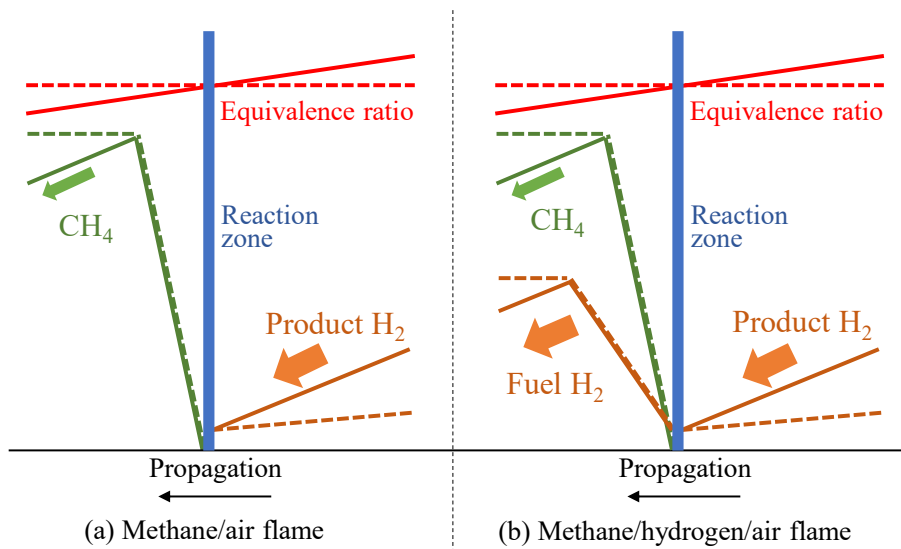
Fig. 5.1: Schematic representation of CH_4 and H_2 profiles upstream and downstream of the reaction zone for (a) methane/air and (b) methane/hydrogen/air stratified flames propagating under decreasing equivalence ratio (solid lines) and a steady flame in a homogeneous mixture (broken lines). The arrows represent the direction of species mass diffusion.

mole fraction gradient of CH_4 is too slow to make an impact on the reaction rate over the influence of the downstream mole fraction gradient of H_2. This is schematically illustrated in **Fig. 5.1**(a), where the arrow sizes represent the diffusive flux of each species.

From the above consideration, one question arises: What if the mole fraction gradient of H_2 exists on the upstream side, too? Such a situation occurs when hydrogen is added to the methane/air mixture, as illustrated in **Fig. 5.1**(b). In this case, when the mixture equivalence ratio decreases with flame propagation, the H_2 mole fraction gradient occurs both on the upstream and the downstream sides. Since the difference in the unburned and the burned gas temperature does not significantly vary the Lewis number [124], it is expected that the diffusive flux of H_2 on both sides occur on the same order of magnitude. Because of the presence of upstream H_2 diffusion, H_2 may "leak" from the flame zone toward the unburned mixture, which could weaken the back-support effect or even override it. However, to the best of the author's knowledge, no literature mention such an influence of upstream and downstream preferential diffusion on the back-support effect of stratified flames. Moreover, this phenomenon is uniquely expected for self-back-supported flames introduced in Chapter 4, where the stratified flame is supported by its own combustion products. Contrarily, in a forced-back-supported situation with the reactant-to-product counterflow flame configuration, the equivalence ratio gradient can be imposed only on the downstream side of the flame. Therefore, the current reactant-to-reactant counterflow flame configuration is suitable for investigating the influence of both upstream and downstream mole fraction gradients on the back-support ef-

fect.

From a practical perspective, hydrogen has attracted significant attention worldwide as one of the most promising alternative fuels. Specifically, the fact that hydrogen can be produced from water by electrolysis makes it an ideal choice as a so-called *electro-fuel* or *e-fuel* to store, transport, and export the power output of renewable energy sources which are highly variable in time [8,141–143]. Although most of the current hydrogen production is through hydrocarbon reforming, which is not carbon-free without a Carbon Capture and Storage (CCS) process, numerous methods including thermochemical, electrochemical, photobiological, and photochemical approaches have been proposed and studied to achieve sustainable and efficient production of hydrogen [141,142,144–146].

In terms of combustion characteristics, hydrogen is carbon-free when burned, producing only oxygen as a primary combustion product [143,145]. In addition, the specific energy of hydrogen is almost three times that of the conventional hydrocarbon fuels, which leads to a wide flammability range, low ignition energy, and a high flame speed of hydrogen/air mixtures [145,147,148]. However, when pure hydrogen is used as a fuel in internal combustion engines, several challenges are encountered. For instance, in spark-ignition (SI) and compression-ignition (CI) engines, the low ignition energy of hydrogen means that it is prone to pre-ignition, which can lead to a loss of combustion phasing control, knocking, and a possible mechanical engine failure [145,147,148]. For gas turbine engines, the higher flame speed of hydrogen than the conventional kerosene fuel leads to an increased risk of flashback, where the flame propagates upstream in an uncontrolled manner, requiring modifications in the combustor design and the fuel supply system [149]. Moreover, the high combustion temperature results in lower thermal efficiency due to increased heat loss and higher levels of nitrogen oxides (NOx) emission [145,147–149]. Last but not least, one of the most challenging aspects of hydrogen as a fuel, in general, is its very low volumetric energy density compared to hydrocarbon fuels, which requires pressurization or liquefaction under severe conditions for storage and transport to attain reasonable energy density [8,147–149]. This last issue will be revisited in Chapter 6.

As seen above, the use of pure hydrogen as a fuel for sustainable combustion is hindered by several factors with current technologies. Therefore, it has been common to use hydrogen as an enriching agent for the combustion of hydrocarbon fuels [147]. This is especially attractive for lean premixed combustion (LPC) of hydrocarbon fuels in gas turbines [150,151], boilers [152], and internal combustion engines [153,154], which are applied to achieve high thermal efficiency and low NOx production through low flame temperature. However, as the flame speed decreases with leaner combustion, LPC is prone to undesirable phenomena such as misfiring and combustion instabilities [34,36,151,154]. Since hydrogen flames have a significantly wider flammability range and higher flame speed than hydrocarbon flames, replac-

ing a part of a hydrocarbon fuel with hydrogen is known to improve flame stability during lean combustion [151]. In addition, since the power output is partially produced from hydrogen, it can reduce the carbon footprint when the hydrogen is supplied sustainably.

Although hydrogen blending has been extensively studied for premixed combustion, there is a limited number of studies on stratified combustion of hydrogen/hydrocarbon/air mixtures [55,155]. It is interesting that in a recent experimental study of turbulent methane/hydrogen/air swirl stratified flame [55], preferential diffusion of H_2 across the flame zone was observed due to the H_2 concentration gradient between the unburned mixture and the burned gas. This resembles the situation of upstream and the downstream H_2 diffusion discussed at the beginning of this section. Therefore, this study extends the numerical setup in Chapter 4 to study the back-support effect on methane/hydrogen/air counterflow flames.

5.2   Numerical setup

The analyses in this study were conducted in the same manner as described in Chapter 4. The major difference is that the mixture composition was changed from methane/air mixtures to methane/hydrogen/air mixtures. Therefore, this section will focus on the changes made from the setup in Chapter 4. Please refer to Chapter 4, Section 4.2 and 4.3 for a detailed explanation of the setup and the definitions.

5.2.1   Unsteady and steady calculations

The reactant-to-reactant (RTR) configuration was used for the calculations of counterflow stratified flames (*stratified flames*). A mixture of methane, hydrogen, and air ($300\,K$, $0.1013\,MPa$) was supplied from the reactant nozzles. The equivalence ratio at the nozzle $\phi_{in}(t)$ was linearly decreased from $\phi_1 = 1.2$ to $\phi_2 = 0.6$ over the duration of the stratification time τ_s, in the same manner as in Chapter 4. The range of the equivalence ratio was determined so that the stratified flames are sufficiently detached from the stagnation plane during their propagation. Note that in this study, the equivalence ratio was defined as the *effective* equivalence ratio, as will be explained in Section 5.3. The stratification time τ_s was adjusted for the stratified flames in each mixture so that the resulting peak values of the equivalence ratio gradient at the upstream edge of the preheat zone, $(\partial\phi/\partial x)_P$, was approximately $0.6\,mm^{-1}$ for all cases. The variations in ϕ_P and $(\partial\phi/\partial x)_P$ of the stratified flames in each mixture are shown in **Fig. 5.2**. The level of stratification is in the same order as in Chapter 4. The nozzle velocities u_{in} were adjusted to the values shown in **Table 5.1** so that the initial local strain rate a_R at the reaction zone x_R was $150\,s^{-1}$ for all cases. The different nozzle velocities were applied because the flame speed for each mixture composition is different, which results in a different flame location x_R and the local strain rate a_R.

The reactant-to-product (RTP) configuration was used for the calculations of steady pre-mixed flames propagating in homogeneous mixtures (*homogeneous flames*). By varying the nozzle equivalence ratio and the velocity to obtain a library of homogeneous flames with different values of the local equivalence ratio ϕ_R and the local strain rate a_R at the reaction zone. The homogeneous flames which have the closest values of ϕ_R and a_R to the stratified flames were chosen as the reference homogeneous flames. For both RTR and RTP calculations, the methane/air detailed reaction mechanism GRI_Mech 3.0 [116] was used. This is reasonable because the methane/air combustion mechanism includes hydrogen combustion as a sub-model [13], and thus has been used for previous methane/hydrogen/air combustion [67].
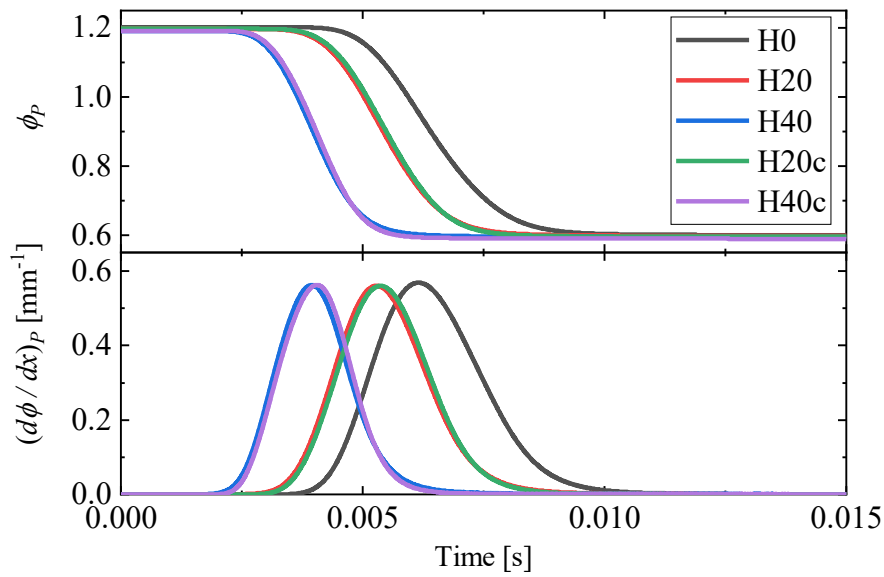
Fig. 5.2: Time variation of local equivalence ratio at the upstream edge of the preheat zone ϕ_P (first low) and its spatial gradient $(\partial\phi/\partial x)_P$ (second low) for the stratified flames in each mixture.

Table 5.1: Nozzle velocity and composition of methane/hydrogen/air mixtures. (Air: 21 vol.% O_2 and 79 vol.% N_2)

Mixture	u_{in} [cm/s]	Fuel H_2 content [fuel vol.%]	Initial H_2 mole fraction ($\phi_{in} = 1.20$)	Final H_2 mole fraction ($\phi_{in} = 0.60$)
H0	50	0	0.0000	0.0000
H20	55	20	0.0256	0.0141
H40	64	40	0.0595	0.0349
H20c	55	initially 20	0.0256	0.0256
H40c	64	initially 40	0.0595	0.0595

5.2.2 Mixture compositions

Five types of mixture compositions were investigated, as shown in **Table 5.1**. Mixture H0 is a pure methane/air mixture with no hydrogen addition. With decreasing nozzle equivalence ratio, the mole fraction of methane was decreased. The calculation results for mixture H10 are the same as those of the low-strain case in Chapter 4. For the hydrogen-blended mixtures, two types of methods to decrease the mixture equivalence ratio was devised. Method A is a common approach [55,67,156,157] where fuel mixture composition is defined by the volume percent of hydrogen in the fuel mixture. With this definition, both methane and hydrogen mole fractions decrease with decreasing equivalence ratio. The mixtures defined by Method A are H20 and H40, whose volume percent of hydrogen in the fuel is kept constant at 20% and 40% (i.e., 80% and 60% methane volume percent), respectively. The maximum extent of hydrogen addition was chosen so that hydrogen can be considered as a minor component in the fuel blend [125,158]. On the other hand, as the purpose of this study is to investigate the influence of decreasing hydrogen mole fraction in the unburned mixture, a reference case is needed, where the hydrogen mole fraction in the mixture is kept constant. Therefore, with Method B, only the methane mole fraction is decreased with decreasing equivalence ratio, and the hydrogen mole fraction is kept constant at a predetermined initial value. In this study, the initial value of the hydrogen mole fraction was chosen as the initial value (at $\phi_{in} = \phi_1 = 1.20$) of the hydrogen mole fraction in mixtures H20 and H40, as shown in **Table 5.1**. These compositions were named H20c and H40c, where "c" stands for "constant".

Figure 5.3 schematically illustrates the different ways of decreasing the equivalence ratio from $\phi_1 = 1.20$ to $\phi_2 = 0.60$ in Method A and B. It is seen that for mixtures H20/H40, the air mole fraction is increased while methane and hydrogen mole fractions are both decreased. On the other hand, for mixtures H20c/H40c, the air and methane mole fractions are increased and decreased, respectively, while the hydrogen mole fraction is kept constant at its initial
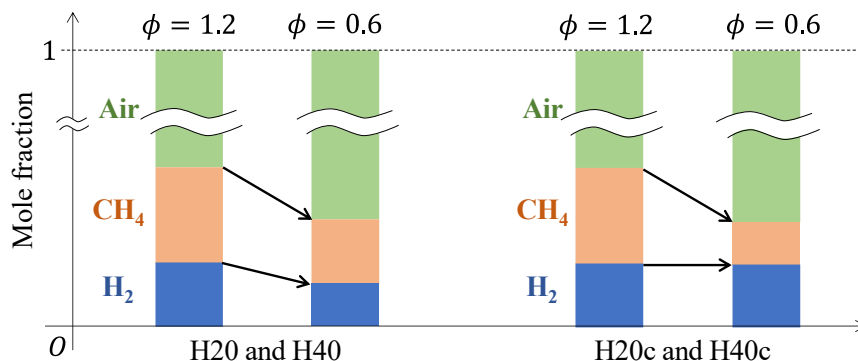
Fig. 5.3: Schematic of different ways to decrease the equivalence ratio of a methane/hydrogen/air mixture. Left (Method A: H20 and H40): The ratio of methane and hydrogen is kept constant. Right (Method B: H20c and H40c): The mole fraction of hydrogen is kept constant.

value. The results of stratified flame propagation in mixtures H20/H40 and H20c/H40c are compared to elucidate the influence of decreasing hydrogen content in the unburned mixture.

5.3 Definitions for methane/hydrogen fuel

5.3.1 Weighted fuel consumption speed

Similar to the approaches in previous chapters, the flame speed in the methane/air mixture H0 was calculated as the consumption speed,

$$S_c = \frac{1}{-\rho_u Y_{CH4,u}} \int_{x_{in}}^{x=0 \text{ mm}} W_{CH4} \dot{\omega}_{CH4} dx \tag{5.1}$$

where ρ_u is the unburned gas density; $Y_{CH4,u}$ is the CH_4 mass fraction in the unburned gas; W_{CH4} and $\dot{\omega}_{CH4}$ are respectively molecular weight and molar reaction rate of CH_4. Here, the mass fraction of CH_4 in the burned gas was neglected, for the reason explained in Chapter 3, Section 3.3. Meanwhile, for methane/hydrogen/air mixtures H20/H40 and H20c/H40c, Eq. (5.1) cannot be used because it does not take the presence of fuel H_2 into account. Therefore, extending the above definition, Sankaran and Im [67] proposed a heating-value-weighted S_c, which is defined as follows:

$$S_c = \frac{1}{-\rho_u \left(q_{CH4} Y_{CH4,u} + q_{H2} Y_{H2,u} \right)} \int_{x_{in}}^{x=0 \text{ mm}} (q_{CH4} W_{CH4} \dot{\omega}_{CH4} + q_{H2} W_{H2} \dot{\omega}_{H2}) dx \tag{5.2}$$

where q_k, W_k, ω_k, and $Y_{k,u}$ are lower heating value, molecular weight, mole production rate, and the unburned mass fraction of species k, respectively. Here, the consumption rates are weighted by the heating value of each species to account for their relative contribution to the total heat release; As the heating value of hydrogen is more than twice larger than that of methane [13], a unit mass of hydrogen is considered to contribute more to flame propagation through heat release than a unit mass of methane does. Therefore, in this study, Eq. (5.2) was used as the definition of the flame speed for methane/hydrogen/air mixtures H20/H40 and H20c/H40c.

5.3.2 Effective local equivalence ratio

As introduced in Chapter 3, for a one-component fuel/air mixture, the equivalence ratio is simply defined as fuel-air ratio divided by its value at stoichiometry,

$$\phi_{\text{species}} = \frac{X_f/X_{\text{air}}}{\left(X_f/X_{\text{air}}\right)_{st}} \tag{5.3}$$

where X_f and X_{air} is the mole fractions of fuel and air, respectively, and $\left(X_f/X_{\text{air}}\right)_{st}$ is the stoichiometric fuel-air molar ratio. A simple way to extend the above definition to a multi-

component fuel/air mixture, such as a methane/hydrogen/air mixture, is to sum up the mole fractions of fuel species, which yields the *overall* equivalence ratio $\phi_{o,\text{species}}$:

$$\phi_{o,\text{species}} = \frac{(X_{\text{CH4}} + X_{\text{H2}})/X_{\text{air}}}{\left((X_{\text{CH4}} + X_{\text{H2}})/X_{\text{air}}\right)_{st}} \tag{5.4}$$

However, for the small extent of hydrogen addition considered in this study, it can be expected that hydrogen in the unburned mixture diffuses faster into the reaction is completely oxidized before the oxidization of methane occurs [125]. Therefore, for methane, the remaining air after complete combustion of hydrogen is used for its combustion. Based on this assumption, the *effective* equivalence ratio was defined by Yu et al. [125] as

$$\phi_{e,\text{species}} = \frac{X_{\text{CH}_4}/\left[X_{\text{air}} - X_{\text{H}_2}/\left(X_{\text{H}_2}/X_{\text{air}}\right)_{st}\right]}{\left(X_{\text{CH}_4}/X_{\text{air}}\right)_{st}} \tag{5.5}$$

Note that the air mole fraction X_{air} in Eq. (5.3) is replaced by $X_{\text{air}} - X_{\text{H}_2}/\left(X_{\text{H}_2}/X_{\text{air}}\right)_{st}$, which represents the remaining air mole fraction after complete combustion of hydrogen. Moreover, it should be kept in mind that Eq. (5.5) is an effective equivalence ratio *for methane*. Therefore, the effective equivalence ratio will be lower than the overall equivalence ratio $\phi_{o,\text{species}}$ in Eq. (5.4). The above definition has been reported to facilitate good data reduction and correlation for methane/hydrogen/air mixtures [125]. Since this study is interested in the effect of hydrogen addition on methane/air stratified flames, Eq. (5.5) is used as the equivalence ratio. For mixture H0 with no hydrogen content, Eq. (5.5) reduces to the conventional definition Eq. (5.3).

Here, a problem arises when applying the effective equivalence ratio $\phi_{e,\text{species}}$ to the characterization of stratified flames. Similar to the studies in Chapters 3 and 4, the local equivalence ratio needs to be defined in terms of elemental composition so that it is defined throughout the flame zone. However, Eq. (5.5) cannot be extended straightforwardly to an element-based expression because the H atoms in CH_4 and H_2 must be distinguished. Therefore, as a remedy, the following procedures were adopted: First, the local equivalence ratio was calculated by the element-based expression,

$$\phi_{o,\text{element}} = \frac{2Z_{\text{C}} + 0.5Z_{\text{H}}}{Z_{\text{O}}} \tag{5.6}$$

where Z_i is the mole fraction of element i. In an unreacted mixture, the above is equivalent to the species-based expression,

$$\phi_{o,\text{species}} = \frac{2X_{\text{CH4}} + 0.5X_{\text{H2}}}{X_{\text{O2}}} \tag{5.7}$$

which is equivalent to the overall equivalence ratio Eq. (5.4). Therefore, since the methane/hydrogen ratio or the hydrogen mole fraction is a known parameter for mixtures

H20/H40 or H20c/H40c, respectively, the mole fractions X_{CH4}, X_{H2}, and X_{O2} of the unburned mixture can be calculated from Eq. (5.7). Lastly, these values were substituted into the following definition to yield the element-based effective equivalence ratio:

$$\phi_{e,\text{element}} = \frac{X_{\text{CH}_4}/\left[X_{\text{air}} - X_{\text{H}_2}/\left(X_{\text{H}_2}/X_{\text{air}}\right)_{st}\right]}{\left(X_{\text{CH}_4}/X_{\text{air}}\right)_{st}} \tag{5.8}$$

Note that Eq. (5.8) is identical to the species-based definition Eq. (5.5). The difference is that the mole fractions in Eq. (5.8) are conserved throughout the reacting flow, while they are not in Eq. (5.5). In this way, the *local* effective equivalence ratio $\phi_{e,\text{element}}$ can be unambiguously determined throughout the flame zone. In the following part, $\phi_{e,\text{element}}$ will be written simply as ϕ.

5.4 Results and discussions

5.4.1 Effect of hydrogen blending

Response of the flame speed $S_{c,s}$ of stratified flames in mixtures H0, H20, and H40 and the corresponding homogeneous flame speed $S_{c,h}$ at each local equivalence ratio ϕ_R are shown in **Fig. 5.4**(a). As expected, $S_{c,h}$ peaks around stoichiometry for all mixtures and becomes larger with increasing hydrogen content. The values of $S_{c,h}$ are consistent with previous experimental results [125]. The stratified flame speed $S_{c,s}$ is increased from $S_{c,h}$ for all mixtures at any values of ϕ_R, indicating that the back-support effect increases $S_{c,s}$ of methane/hydrogen/air flames under rich-to-lean propagation regardless of the extent of the hydrogen content considered in this study. Meanwhile, the difference $S_{c,s} - S_{c,h}$ appears slightly smaller for mixtures with higher hydrogen content. For a quantitative comparison, the relative increase $(S_{c,s} - S_{c,h})/S_{c,h}$ for each mixture is shown in **Fig. 5.4**(b). It is seen that the relative increase is smaller for mixtures with higher hydrogen content. Two factors are responsible for this trend. First, as seen in **Fig. 5.4**(a), the (absolute) increase of $S_{c,s}$ from $S_{c,h}$ becomes slightly smaller with increasing hydrogen content. Secondly, the homogeneous flame speed $S_{c,h}$ is higher with increasing hydrogen content. In other words, the numerator and denominator of $(S_{c,s} - S_{c,h})/S_{c,h}$ becomes smaller and larger with an increasing hydrogen content, respectively. Since the cause of the second factor is straightforward, the cause of the first factor is investigated by observing the flame structure for each mixture.

Assuming that the primary mechanism of the back-support effect observed above is the same as that in the methane/air stratified flames studied in previous chapters, the mole fraction profiles of CH_4, H_2, H, and OH of the stratified flames in each mixture at $\phi_R \cong 0.90$ along with those of the corresponding homogeneous flames are shown in **Fig. 5.5**. On the upstream side of the reaction zone ($x - x_R < 0$ mm), the CH_4 mole fractions of the stratified
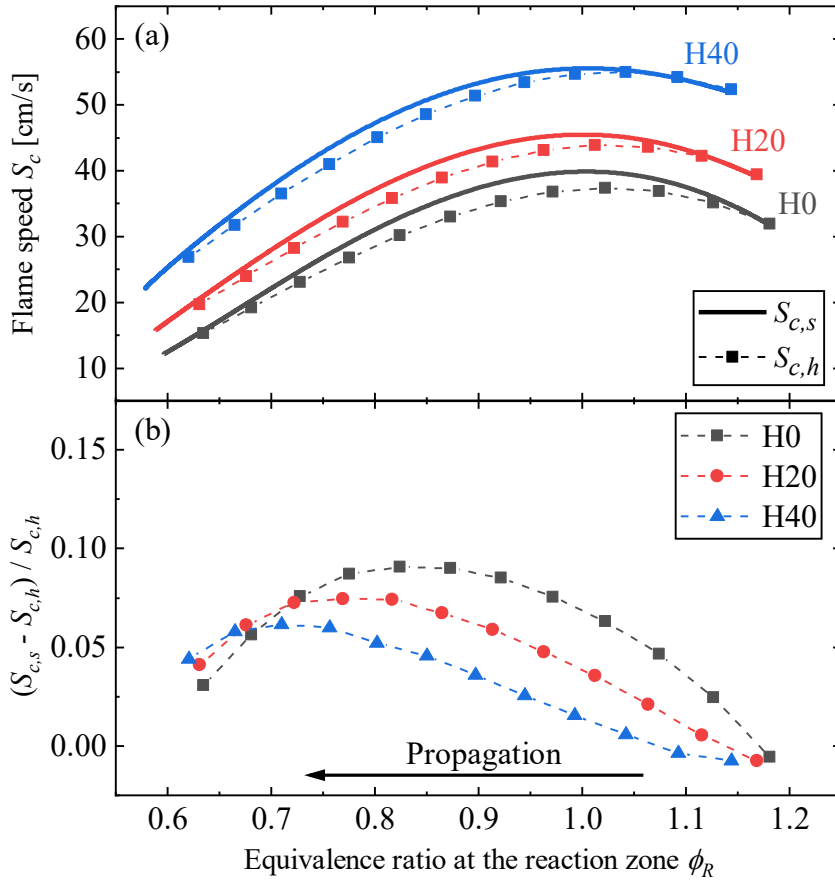
Fig. 5.4: Response of the flame speed $S_{c,s}$ of the stratified flames, the flame speed $S_{c,h}$ of homogeneous flames with the same ϕ_R, and the relative increase in $S_{c,s}$ as compared to $S_{c,h}$ for mixtures H0, H20, and H40.

flame in the unburned mixture decrease toward the upstream side as the mixture becomes leaner. It is also seen that for H20 and H40, the H_2 mole fractions of the stratified flame in the unburned mixture decrease with the methane mole fractions. On the downstream side ($x - x_R > 0$ mm), the H_2 mole fractions of the stratified flame are increased for all mixtures.

Interestingly, the H_2 mole fractions on the downstream side are not significantly affected by an increasing hydrogen content on the upstream side for both stratified and homogeneous flames. This is because, as shown in **Fig. 5.6**, the H_2 mole fraction of the equilibrium composition only slightly increases with increasing hydrogen content. Due to this nature, the increase in H_2 mole fraction in the burned gas of the stratified flame is of a similar magnitude for all mixtures. It is also seen that the increase in H_2 mole fractions around the reaction zone ($x - x_R = 0$ mm) of the stratified flame becomes smaller with higher hydrogen content. Since the diffusive flux of H_2 from burned gas is mostly the same for all mixtures, the smaller increase of H_2 in the reaction zone of the stratified flame with a higher hydrogen content seems to be caused by an increased diffusive flux of H_2 from the flame zone toward the
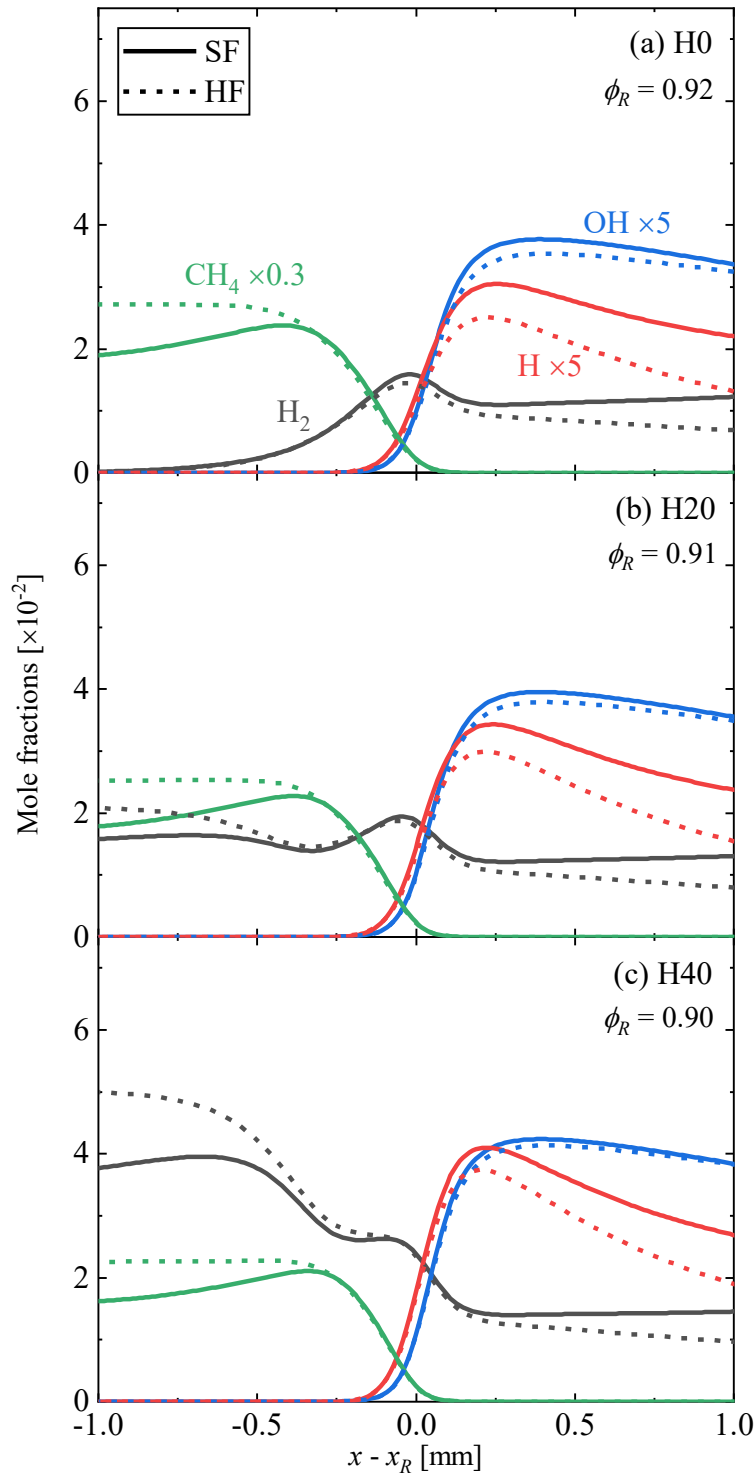
Fig. 5.5: Mole fraction profiles of CH_4, H_2, H, and OH of the stratified flames (SF) in mixtures H0, H20, and H40 at $\phi_R = 0.92$, $\phi_R = 0.91$, and $\phi_R = 0.90$, respectively, and those of the corresponding homogeneous flames (HF) with the same ϕ_R. The x-axes are shifted so that the reaction zone is at $x - x_R = 0$ mm for all flames.
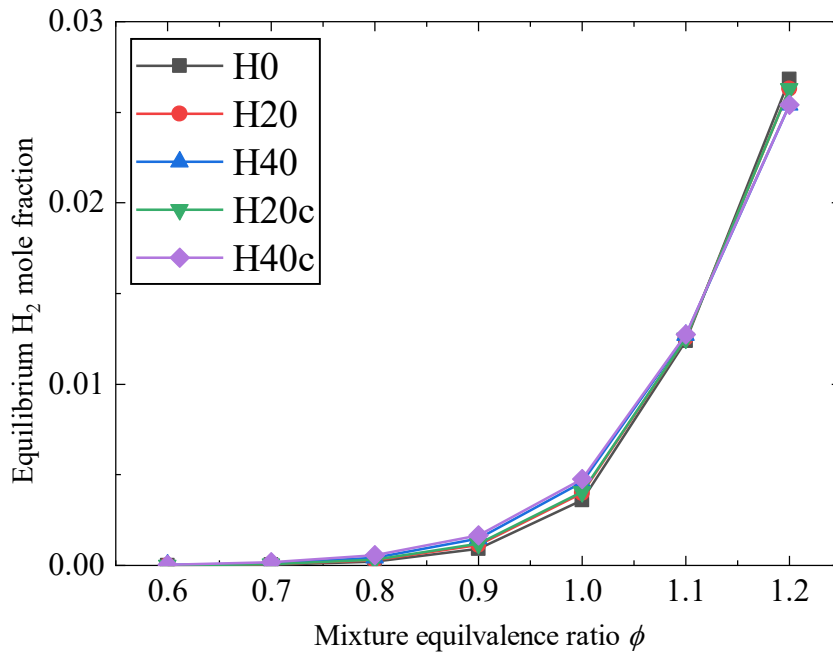
Fig. 5.6: H_2 mole fractions of equilibrium composition for mixtures H0, H20, H40, H20c, and H40c under different equivalence ratios ϕ.

unburned mixture. In short, the H_2 mole fraction around the reaction zone of the stratified flame seems to "leak" more toward the unburned mixture for a higher hydrogen content. This hypothesis is investigated later.

Meanwhile, both H and OH mole fractions are increased in the burned gas. As the local equivalence ratio ϕ_R is close to stoichiometry, the diffusive flux of H and OH from the burned gas are not expected to be large. This is because the equilibrium H and OH mole fractions of methane/air mixture peak around stoichiometry, as seen in Chapter 3, Section 3.4. Therefore, the increased H and OH mole fractions in the burned gas seems to be increased by the chain-branching reactions enhanced by the increased diffusive flux of H_2 from the burned gas, as also discussed in Chapter 3, Section 3.4. Consequently, due to the smaller increase in H_2 mole fractions around the reaction zone of the stratified flame, the increase in the H and OH mole fractions become smaller for a higher hydrogen content.

Figure 5.7 shows the profiles of temperature and species reaction rates for the stratified and the homogeneous flames considered in **Fig. 5.5**. Here, the positive and the negative reaction rates correspond to the production and consumption of the species, respectively. The temperature profiles in **Fig. 5.7**(a) show that in the burned gas, the temperature slightly increases for the stratified flame, though no difference is observed between each mixture. Meanwhile, in the preheat zone (-0.5 mm $< x - x_R < 0$ mm), the temperature profile is steeper for the stratified flames, which indicates the increased flame speed. Therefore, similar to the methane/air stratified flames, heat conduction from the burned gas is not the cause of
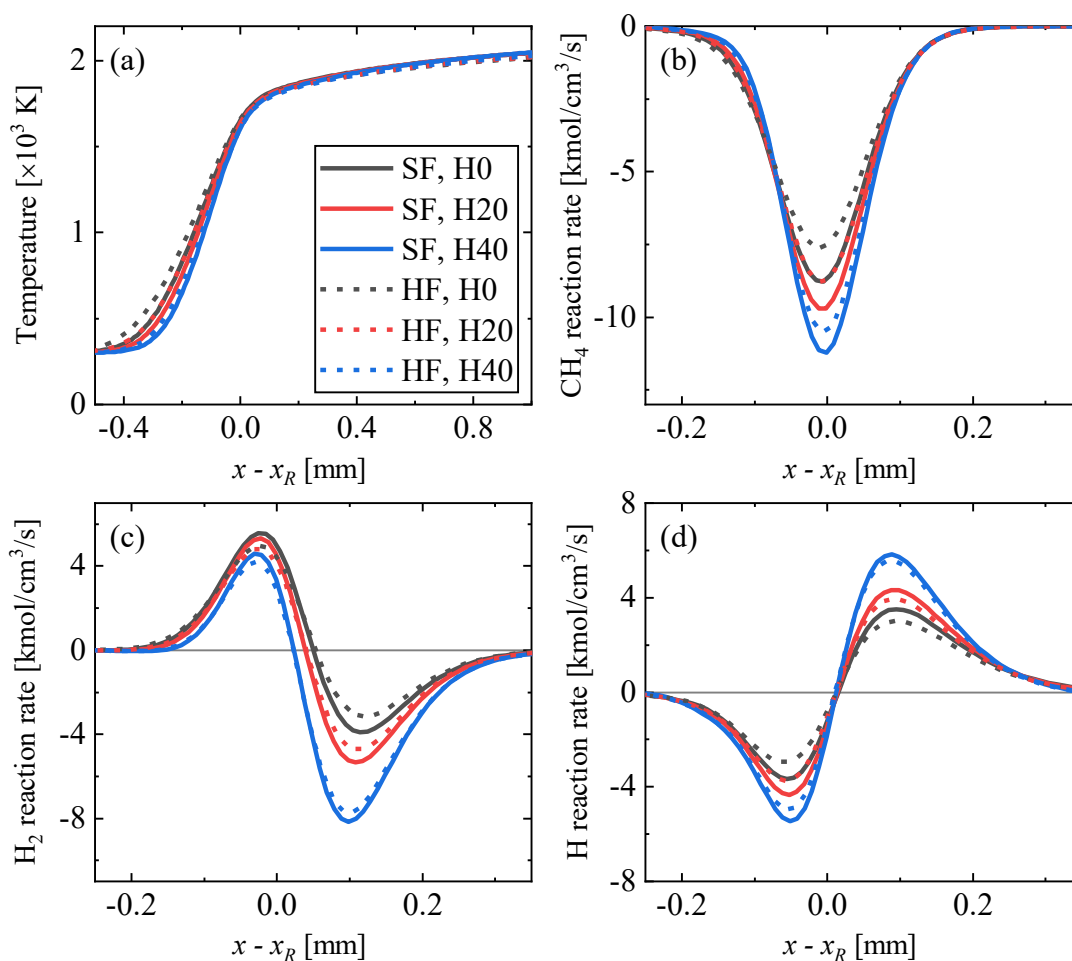
Fig. 5.7: Profiles of temperature and reaction rates of CH_4, H_2, and H of the stratified flames (SF) and the corresponding homogeneous flames (HF) in **Fig. 5.5**. The x-axes are shifted so that the reaction zone is at $x - x_R = 0$ mm for all flames.

the increased flame speed of methane/hydrogen/air stratified flames. The reaction rates of CH_4 and H_2 in **Figs. 5.7**(a) and (b) show that the consumption rates of CH_4 and H_2 for homogeneous flames become higher for a higher hydrogen content. Meanwhile, the increase in the consumption rates of the stratified flame from those of the corresponding homogeneous flames becomes smaller for a higher hydrogen content. These trends correspond to the response of the flame speeds in **Fig. 5.4**. The same trend is also seen in the consumption and the production rates of H in **Fig. 5.7**(c).

The above observations can be summarized as follows: The increase in the H_2 mole fractions around the reaction zone of a stratified flame lead to an increase in the consumption rate of H_2, which enhances the production of reactive species such as H through chain-branching reactions, as mentioned in Chapter 3. As a result, the consumption of CH_4 is enhanced by the increased reactive species, resulting in an increased flame speed. However, with a higher hy-

drogen content, the increase in the H_2 mole fractions around the reaction zone of the stratified flame are smaller, which results in a smaller increase in the flame speed. As mentioned above, the smaller H_2 mole fraction around the reaction zone seems to be due to more H_2 around the reaction zone "leaking" toward the unburned mixture for a higher hydrogen content. This is investigated in the following results and discussion.

5.4.2 Effect of upstream hydrogen diffusion

Response of the flame speed $S_{c,s}$ of stratified flames in mixture H20, H40, H20c, and H40c and the corresponding homogeneous flame speed $S_{c,h}$ at each local equivalence ratio ϕ_R are shown in **Fig. 5.8**(a). The calculation results for mixtures H20/H40 are the same as the previous ones. As explained in Section 5.2, both methane and hydrogen are decreased in mixtures H20 and H40. Meanwhile, only methane is decreased and the H_2 mole fraction is kept constant at the initial value in mixtures H20c and H40c. Therefore, as seen in the figure, $S_{c,h}$ is higher for H20c/H40c than for H20/H40 because a higher hydrogen content results in a higher flame speed. Similar to the results with mixtures H20/H40, $S_{c,s}$ is increased from $S_{c,h}$ for mixtures H20c/H40c. Moreover, the increase in $S_{c,s}$ from $S_{c,h}$ appears to be slightly larger for H20c/H40c than that for H20/H40, respectively. In **Fig. 5.8**(b), the relative increase $\left(S_{c,s} - S_{c,h}\right)/S_{c,h}$ is shown. It can be seen that $\left(S_{c,s} - S_{c,h}\right)/S_{c,h}$ is larger for mixtures H20c/H40c than for mixtures H20/H40, even though the denominator $S_{c,h}$ is larger for mixtures H20c/H40c, respectively. Therefore, it is seen that the magnitude of the back-support effect is larger for H20c/H40c than for mixtures H20/H40, respectively. Moreover, it is also seen that the difference in $\left(S_{c,s} - S_{c,h}\right)/S_{c,h}$ is larger between mixtures H40c and H40 than for H20c and H20.

The mole fraction profiles of CH_4, H_2, H, and OH of the stratified flames in mixtures H20c and H40c at $\phi_R \cong 0.90$ along with those of the corresponding homogeneous flames are shown in **Fig. 5.9**. In contrast to the H_2 fraction profiles of mixtures H20 and H40 in **Figs. 5.5**(b) and (c), the H_2 mole fractions on the far upstream side ($x - x_R = -1.0$ mm) retains the same value as those of the homogeneous flames, as expected from the definition of mixtures H20c/H40c. More importantly, the H_2 mole fraction is increased from those of the homogeneous flame for the entire flame zone, even extending out of the preheat zone ($x - x_R < -0.5$ mm). This is caused by an accumulation of H_2 that diffused from the burned gas. Moreover, since the H_2 mole fraction of the equilibrium composition is the same for mixture H20/H20 and H20c/H40c, respectively (see **Fig. 5.6**), the increase in the diffusive flux of H_2 from the burned gas is considered to be of the same magnitude for both mixtures. Therefore, it can be said that the absence of upstream ($x - x_R < -0.5$ mm) H_2 mole fraction gradient, which was present in mixtures H20/H40, is the primary cause that led to the increased H_2
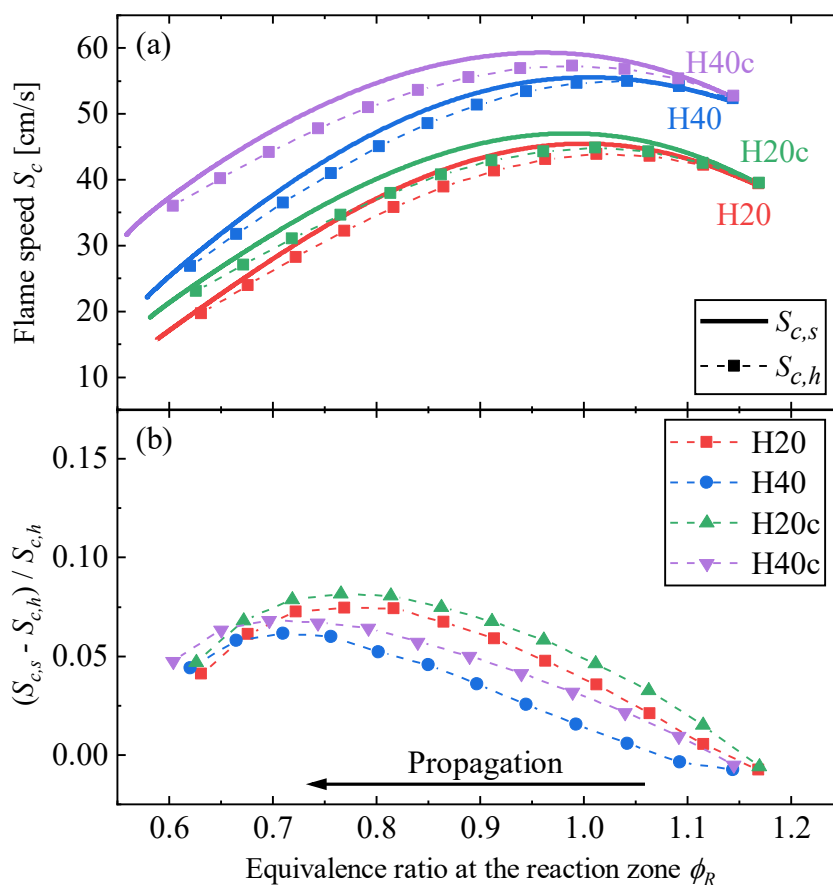
Fig. 5.8: Response of the flame speed $S_{c,s}$ of the stratified flames, the flame speed $S_{c,h}$ of homogeneous flames with the same ϕ_R, and the relative increase in $S_{c,s}$ as compared to $S_{c,h}$ for mixtures H20, H40, H20c, and H40c.

mole fraction in the flame zone. It is also seen that the increase in the H and OH mole fraction profiles of the stratified flame is larger for mixtures H20c/H40c than for mixtures H20/H40, implying that the increased H_2 mole fraction led to increased production of H and OH around the reaction zone.

The profiles of temperature and species reaction rates for the stratified and the homogeneous flames in mixtures H40 and H40c are compared in **Fig. 5.10**. The temperature profiles of stratified and homogeneous flames show insignificant differences between the two mixtures. On the other hand, the increase in the H_2 consumption rate of the stratified flame is larger for mixture H40c. This led to a larger increase in the CH_4 and H reaction rates in **Fig. 5.10**(b) and (c) through the enhanced chain-branching reactions.

In conclusion, when the hydrogen content of methane/hydrogen/air mixture is decreased with decreasing equivalence ratio, H_2 around the reaction zone diffuses out toward the unburned mixture, which weakens the back-support effect. Moreover, for a given variation in the effective equivalence ratio (defined in Section 5.3), the variation in the H_2 mole fraction in

the unburned mixture is larger with a higher hydrogen content, as shown in **Table 5.1**. Therefore, more H_2 would leak out from the reaction zone with a higher hydrogen content due to a larger mole fraction gradient formed in the unburned mixture, as seen in **Fig. 5.5**. It should be noted that, as discussed in Section 5.1, the above influence of the fuel species diffusing out toward the unburned mixture under stratification will be negligible for pure methane/air flames. The crucial point is that hydrogen is a fast-diffusing species that preferentially diffuses over methane. Meanwhile, when a methane/hydrogen/air flame propagates in a lean-to-rich mixture, it is expected that a decrease in the stratified flame speed caused by the (opposite) back-support effect is mitigated through increased H_2 diffusion from the unburned mixture.
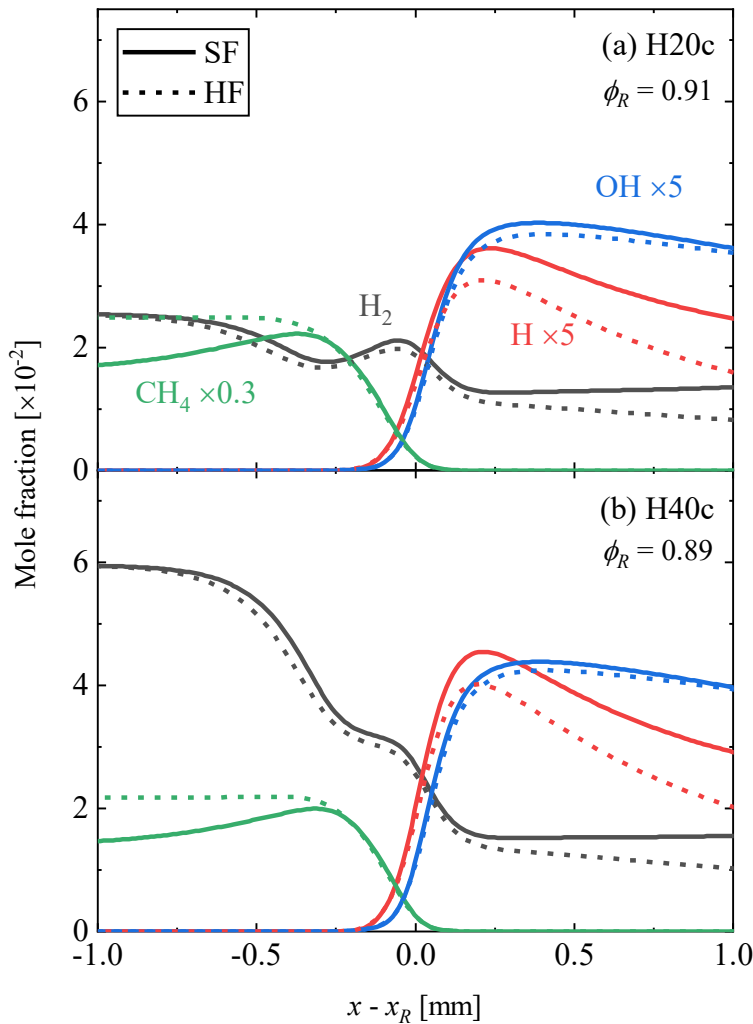
Fig. 5.9: Mole fraction profiles of CH_4, H_2, H, and OH of the stratified flames (SF) in mixtures H20c and H40c at $\phi_R = 0.91$ and $\phi_R = 0.89$, respectively, and those of the corresponding homogeneous flames (HF) with the same ϕ_R. The x-axes are shifted so that the reaction zone is at $x - x_R = 0$ mm for all flames.

Therefore, it can be said that the flame speed in a stratified methane/hydrogen/air mixture with a constant methane-to-hydrogen ratio will be less sensitive to the back-support effect under increasing hydrogen content within the range (0 to 40%) studied here.
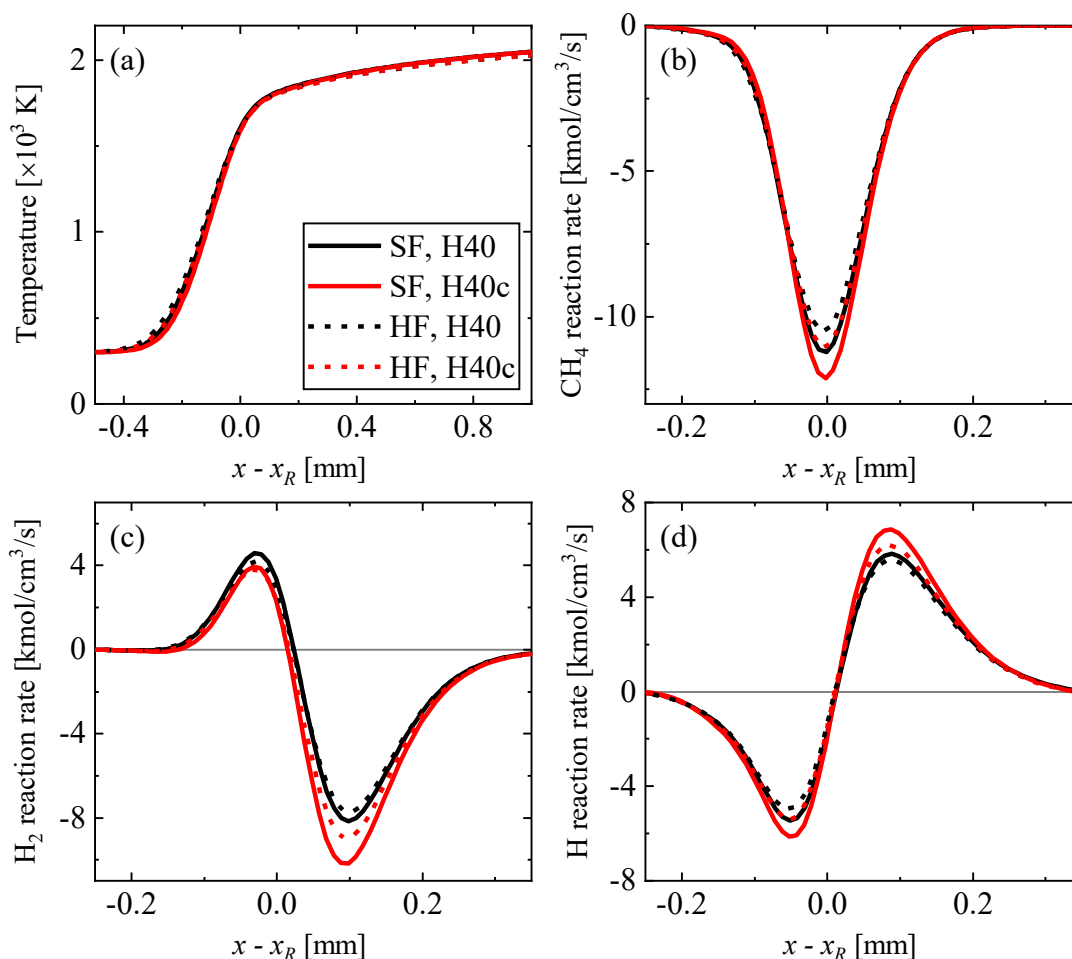
Fig. 5.10: Profiles of temperature and reaction rates of CH_4, H_2, and H of the stratified flames (SF) in mixtures H40 and H40c at $\phi_R = 90$ and $\phi_R = 89$, respectively, and those of the homogeneous flames (HF) with the same ϕ_R. The x-axes are shifted so that the reaction zone is at $x - x_R = 0$ mm for all flames.

5.5 Summary

A numerical study of methane/hydrogen/air counterflow flames under rich-to-lean mixture stratification is conducted under the hydrogen content of 0, 20, and 40% in the fuel blend. In particular, the influence of upstream H_2 mole fraction on the magnitude of the back-support effect is investigated by preparing two methods of mixture stratification: One way is to decrease the methane and the hydrogen content with the decreasing equivalence ratio under a constant methane-to-hydrogen volumetric ratio; The other way is to decrease only methane

mole fraction with decreasing equivalence ratio and the hydrogen mole fraction is kept constant. The results show that the stratified flame speed $S_{c,s}$ is increased from the corresponding homogeneous flame speed $S_{c,h}$ for all cases. Meanwhile, when the hydrogen content is decreased with the mixture equivalence ratio, H_2 diffuses preferentially toward the unburned mixture due to a decreasing mole fraction gradient and mitigates H_2 accumulation in the flame zone, which weakens the back-support effect. The extent of the above effect becomes larger with a higher hydrogen content because of the larger H_2 mole fraction gradient formed in the unburned mixture. From the above results, it is expected that the flame speed in a stratified methane/hydrogen/air mixture with a constant methane-to-hydrogen ratio will be less sensitive to the back-support effect under increasing hydrogen content within the range (0 to 40%) studied here.

Chapter 6

Stratified Combustion of Alternative Fuels – Ammonia

In this chapter, stratified flame propagation in an ammonia/air mixture is numerically investigated. First, ammonia is introduced as one of the promising hydrogen carriers, and issues associated with the use of ammonia as a fuel for combustion devices are discussed. Then, modifications to the numerical setup from Chapters 4 and 5 are explained, followed by definitions of flame characterization methods. In particular, a specific method was devised to characterize local burned gas composition in transiently propagating stratified flames. Lastly, the calculation results and their interpretations are presented.

6.1   Introduction

In the introduction of the previous chapter, the advantages and disadvantages of hydrogen as a carbon-free alternative fuel were discussed. One of the major issues addressed was that the volumetric energy density is much lower than that of hydrocarbon fuels. For example, the volumetric energy density of hydrogen is 10.7 MJ/m^3, while that of gasoline and diesel fuels are respectively 33×10^3 MJ/m^3 and 35×10^3 MJ/m^3 [147]. Therefore, for storage and transport, hydrogen needs to be liquified or compressed under severe conditions. Specifically, a temperature of as low as $-252.9℃$ is required for liquefaction [9], where up to 40% of the energy content of hydrogen must be expended [8,159]. In addition, due to its low molecular weight, hydrogen is known to boil off from the cryogenic tanks, which hinders its long-term storage [8]. On the other hand, to achieve an energy density similar to gasoline or diesel engines, hydrogen needs to be compressed up to 700 atm, which results in costly storage equipment [9] and safety concerns [159]. Therefore, it is seen that a more efficient and stable storage method is required for hydrogen to be used widely as an alternative fuel.

The above issues have spawned the idea of "hydrogen carriers" which store hydrogen in the form of chemical compounds to transport and distribute it in cost-competitive ways [9,159]. Christensen et al. [160] have categorized these approaches into direct and indirect

methods. In the direct hydrogen storage method, hydrogen is directly liberated from compounds when they are heated and/or pressures are lowered. This method is attractive since only absorption/adsorption and desorption processes are involved. Hence, a large variety of materials has been investigated for their applicability and efficiency as potential direct hydrogen storage materials [159,161]. Especially, solid-state nanoscale materials have gained considerable interest in recent years [161]. For example, metal hydrides and complex hydrides have attracted intensive attention due to their high storage capacities; though their poor reversibility and cost-effectiveness should be addressed for practical application [161]. Meanwhile, carbonaceous materials and metal-organic frameworks (MOFs) have also gained considerable interest for their high reversibility and fast kinetics. However, their storage capacities are impractically low under ambient temperatures [161]. Therefore, the direct storage method still needs a breakthrough in material properties to effectively meet various transportation applications [159].

On the other hand, in the indirect methods, hydrogen is separated from compounds through one or more separate chemical transformations such as reforming and decomposition reactions [160]. In addition, the hydrogen carriers need to be chemically or biologically synthesized sustainably. While such synthesis and extraction processes are not as simple as the direct method, the indirect method often provides significantly higher energy densities [160]. Some of the candidates are hydrocarbons, methanol, ethanol, and ammonia [160]. Especially, the production of methane from hydrogen and carbon oxides (CO or CO_2) using renewable energies is known as methanation, in which thermochemical [162] and biological [163] processes are studied extensively. Similarly, methanol and ethanol can be synthesized from hydrogen and carbon oxides [96]. One disadvantage associated with these carbon-based carriers is that the collection and conversion of atmospheric CO_2 is inefficient and energy-intensive due to the low CO_2 concentration [8]. Therefore, pure or high-concentration CO_2 exhaust gas streams from hydrocarbon-fueled power systems are necessary as the carbon feedstock [8]. In addition, consumption of these carbon-based carriers, either through hydrogen extraction or direct use in fuel cells and internal combustion engines, a carbon capture process is required to achieve carbon emission reductions, which adds to the cost.

Meanwhile, ammonia (NH_3) is a carbon-free carrier that can be synthesized using renewable energy sources from nitrogen, which is abundant in air, and hydrogen. Although, it should be noted that the current ammonia production method, primarily through the Haber Bosch process, is energy-intensive and heavily depends on fossil fuels; it is estimated that 1% of the total CO_2 released globally is produced in ammonia production plants [6,9,164]. As this estimate includes fossil fuels consumed for the production of hydrogen, the carbon footprint can be reduced or eliminated by using hydrogen produced from renewable energy sources in combination with carbon capture technologies for the Haber Bosch process. Moreover, re-

newable production of ammonia using an electrochemical reactor with water or steam and nitrogen as feedstocks has been studied on a fundamental scale [164].

In terms of chemical properties, ammonia possesses both advantageous and disadvantageous factors for storage and transportation. It is a toxic substance that poses a high risk for health, which is especially a concern for transport applications [6,8]. Moreover, it is also corrosive; modifications on pipelines and structural components are required when using ammonia for non-conventional applications [6]. Despite these issues, ammonia has attracted global interest as one of the promising hydrogen carriers because of the following characteristics: Due to its low reactivity, the risk of ammonia combustion or explosion hazards are much lower than those of hydrocarbon fuels [6]. In addition, it has a specific energy density of 22.5 MJ/kg, which is comparable to conventional fossil fuels; natural gas has around 55 MJ/kg [6]. This enables direct use of ammonia as a fuel for combustion devices, as will be explained. As a hydrogen carrier, ammonia has a very high volumetric and gravimetric hydrogen density compared to other known candidate compounds [6,9]. Moreover, the storage requirements for ammonia are similar to that of propane, where ammonia is liquified at room temperature under 9.90 atm or temperature of $-33.4℃$ under atmospheric pressure [6,9]. In fact, as ammonia is the second most chemical produced in the world primarily for fertilizers, there exists an established, reliable handling and shipping infrastructure including regulations for transportation [6,164]. This mitigates the above-mentioned hurdles associated with toxicity and safety.

In terms of utilization, ammonia can be used in a variety of ways. Ammonia has long been used as a hydrogen career to generate forming gas ($3H_2 + N_2$) through cracking under high temperatures. Studies on scrubbing residual NH_3 from cracked ammonia is being conducted to produce high purity hydrogen for use in low-temperature fuel cells such as polymer electrolyte membrane fuel cells (PEMFCs) and phosphoric acid fuel cells (PAFCs) [164]. For high-temperature fuel cells such as solid-oxide fuel cells (SOFCs), ammonia can be utilized directly without pretreatment since cracking occurs inside the fuel cell [164]. Another direct utilization of ammonia is its use as a fuel in combustion devices such as internal combustion engines, gas turbines, and boilers [6,9,164]. However, in terms of combustion characteristics of ammonia/air flames, several challenges must be overcome.

Two of the major obstacles associated with ammonia combustion are low flammability and high nitrogen oxide (NOx) emissions, which inhibit stable and clean combustion of ammonia in practical combustors [6,9]. For example, the maximum flame speed of ammonia/air premixed flames is about 7 cm/s, which is about one-fifth of that of methane/air flames [6,9]. Moreover, the minimum ignition energy of ammonia is 8.00 mJ, which is 28 times larger than 0.28 mJ for methane [6]. As for NOx emissions, while NOx in conventional hydrocarbon flames is produced through the oxidation of N_2 in the air, NOx in ammonia/air flames is produced through the oxidation of N content in the fuel, which results in significantly higher

NOx emissions. To tackle these problems, extensive studies have been conducted to develop strategies to stabilize premixed/non-premixed flames and mitigate pollutant emissions. An established approach is the use of a swirl burner configuration. In a swirl burner, the reactant mixture is supplied with a tangentially angled flow at the nozzle, which results in a poloidal recirculation zone. This creates a low-velocity zone that prevents flame blow-off. In addition, the recirculation zone supplies hot burned gases and active radicals to the unburned mixture which enhances combustion [9]. Valera-Medina et al. [165,166] in Cardiff University conducted preliminary experimental studies to investigate stability and emission characteristics of premixed hydrogen- or methane-blended ammonia/air flames on a swirl burner. On the other hand, a series of studies [167–174] promoted by the Cross-Ministerial Strategic Innovation Program (SIP) of Japan has shown that premixed [167,170] and non-premixed [171] pure ammonia/air flames can be stabilized for various equivalence ratio and nozzle velocity by using a laboratory-scale swirl burner. Additionally, it was found that secondary air injection is effective for reducing NO and unburned NH_3 emission [169,173,174]. These findings were reproduced on a 50-kW class micro-gas-turbine system [168,172]. Recently, it was reported that liquid ammonia spray flame was successfully stabilized on a single-stage swirl combustor with preheated air [175]. Meanwhile, a research group from KAUST has begun experimental studies [176–179] on the stability of methane- and hydrogen- blended premixed ammonia/air swirl flames under a very lean ($\phi < 0.7$) equivalence ratio to achieve low NOx emission.

In the above setup, localized pockets of rich or lean unburned mixtures may exist due to insufficient mixing of fuel and the oxidizer, staged air injection, and incomplete evaporation of fuel droplets [33]. This necessitates an understanding of a premixed flame propagating in compositionally stratified mixtures. Especially, considering the results presented in the following chapters, one question arises: Do ammonia/air stratified flames exhibit a back-support like the methane/air flames? Although the majority of previous studies on the back-support effect have been conducted for methane/air flames, it is known that the influence of such effect may vary depending on the fuel species [112,113,115] or the temperature regime [119] as characteristics of the burned gas play crucial roles. As hydrogen molecule is a major component in the burned gas of ammonia/air flames, a mechanism similar to the one in methane/air flames may modify the flame speed in stratified mixtures. However, to the best of the author's knowledge, there has been no report of the back-support effect on ammonia/air flames. Moreover, although emission characteristics of nitrogen monoxide (NO) in ammonia/air flames have been studied for homogeneous mixtures [180], little is known about that of flames propagating in stratified mixtures. Therefore, the study in this chapter aims to elucidate the following points:

- How does mixture stratification affect the flame speed of ammonia/air stratified flames?

Does the back-support effect occur in a similar manner as in methane/air flames?

- How does mixture stratification affect the NO emission characteristics of ammonia/air flames?

Numerical analysis with detailed kinetics is conducted to observe the chemical process and transport phenomena in detail. While it is common to blend ammonia fuels with hydrogen or hydrocarbons to enhance flame stability [165,166,168,174,176–179], this study focuses on pure ammonia fuels to clarify the basic properties of stratified ammonia/air combustion.

6.2 Numerical setup

The analyses in this study were conducted in a similar manner as described in Chapter 4. The major difference is that the mixture composition was changed from methane/air mixtures to ammonia/air mixtures. Therefore, this section will focus on the changes made from the setup in Chapter 4. Please refer to Chapter 4, Section 4.2 and 4.3 for a detailed explanation of the setup and the definitions.

6.2.1 Unsteady and steady calculations

Numerical simulations of unsteady premixed flames propagating in rich-to-lean and lean-to-rich stratified mixtures (*stratified flames*) and steady premixed flames propagating in homogeneous mixtures (*homogeneous flames*) were conducted using OPUS. For the study in this chapter, both the stratified and the homogeneous flames were calculated in a reactant-to-reactant (RTR) configuration, schematically shown in **Fig. 6.1**. Unlike in the previous chapters, the reactant-to-product (RTP) configuration was not used for the calculation of homogeneous flames for the sake of simplicity. This became possible for the current study as the flow velocity was kept sufficiently low and the distance between the nozzle and the stagnation
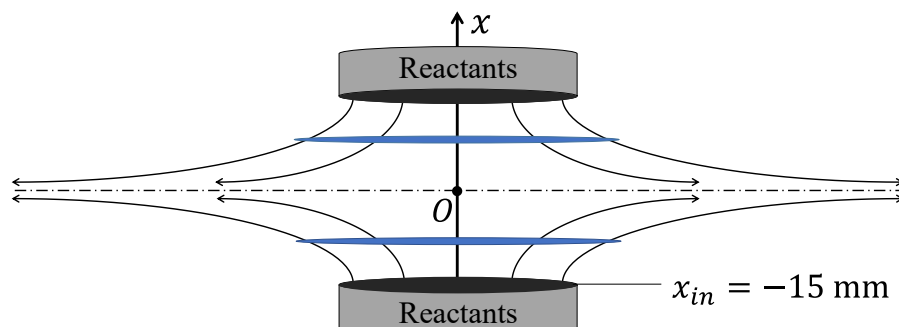
Fig. 6.1: Schematic representation of counterflow premixed flames in the reactant-to-reactant (RTR) configuration.

plane was widened to 15 mm so that the steady flames were always detached from the stagnation plane. For all cases, a uniform grid of 10 μm was applied. A mixture of ammonia and air (mole fraction: 21% O_2 and 79% N_2) was supplied from the reactant nozzle at 300 K and 0.1013 MPa.

Unsteady calculations were performed for the stratified flames. The nozzle velocity was fixed at 0.10 m/s, which is much lower than in the previous chapters because of the low flame speed of ammonia/air mixtures. Meanwhile, in a similar manner as in Chapters 4 and 5, the inlet equivalence ratio ϕ_{in} was transiently decreased from $\phi_1 = 1.4$ to $\phi_2 = 0.8$ for a rich-to-lean stratified flame. In addition, a lean-to-rich stratified flame was studied by transiently increasing ϕ_{in} from $\phi_1 = 0.8$ to $\phi_2 = 1.4$. Here, the rich limit, $\phi = 1.4$, was chosen to match the rich flammability limit of ammonia/air flames [181], while the lean limit, $\phi = 0.8$, was chosen so that the flame speed at the lean limit is approximately the same as the flame speed at the rich limit. Also, the lean limit in this study is close to the lean flammability limit, which is reported as around $\phi = 0.7$ [181]. **Figure 6.2** shows the resulting variation in the local equivalence ratio ϕ_P and its spatial gradient $(d\phi/dx)_P$ at the upstream edge of the preheat zone. The peak spatial gradient $(d\phi/dx)_P$ was adjusted to be 0.2 mm^{-1} for rich-to-lean and −0.2 mm^{-1} for lean-to-rich stratified flames, respectively. This corresponds to a non-dimensional stratification thickness of $\delta_s/\delta_T = 1.7$ at $\phi = 1.1$, where δ_s is the stratification thickness $\delta_s = \Delta\phi/(d\phi/dx)_{P,max}$ [18,114] and δ_T is the thermal flame thickness $\delta_T = \Delta T/(dT/dx)_{max}$. The current value of δ_s/δ_T is comparable to previous numerical studies on
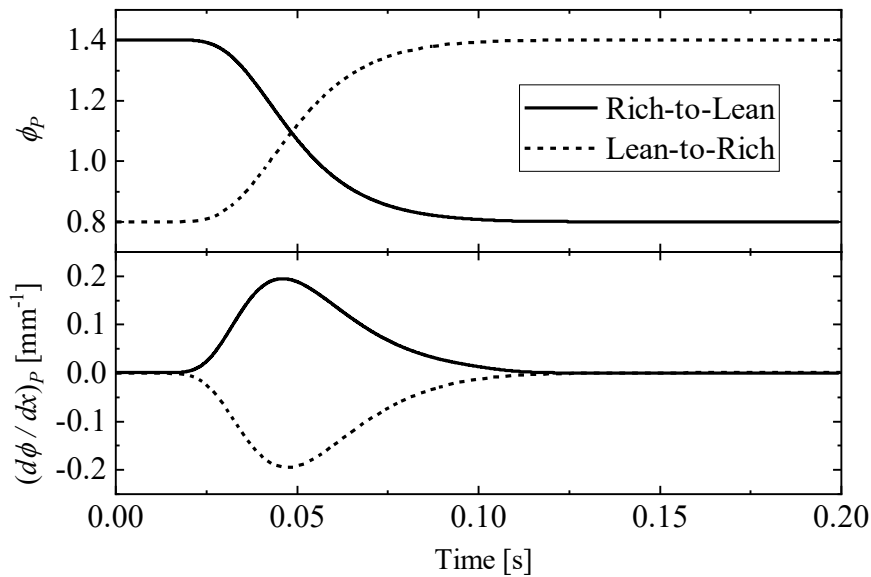
Fig. 6.2: Time variation of local equivalence ratio at the upstream edge of the preheat zone ϕ_P (first low) and its spatial gradient $(\partial\phi/\partial x)_P$ (second low) for the rich-to-lean and lean-to-rich stratified flames.

laminar stratified flames [18,112,114].

Steady calculations were performed for the homogeneous flames. The nozzle equivalence ratio ϕ_{in} and the velocity u_{in} were varied to obtain a library of homogeneous flames with different values of local equivalence ratio ϕ_R and local strain rate a_R at the reaction zone. In the same manner as described in Chapter 4, the homogeneous flames which have the closest values of ϕ_R and a_R to the stratified flames were chosen as the reference homogeneous flames.

6.2.2   Chemical kinetics

For the ammonia/air chemical kinetics, a detailed mechanism recently developed by Okafor et al. [182] was used. This mechanism consists of 59 species and 356 reactions and is based on GRI-Mech 3.0 [116] and the mechanism by Tian et al. [183]. The predicted laminar NH_3/air flame speed under standard temperature and pressure has been validated against several experimental data [184,185]. Although uncertainty in the flame speed of approximately ± 1 cm/ s still exists due to scattered experimental values, it is not expected to impair the generality of the conclusions of this study as reaction kinetics of NH_3/air combustion is well-understood [9,186] and is incorporated in the mechanism. In this study, the elementary reactions in the mechanism by Okafor et al. [182] will be referred to as (OK #), where # is the number of the reactions compiled in **Table A.2** in Appendix A.

6.3   Method of flame characterization

6.3.1   Flame speed

Similar to the previous chapters, the flame speed is evaluated as the fuel consumption speed S_c:

$$S_c = \frac{1}{\rho_u(Y_{f,u} - Y_{f,b})} \int_{x_{in}}^{x_{5\%}} (-W_f \dot{\omega}_f) dx \tag{6.1}$$

where ρ_u is the unburned gas density; $Y_{f,u}$ and $Y_{f,b}$ are respectively fuel mass fraction in the unburned and the burned gas; W_f and $\dot{\omega}_f$ are respectively molecular weight and molar reaction rate of the fuel. Unburned mixture properties ρ_u and $Y_{f,u}$ are calculated from ϕ_R. Here, the integration range is limited to $[x_{in}, \ x_{5\%}]$ for reasons discussed later.

In the previous chapters, the fuel mass fraction in the burned gas $Y_{f,b}$ was excluded from the definition since the amount of unburned fuel in the burned gas is negligibly small for methane/air flames even in rich mixtures, as seen in Chapter 3. On the other hand, $Y_{f,b}$ is a major component in the burned gas of rich ammonia/air flames [9], thus neglecting $Y_{f,b}$ in the above definition results in an underestimation of the actual flame speed as the denominator

$\rho_u(Y_{f,u} - Y_{f,b})$ is overestimated. Recently, Inanc et al. [18] proposed obtaining $Y_{f,b}$ from homogeneous flames calculations at corresponding values of ϕ_R, and using them for evaluating S_c of both stratified and homogeneous flames. Although, $Y_{f,b}$ defined in this way should be considered as approximate values for the case of stratified flames. This is because the burned gas composition continuously varies in the downstream direction and $Y_{f,b}$ cannot be evaluated unambiguously, as already mentioned in Chapter 3, Section 3.3. Nevertheless, the same method as Inanc et al. [18] was applied in this study to minimize the underestimation of S_c in rich mixtures. The above ambiguity in the definition of $Y_{f,b}$ can be circumvented by using the integrated fuel consumption rate $\int(-W_f\dot\omega_f)dx$ as a measure of the burning rate. This approach has been recently adopted by Wang et al. [119]. Therefore, in addition to the stratified flame speed $S_{c,s}$ and the homogeneous flame speed $S_{c,h}$, the relative increase $(S_{c,s} - S_{c,h})/S_{c,h}$ is also presented in the results, as done in previous chapters. According to Eq. (6.1), $(S_{c,s} - S_{c,h})/S_{c,h}$ is equivalent to the relative increase in the integrated fuel consumption rate $\int(-W_f\dot\omega_f)dx$ since the factor $\rho_u(Y_{f,u} - Y_{f,b})$ cancels out, thus the ambiguity in $Y_{f,b}$ is eliminated.

In rich ammonia/air flames, unburned NH_3 is a major component in the burned gas [9], thus the reaction rate profile of NH_3 exhibits a long tail on the downstream side of the reaction zone. Especially for rich-to-lean stratified flames, more unburned NH_3 exists in the burned gas than that in the corresponding homogeneous flames, which results in additional fuel consumption in the burned gas. This causes an overestimation of $S_{c,s}$ when the integral is performed over the entire calculation domain, i.e., $[x_{in}, 0\text{ mm}]$. To minimize this effect, the upper bound of the integration was set at $x = x_{5\%}$, where the heat release rate downstream of the flame becomes 5% of the peak value, as illustrated in **Fig. 6.3**. The 5%-threshold has also been applied in previous studies for integrating the fuel consumption rate in stratified hydrogen/air flames [113] and cool flames [119]. It has been confirmed that 5% is sufficient for excluding downstream fuel consumption in ammonia/air stratified flames, as discussed in Appendix C.
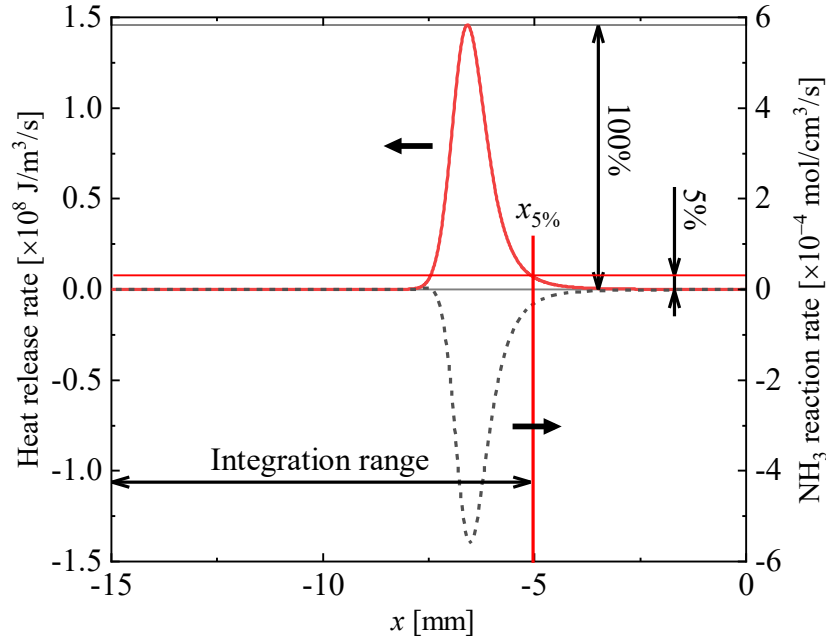
Fig. 6.3: Example of integration range $[x_{in}, x_{5\%}]$ for the evaluation of the flame speed S_c, where $x_{in} = -15$ mm and $x_{5\%}$ is the location at which the downstream heat release rate is 5% of the maximum value.

6.3.2 Local equivalence ratio

As explained in previous chapters, the local equivalence ratio must be defined in terms of element composition. First, the conventional species-based equivalence ratio is written as

$$\phi_{\text{species}} = \frac{X_{\text{NH3}}/X_{\text{air}}}{(X_{\text{NH3}}/X_{\text{air}})_{st}} \tag{6.2}$$

where X_k is the mole fraction of a mixture component k, and $(X_{\text{NH3}}/X_{\text{air}})_{st}$ is the stoichiometric fuel-air molar ratio. Based on the definition of the fuel-air ratio, the above is expression is equivalent to

$$\phi_{\text{species}} = \frac{0.75 X_{\text{NH3}}}{X_{\text{O2}}} \tag{6.3}$$

considering the global reaction $\text{NH}_3 + 0.75\text{O}_2 \rightarrow \text{N}_2 + 1.5\text{H}_2\text{O}$. However, unlike in methane/air mixtures, the above species-based definition cannot be straightforwardly extended to an element-based definition. This is because the element N exists both in the fuel as NH_3 and the air as N_2. Therefore, an alternative approach was taken, as was done in previous studies [171,187].

First, considering the elemental stoichiometric relations in the above global reaction, a conserved scalar β is expressed as

$$\beta = 0.75 \frac{Z_N}{W_N} + 0.25 \frac{Z_H}{W_H} - \frac{Z_O}{W_O} \tag{6.4}$$

where Z_k and W_k are respectively the elemental mass fraction and atomic mass of element k. Here, β retains its value as the reaction proceeds and it is only modified by mixing of different mixture compositions. Next, two virtual streams of fuel and air, respectively, are considered. Stream 1 consists of pure air. Therefore, the conserved scalar β_1 is expressed as

$$\beta_1 = 0.75 \frac{Z_{N,1}}{W_N} - \frac{Z_{O,1}}{W_O} \tag{6.5}$$

Note that $Z_{H,1} = 0$ as no fuel exists. The values $Z_{N,1}$ and $Z_{O,1}$ are evaluated from the air composition (21 vol.% O_2 and 79 vol.% N_2). On the other hand, Stream 2 consists of pure fuel. Therefore, the conserved scalar β_2 is expressed as

$$\beta_2 = 0.75 \frac{Z_{N,2}}{W_N} + 0.25 \frac{Z_{H,2}}{W_H} \tag{6.6}$$

Note that $Z_{O,2} = 0$ as no air exists. The values $Z_{N,2}$ and $Z_{H,2}$ are evaluated from the composition of NH_3. It should be noted that in the above, β_1 and β_2 are both constants, while β is a variable evaluated based on the local elemental composition of the mixture. Consequently, the Bilger's mixture fraction [188] for ammonia/air mixtures is defined using β_1, β_2, and β as

$$Z = \frac{\beta - \beta_2}{\beta_1 - \beta_2} \tag{6.7}$$

Note that $Z = 1$ for a pure air stream, $Z = 0$ for a pure ammonia stream, and $0 < Z < 1$ for an ammonia/air mixture. Since β is a conserved scalar, Z is also a conserved scalar that is only determined by the extent of mixing of fuel and air streams. With further derivation, it can be shown that the relation between Z and ϕ is

$$\phi = \left(\frac{Z}{1-Z} \right) \left(\frac{1 - Z_{st}}{Z_{st}} \right) \tag{6.8}$$

where $Z_{st} = 0.142$ is the value of Z in a stoichiometric mixture. In the above definition, ϕ becomes a conserved scalar and is defined throughout the reacting flow.

6.3.3 Fluid particle tracking

In addition to the flame speed, another goal of this study is to compare the NO emission characteristics of stratified ammonia/air flames with that of homogeneous flames. In homogeneous flames, the burned gas composition depends on the flow residence time downstream of the flame. This is because, especially for ammonia/air flames whose burned gas is far from equilibrium [9], the burned gas continues to react and its composition transiently varies as it is convected downstream. Moreover, for stratified flames, the burned gas composition additionally depends on the local equivalence ratio. Therefore, the emission characteristics of strati-

fied flames should be identified as the *local* emission characteristics that depend both on the residence time and the local equivalence ratio of the burned gas. This means that both the time and location of each local portion of the burned gas need to be identified. The particle tracking method is as follows.

The local burned gas composition in the stratified flame is characterized by a total of N fluid particles whose initial equivalence ratios are $\phi_{init,n}$ $(n = 1, 2, ..., N)$ at the reaction zone. Specifically, in the stratified flame, the local equivalence ratio $\phi_{R,s}(t)$ at the reaction zone $x_{R,s}(t)$ varies transiently as the flame propagates toward leaner or richer mixtures. At the instant $t = t_n$ where $\phi_{R,s}(t_n) = \phi_{init,n}$, the nth fluid particle initially at the reaction zone $x_{R,s}(t_n)$ is tracked downstream in a Lagrangian manner for a finite travel time $\tau_{ptcl,n}$. As such, the history of the nth fluid particle can be interpreted as the history of a local portion of the burned gas with the local equivalence ratio $\phi_{init,n}$ and the residence time $\tau_{ptcl,n}$. In addition, the history of the nth fluid particle in the stratified flame is compared with that of a corresponding fluid particle in a homogeneous flame. To this end, a fluid particle is tracked from the reaction zone in a homogeneous flame whose equivalence ratio at the reaction zone $\phi_{R,h}$ equals $\phi_{init,n}$. In this way, the histories of NO reaction rate and NO concentration for the nth fluid particle in the stratified flame can be compared with those of the corresponding fluid particle in the homogeneous flame. Here, the local strain rate a_R of the homogeneous flame is adjusted to equal the initial a_R of the corresponding fluid particle in the stratified flame.

Figure 6.4 shows the reaction zone location $x_{R,s}$ of the stratified flame and the trajectory $x_{ptcl,s}$ of the fluid particles with different initial equivalent ratios ϕ_{init}. Total of 11 particles were tracked for each stratified flame. All particles are convected from $x_{R,s}$ toward the stagnation plane $(x = 0$ mm$)$. In the current stagnation flow, it is necessary to stop tracking particles in a finite time, because the velocity of the fluid particles approaches zero, and the residence time diverges to infinity. Therefore, in this analysis, the tracking was stopped at $\tau_{ptcl} = 20$ ms for each particle. From **Fig. 6.4**, it is seen that the location where the tracking was stopped (the upper end of the broken line) is at least 1 mm away from the stagnation plane, and the particles travel in the burned gas for about 4 to 6 mm. The reason why the particles in the rich-to-lean stratified flame in **Fig. 6.4**(a) have a relatively long travel distance than the lean-to-rich case in **Fig. 6.4**(b) is that the flame speed is larger for the former case and thus the downstream flow is faster, as will be shown in the results.
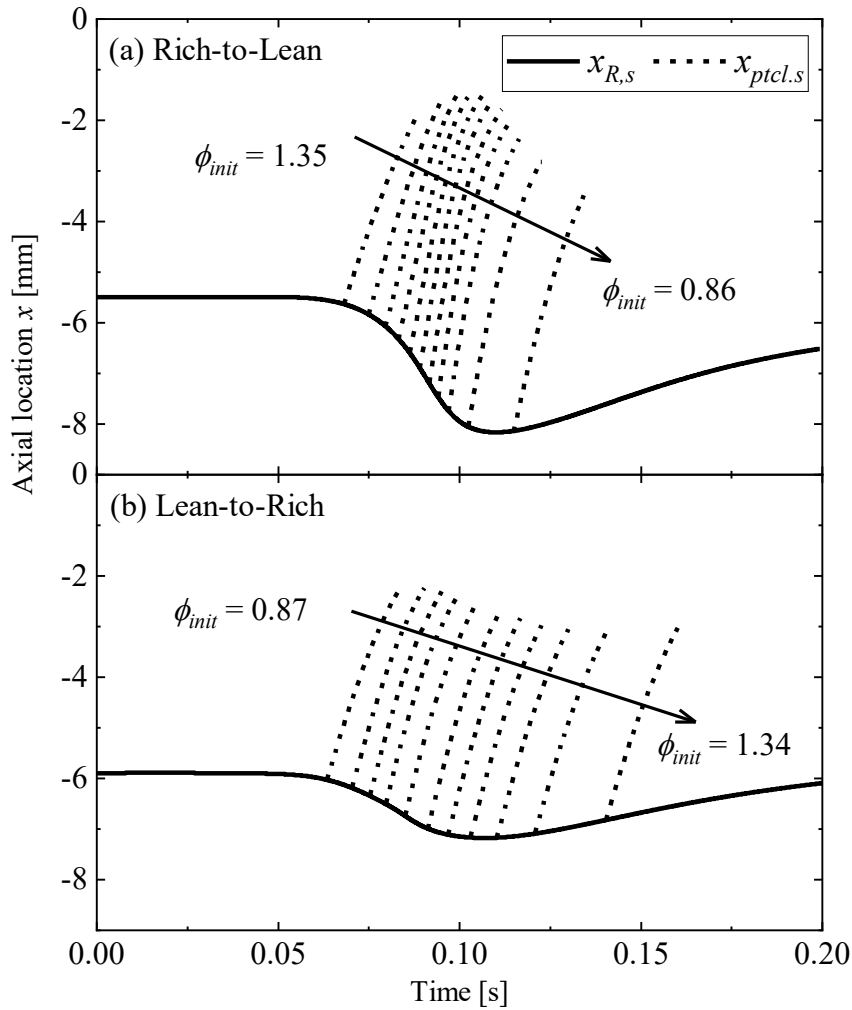
Fig. 6.4: Trajectories of the reaction zone location $x_{R,s}$ and the fluid particle location $x_{ptcl,s}$ of stratified flames with (a) decreasing and (b) increasing equivalence ratio. ϕ_{init} denotes the initial equivalence ratio of fluid particles.

6.4 Results and discussions

6.4.1 Characteristics of burned gas compositions

It has been shown in previous chapters that the composition of the burned gas plays a crucial role in modifying the flame properties. Therefore, it is beneficial to clarify the burned gas composition of homogeneous ammonia/air flames for different mixture equivalence ratios ϕ. In Chapter 3, the burned gas composition of methane/air flames was approximated by the mixture composition at thermodynamic equilibrium. However, for ammonia/air flames, it is known that the burned gas composition is far from equilibrium due to the low reactivity [189]. Therefore, following the approach by Kobayashi et al. [189], mole fractions of some relevant species 2.5 mm downstream of the reaction zone in a one-dimensional homogeneous flame,

obtained from the PREMIX code [189], are plotted in **Fig. 6.5**. Here, the mole fractions of O_2, N_2, and H_2O are not shown because of their minor importance in the following discussions. Compared to the burned gas composition of methane/air mixtures in Chapter 3, Section 3.4, some important differences are observed. First, while the unburned CH_4 was negligibly small regardless of mixture stoichiometry in methane/air flames, the unburned NH_3 rapidly increases with increasing equivalence ratio when $\phi > 1.10$ and becomes one of the major species in the burned gas in ammonia/air flames. Although much smaller in quantity, NH_i radicals, i.e., NH_2, NH, and N radicals, also increase rapidly in the burned gas when $\phi > 1.10$; Here, only NH_2 mole fractions are shown. These radicals are products of partially oxidized NH_3, and they play major roles in the ammonia/air chemistry, as will be seen later. Contrarily, the mole fractions of NO and OH are small when $\phi > 1.10$, but they increase rapidly with decreasing equivalence ratio when $\phi < 1.10$ and peaks around $\phi = 0.90$ and 0.95, respectively. The trends of NO and OH coincide because the presence of abundant OH is crucial for the production of NO. From the above trends, it can be seen that $\phi = 1.10$ is the optimal equivalence ratio that minimizes the sum of the major pollutants of ammonia/air flames, i.e., the unburned NH_3 and NO, as also noted by Kobayashi et al. [189]. Meanwhile, the H mole fraction peaks around $\phi = 1.05$ and rapidly decreases toward richer and leaner sides, which is similar to the trend seen in methane/air mixtures. On the other hand, the H_2 mole fraction is almost non-existent in lean mixtures, increases rapidly around $\phi = 1.05$, and then reaches a
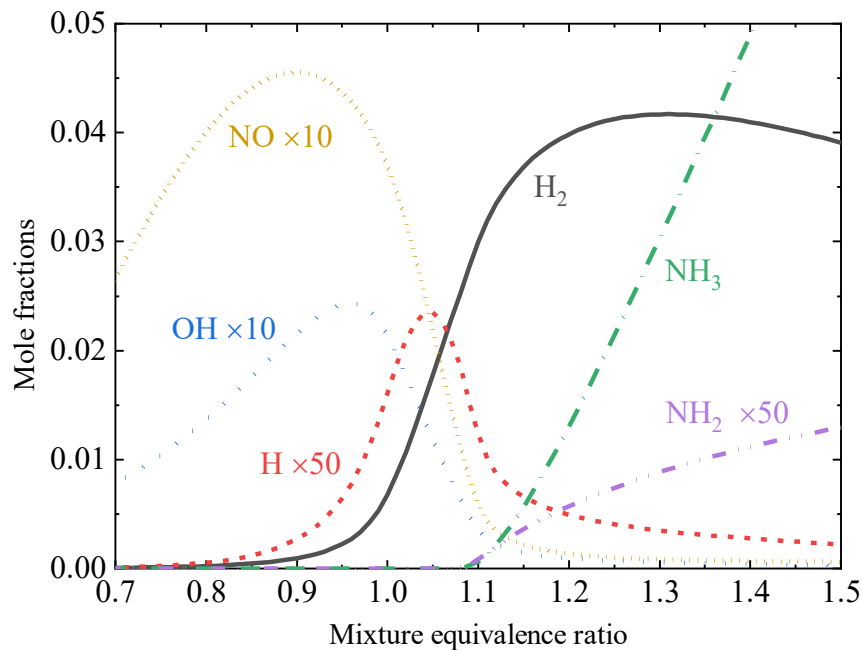
Fig. 6.5: Major species mole fractions 2.5 mm downstream of the reaction zone in one-dimensional premixed flames calculated by PREMIX [189] code.

plateau for $\phi > 1.20$. This is in contrast to the trend in the methane/air mixtures, where the H_2 mole fraction increases monotonically in rich mixtures. These trends will be revisited for interpreting the results obtained for stratified flames in the following discussions.

6.4.2   Response of the flame speed

Response of the flame speed $S_{c,s}$ of (a) rich-to-lean and (b) lean-to-rich stratified flames and the corresponding flame speed $S_{c,h}$ of homogeneous flames at each local mixture equivalence ratio ϕ_R are shown in **Fig. 6.6**. For the rich-to-lean stratified flame, the values of $S_{c,s}$ are mostly the same with $S_{c,h}$ when $1.2 \leq \phi_R \leq 1.4$. However, $S_{c,s}$ gradually becomes larger than $S_{c,h}$ as ϕ_R further decreases, and at around $\phi_R = 0.95$, the relative increase ($S_{c,s} - S_{c,h})/S_{c,h}$ reaches the peak value of more than 40%. With a further decrease in ϕ_R, the increase in $S_{c,s}$ diminishes as the mixture becomes homogeneous. Meanwhile, for the lean-to-rich stratified flame, an opposite trend is observed; $S_{c,s}$ becomes smaller than $S_{c,h}$ as ϕ_R increases. However, there are some differences from the rich-to-lean case: $S_{c,s}$ starts to deviate from $S_{c,h}$ from the early stage of propagation; the maximum relative ($S_{c,s} - S_{c,h})/S_{c,h}$ is now slightly on a slightly richer side, $\phi_R = 1.05$; and its magnitude is smaller, approximately 20%. Nevertheless, regardless of the direction of stratification, the response of $S_{c,s}$ resembles the back-supported stratified flame propagation in methane/air mixtures observed in Chapters 3 and 4 and previous studies [20,78,104,114,115]. Therefore, it is expected that a similar mechanism of back-supporting phenomenon exists for the stratified ammonia/air flames. As the response of the stratified flame speed for the lean-to-rich case is qualitatively the opposite of the rich-to-lean case, the following discussion will focus on the mechanism of rich-to-lean stratified flame propagation.

In **Fig. 6.7**, Profiles of heat release rate, temperature, and major species mole fractions at $\phi_R = 0.94$ of the rich-to-lean stratified flame in **Fig. 6.6**(a), along with those of the corresponding homogeneous flame, are shown. In **Fig. 6.7**(a), the heat release rate of the stratified flame is increased, as expected from the increased flame speed. Moreover, the thermal thickness of the stratified flame is thinner, as indicated by the steeper temperature gradient in the preheat zone ($-2.0 \,\text{mm} < x - x_R < 0 \,\text{mm}$), which is also a sign of the increased flame speed. Nevertheless, it can be seen that the ammonia/air flames are much thicker than the methane/air flames, whose preheat zone thickness was around 0.5 mm in Chapter 3, due to the lower flame speed. Meanwhile, at the downstream of the burned gas ($3 \,\text{mm} \leq x - x_R$), the temperature profile exhibits a negative gradient toward the downstream side of the stratified flame. This shows that an increase in heat flux from the burned gas is not the cause of the increase in the stratified flame speed; the slight increase in the temperature downstream of the reaction zone ($0 \,\text{mm} \leq x - x_R \leq 2 \,\text{mm}$) seems to be a consequence of the increased heat
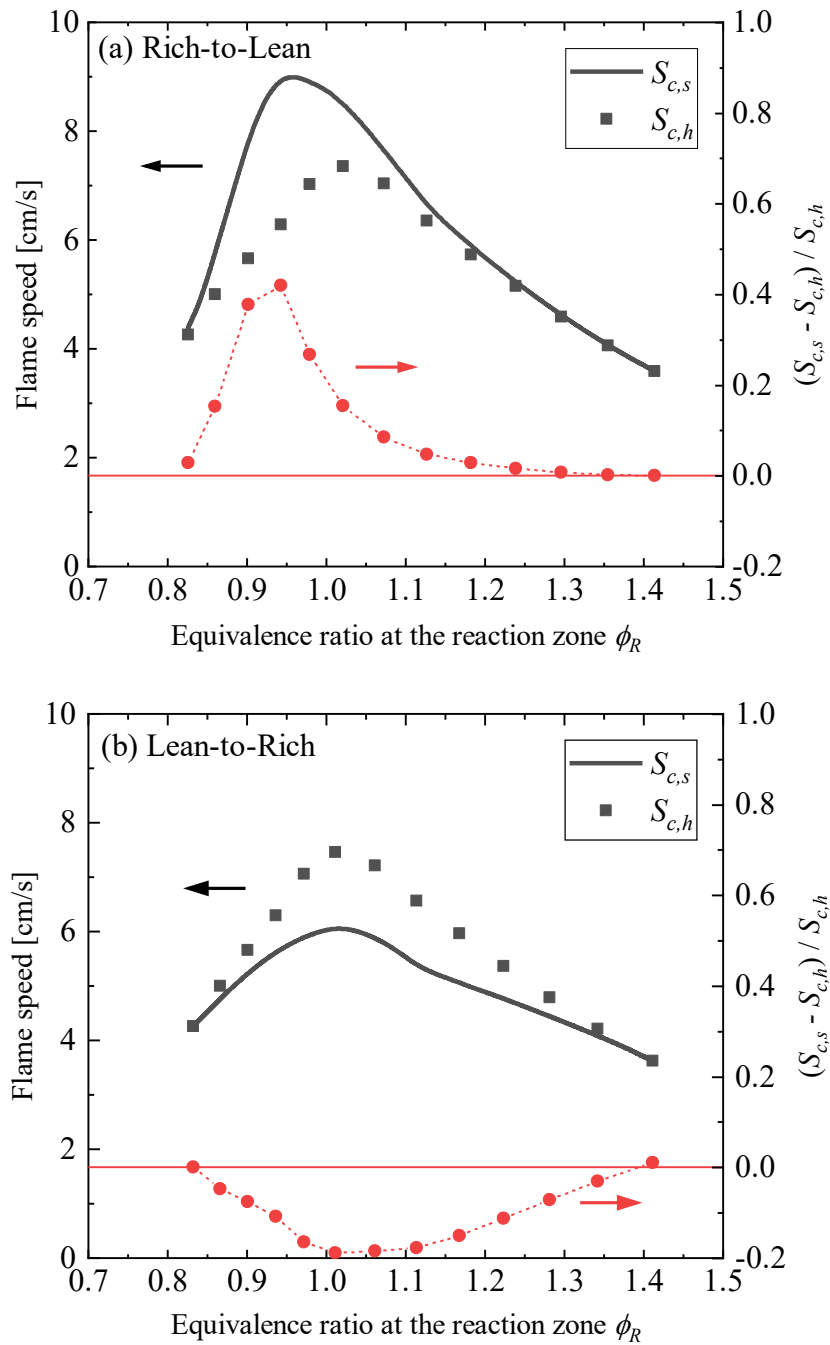
Fig. 6.6: Response of the flame speed $S_{c,s}$ of (a) rich-to-lean and (b) lean-to-rich stratified flames, the flame speed $S_{c,h}$ of homogeneous flames with the same ϕ_R, and the relative increase in $S_{c,s}$ as compared to $S_{c,h}$.

release rate. Therefore, similar to the back-support effect of stratified methane/air flames, the increase in the stratified flame speed seems to be due to an increase in the mass flux of chemical species from the burned gas.

In **Fig. 6.7**(b), mole fractions of major reactants and products are shown. From the upstream side, the fuel, NH_3, and the oxidizer, O_2, are supplied. It is seen that their mole fraction gradients are thinner in the preheat zone due to the increased flame speed. Meanwhile, mole fractions of N_2 and H_2O are increased in the burned gas. It is interesting to note that N_2 exists as a component of air on the upstream side, and its mole fraction is increased as additional N_2 is produced in the reaction zone; In methane/air flames, the mole fraction of N_2 hardly varies across the reaction zone. Moreover, at the downstream of the burned gas ($4 \text{ mm} \leq x - x_R$) of the stratified flame, accumulation of unburned NH_3 is observed. As the burned gas is richer, this is expected from the trend of the unburned NH_3 observed in **Fig. 6.5**.

As seen in the previous chapters, back-diffusion of species such as H_2, OH, and H from the burned gas in methane/air stratified flames were crucial for modifying the flame speed as they are involved with the chain-branching loop and fuel decomposition reactions. Therefore, profiles of those species are shown in **Fig. 6.7**(c), as they are also abundant in ammonia/air flames. While H_2 and H are increased for the stratified flame, OH is decreased in the burned gas. The reason for this is easily seen in **Fig. 6.5**; considering that $\phi_R = 0.94$ and the stratified flame is propagating toward a leaner mixture, more H_2/H and less OH are expected to exist in the richer (around $\phi = 1.05$) burned gas as compared to the corresponding homogeneous flame. Therefore, diffusion of H_2 and H into the reaction zone seems to be increased for the stratified flame. How these species affect the chemical process in the reaction zone will be analyzed next.
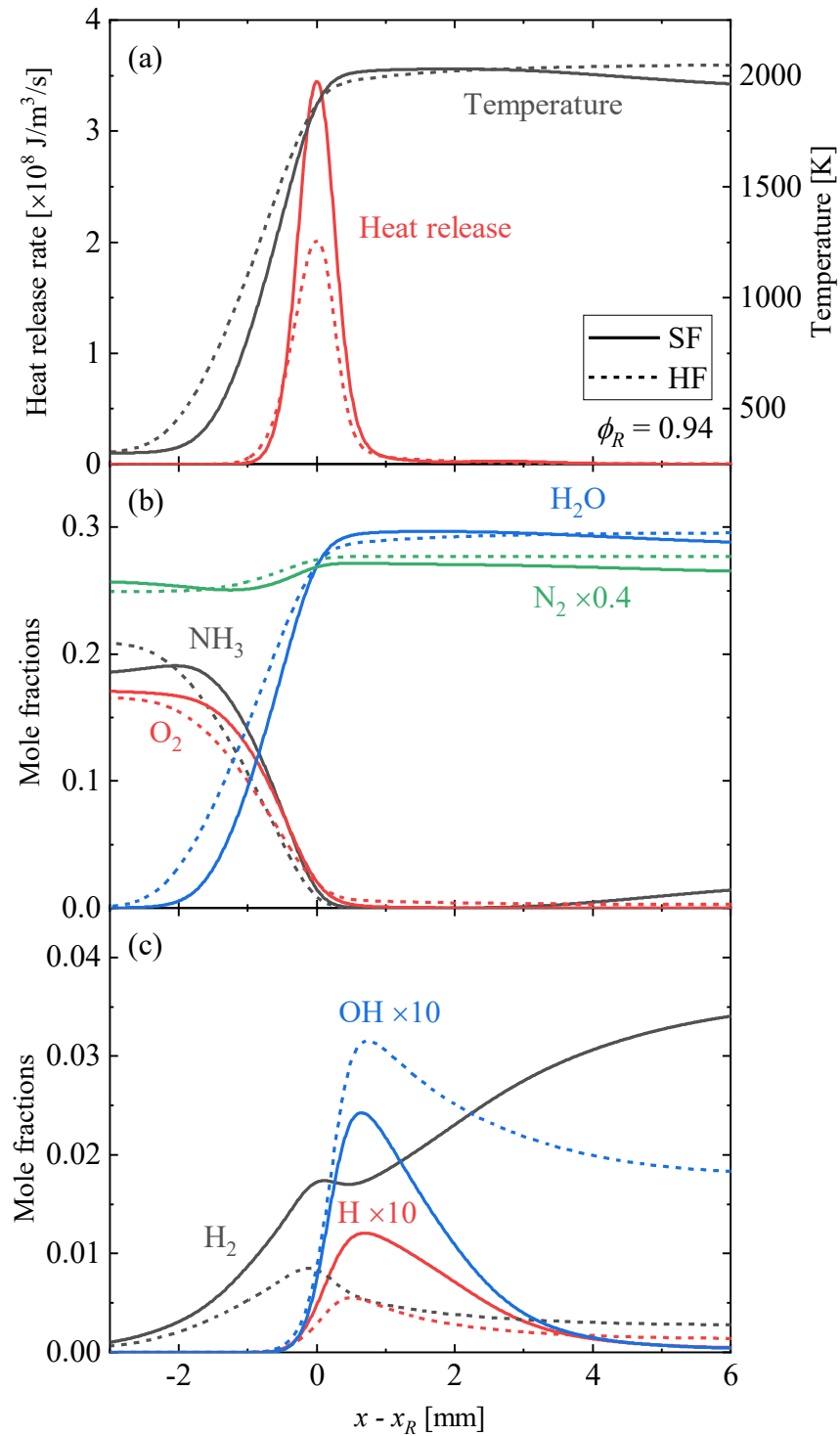
Fig. 6.7: Profiles of heat release rate, temperature, and major species of the rich-to-lean stratified flame (SF) at ϕ_R=0.94 in **Fig. 6.6**(a) and the homogeneous flame (HF) with the same ϕ_R. The x-axes are shifted so that at the reaction zone $x - x_R = 0$ mm for both flames.

To elaborate on the chemical process that contributed to the increase in the stratified flame speed, a reaction flow analysis [84] was conducted for the rich-to-lean stratified flame at $\phi_R = 0.94$ in **Fig. 6.6**(a) and the corresponding homogeneous flame. The resulting diagram is illustrated in in **Fig. 6.8**. To create this diagram, the following procedure was adopted. First, the integrated rate of production of kth species in ith elementary reaction, $\dot{\Omega}_{k,i}$, was evaluated in the following manner: As mentioned in Chapter 2, Section 2.2, a system of elementary reactions consisting of K species and N reactions can be written in a general form as

$$\sum_{k=1}^{K} v'_{k,i} M_k \underset{k_{b,i}}{\overset{k_{f,i}}{\rightleftarrows}} \sum_{k=1}^{K} v''_{k,i} M_k \ , \qquad (i = 1, 2, \dots, N) \tag{6.9}$$
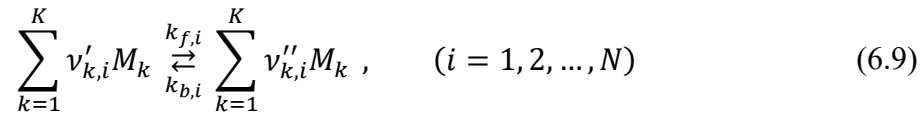
where M_k is the chemical symbol of kth species; $v'_{k,i}$ and $v''_{k,i}$ are stoichiometric coefficients of kth reactant and product species, respectively, in the ith reaction; and $k_{f,i}$ and $k_{b,i}$ are reaction rate constants of forward and backward reactions in the ith reaction, which are evaluated by the Arrhenius equations [13]. The rate of progress of the ith reaction, $\hat{\omega}_i$, is calculated as follows

$$\hat{\omega}_i = \hat{\omega}_{f,i} - \hat{\omega}_{b,i} = k_{f,i} \prod_{k=1}^{K} C_k^{n'_{k,i}} - k_{b,i} \prod_{k=1}^{K} C_k^{n''_{k,i}} \tag{6.10}$$

where $\hat{\omega}_{f,i}$ and $\hat{\omega}_{b,i}$ are the rate of progress of ith forward and backward reactions; $n'_{k,i}$ and $n''_{k,i}$ are reaction orders of kth species in the ith forward and backward reactions; and C_k is the mole concentration of kth species. Consequently, the rate of production of kth species in ith elementary reaction, $\dot{\omega}_{k,i}$, is calculated as

$$\dot{\omega}_{k,i} = \left(v''_{k,i} - v'_{k,i}\right)\hat{\omega}_i \tag{6.11}$$

Therefore, the integrated rate of production of kth species in the reaction zone is expressed as

$$\dot{\Omega}_{k,i} = \int_{x_{in}}^{x_{5\%}} \dot{\omega}_{k,i} dx \tag{6.12}$$

As seen above, the integral was performed over the same range as in Eq. (6.1), specifically $[x_{in}, x_{5\%}]$, so as not to account for reactions in the burned gas. In addition, $\dot{\Omega}_{k,i}$ for N-containing species in a reaction path $M_j \rightarrow M_k$ $(j \neq k)$ was summed up as follows:

$$\dot{\Psi}_{j \rightarrow k} = \sum_{\text{reaction } i \text{ in } M_j \rightarrow M_k \ (j \neq k)} \dot{\Omega}_{k,i} \tag{6.13}$$

Hence, $\dot{\Psi}_{j \rightarrow k}$ represents the total integrated production rate in each reaction path. In **Fig. 6.8**, reaction paths whose $\dot{\Psi}_{j \rightarrow k}$ are more than 3% of $\dot{\Psi}_{j \rightarrow k}$ of the initial $NH_3 \rightarrow NH_2$ path, which is the largest reaction path, were illustrated as arrows. The thickness of each arrow represents the logarithm of the $\dot{\Psi}_{j \rightarrow k,h}$ in a homogeneous flame whose $\phi_R = 0.94$ in **Fig. 6.6**(a).
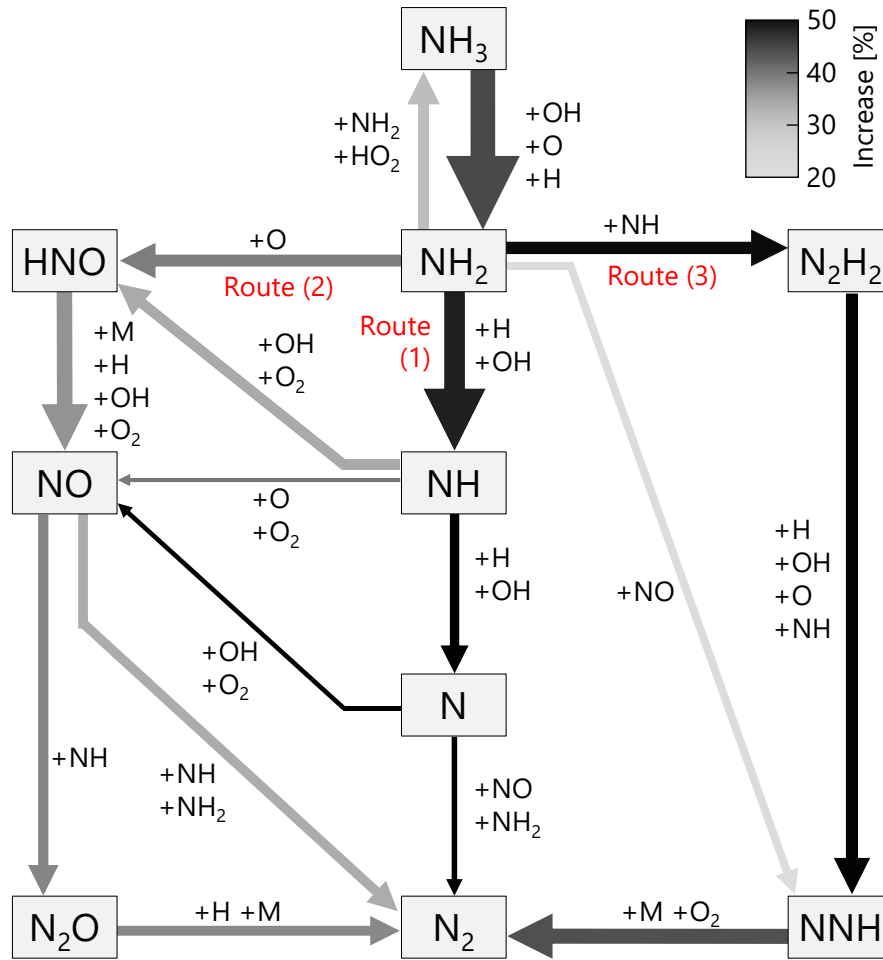
Fig. 6.8: Reaction flow diagram at $\phi_R = 0.94$ in **Fig. 6.6**(a). The thickness of the arrow is proportional to the logarithm of the integrated rate of species production (ROP) of the homogeneous flame, while the darkness of the arrow is proportional to the magnitude of a relative increase in the ROP of the stratified flame as compared to that of the corresponding homogeneous flame.

Meanwhile, the color of each arrow represents a relative increase in $\dot{\Psi}_{j \to k,s}$ in the stratified flame from the corresponding $\dot{\Psi}_{j \to k,h}$ in the homogeneous flame, $(\dot{\Psi}_{j \to k,s} - \dot{\Psi}_{j \to k,h})/\dot{\Psi}_{j \to k,h} \times 100$ [%]. As indicated by the color bar in the figure, the arrow becomes linearly darker as the relative increase in $\dot{\Psi}_{j \to k}$ varies from 20% to 50%. Note that $\dot{\Psi}_{j \to k}$ for all reaction paths shown in the diagram was increased in the stratified flame.

It can be seen in **Fig. 6.8** that the oxidation process of NH_3 begins with H-abstraction reactions by OH, O, and H. Subsequently, oxidation of NH_2 diverges into three main routes [185,190]: (1) $NH_2 \to NH \to N$, (2) $NH_2 \to HNO \to NO$, and (3) $NH_2 \to N_2H_2 \to NNH \to N_2$. Route (1) represents further H-abstraction of NH_2 by OH and H, leading to the production of NH and N radicals which may react with O, OH, or O_2 to form NO, or with NO to form N_2.

The former is favored in lean flames due to the abundance of O and OH radicals, while the latter is a major NO reduction process in rich flames [9]. Through Route (2), NH_2 itself is converted to NO via HNO. While this route is also favored in lean flames, the HNO → NO path is the dominant NO production route for all conditions [9]. Through Route (3), NH_2 reacts with NH to produce N_2 via N_2H_2 and NNH. This route is favored in rich flames, which contributes to low NO production by depleting the NH_i radicals [9].

The color of the arrows in **Fig. 6.8** indicates that Routes (1) and (3), represented by the middle and the right vertical branches, are more enhanced in the stratified flame than Route (2) represented by the left branch. This implies that the relative increase in the stratified flame speed was primarily driven by the H-abstraction route (1) and the NNH route (3). Based on this observation, variations in the contribution of major elementary reactions constituting the NH_2 production path $NH_3 → NH_2$ and each path in Routes (1) and (3) are arranged in **Table 6.1**. Here, the contribution of ith reaction in a reaction path $M_j → M_k$ ($j ≠ k$) is calculated by

$$R_{j→k,i} = \frac{\dot{\Omega}_{k,i}}{\sum_{\text{reaction } i \text{ in } M_j→M_k \ (j≠k)} \dot{\Omega}_{k,i}} \times 100 \ [\%] \tag{6.14}$$

The path NNH → N_2 is not considered here as it consists of unimolecular decomposition reactions. In the table, reactions with the largest increase in their contributions, written in bold letters, turned out to be H-abstraction reactions by H atoms. In contrast, contributions of elementary reactions involving OH radicals are all decreased in the stratified flame. As an exception, the reaction path $NH_2 → N_2H_2$ is solely through a reaction with NH radicals (OK 252), thus the increase in the reaction rate of OK 252 is likely a consequence of increased NH_i radicals in the reaction zone. Therefore, the above reaction flow analysis shows that the increase in the NH_3 consumption rate and thus in the stratified flame speed is due to enhanced H-abstraction reactions by H atoms.

Considering the mole fraction profiles in **Fig. 6.7** (c), two factors are responsible for the increase in H atoms that led to the increase in the H-abstraction reactions. As mentioned previously, H and H_2 in the burned gas was increased for the stratified flame in **Fig. 6.7** (c). First, as H atoms diffuse preferentially against other species, the larger H content in the burned gas leads to increased back-diffusion of H atoms into the reaction zone, resulting in direct enhancement of the H-abstraction reactions. Secondly, diffusion of H_2 from the burned gas into the reaction zone is also increased. In the reaction zone, H_2 reacts with O and OH to accelerate major chain-branching reactions $O + H_2 \rightleftarrows H + OH$ (OK 3), $OH + H_2 \rightleftarrows H + H_2O$ (OK 85), and $H + O_2 \rightleftarrows O + OH$ (OK 39) [78], which leads to a higher H content in the reaction zone, indirectly enhancing the H-abstraction reactions.

The role of the second factor, H_2 back-diffusion, becomes apparent when ϕ_R is around 1.05, where there is less H in the burned gas of the stratified flame, as shown in **Fig. 6.9**.

Table 6.1: Variation in the contribution of elementary reactions in selected reaction paths at $\phi_R = 0.94$ in **Fig. 6.6**(a). Reactions with the largest increase in their contributions are written in bold letters.

Reaction path	No.	Elementary reactions	Contribution [%] Homogeneous → Stratified		
$NH_3 \rightarrow NH_2$	OK 278	$NH_3 + OH \leftrightarrow NH_2 + H_2O$	86.0	→	82.5
	OK 279	$NH_3 + O \leftrightarrow NH_2 + OH$	9.3	→	10.3
	OK 277	$\mathbf{NH_3 + H \leftrightarrow NH_2 + H_2}$	**4.7**	→	**7.3**
$NH_2 \rightarrow NH$	OK 248	$NH_2 + OH \leftrightarrow NH + H_2O$	47.1	→	35.3
	OK 245	$\mathbf{NH_2 + H \leftrightarrow NH + H_2}$	**32.1**	→	**46.8**
	OK 251	$NH_2 + NH_2 \leftrightarrow NH + NH_3$	18.2	→	15.5
$NH \rightarrow N$	**OK 232**	$\mathbf{NH + H \leftrightarrow N + H_2}$	**39.3**	→	**56.0**
	OK 235	$NH + OH \leftrightarrow N + H_2O$	57.5	→	41.3
$NH_2 \rightarrow N_2H_2$	OK 252	$NH_2 + NH \leftrightarrow N_2H_2 + H$	100.0	→	100.0
$N_2H_2 \rightarrow NNH$	**OK 288**	$\mathbf{N_2H_2 + H \leftrightarrow NNH + H_2}$	**57.9**	→	**69.0**
	OK 291	$N_2H_2 + OH \leftrightarrow NNH + H_2O$	23.8	→	15.8
	OK 289	$N_2H_2 + O \leftrightarrow NNH + OH$	9.3	→	7.8
	OK 292	$N_2H_2 + NH \leftrightarrow NNH + NH_2$	9.0	→	7.4

Considering the reduced back-diffusion of H into the reaction zone, the stratified flame speed is expected to be decreased. However, as the H_2 content in the burned gas is still higher for the stratified flame, H_2 diffuses preferentially into the reaction zone and enhances the chain-branching reactions. This effect overrides the decrease in the diffusive flux of H atom from the burned gas, which can be observed in the slight increase in the H profile around the reaction zone ($x - x_R = 0$ mm) in **Fig. 6.9**.

Because the chain-branching reaction driven by H_2 can override the effect of variation in the H content in the burned gas, an increase or decrease in H_2 content in the burned gas determines whether the stratified flame speed will be increased or decreased, respectively. As H_2 content in the burned gas increases almost monotonically with the mixture equivalence ratio, there will be higher or lower H_2 content in the burned gas of rich-to-lean or lean-to-rich stratified flames, respectively. This results in the increased or decreased stratified flame speed $S_{c,s}$ as compared to the corresponding homogeneous flame speed $S_{c,h}$, as seen in **Fig. 6.6**. The above mechanism is very similar to the back-support effect observed in methane/air stratified flames in Chapter 3.
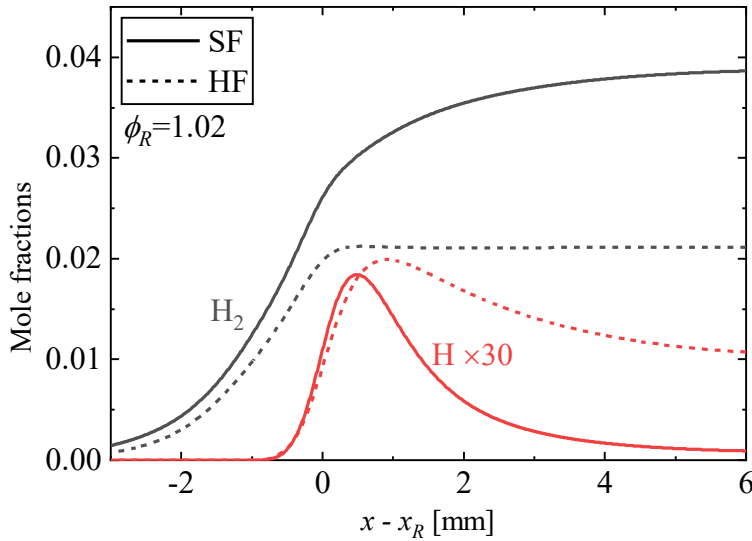
Fig. 6.9: Profiles of H_2, H, and OH of the rich-to-lean stratified flame at $\phi_R = 1.02$ in **Fig. 6.6** (a) and the homogeneous flame with the same ϕ_R. The x-axes are shifted so that at the reaction zone $x − x_R = 0$ mm for both flames.

6.4.3 NO reduction in the burned gas

To characterize the local burned gas composition, fluid particles with different values of initial equivalence ratio ϕ_{init} at the reaction zone were tracked in the stratified flames and the corresponding homogeneous flames, as described in Section 6.3. As an example, **Fig. 6.10** shows the time variation of NO reaction rate and NO mole concentration profiles as fluid particles whose $\phi_{init} = 1.02$ and $\phi_{init} = 1.06$ are tracked in (a) rich-to-lean and (b) lean-to-rich stratified flames, respectively. The leftmost panel corresponds to the initial particle location $x_{ptcl,s} = x_{R,s}$ at $\tau_{ptcl} = 0$ ms. In addition, steady profiles of corresponding homogeneous flames with the same values of ϕ_{init} are drawn with broken lines. The locations of each particle are plotted by circle and square symbols for stratified and homogeneous flames, respectively. It can be observed that, in the rich-to-lean stratified flame, the fluid particle is convected faster downstream than the corresponding fluid particle in the homogeneous flame, while the opposite trend is observed in the lean-to-rich stratified flame. This is because, as shown in **Fig. 6.6**, $S_{c,s} > S_{c,h}$ for the rich-to-lean stratified flame and $S_{c,s} < S_{c,h}$ for the lean-to-rich stratified flame, which results in faster and slower downstream convection for the former and the latter stratified flames, respectively. As reactive and diffusive processes in the local burned gas proceed with time and not with distance, it is important to compare the properties of the burned gas under the same residence time τ_{ptcl}.
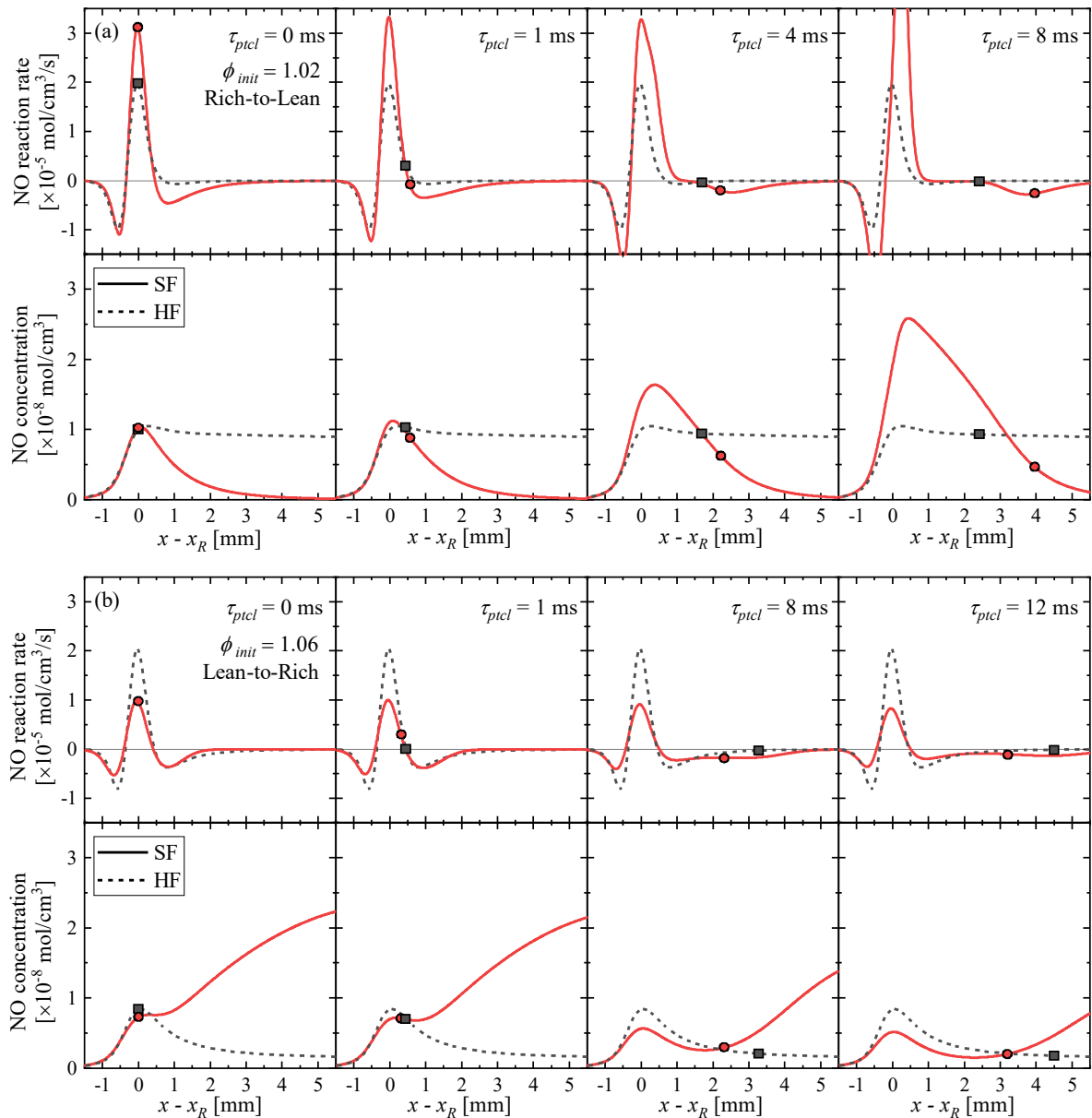
Fig. 6.10: Solid lines: Variation of NO reaction rate (upper low) and NO mole concentration (lower low) profiles of (a) rich-to-lean and (b) lean-to-rich stratified flames with increasing travel time τ_{ptcl} of fluid particles whose $\phi_{init} = 1.02$ and 1.06, respectively. Broken lines: NO reaction rate and mole concentration profiles of a homogeneous flame where the fluid particle has the same value of ϕ_{init} as the corresponding stratified flame. The locations of fluid particles in stratified and homogeneous flames are shown as circle and square symbols, respectively. The x-axes are shifted so that the starting point of fluid particle tracking is at 0 mm for all cases.

Before analyzing the histories of NO reaction rate and NO mole fraction in each fluid particle, variations in the NO reaction rate profiles in **Fig. 6.10** are observed. At the initial moment ($\tau_{ptcl} = 0$ ms), the production rate of NO is higher and lower in the rich-to-lean and lean-to-rich stratified flames, respectively, than in the corresponding homogeneous flames. This is due to the increased and decreased reaction rates of the stratified flames, respectively. Moreover, in the stratified flame, the NO reaction rate profiles display peculiar transient behaviors. In the rich-to-lean stratified flame in **Fig. 6.10** (a)**,** an NO reduction zone exists downstream of the reaction zone ($0.5 \text{ mm} \leq x - x_R \leq 2.5 \text{ mm}$) at the initial moment ($\tau_{ptcl} = 0$ ms). With increasing tracking time τ_{ptcl}, it detaches from the reaction zone and is convected downstream in the burned gas. On the other hand, in the lean-to-rich stratified flame in **Fig. 6.10** (b), the NO reduction zone downstream of the reaction zone ($0.3 \text{ mm} \leq x - x_R \leq 1.5 \text{ mm}$) stretches further downstream with increasing τ_{ptcl}. It is of interest to elucidate how these NO reduction zones in the burned gas are formed and affect the NO emission characteristics of stratified flames.

The histories of NO reaction rate and NO mole concentration experienced by the fluid particles tracked in **Fig. 6.10** (particles with $\phi_{init} = 1.02$ in the rich-to-lean stratified flame and with $\phi_{init} = 1.06$ in the lean-to-rich stratified flame) are shown in **Fig. 6.11**; these particles are chosen because they are convected along with the downstream NO reduction zones. The beginning of the NO consumption reaction is marked with a vertical line for each particle. For a wide range of the reaction rate history, the NO consumption rate experienced by the fluid particles in rich-to-lean and lean-to-rich stratified flames is larger than that in corresponding homogeneous flames. However, for the stratified flames, the history of NO consumption rate is not exactly reflected in the history of NO mole concentration. In the rich-to-lean stratified flame, the mole concentration starts to increase after $\tau_{ptcl} = 0.012$ s, even though the consumption reaction persists. In the lean-to-rich stratified flame, the mole concentration continues to decrease at a constant rate, despite the consumption reaction gradually diminishing.

The discrepancies between the histories of the reaction rate and the mole concentration in stratified flames are caused by the mass diffusion of NO in the burned gas. This is because the diffusive effect becomes stronger as the particle approaches the stagnation plane. As can be observed from the NO profiles of stratified flames in **Fig. 6.10**, NO diffuses downstream in the burned gas of the rich-to-lean stratified flame. Therefore, NO diffuses into the fluid particle from the upstream side. Contrarily, NO diffuses out of the fluid particle in lean-to-rich stratified flames. These effects result in the gradually increasing and decreasing trend of the NO mole concentration histories in **Fig. 6.11**(a) and **Fig. 6.11**(b), respectively. Consequently, the history of NO mole concentration experienced by fluid particles cannot be interpreted simply as the local emission characteristics of stratified flames, as it is influenced by diffusive mixing
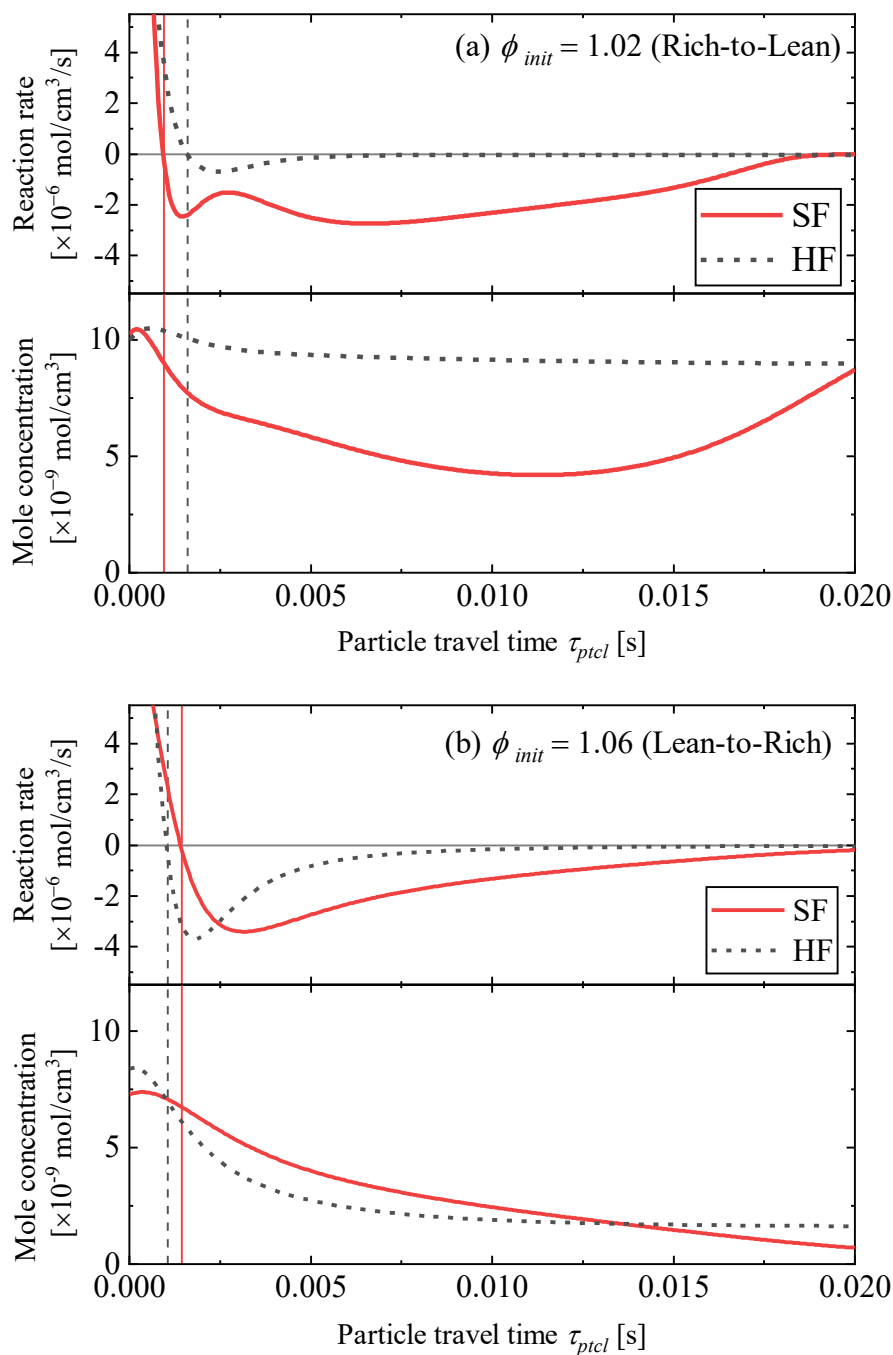
Fig. 6.11: Solid lines: Histories of reaction rate and mole concentration of NO for a fluid particle with (a) $\phi_{init} = 1.02$ and (b) $\phi_{init} = 1.06$ tracked in rich-to-lean and lean-to-rich stratified flames (SF), respectively. Broken lines: Histories of reaction rate and mole concentration of NO for a fluid particle tracked in steady homogeneous flames (HF) where the fluid particle has the same value of ϕ_{init} as the corresponding stratified flame. Vertical lines: Beginning of NO consumption reaction $\tau_{ptcl} = \tau_{ptcl,c}$ for each fluid particle.

of local mole fractions.

As an alternative approach to estimating local burned gas composition in stratified flames, NO consumption rate of each fluid particle was integrated over the range of the travel time $[\tau_{ptcl,c}, 20 \text{ ms}]$, where $\tau_{ptcl} = \tau_{ptcl,c}$ is the beginning of NO consumption reaction marked with vertical lines in **Fig. 6.11**. Then, the time-integrated NO consumption was compared with the mole concentration at $\tau_{ptcl} = \tau_{ptcl,c}$ for each fluid particle in stratified and homogeneous flames. The results are shown in **Fig. 6.12**. Note that the dimension of both quantities is $[\text{mol/cm}^3]$

The mole concentrations at $\tau_{ptcl} = \tau_{ptcl,c}$, shown in squares, are mostly the same for fluid particles in stratified and homogeneous flames; both increase monotonically as ϕ_{init} becomes smaller. This implies that although it was observed in **Fig. 6.10** that the NO production rate was increased or decreased in stratified flames from that of homogeneous flames, the NO concentration inside the reaction zone was not significantly affected. On the other hand, the time-integrated consumption rate, shown in circles, shows different trends between stratified and homogeneous cases. For the homogeneous flames, NO is negligibly consumed in fluid particles with $\phi_{init} < 1.05$, while NO consumption occurs in fluid particles with $\phi_{init} > 1.05$, which attenuates moderately with increasing ϕ_{init}. This trend is caused by the abundance of NH_I radicals reducing NO in the rich burned gas [9]. Meanwhile, for the stratified flames, the time-integrated NO consumption is augmented for fluid particles with $\phi_{init} = 1.05 \pm 0.10$ as compared to the homogeneous flames. The increase in the NO consumption is up to 3.06×10^{-8} mol/cm^3 for the rich-to-lean case and 2.63×10^{-8} mol/cm^3 for the lean-to-rich case, which is comparable to the mole concentrations at the beginning of the consumption reaction. Therefore, the above results show that NO is expected to be reduced by a considerable amount in the vicinity of stoichiometric burned gas of rich-to-lean and lean-to-rich stratified flames.

To elucidate the chemical process in detail, a reaction flow analysis was conducted for the downstream NO reduction zone $[1.32 \text{ mm}, 5.43 \text{ mm}]$ in the rich-to-lean stratified flame at $\tau_{ptcl} = 4 \text{ ms}$ in **Fig. 6.10**(a). The resulting diagram is shown in **Fig. 6.13**. To visualize the reaction path involved with NO, the arrows are rearranged from the previous diagram in **Fig. 6.8**. The thickness of the arrow is proportional to the logarithm of the integrated rate of species production. The three routes that stand out are: NH_3 dehydration $NH_3 \rightarrow NH_2 \rightarrow NH \rightarrow N$, NO formation $NH \rightarrow HNO \rightarrow NO$, and NO reduction $NO(\rightarrow N_2O$ or $\rightarrow NNH) \rightarrow N_2$. It should be noted that NO reduction prevails over the formation, as indicated by the net NO consumption in this zone. Though not shown here, a similar result was obtained for the downstream NO reduction zone in the rich-to-lean stratified flame at $\tau_{ptcl} = 8 \text{ ms}$ in **Fig. 6.10**(b). Therefore, it seems that NO reduction in the burned gas of stratified flames is facilitated by
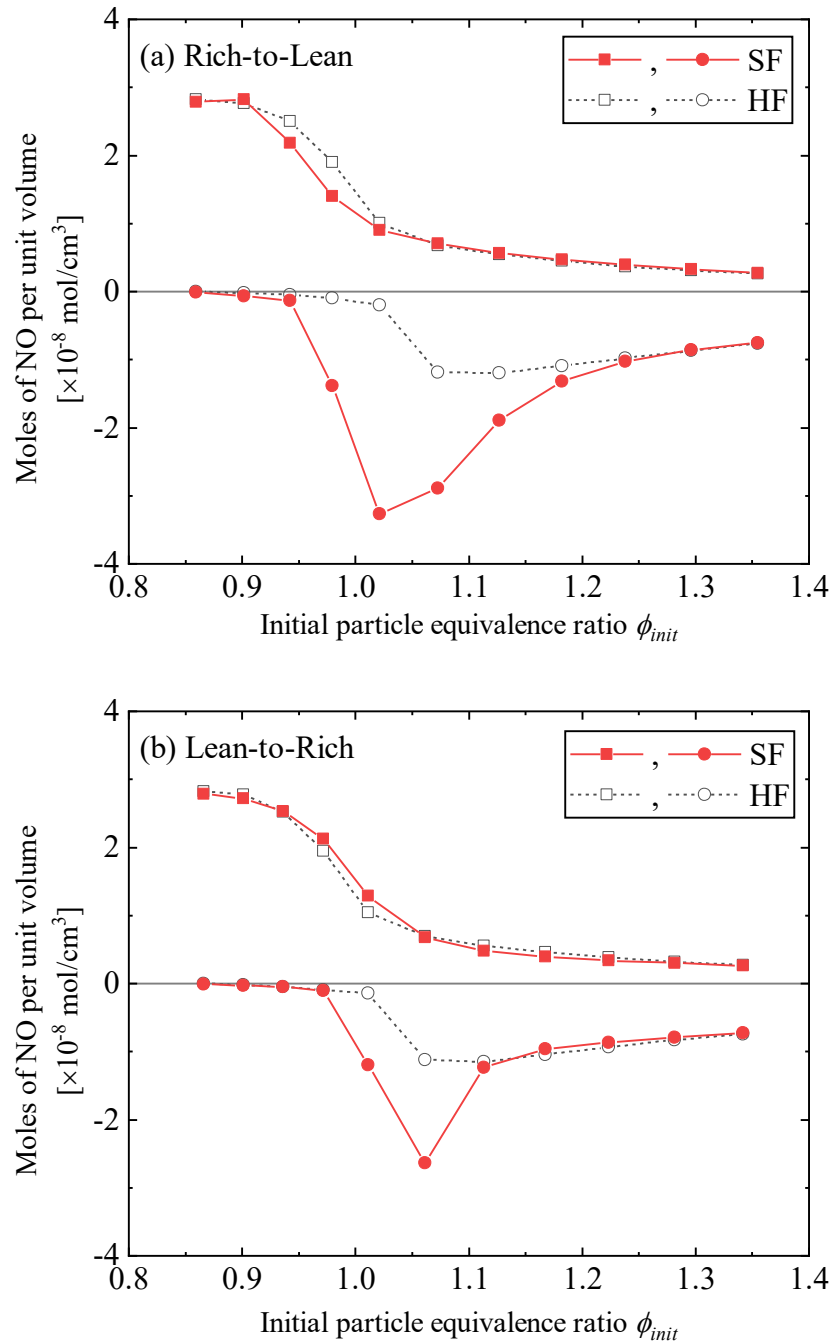
Fig. 6.12: Squares: NO mole concentration of each fluid particle at the beginning of NO consumption $\tau_{ptcl} = \tau_{ptcl,c}$. Circles: Time-integrated NO consumption rate in each fluid particle over the range of the travel time $[\tau_{ptcl,c}, 20 \text{ ms}]$. The plots are compared for fluid particles with the same ϕ_{init} in (a) rich-to-lean and (b) lean-to-rich stratified flames (SF, filled symbols) and homogeneous flames (HF, blank symbols).

NH$_3$

+NH$_2$ +OH
+NH   +H

HNO   +O   NH$_2$ +NH   N$_2$H$_2$

+H
+OH

+M   +OH
+H
+OH

NO   NH

+H
+OH

+OH

+H
+OH

N

+NH

+N
+NH
+NH$_2$

+NH$_2$ +NH$_2$
+NH

N$_2$O   +H +M   N$_2$ +M   NNH
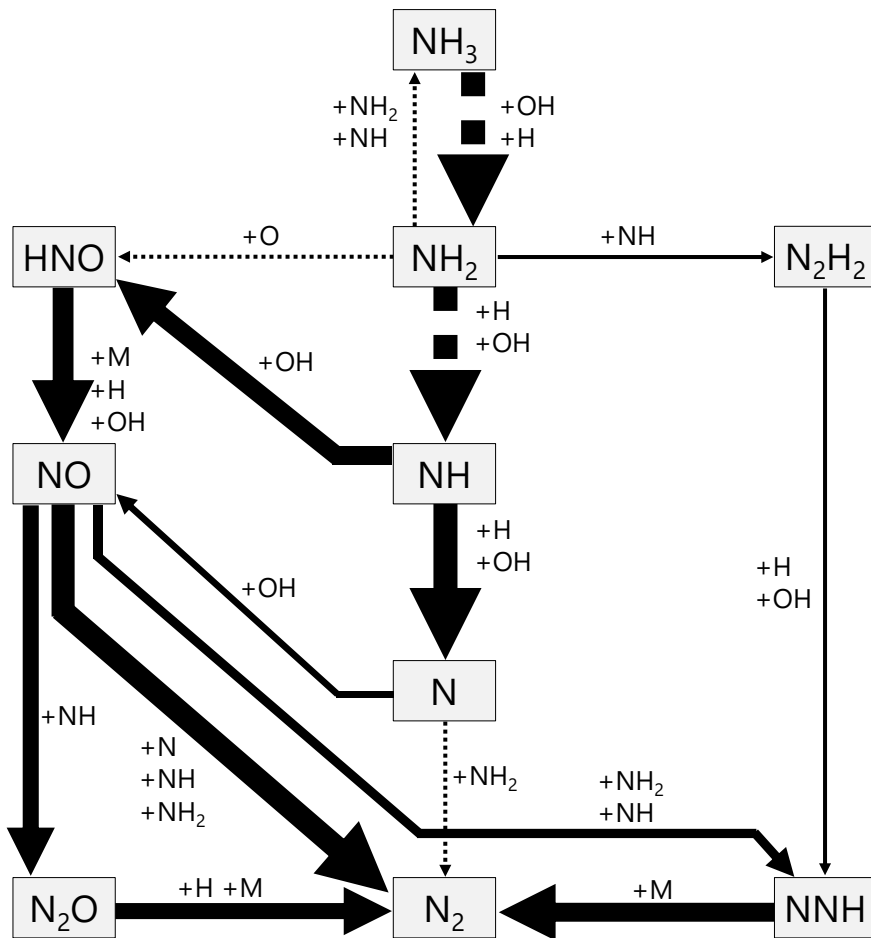
Fig. 6.13: Reaction flow diagram for the downstream NO reduction zone [1.32 mm, 5.43 mm] at $\tau_{ptcl} = 4$ ms of the rich to lean stratified flame in **Fig. 6.10**(a). The thickness of the arrow s is proportional to the logarithm of the integrated rate of species production. To clarify differences in the thickness of reaction paths involved with NO, arrows thicker or thinner than the path NH → N or N$_2$H$_2$ → NNH respectively, are drawn with broken lines.

the abundance of NH$_i$ radicals produced from the unburned NH$_3$. This is a common NO reduction process in rich NH$_3$/air flames [9,186], but here it occurs in the burned gas of mostly stoichiometric mixtures with an even larger reduction rate than in burned gas of rich mixtures, as seen in **Fig. 6.12**. Two factors are required for this to occur: an abundance of unburned NH$_3$ in the neighboring rich burned gas and an abundance of H/OH radicals in the neighboring lean burned gas, as will be shown next.

In **Fig. 6.14**, NH$_3$, O$_2$, OH and H mole fraction and NH$_3$ reaction rate profiles at (a) $\tau_{ptcl} = 4$ ms of the rich-to-lean stratified flame in **Fig. 6.10**(a) and at (b) $\tau_{ptcl} = 8$ ms of the lean-to-rich stratified flame in **Fig. 6.10**(b) are plotted. In the rich-to-lean stratified case in
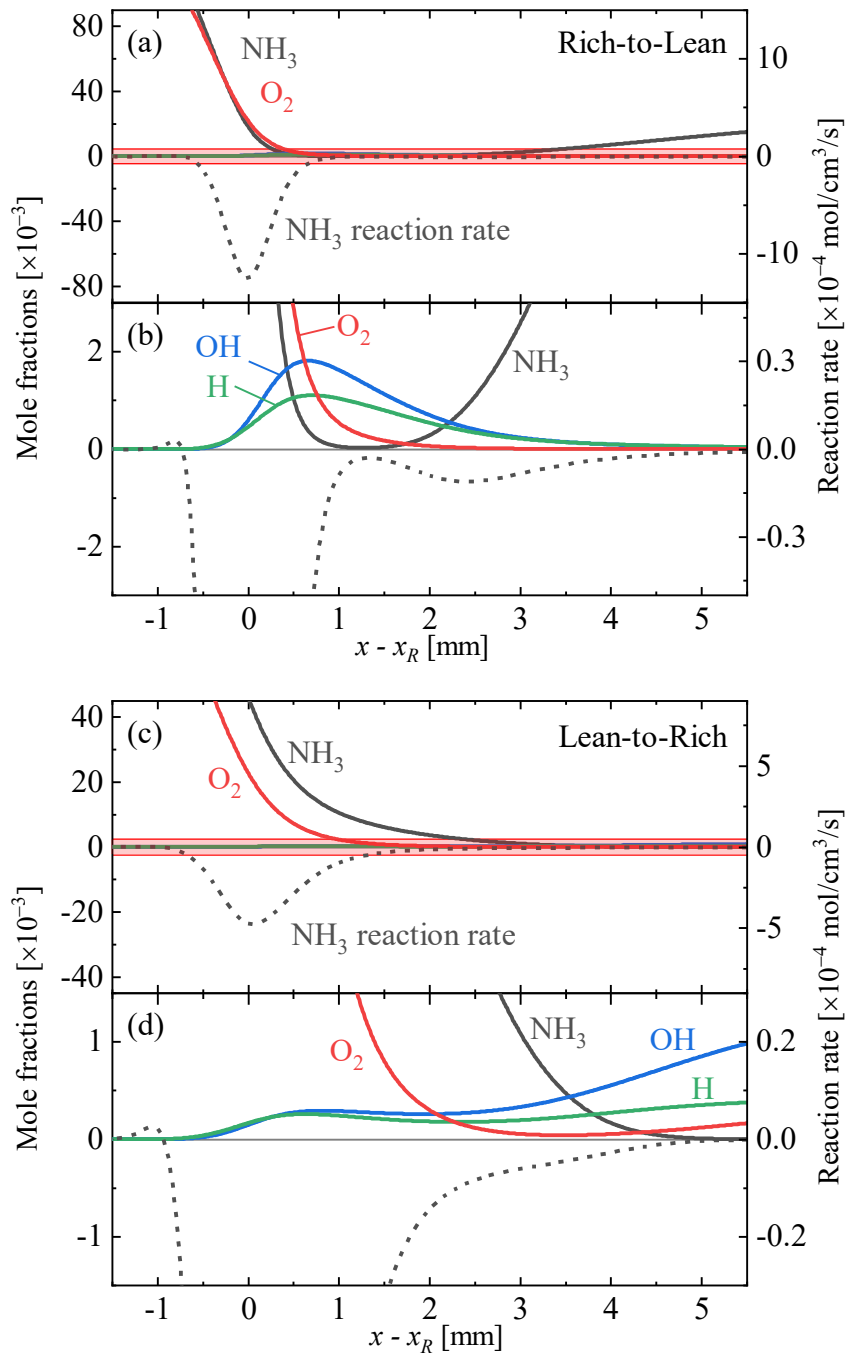
Fig. 6.14: Profiles of NH_3, O_2, OH, and H mole fractions and NH_3 reaction rates at (a, b) $\tau_{ptcl} = 4$ ms and (c, d) $\tau_{ptcl} = 8$ ms of stratified flames in **Fig. 6.10**(a) and **Fig. 6.10**(b), respectively. In (b) and (d), the highlighted zones in (a) and (c), respectively, are magnified in the vertical axis by 30 times.

Fig. 6.14(a), the NO reduction zone is located around $x - x_R = 2.5$ mm, as seen at $\tau_{ptcl} = 4$ ms locally consumed at $x - x_R = 2.5$ mm, where it meets OH and H diffusing from the in **Fig. 6.10**(a). Considering that this is zone is stoichiometric, the burned gas upstream and downstream of this region is slightly lean and rich, respectively. This can be observed in **Fig. 6.14**(a), where unburned NH_3 profile gradually increases downstream of $x - x_R = 2.5$ mm. The magnified profiles in **Fig. 6.14**(b) further illustrate that the unburned NH_3 is upstream lean burned gas. On the other hand, in the lean-to-rich stratified case in **Fig. 6.14**(b), the NO reduction zone exists for a range of 1.5 mm $\leq x - x_R = 4.5$ mm, as seen at $\tau_{ptcl} = 8$ ms in **Fig. 6.10**(b). As this zone is around stoichiometric, the upstream and downstream sides of this zone are respectively rich and lean, respectively. This can be observed in the abundance of NH_3 on the upstream side in **Fig. 6.14**(c). The magnified profiles in **Fig. 6.14**(d) show that the excess NH_3 from the upstream side reacts with OH and H diffusing from the downstream lean burned gas.

It is also seen in **Fig. 6.14** that, in the rich-to-lean case, the downstream NH_3 reaction zone is localized around $x - x_R = 2.5$ mm, while in the lean-to-rich case, the NH_3 reaction zone continuously extends from the main reaction zone at $x - x_R = 0$ mm toward the burned gas. This is because, in the rich-to-lean case, NH_3 is depleted at $x - x_R = 2.5$ mm, while in the lean-to-rich case, NH_3 exists continuously on the downstream side of the reaction zone. These contrasting profiles of the downstream NH_3 reaction rate result in the different behaviors of the downstream NO reduction zone in **Fig. 6.10**(a) and **Fig. 6.10**(b).

The above results explain the mechanism of NO reduction in the burned gas of stratified flames as follows: When a flame propagates in a rich-to-lean or lean-to-rich stratified mixture, unburned NH_3 from the rich region and OH/H from the lean region meets at the stoichiometric region of the burned gas, resulting in a local production of NH_i radicals. The increased NH_i radicals cause increased NO consumption in the burned gas of stratified flames. While the extent of such NO reduction was considerably large, as seen in **Fig. 6.12**, the downstream consumption of unburned NH_3 was found negligibly small for both stratified cases.

It should be noted that the above-explained NO reduction process driven by the unburned NH_3 resembles the well-known selective non-catalytic reduction (SNCR), also called the thermal DeNOx process [9,186,191]. In the thermal DeNOx process, a particular regent, usually NH_3 or urea, is injected and mixed in a flue gas stream containing NOx. Under a certain temperature range and concentration of O_2, the reagent selectively reduces NOx to N_2 without a need for catalyst [192]. This process has been widely adopted in various combustion systems as it is easy to install, economical as no catalyst is used, generally not affected by the presence of fly ash, and can be used as a hybrid with other NOx reduction technologies [193].

In the thermal DeNOx process, the key step consists of the reaction between NH_2 and NO: $NH_2 + NO \rightleftarrows NNH + OH$ (OK 257) and $NH_2 + NO \rightleftarrows N_2 + H_2O$ (OK 256). Here, NH_2 is

produced from the injected NH_3. For the thermal DeNOx process to be self-sustainable, it requires a chain-branching cycle $NH_2 + NO \rightleftarrows NNH + OH$ (OK 257), $O + H_2O \rightleftarrows OH + OH$ (OK 3), and $H + O_2 \rightleftarrows O + OH$ (OK 39) to be promoted under sufficiently high temperature. However, when the temperature is too high, the above cycle produces O/H radicals too rapidly, leading to a net formation of NO through oxidation of NH_i radicals. Consequently, there is an optimal temperature window for the thermal DeNOx to be effective, which is reported as 1100 to 1400 K [9,186,191] depending on the initial O_2 concentration [194,195]. Meanwhile, the current NO reduction process in **Fig. 6.14** takes place in the burned gas, whose temperature is around 2000 K. Therefore, from the aspect of the above thermal DeNOx mechanism, NO production, instead of reduction, should occur in the burned gas

The critical difference between the thermal DeNOx process and the current NO reduction process observed in the burned gas is that the initial reactants, in addition to NO, are NH_3 and O_2 for the former and NH_3 and O/H radicals for the latter. In fact, **Fig. 6.14** shows that in the downstream NO reduction zone, O_2 is almost depleted while OH and H radicals are abundant. Although it is known that the DeNOx window shifts to higher temperatures under extremely low O_2 concentration (trace impurities around 0.01%), the optimal temperature is still as low as 1373 K [195], likely due to depletion of O_2. Therefore, it is considered that the current NO reduction process in the burned gas is different from that of the thermal DeNOx process. For the current case, the reduction process is sustained by O/H radicals that diffused from the lean burned gas, rather than by those produced from the chain-branching cycle.

6.5   Summary

A numerical study of ammonia/air counterflow premixed flames under rich-to-lean and lean-to-rich mixture stratification (*stratified flames*) is conducted. In particular, the effect of mixture stratification on the response of the flame speed and NO emission was investigated. The following conclusions are drawn from a comparison of the stratified flames with corresponding steady flames in homogeneous mixtures (*homogeneous flames*):

- The relationship between the stratified flame speed $S_{c,s}$ and the homogeneous flame speed $S_{c,h}$ under the same local equivalence ratio is $S_{c,s} > S_{c,h}$ for the rich-to-lean stratified flame and $S_{c,s} < S_{c,h}$ for the lean-to-rich stratified flame. In particular, the relative increase in the integrated fuel consumption rate was up to more than 40% under the magnitude of stratification imposed in this study.

- The changes in $S_{c,s}$ were driven principally by an increase or decrease in the H atom concentration in the reaction zone, which respectively leads to increased or decreased

rate of H-abstraction reactions of NH_3/NH_i radicals by H atoms.

- The modification of H atom concentration in the reaction zone of stratified flames is primarily caused by variation in the H_2 content in the burned gas. When the flame propagates from rich to lean mixtures, the abundance of H_2 in the burned gas leads to increased H_2 back-diffusing into the reaction zone, which enhances H atom production through chain-branching reactions. The opposite occurs when the flame propagates from lean to rich mixtures. In addition to the above effect, under stoichiometric-to-lean propagation, the abundance of H atoms in the stoichiometric burned gas leads to increased back-diffusion of H atoms into the reaction zone. The opposite occurs under lean-to-stoichiometric propagation.

- In both rich-to-lean and lean-to-rich stratified flames, additional consumption of NO occurs in the downstream stoichiometric burned gas. Therefore, NO emission from stratified flames is expected to be smaller than that predicted from homogeneous flame emission characteristics.

- The mechanism of NO consumption downstream of the stratified flames are as follows: As the neighboring regions of the stoichiometric burned gas are rich and lean, unburned NH_3 diffused from the rich region is decomposed by OH/H diffused from the lean region. This leads to the production of NH_i radicals which reduce NO in the burned gas.

Chapter 7
Concluding Remarks

In this chapter, primary results and conclusions drawn from the current studies are summarized. Based on the conclusions, suggestions for future research topics are presented.

7.1 Conclusions

Using an unsteady counterflow flame solver OPUS, premixed flames propagating in stratified mixtures (*stratified flames*) are numerically analyzed. Especially, an equivalence ratio gradient normal to the flame surface was imposed on the flame. The nondimensionalized stratification thickness was in the order of $O(15)$ for cases with oscillating equivalence ratio and $O(2)$ for cases with monotonically varying equivalence ratios. The results of the stratified flames are compared with those of corresponding premixed flames in homogeneous mixtures (*homogeneous flames*). In particular, the basic mechanism of stratified flame speed modification ("back-support effect"), stratified flame propagation in a strained flow, and stratified flame propagation with alternative fuels such as hydrogen and ammonia are investigated. The primary results of this work are summarized in the following:

- Stratified methane/air flames propagate faster or slower than homogeneous flames under decreasing or increasing equivalence ratios, respectively. In lean stratified mixtures, preferential diffusion of reactive species such as H_2, H, OH, and O from the burned gas is the driving factor of the increase or decrease in the flame speed. Contrary to the previous reports, it is shown that variations in the burned gas temperature of stratified flames do not contribute to the increase or decrease in the stratified flame speed. Meanwhile, in rich stratified mixtures, preferential diffusion of H_2 from the burned gas is the driving factor of the increase or decrease in the flame speed.

- Due to the presence of the above "back-support" effect, when the flame is exposed to mixture equivalence ratio oscillations, the stratified flame speed is modified from the

homogeneous flame speed even when the oscillation frequency is sufficiently low that the flame is expected to respond in a quasi-steady manner. Therefore, in addition to the oscillation timescale, flame response under compositional oscillation should be considered in terms of amplitudes of variations in the equivalence ratio gradient.

- When a rich-to-lean stratified methane/air flame propagates under compressible flow strain, a higher strain rate decelerates the attenuation of equivalence ratio gradient in the flame zone, which results in a larger increase in the stratified flame speed due to the back-support effect. Therefore, it is suggested that evaluation and control of mixture stratification in practical applications may need to consider the influence of flow non-uniformity.

- When a rich-to-lean stratified methane/air flame propagates with added hydrogen content in the unburned mixture, the flame speed will be less sensitive to the back-support effect for a higher hydrogen content within the range of 0 to 40%. This is because H_2 preferentially diffuses out of the flame zone toward the unburned mixture, mitigating the accumulation of H_2 that diffused from the burned gas into the reaction zone.

- When a stratified ammonia/air flame propagates in rich-to-lean and lean-to-rich stratified mixtures, the stratified flame speed is respectively increased and decreased from the corresponding homogeneous flame speeds. The mechanism behind this behavior is similar to the back-support effect observed in methane/air stratified flames, i.e., preferential diffusion of H_2 from the burned gas dominates the variation in the fuel consumption rate.

- In both rich-to-lean and lean-to-rich stratified ammonia/air flames, additional consumption of NO occurs in the downstream stoichiometric burned gas. This is caused by the production of additional NH_i radicals which reduce NO in the stoichiometric region of the burned gas. Therefore, NO emission from stratified flames is expected to be smaller than that predicted from homogeneous flame emission characteristics.

7.2   Relevance to practical applications

In addition to the increased understanding of the mechanism and characteristics of local stratification effects on flame propagation, namely the back-support effect, the above conclusions are relevant to the development of new combustion technologies in practical combustors in terms of the following points:

- In internal combustion engines that utilize direct fuel injection into the combustion chamber, mixture concentration distribution can be controlled by modifying injection timing and the mixing process induced by the velocity field. Adjusting the extent of mixture stratification and the location of the ignition kernel so that the flame propagates toward leaner mixtures, it is possible to make use of the back-support effect to achieve faster flame propagation. On the other hand, by making the flame propagate into richer mixtures, it is possible to decelerate the rate of combustion, which is beneficial for mitigating the unwanted rapid increase in pressure. As such, the back-support effect can be utilized to control the rate of the combustion process without modifying the overall mixture reactivity.

- The thermo-acoustic oscillations observed in gas turbine combustors or liquid propellant rocket engines are known to be associated with fuel concentration fluctuation caused by pressure fluctuation at the injector, which sustains the feedback loop of pressure fluctuation through heat release fluctuation of the flame. Here, the phase difference between each fluctuation plays a critical role in driving the feedback loop. Without the back-support effect in mind, the heat release fluctuation is always in phase with the fuel concentration fluctuation at the flame location. However, due to the back-support effect, a phase delay is expected to exist between the heat release and the fuel concentration fluctuations. Moreover, the phase delay is expected to depend on the spatial gradient of the fluctuation. Therefore, an additional phase delay associated with the back-support effect needs to be considered to control and mitigate thermo-acoustic oscillations in the combustors.

7.3 Suggestions for future work

This study has deepened the understanding of the local effects of mixture stratification on premixed flame propagation from a variety of aspects including a non-uniform flow and non-conventional fuels such as hydrogen-blended methane and ammonia. However, some points still require further investigation. Some of them are suggested below:

- In addition to the flow non-uniformity, the flame surface is highly curved in practical turbulent stratified flames. However, studies on the effect of flame curvature on local stratification effects such as the back-support effect are very limited [111]. Further investigations on detailed kinetics and transport phenomena in curved stratified flames are required.

- Contrarily to hydrocarbon/air stratified flames, the back-support effect of hydrogen/air

stratified flames are known to be driven by diffusion of H atoms, as mentioned in Chapter 3. Meanwhile, as shown in this study, the back-support effect of methane/air and ammonia/air stratified flames are driven primarily by preferential diffusion of H_2. Moreover, it was shown that the methane/hydrogen/air stratified flame is still primarily driven by H_2 for the hydrogen content of up to 40%. Therefore, it would be interesting to study the propagation of methane/hydrogen/air or ammonia/hydrogen/air stratified flames under a higher hydrogen content to investigate the shift from the H_2-driven back-supporting mode to the H-driven back-supporting mode.

- Previous studies on the back-support effect, including the current effort, have characterized the extent of mixture stratification in terms of equivalence ratio gradient. However, a more essential degree of stratification should be weighted by the sensitivity of burned gas composition to the mixture equivalence ratio. For example, under decreasing equivalence ratio, the rate of variation in the H_2 content in the burned gas of ammonia/air flames is larger around stoichiometry than in lean or rich mixtures, as shown in Chapter 6. Therefore, under the same equivalence ratio gradient, more H_2 is expected to diffuse from near stoichiometric mixtures than from lean or rich mixtures. A further consideration is required when more than one species, such as H_2 and H, are associated with the back-supporting mechanism. Such an aspect would be important for a more detailed characterization of stratified mixtures.

- All of the numerical analyses in this study were conducted under standard temperature and pressure. However, to the best of the author's knowledge, there has been no report on the effect of increased temperature or pressure on the local stratification effects including the back-support effect, except for one recent study on stratified cool flames under ambient pressure [119]. Such studies are crucial for predicting the influence of such effects in practical combustors.

Appendices

Appendix A Chemical Kinetics

Table A.1 shows the elementary reactions in GRI_mech 3.0 [116].

Table A.1: Elementary reactions in GRI_mech 3.0 [116].

No.	Reactions	No.	Reactions
1	2O+M<=>O2+M	164	CH3+C2H4<=>C2H3+CH4
2	O+H+M<=>OH+M	165	CH3+C2H6<=>C2H5+CH4
3	O+H2<=>H+OH	166	HCO+H2O<=>H+CO+H2O
4	O+HO2<=>OH+O2	167	HCO+M<=>H+CO+M
5	O+H2O2<=>OH+HO2	168	HCO+O2<=>HO2+CO
6	O+CH<=>H+CO	169	CH2OH+O2<=>HO2+CH2O
7	O+CH2<=>H+HCO	170	CH3O+O2<=>HO2+CH2O
8	O+CH2(S)<=>H2+CO	171	C2H+O2<=>HCO+CO
9	O+CH2(S)<=>H+HCO	172	C2H+H2<=>H+C2H2
10	O+CH3<=>H+CH2O	173	C2H3+O2<=>HCO+CH2O
11	O+CH4<=>OH+CH3	174	C2H4(+M)<=>H2+C2H2(+M)
12	O+CO(+M)<=>CO2(+M)	175	C2H5+O2<=>HO2+C2H4
13	O+HCO<=>OH+CO	176	HCCO+O2<=>OH+2CO
14	O+HCO<=>H+CO2	177	2HCCO<=>2CO+C2H2
15	O+CH2O<=>OH+HCO	178	N+NO<=>N2+O
16	O+CH2OH<=>OH+CH2O	179	N+O2<=>NO+O
17	O+CH3O<=>OH+CH2O	180	N+OH<=>NO+H
18	O+CH3OH<=>OH+CH2OH	181	N2O+O<=>N2+O2
19	O+CH3OH<=>OH+CH3O	182	N2O+O<=>2NO
20	O+C2H<=>CH+CO	183	N2O+H<=>N2+OH
21	O+C2H2<=>H+HCCO	184	N2O+OH<=>N2+HO2
22	O+C2H2<=>OH+C2H	185	N2O(+M)<=>N2+O(+M)
23	O+C2H2<=>CO+CH2	186	HO2+NO<=>NO2+OH
24	O+C2H3<=>H+CH2CO	187	NO+O+M<=>NO2+M
25	O+C2H4<=>CH3+HCO	188	NO2+O<=>NO+O2
26	O+C2H5<=>CH3+CH2O	189	NO2+H<=>NO+OH
27	O+C2H6<=>OH+C2H5	190	NH+O<=>NO+H
28	O+HCCO<=>H+2CO	191	NH+H<=>N+H2
29	O+CH2CO<=>OH+HCCO	192	NH+OH<=>HNO+H
30	O+CH2CO<=>CH2+CO2	193	NH+OH<=>N+H2O
31	O2+CO<=>O+CO2	194	NH+O2<=>HNO+O
32	O2+CH2O<=>HO2+HCO	195	NH+O2<=>NO+OH
33	H+O2+M<=>HO2+M	196	NH+N<=>N2+H
34	H+2O2<=>HO2+O2	197	NH+H2O<=>HNO+H2

Table A.1 continued.

No.	Reactions	No.	Reactions
35	H+O2+H2O<=>HO2+H2O	198	NH+NO<=>N2+OH
36	H+O2+N2<=>HO2+N2	199	NH+NO<=>N2O+H
37	H+O2+AR<=>HO2+AR	200	NH2+O<=>OH+NH
38	H+O2<=>O+OH	201	NH2+O<=>H+HNO
39	2H+M<=>H2+M	202	NH2+H<=>NH+H2
40	2H+H2<=>2H2	203	NH2+OH<=>NH+H2O
41	2H+H2O<=>H2+H2O	204	NNH<=>N2+H
42	2H+CO2<=>H2+CO2	205	NNH+M<=>N2+H+M
43	H+OH+M<=>H2O+M	206	NNH+O2<=>HO2+N2
44	H+HO2<=>O+H2O	207	NNH+O<=>OH+N2
45	H+HO2<=>O2+H2	208	NNH+O<=>NH+NO
46	H+HO2<=>2OH	209	NNH+H<=>H2+N2
47	H+H2O2<=>HO2+H2	210	NNH+OH<=>H2O+N2
48	H+H2O2<=>OH+H2O	211	NNH+CH3<=>CH4+N2
49	H+CH<=>C+H2	212	H+NO+M<=>HNO+M
50	H+CH2(+M)<=>CH3(+M)	213	HNO+O<=>NO+OH
51	H+CH2(S)<=>CH+H2	214	HNO+H<=>H2+NO
52	H+CH3(+M)<=>CH4(+M)	215	HNO+OH<=>NO+H2O
53	H+CH4<=>CH3+H2	216	HNO+O2<=>HO2+NO
54	H+HCO(+M)<=>CH2O(+M)	217	CN+O<=>CO+N
55	H+HCO<=>H2+CO	218	CN+OH<=>NCO+H
56	H+CH2O(+M)<=>CH2OH(+M)	219	CN+H2O<=>HCN+OH
57	H+CH2O(+M)<=>CH3O(+M)	220	CN+O2<=>NCO+O
58	H+CH2O<=>HCO+H2	221	CN+H2<=>HCN+H
59	H+CH2OH(+M)<=>CH3OH(+M)	222	NCO+O<=>NO+CO
60	H+CH2OH<=>H2+CH2O	223	NCO+H<=>NH+CO
61	H+CH2OH<=>OH+CH3	224	NCO+OH<=>NO+H+CO
62	H+CH2OH<=>CH2(S)+H2O	225	NCO+N<=>N2+CO
63	H+CH3O(+M)<=>CH3OH(+M)	226	NCO+O2<=>NO+CO2
64	H+CH3O<=>H+CH2OH	227	NCO+M<=>N+CO+M
65	H+CH3O<=>H2+CH2O	228	NCO+NO<=>N2O+CO
66	H+CH3O<=>OH+CH3	229	NCO+NO<=>N2+CO2
67	H+CH3O<=>CH2(S)+H2O	230	HCN+M<=>H+CN+M
68	H+CH3OH<=>CH2OH+H2	231	HCN+O<=>NCO+H
69	H+CH3OH<=>CH3O+H2	232	HCN+O<=>NH+CO
70	H+C2H(+M)<=>C2H2(+M)	233	HCN+O<=>CN+OH
71	H+C2H2(+M)<=>C2H3(+M)	234	HCN+OH<=>HOCN+H
72	H+C2H3(+M)<=>C2H4(+M)	235	HCN+OH<=>HNCO+H
73	H+C2H3<=>H2+C2H2	236	HCN+OH<=>NH2+CO
74	H+C2H4(+M)<=>C2H5(+M)	237	H+HCN(+M)<=>H2CN(+M)
75	H+C2H4<=>C2H3+H2	238	H2CN+N<=>N2+CH2
76	H+C2H5(+M)<=>C2H6(+M)	239	C+N2<=>CN+N
77	H+C2H5<=>H2+C2H4	240	CH+N2<=>HCN+N
78	H+C2H6<=>C2H5+H2	241	CH+N2(+M)<=>HCNN(+M)
79	H+HCCO<=>CH2(S)+CO	242	CH2+N2<=>HCN+NH
80	H+CH2CO<=>HCCO+H2	243	CH2(S)+N2<=>NH+HCN
81	H+CH2CO<=>CH3+CO	244	C+NO<=>CN+O
82	H+HCCOH<=>H+CH2CO	245	C+NO<=>CO+N
83	H2+CO(+M)<=>CH2O(+M)	246	CH+NO<=>HCN+O
84	OH+H2<=>H+H2O	247	CH+NO<=>H+NCO

Table A.1 continued.

No.	Reactions	No.	Reactions
85	2OH(+M)<=>H2O2(+M)	248	CH+NO<=>N+HCO
86	2OH<=>O+H2O	249	CH2+NO<=>H+HNCO
87	OH+HO2<=>O2+H2O	250	CH2+NO<=>OH+HCN
88	OH+H2O2<=>HO2+H2O	251	CH2+NO<=>H+HCNO
89	OH+H2O2<=>HO2+H2O	252	CH2(S)+NO<=>H+HNCO
90	OH+C<=>H+CO	253	CH2(S)+NO<=>OH+HCN
91	OH+CH<=>H+HCO	254	CH2(S)+NO<=>H+HCNO
92	OH+CH2<=>H+CH2O	255	CH3+NO<=>HCN+H2O
93	OH+CH2<=>CH+H2O	256	CH3+NO<=>H2CN+OH
94	OH+CH2(S)<=>H+CH2O	257	HCNN+O<=>CO+H+N2
95	OH+CH3(+M)<=>CH3OH(+M)	258	HCNN+O<=>HCN+NO
96	OH+CH3<=>CH2+H2O	259	HCNN+O2<=>O+HCO+N2
97	OH+CH3<=>CH2(S)+H2O	260	HCNN+OH<=>H+HCO+N2
98	OH+CH4<=>CH3+H2O	261	HCNN+H<=>CH2+N2
99	OH+CO<=>H+CO2	262	HNCO+O<=>NH+CO2
100	OH+HCO<=>H2O+CO	263	HNCO+O<=>HNO+CO
101	OH+CH2O<=>HCO+H2O	264	HNCO+O<=>NCO+OH
102	OH+CH2OH<=>H2O+CH2O	265	HNCO+H<=>NH2+CO
103	OH+CH3O<=>H2O+CH2O	266	HNCO+H<=>H2+NCO
104	OH+CH3OH<=>CH2OH+H2O	267	HNCO+OH<=>NCO+H2O
105	OH+CH3OH<=>CH3O+H2O	268	HNCO+OH<=>NH2+CO2
106	OH+C2H<=>H+HCCO	269	HNCO+M<=>NH+CO+M
107	OH+C2H2<=>H+CH2CO	270	HCNO+H<=>H+HNCO
108	OH+C2H2<=>H+HCCOH	271	HCNO+H<=>OH+HCN
109	OH+C2H2<=>C2H+H2O	272	HCNO+H<=>NH2+CO
110	OH+C2H2<=>CH3+CO	273	HOCN+H<=>H+HNCO
111	OH+C2H3<=>H2O+C2H2	274	HCCO+NO<=>HCNO+CO
112	OH+C2H4<=>C2H3+H2O	275	CH3+N<=>H2CN+H
113	OH+C2H6<=>C2H5+H2O	276	CH3+N<=>HCN+H2
114	OH+CH2CO<=>HCCO+H2O	277	NH3+H<=>NH2+H2
115	2HO2<=>O2+H2O2	278	NH3+OH<=>NH2+H2O
116	2HO2<=>O2+H2O2	279	NH3+O<=>NH2+OH
117	HO2+CH2<=>OH+CH2O	280	NH+CO2<=>HNO+CO
118	HO2+CH3<=>O2+CH4	281	CN+NO2<=>NCO+NO
119	HO2+CH3<=>OH+CH3O	282	NCO+NO2<=>N2O+CO2
120	HO2+CO<=>OH+CO2	283	N+CO2<=>NO+CO
121	HO2+CH2O<=>HCO+H2O2	284	O+CH3=>H+H2+CO
122	C+O2<=>O+CO	285	O+C2H4<=>H+CH2CHO
123	C+CH2<=>H+C2H	286	O+C2H5<=>H+CH3CHO
124	C+CH3<=>H+C2H2	287	OH+HO2<=>O2+H2O
125	CH+O2<=>O+HCO	288	OH+CH3=>H2+CH2O
126	CH+H2<=>H+CH2	289	CH+H2(+M)<=>CH3(+M)
127	CH+H2O<=>H+CH2O	290	CH2+O2=>2H+CO2
128	CH+CH2<=>H+C2H2	291	CH2+O2<=>O+CH2O
129	CH+CH3<=>H+C2H3	292	CH2+CH2=>2H+C2H2
130	CH+CH4<=>H+C2H4	293	CH2(S)+H2O=>H2+CH2O
131	CH+CO(+M)<=>HCCO(+M)	294	C2H3+O2<=>O+CH2CHO
132	CH+CO2<=>HCO+CO	295	C2H3+O2<=>HO2+C2H2
133	CH+CH2O<=>H+CH2CO	296	O+CH3CHO<=>OH+CH2CHO
134	CH+HCCO<=>CO+C2H2	297	O+CH3CHO=>OH+CH3+CO

Table A.1 continued.

No.	Reactions	No.	Reactions
135	CH2+O2=>OH+H+CO	298	O2+CH3CHO=>HO2+CH3+CO
136	CH2+H2<=>H+CH3	299	H+CH3CHO<=>CH2CHO+H2
137	2CH2<=>H2+C2H2	300	H+CH3CHO=>CH3+H2+CO
138	CH2+CH3<=>H+C2H4	301	OH+CH3CHO=>CH3+H2O+CO
139	CH2+CH4<=>2CH3	302	HO2+CH3CHO=>CH3+H2O2+CO
140	CH2+CO(+M)<=>CH2CO(+M)	303	CH3+CH3CHO=>CH3+CH4+CO
141	CH2+HCCO<=>C2H3+CO	304	H+CH2CO(+M)<=>CH2CHO(+M)
142	CH2(S)+N2<=>CH2+N2	305	O+CH2CHO=>H+CH2+CO2
143	CH2(S)+AR<=>CH2+AR	306	O2+CH2CHO=>OH+CO+CH2O
144	CH2(S)+O2<=>H+OH+CO	307	O2+CH2CHO=>OH+2HCO
145	CH2(S)+O2<=>CO+H2O	308	H+CH2CHO<=>CH3+HCO
146	CH2(S)+H2<=>CH3+H	309	H+CH2CHO<=>CH2CO+H2
147	CH2(S)+H2O(+M)<=>CH3OH(+M)	310	OH+CH2CHO<=>H2O+CH2CO
148	CH2(S)+H2O<=>CH2+H2O	311	OH+CH2CHO<=>HCO+CH2OH
149	CH2(S)+CH3<=>H+C2H4	312	CH3+C2H5(+M)<=>C3H8(+M)
150	CH2(S)+CH4<=>2CH3	313	O+C3H8<=>OH+C3H7
151	CH2(S)+CO<=>CH2+CO	314	H+C3H8<=>C3H7+H2
152	CH2(S)+CO2<=>CH2+CO2	315	OH+C3H8<=>C3H7+H2O
153	CH2(S)+CO2<=>CO+CH2O	316	C3H7+H2O2<=>HO2+C3H8
154	CH2(S)+C2H6<=>CH3+C2H5	317	CH3+C3H8<=>C3H7+CH4
155	CH3+O2<=>O+CH3O	318	CH3+C2H4(+M)<=>C3H7(+M)
156	CH3+O2<=>OH+CH2O	319	O+C3H7<=>C2H5+CH2O
157	CH3+H2O2<=>HO2+CH4	320	H+C3H7(+M)<=>C3H8(+M)
158	2CH3(+M)<=>C2H6(+M)	321	H+C3H7<=>CH3+C2H5
159	2CH3<=>H+C2H5	322	OH+C3H7<=>C2H5+CH2OH
160	CH3+HCO<=>CH4+CO	323	HO2+C3H7<=>O2+C3H8
161	CH3+CH2O<=>HCO+CH4	324	HO2+C3H7=>OH+C2H5+CH2O
162	CH3+CH3OH<=>CH2OH+CH4	325	CH3+C3H7<=>2C2H5
163	CH3+CH3OH<=>CH3O+CH4		

Table A.2 shows the elementary reactions in ammonia/air kinetics by Okafor et al. [182].

Table A.2: Elementary reactions in ammonia/air kinetics by Okafor et al. [182].

No.	Reactions	No.	Reactions
1	2O+M<=>O2+M	179	HCCO+O2<=>OH+2CO
2	O+H+M<=>OH+M	180	2HCCO<=>2CO+C2H2
3	O+H2<=>H+OH	181	O+C2H4<=>H+CH2CHO
4	O+HO2<=>OH+O2	182	O+C2H5<=>H+CH3CHO
5	O+H2O2<=>OH+HO2	183	CH+H2(+M)<=>CH3(+M)
6	O+CH<=>H+CO	184	CH2+O2=>2H+CO2
7	O+CH2<=>H+HCO	185	CH2+O2<=>O+CH2O
8	O+CH2(S)<=>H2+CO	186	CH2+CH2=>2H+C2H2
9	O+CH2(S)<=>H+HCO	187	CH2(S)+H2O=>H2+CH2O
10	O+CH3<=>H+CH2O	188	C2H3+O2<=>O+CH2CHO
11	O+CH3=>H+H2+CO	189	C2H3+O2<=>HO2+C2H2
12	O+CH4<=>OH+CH3	190	O+CH3CHO<=>OH+CH2CHO
13	O+CO(+M)<=>CO2(+M)	191	O+CH3CHO=>OH+CH3+CO
14	O+HCO<=>OH+CO	192	O2+CH3CHO=>HO2+CH3+CO
15	O+HCO<=>H+CO2	193	H+CH3CHO<=>CH2CHO+H2
16	O+CH2O<=>OH+HCO	194	H+CH3CHO=>CH3+H2+CO
17	O+CH2OH<=>OH+CH2O	195	OH+CH3CHO=>CH3+H2O+CO
18	O+CH3O<=>OH+CH2O	196	HO2+CH3CHO=>CH3+H2O2+CO
19	O+CH3OH<=>OH+CH2OH	197	CH3+CH3CHO=>CH3+CH4+CO
20	O+CH3OH<=>OH+CH3O	198	H+CH2CO(+M)<=>CH2CHO(+M)
21	O+C2H<=>CH+CO	199	O+CH2CHO=>H+CH2+CO2
22	O+C2H2<=>H+HCCO	200	O2+CH2CHO=>OH+CO+CH2O
23	O+C2H2<=>OH+C2H	201	O2+CH2CHO=>OH+2HCO
24	O+C2H2<=>CO+CH2	202	H+CH2CHO<=>CH3+HCO
25	O+C2H3<=>H+CH2CO	203	H+CH2CHO<=>CH2CO+H2
26	O+C2H4<=>CH3+HCO	204	OH+CH2CHO<=>H2O+CH2CO
27	O+C2H5<=>CH3+CH2O	205	OH+CH2CHO<=>HCO+CH2OH
28	O+C2H6<=>OH+C2H5	206	CH3+C2H5(+M)<=>C3H8(+M)
29	O+HCCO<=>H+2CO	207	O+C3H8<=>OH+C3H7
30	O+CH2CO<=>OH+HCCO	208	H+C3H8<=>C3H7+H2
31	O+CH2CO<=>CH2+CO2	209	OH+C3H8<=>C3H7+H2O
32	O2+CO<=>O+CO2	210	C3H7+H2O2<=>HO2+C3H8
33	O2+CH2O<=>HO2+HCO	211	CH3+C3H8<=>C3H7+CH4
34	H+O2+M<=>HO2+M	212	CH3+C2H4(+M)<=>C3H7(+M)
35	H+2O2<=>HO2+O2	213	O+C3H7<=>C2H5+CH2O
36	H+O2+H2O<=>HO2+H2O	214	H+C3H7(+M)<=>C3H8(+M)
37	H+O2+N2<=>HO2+N2	215	H+C3H7<=>CH3+C2H5
38	H+O2+AR<=>HO2+AR	216	OH+C3H7<=>C2H5+CH2OH
39	H+O2<=>O+OH	217	HO2+C3H7<=>O2+C3H8
40	2H+M<=>H2+M	218	HO2+C3H7=>OH+C2H5+CH2O
41	2H+H2<=>2H2	219	CH3+C3H7<=>2C2H5
42	2H+H2O<=>H2+H2O	220	N+NO<=>N2+O
43	2H+CO2<=>H2+CO2	221	N+O2<=>NO+O
44	H+OH+M<=>H2O+M	222	N+OH<=>NO+H
45	H+HO2<=>O+H2O	223	N2O+O<=>N2+O2
46	H+HO2<=>O2+H2	224	N2O+O<=>2NO
47	H+HO2<=>2OH	225	N2O+H<=>N2+OH
48	H+H2O2<=>HO2+H2	226	N2O+OH<=>N2+HO2

Table A.2 continued.

No.	Reactions	No.	Reactions
49	H+H2O2<=>OH+H2O	227	N2O(+M)<=>N2+O(+M)
50	H+CH<=>C+H2	228	HO2+NO<=>NO2+OH
51	H+CH2(+M)<=>CH3(+M)	229	NO+O+M<=>NO2+M
52	H+CH2(S)<=>CH+H2	230	NO2+O<=>NO+O2
53	H+CH3(+M)<=>CH4(+M)	231	NO2+H<=>NO+OH
54	H+CH4<=>CH3+H2	232	NH+H=N+H2
55	H+HCO(+M)<=>CH2O(+M)	233	NH+O=NO+H
56	H+HCO<=>H2+CO	234	NH+OH=HNO+H
57	H+CH2O(+M)<=>CH2OH(+M)	235	NH+OH=N+H2O
58	H+CH2O(+M)<=>CH3O(+M)	236	NH+O2=HNO+O
59	H+CH2O<=>HCO+H2	237	NH+O2=NO+OH
60	H+CH2OH(+M)<=>CH3OH(+M)	238	NH+NH=N2+H+H
61	H+CH2OH<=>H2+CH2O	239	NH+N=N2+H
62	H+CH2OH<=>OH+CH3	240	NH+NO=N2O+H
63	H+CH2OH<=>CH2(S)+H2O	241	NH+NO=N2O+H
64	H+CH3O(+M)<=>CH3OH(+M)	242	NH+NO=N2+OH
65	H+CH3O<=>H+CH2OH	243	NH+HONO=NH2+NO2
66	H+CH3O<=>H2+CH2O	244	NH+NO2=N2O+OH
67	H+CH3O<=>OH+CH3	245	NH2+H=NH+H2
68	H+CH3O<=>CH2(S)+H2O	246	NH2+O=HNO+H
69	H+CH3OH<=>CH2OH+H2	247	NH2+O=NH+OH
70	H+CH3OH<=>CH3O+H2	248	NH2+OH=NH+H2O
71	H+C2H(+M)<=>C2H2(+M)	249	NH2+HO2=NH3+O2
72	H+C2H2(+M)<=>C2H3(+M)	250	NH2+O2=H2NO+O
73	H+C2H3(+M)<=>C2H4(+M)	251	NH2+NH2=NH3+NH
74	H+C2H3<=>H2+C2H2	252	NH2+NH=N2H2+H
75	H+C2H4(+M)<=>C2H5(+M)	253	NH2+NH=NH3+N
76	H+C2H4<=>C2H3+H2	254	NH2+N=N2+H+H
77	H+C2H5(+M)<=>C2H6(+M)	255	NH2+HNO=NH3+NO
78	H+C2H5<=>H2+C2H4	256	NH2+NO=N2+H2O
79	H+C2H6<=>C2H5+H2	257	NH2+NO=NNH+OH
80	H+HCCO<=>CH2(S)+CO	258	NH2+HONO=NH3+NO2
81	H+CH2CO<=>HCCO+H2	259	NH2+NO2=N2O+H2O
82	H+CH2CO<=>CH3+CO	260	NNH=N2+H
83	H+HCCOH<=>H+CH2CO	261	NNH+H=N2+H2
84	H2+CO(+M)<=>CH2O(+M)	262	NNH+O=N2O+H
85	OH+H2<=>H+H2O	263	NNH+O=NH+NO
86	2OH(+M)<=>H2O2(+M)	264	NNH+OH=N2+H2O
87	2OH<=>O+H2O	265	NNH+O2=N2+HO2
88	OH+HO2<=>O2+H2O	266	NNH+O2=N2+H+O2
89	OH+HO2<=>O2+H2O	267	NNH+NH=N2+NH2
90	OH+H2O2<=>HO2+H2O	268	NNH+NH2=N2+NH3
91	OH+H2O2<=>HO2+H2O	269	NNH+NO=N2+HNO
92	OH+C<=>H+CO	270	NNH+CH3<=>CH4+N2
93	OH+CH<=>H+HCO	271	H+NO+M<=>HNO+M
94	OH+CH2<=>H+CH2O	272	HNO+O<=>NO+OH
95	OH+CH2<=>CH+H2O	273	HNO+H<=>H2+NO
96	OH+CH2(S)<=>H+CH2O	274	HNO+OH<=>NO+H2O
97	OH+CH3=>H2+CH2O	275	HNO+O2<=>HO2+NO
98	OH+CH3(+M)<=>CH3OH(+M)	276	HNO+NO2=HONO+NO

Table A.2 continued.

No.	Reactions	No.	Reactions
99	OH+CH3<=>CH2+H2O	277	NH3+H<=>NH2+H2
100	OH+CH3<=>CH2(S)+H2O	278	NH3+OH=NH2+H2O
101	OH+CH4<=>CH3+H2O	279	NH3+O<=>NH2+OH
102	OH+CO<=>H+CO2	280	NH+CO2<=>HNO+CO
103	OH+HCO<=>H2O+CO	281	NH2+NH2=N2H4
104	OH+CH2O<=>HCO+H2O	282	N2H4+O=NH2OH+NH
105	OH+CH2OH<=>H2O+CH2O	283	N2H3=N2H2+H
106	OH+CH3O<=>H2O+CH2O	284	N2H3+H=N2H2+H2
107	OH+CH3OH<=>CH2OH+H2O	285	N2H3+HO2=N2H2+H2O2
108	OH+CH3OH<=>CH3O+H2O	286	N2H3+HO2=N2H4+O2
109	OH+C2H<=>H+HCCO	287	N2H3+NH=N2H2+NH2
110	OH+C2H2<=>H+CH2CO	288	N2H2+H=NNH+H2
111	OH+C2H2<=>H+HCCOH	289	N2H2+O=NNH+OH
112	OH+C2H2<=>C2H+H2O	290	N2H2+O=NH2+NO
113	OH+C2H2<=>CH3+CO	291	N2H2+OH=NNH+H2O
114	OH+C2H3<=>H2O+C2H2	292	N2H2+NH=NNH+NH2
115	OH+C2H4<=>C2H3+H2O	293	H2NO+OH=HNO+H2O
116	OH+C2H6<=>C2H5+H2O	294	CN+NO2<=>NCO+NO
117	OH+CH2CO<=>HCCO+H2O	295	NCO+NO2<=>N2O+CO2
118	2HO2<=>O2+H2O2	296	N+CO2<=>NO+CO
119	2HO2<=>O2+H2O2	297	CN+O<=>CO+N
120	HO2+CH2<=>OH+CH2O	298	CN+OH<=>NCO+H
121	HO2+CH3<=>O2+CH4	299	CN+H2O<=>HCN+OH
122	HO2+CH3<=>OH+CH3O	300	CN+O2<=>NCO+O
123	HO2+CO<=>OH+CO2	301	CN+H2<=>HCN+H
124	HO2+CH2O<=>HCO+H2O2	302	NCO+O<=>NO+CO
125	C+O2<=>O+CO	303	NCO+H<=>NH+CO
126	C+CH2<=>H+C2H	304	NCO+OH<=>NO+H+CO
127	C+CH3<=>H+C2H2	305	NCO+N<=>N2+CO
128	CH+O2<=>O+HCO	306	NCO+O2<=>NO+CO2
129	CH+H2<=>H+CH2	307	NCO+M<=>N+CO+M
130	CH+H2O<=>H+CH2O	308	NCO+NO<=>N2O+CO
131	CH+CH2<=>H+C2H2	309	NCO+NO<=>N2+CO2
132	CH+CH3<=>H+C2H3	310	HCN+M<=>H+CN+M
133	CH+CH4<=>H+C2H4	311	HCN+O<=>NCO+H
134	CH+CO(+M)<=>HCCO(+M)	312	HCN+O<=>NH+CO
135	CH+CO2<=>HCO+CO	313	HCN+O<=>CN+OH
136	CH+CH2O<=>H+CH2CO	314	HCN+OH<=>HOCN+H
137	CH+HCCO<=>CO+C2H2	315	HCN+OH<=>HNCO+H
138	CH2+O2=>OH+H+CO	316	HCN+OH<=>NH2+CO
139	CH2+H2<=>H+CH3	317	H+HCN(+M)<=>H2CN(+M)
140	2CH2<=>H2+C2H2	318	H2CN+N<=>N2+CH2
141	CH2+CH3<=>H+C2H4	319	C+N2<=>CN+N
142	CH2+CH4<=>2CH3	320	CH+N2<=>HCN+N
143	CH2+CO(+M)<=>CH2CO(+M)	321	CH+N2(+M)<=>HCNN(+M)
144	CH2+HCCO<=>C2H3+CO	322	CH2+N2<=>HCN+NH
145	CH2(S)+N2<=>CH2+N2	323	CH2(S)+N2<=>NH+HCN
146	CH2(S)+AR<=>CH2+AR	324	C+NO<=>CN+O
147	CH2(S)+O2<=>H+OH+CO	325	C+NO<=>CO+N
148	CH2(S)+O2<=>CO+H2O	326	CH+NO<=>HCN+O

Table A.2 continued.

No.	Reactions	No.	Reactions
149	CH2(S)+H2<=>CH3+H	327	CH+NO<=>H+NCO
150	CH2(S)+H2O(+M)<=>CH3OH(+M)	328	CH+NO<=>N+HCO
151	CH2(S)+H2O<=>CH2+H2O	329	CH2+NO<=>H+HNCO
152	CH2(S)+CH3<=>H+C2H4	330	CH2+NO<=>OH+HCN
153	CH2(S)+CH4<=>2CH3	331	CH2+NO<=>H+HCNO
154	CH2(S)+CO<=>CH2+CO	332	CH2(S)+NO<=>H+HNCO
155	CH2(S)+CO2<=>CH2+CO2	333	CH2(S)+NO<=>OH+HCN
156	CH2(S)+CO2<=>CO+CH2O	334	CH2(S)+NO<=>H+HCNO
157	CH2(S)+C2H6<=>CH3+C2H5	335	CH3+NO<=>HCN+H2O
158	CH3+O2<=>O+CH3O	336	CH3+NO<=>H2CN+OH
159	CH3+O2<=>OH+CH2O	337	HCNN+O<=>CO+H+N2
160	CH3+H2O2<=>HO2+CH4	338	HCNN+O<=>HCN+NO
161	2CH3(+M)<=>C2H6(+M)	339	HCNN+O2<=>O+HCO+N2
162	2CH3<=>H+C2H5	340	HCNN+OH<=>H+HCO+N2
163	CH3+HCO<=>CH4+CO	341	HCNN+H<=>CH2+N2
164	CH3+CH2O<=>HCO+CH4	342	HNCO+O<=>NH+CO2
165	CH3+CH3OH<=>CH2OH+CH4	343	HNCO+O<=>HNO+CO
166	CH3+CH3OH<=>CH3O+CH4	344	HNCO+O<=>NCO+OH
167	CH3+C2H4<=>C2H3+CH4	345	HNCO+H<=>NH2+CO
168	CH3+C2H6<=>C2H5+CH4	346	HNCO+H<=>H2+NCO
169	HCO+H2O<=>H+CO+H2O	347	HNCO+OH<=>NCO+H2O
170	HCO+M<=>H+CO+M	348	HNCO+OH<=>NH2+CO2
171	HCO+O2<=>HO2+CO	349	HNCO+M<=>NH+CO+M
172	CH2OH+O2<=>HO2+CH2O	350	HCNO+H<=>H+HNCO
173	CH3O+O2<=>HO2+CH2O	351	HCNO+H<=>OH+HCN
174	C2H+O2<=>HCO+CO	352	HCNO+H<=>NH2+CO
175	C2H+H2<=>H+C2H2	353	HOCN+H<=>H+HNCO
176	C2H3+O2<=>HCO+CH2O	354	HCCO+NO<=>HCNO+CO
177	C2H4(+M)<=>H2+C2H2(+M)	355	CH3+N<=>H2CN+H
178	C2H5+O2<=>HO2+C2H4	356	CH3+N<=>HCN+H2

Appendix B   Influence of viscosity on counterflow premixed flames

In the numerical code OPUS used in this study, viscous force is included in both axial and radial momentum equations. However, as the flow is quasi-one-dimensional, it is questionable whether the viscosity has any influence on the velocity profiles. To examine this matter, a steady flame with the mixture equivalence ratio of 1.2 was calculated with and without the viscous terms in the momentum equations. Profiles of the axial velocity u and radial velocity gradient V are shown in **Fig. B.1**. It is seen that the u profiles are mostly identical for viscous and non-viscous cases. Meanwhile, the V profile near the stagnation point ($x = 0$ mm) is distinctly different for the two cases. At the stagnation point, symmetric boundary $\partial V/\partial x = 0$ is imposed. With the non-viscous case, the condition at the boundary does not influence the up-

stream flow and a linear profile is achieved. On the other hand, viscosity attenuates the sharp variation in the V gradient at the symmetric boundary. Nevertheless, the influence of viscosity on the flame structure is negligibly small, as seen in the temperature and heat release rate profiles in **Fig. B.2**. Therefore, it can be said that viscosity can be neglected as long as the flame is sufficiently far from the stagnation point. In the current study, the viscous terms are included in the momentum equations as the flame is sometimes attached to the stagnation plane.
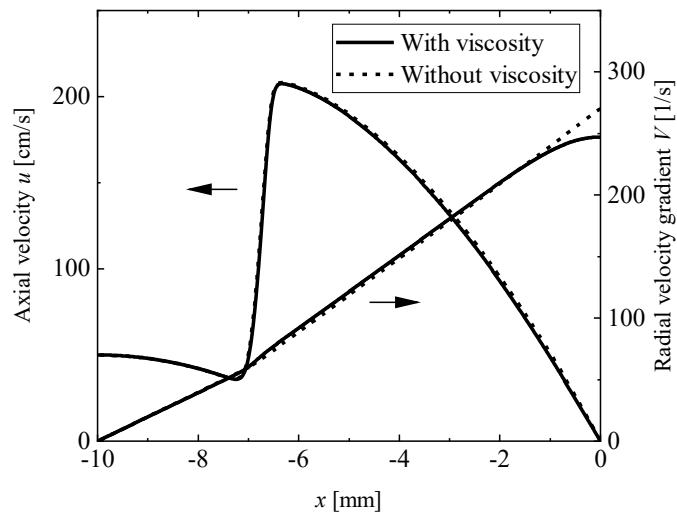
Fig. B.1: Profiles of axial velocity and radial velocity gradient of steady homogeneous flames with and without viscosity under the mixture equivalence ratio of 1.2.
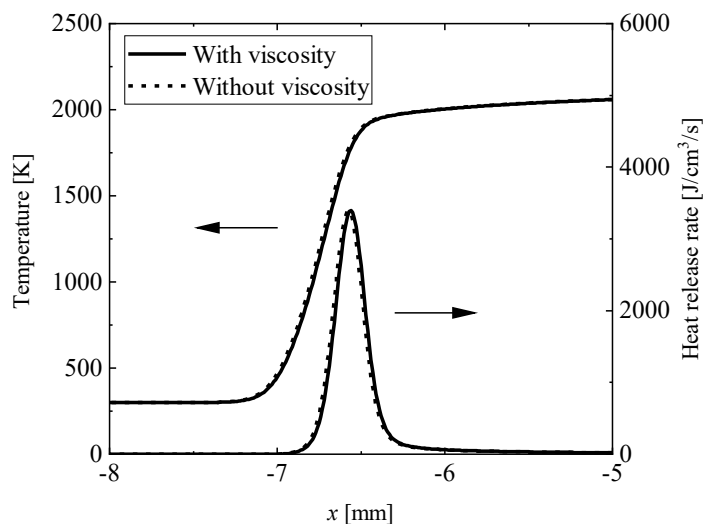
Fig. B.2: Profiles of temperature and heat release rate of steady homogeneous flames with and without viscosity under the mixture equivalence ratio of 1.2.

Appendix C Cutoff threshold for the flame speed of ammonia/air flames

The rich-to-lean stratified flame speed $S_{c,s}$ and the homogeneous flame speed $S_{c,h}$ in Chapter 6 were evaluated with different values of cutoff threshold for the integration of the fuel consumption rate. The relative increase in $S_{c,s}$ from $S_{c,h}$ are shown in **Fig. C.1** for the cases of no integration cutoff, 5% cutoff, and 10% cutoff. As expected, it is seen that the no-cutoff case overestimates the increase in $S_{c,s}$ as fuel consumption in the burned gas is included in the integration. Meanwhile, the results of 5% and 10% cutoff show little difference. Therefore, it can be considered that 5% cutoff is sufficient for excluding fuel consumption in the burned gas from the evaluation of the flame speed.
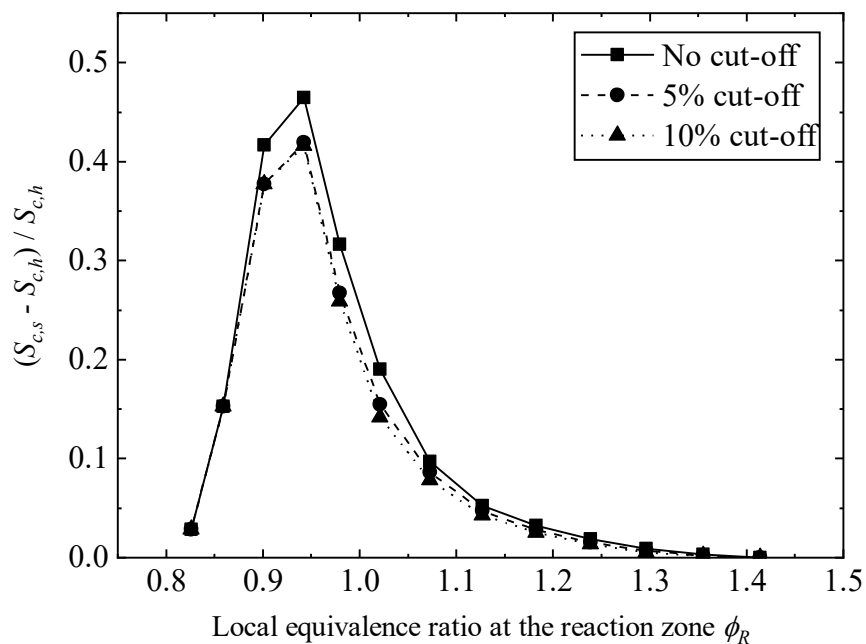
Fig. C.1: The relative increase in the flame speed $S_{c,s}$ of the rich-to-lean stratified flame as compared to the flame speed $S_{c,h}$ of corresponding homogeneous flames in Chapter 6 with different values of cutoff threshold for the integration of the fuel consumption speed.

Appendix D Publications

This dissertation is partly based on the following publications:

- T. Tomidokoro, T. Yokomori, H.G. Im, T. Ueda, Characteristics of counterflow premixed flames with low frequency composition fluctuations, Combustion and Flame 212 (2020) 13–24.

- T. Tomidokoro, T. Yokomori, T. Ueda, H.G. Im, A computational analysis of strained laminar flame propagation in a stratified CH_4/H_2/air mixture, Proceedings of the Combustion Institute 38 (2021) 2543–2550.

References

[1] Britannica, The Editors of Encyclopaedia, "Industrial Revolution", Encyclopedia Britannica, https://www.britannica.com/event/Industrial-Revolution, accessed Oct. 10, 2021.

[2] IEA, World Energy Outlook 2020, Internationa Energy Agency, France, 2020.

[3] IPCC, Summary for Policymakers, in: V. Masson-Delmotte, P. Zhai, A. Pirani, S.L. Connors, C. Péan, S. Berger, N. Caud, Y. Chen, L. Goldfarb, M.I. Gomis, M. Huang, K. Leitzell, E. Lonnoy, J.B.R. Matthews, T.K. Maycock, T. Waterfield, O. Yelekçi, R. Yu, B. Zhou (Eds.), Climate Change 2021: The Physical Science Basis. Contribution of Working Group I to the Sixth Assessment Report of the Intergovernmental Panel on Climate Change, Cambridge Univeristy Press, In Press.

[4] The Paris Agreement: UNFCC, https://unfccc.int/process-and-meetings/the-paris-agreement/the-paris-agreement, accessed Oct. 10, 2021.

[5] Nobel Prize Outreach AB 2021, Press release: The Nobel Prize in Physics 2021, https://www.nobelprize.org/prizes/physics/2021/press-release/, accessed Oct. 10, 2021.

[6] A. Valera-Medina, H. Xiao, M. Owen-Jones, W.I.F. David, P.J. Bowen, Ammonia for power, Prog. Energy Combust. Sci. 69 (2018) 63–102.

[7] IRENA, World Energy Transitions Outlook: 1.5$°C$ Pathway, International Renewable Energy Agency, Abu Dhabi, 2021.

[8] J.M. Bergthorson, Recyclable metal fuels for clean and compact zero-carbon power, Prog. Energy Combust. Sci. 68 (2018) 169–196.

[9] H. Kobayashi, A. Hayakawa, K.D.K.A. Somarathne, E.C. Okafor, Science and technology of ammonia combustion, Proc. Combust. Inst. 37 (2019) 109–133.

[10] A. Giusti, E. Mastorakos, Turbulent Combustion Modelling and Experiments: Recent Trends and Developments, Flow, Turbul. Combust. 103 (2019) 847–869.

[11] A.W. Skiba, On the Structure of Premixed Flames Subjected to Extreme Levels of Turbulence, Ph.D. dissertation, University of Michigan, 2017.

[12] D. Veynante, L. Vervisch, Turbulent combustion modeling, Prog. Energy Combust. Sci. 28 (2002) 193–266.

[13] C.K. Law, Combustion Physics, Cambridge University Press, New York, U.S., 2006.

[14] A.A. Konnov, A. Mohammad, V.R. Kishore, N. Il Kim, C. Prathap, S. Kumar, A comprehensive review of measurements and data analysis of laminar burning velocities for various fuel+air mixtures, Prog. Energy Combust. Sci. 68 (2018) 197–267.

[15] X. Shi, Fundamental Processes in Combustion of Stratified Mixtures, Ph.D. dissertation, Univeresity of California, Berkeley, 2017.

[16] T. Poinsot, T. Echekki, M.G. Mungal, A study of the Laminar Flame Tip and Implications for Premixed Turbulent Combustion, Combust. Sci. Technol. 81 (1992) 45–73.

[17] T. Echekki, J.H. Chen, Unsteady strain rate and curvature effects in turbulent premixed methane-air flames, Combust. Flame 106 (1996) 184–202.

[18] E. Inanc, N. Chakraborty, A.M. Kempf, Analysis of mixture stratification effects on unstrained laminar flames, Combust. Flame 219 (2020) 339–348.

[19] W. Wei, Z. Yu, T. Zhou, T. Ye, A numerical study of laminar flame speed of stratified syngas/air flames, Int. J. Hydrogen Energy 43 (2018) 9036–9045.

[20] E.S. Richardson, V.E. Granet, A. Eyssartier, J.H. Chen, Effects of equivalence ratio on lean, stratified methane-air laminar counterflow flames, Combust. Theory Model. 14 (2010) 775–792.

[21] R.S. Cant, K.N.C. Bray, L.W. Kostiuk, B. Rogg, Flow divergence Effects in Strained Laminar Flames for Premixed Turbulent Combustion, Combust. Sci. Technol. 95 (1994) 261–276.

[22] C.K. Wu, C.K. Law, On the determination of laminar flame speeds from stretched flames, Symp. Combust. 20 (1985) 1941–1949.

[23] C.J. Sung, C.K. Law, Structural sensitivity, response, and extinction of diffusion and premixed flames in oscillating counterflow, Combust. Flame 123 (2000) 375–388.

[24] C.M. Vagelopoulos, F.N. Egolfopoulos, C.K. Law, Further Considerations on the Determination of Laminar Flame Speeds with the Counterflow Twin-Flame Technique, Symp. Combust. 25 (1994) 1341–1347.

[25] N. Peters, Turbulent Combustion, Cambridge University Press, New York, U.S., 2000.

[26] R. Borghi, On the Structure and Morphology of Turbulent Premixed Flames, in: C. Casci, C. Bruno (Eds.), Recent Advances in the Aerospace Sciences, Springer, Boston, MA, 1985.

[27] A.W. Skiba, T.M. Wabel, C.D. Carter, S.D. Hammack, J.E. Temme, J.F. Driscoll, Premixed flames subjected to extreme levels of turbulence part I: Flame structure and a new measured regime diagram, Combust. Flame 189 (2018) 407–432.

[28] L.Y.M. Gicquel, G. Staffelbach, T. Poinsot, Large Eddy Simulations of gaseous flames in gas turbine combustion chambers, Prog. Energy Combust. Sci. 38 (2012) 782–817.

[29] E. Knudsen, H. Kolla, E.R. Hawkes, H. Pitsch, LES of a premixed jet flame DNS using a strained flamelet model, Combust. Flame 160 (2013) 2911–2927.

[30] P. Trisjono, K. Kleinheinz, E.R. Hawkes, H. Pitsch, Modeling turbulence–chemistry interaction in lean premixed hydrogen flames with a strained flamelet model, Combust. Flame 174 (2016) 194–207.

[31] H. Kolla, N. Swaminathan, Strained flamelets for turbulent premixed flames II: Laboratory flame results, Combust. Flame 157 (2010) 1274–1289.

[32] A.R. Masri, Partial premixing and stratification in turbulent flames, Proc. Combust. Inst. 35 (2015) 1115–1136.

[33] A.N. Lipatnikov, Stratified turbulent flames: Recent advances in understanding the influence of mixture inhomogeneities on premixed combustion and modelling challenges, Prog. Energy Combust. Sci. 62 (2017) 1339–1351.

[34] S. Candel, Combustion dynamics and control: Progress and challenges, Proc. Combust. Inst. 29 (2002) 1–28.

[35] T.J. Poinsot, Prediction and control of combustion instabilities in real engines, Proc. Combust. Inst. 36 (2017) 1–28.

[36] T. Lieuwen, H. Torres, C. Johnson, B.T. Zinn, A Mechanism of Combustion Instability in Lean Premixed Gas Turbine Combustors, J. Eng. Gas Turbines Power 123 (2001) 182.

[37] A.P. Dowling, Y. Mahmoudi, Combustion noise, Proc. Combust. Inst. 35 (2015) 65–100.

[38] R.W. Bilger, S.B. Pope, K.N.C. Bray, J.F. Driscoll, Paradigms in turbulent combustion research, Proc. Combust. Inst. 30 (2005) 21–42.

[39] A.C. Alkidas, Combustion advancements in gasoline engines, Energy Convers. Manag. 48 (2007) 2751–2761.

[40] R.D. Reitz, Directions in internal combustion engine research, Combust. Flame 160 (2013) 1–8.

[41] M. Bau, G. Hyeon, S. Ho, C. Sang, Ignition of a lean PRF/air mixture under RCCI/SCCI conditions : Chemical aspects, Proc. Combust. Inst. 36 (2017) 3587–3596.

[42] J. Zhang, M. Bau, F.E. Hernández, D. Han, H.G. Im, Z. Huang, Exergy loss characteristics of DME/air and ethanol/air mixtures with temperature and concentration fluctuations under HCCI/SCCI conditions : A DNS study, Combust. Flame 226 (2021) 334–346.

[43] Z. Zheng, X. Fang, H. Liu, C. Geng, Z. Yang, L. Feng, Y. Wang, M. Yao, Study on the flame development patterns and flame speeds from homogeneous charge to stratified charge by fueling n-heptane in an optical engine, Combust. Flame 199 (2019) 213–229.

[44] J. Buckmaster, M. Matalon, Anomalous Lewis number effects in tribrachial flames, Symp. Combust. 22 (1988) 1527–1535.

[45] B. Fiorina, R. Mercier, G. Kuenne, A. Ketelheun, A. Avdić, J. Janicka, D. Geyer, A. Dreizler, E. Alenius, C. Duwig, P. Trisjono, K. Kleinheinz, S. Kang, H. Pitsch, F. Proch, F. Cavallo Marincola, A. Kempf, Challenging modeling strategies for LES of non-adiabatic turbulent stratified combustion, Combust. Flame 162 (2015) 4264–4282.

[46] T. Brauner, W.P. Jones, A.J. Marquis, LES of the Cambridge Stratified Swirl Burner using a Sub-grid pdf Approach, Flow, Turbul. Combust. 96 (2016) 965–985.

[47] C. Straub, A. Kronenburg, O.T. Stein, R.S. Barlow, D. Geyer, Modeling stratified flames with and without shear using multiple mapping conditioning, Proc. Combust. Inst. 37 (2019) 2317–2324.

[48] Y. Hu, R. Kurose, Nonpremixed and premixed flamelets LES of partially premixed spray flames using a two-phase transport equation of progress variable, Combust. Flame 188 (2018) 227–242.

[49] K. Kleinheinz, T. Kubis, P. Trisjono, M. Bode, H. Pitsch, Computational study of flame characteristics of a turbulent piloted jet burner with inhomogeneous inlets, Proc. Combust. Inst. 36 (2017) 1747–1757.

[50] A. Benarous, D. Karmed, A. Liazid, M. Champion, Numerical simulation of a turbulent partially premixed flame with inhomogeneous equivalence ratio, Fuel 124 (2014) 57–65.

[51] P.C. Vena, B. Deschamps, H. Guo, G.J. Smallwood, M.R. Johnson, Heat release rate variations in a globally stoichiometric, stratified iso-octane/air turbulent V-flame, Combust. Flame 162 (2015) 944–959.

[52] P.C. Vena, B. Deschamps, H. Guo, M.R. Johnson, Effects of stratification on locally lean, near-stoichiometric, and rich iso-octane/air turbulent V-flames, Combust. Flame 162 (2015) 4231–4240.

[53] M.M. Kamal, R.S. Barlow, S. Hochgreb, Scalar structure of turbulent stratified swirl flames conditioned on local equivalence ratio, Combust. Flame 166 (2016) 76–79.

[54] M.M. Kamal, R.S. Barlow, S. Hochgreb, Conditional analysis of turbulent premixed and stratified flames on local equivalence ratio and progress of reaction, Combust. Flame 162 (2015) 3896–3913.

[55] S. Schneider, D. Geyer, G. Magnotti, M.J. Dunn, R.S. Barlow, A. Dreizler, Structure of a stratified CH_4 flame with H_2 addition, Proc. Combust. Inst. 37 (2019) 2307–2315.

[56] T. Stahler, D. Geyer, G. Magnotti, P. Trunk, M.J. Dunn, R.S. Barlow, A. Dreizler, Multiple conditioned analysis of the turbulent stratified flame A, Proc. Combust. Inst. 36 (2017) 1947–1955.

[57] H.C. Cutcher, R.S. Barlow, G. Magnotti, A.R. Masri, Turbulent flames with compositionally inhomogeneous inlets: Resolved measurements of scalar dissipation rates, Proc. Combust. Inst. 36 (2017) 1737–1745.

[58] R.S. Barlow, S. Meares, G. Magnotti, H. Cutcher, A.R. Masri, Local extinction and near-field structure in piloted turbulent CH_4/air jet flames with inhomogeneous inlets, Combust. Flame 162 (2015) 3516–3540.

[59] H. Wang, E.R. Hawkes, B. Savard, J.H. Chen, Direct numerical simulation of a high Ka CH_4/air stratified premixed jet flame, Combust. Flame 193 (2018) 229–245.

[60] A. Gruber, E.S. Richardson, K. Aditya, J.H. Chen, Direct numerical simulations of premixed and stratified flame propagation in turbulent channel flow, Phys. Rev. Fluids 3 (2018) 1–22.

[61] E.S. Richardson, J.H. Chen, Analysis of turbulent flame propagation in equivalence ratio-stratified flow, Proc. Combust. Inst. 36 (2017) 1729–1736.

[62] H.G. Im, L.L. Raja, R.J. Kee, A.E. Lutz, L.R. Petzold, OPUS: A Fortran Program for Unsteady Opposed-Flow Flames, Report No. SAND2000-8211, Sandia National Laboratories, Livermore, CA, USA, 2000.

[63] H.G. Im, L.L. Raja, R.J. Kee, L.R. Petzold, A numerical study of transient ignition in a counterflow nonpremixed methane-air flame using adaptive time integration, Combust. Sci. Technol. 158 (2000) 341–363.

[64] A.E. Lutz, R.J. Kee, J.F. Grcar, F.M. Rupley, OPPDIF: A Fortran program for compu-

ting opposed-flow diffusion flames, Report No. SAND96-8243, Sandia National Laboratories, 1997.

[65] W. Song, E. Al Tingas, H.G. Im, A computational analysis of methanol autoignition enhancement by dimethyl ether addition in a counterflow mixing layer, Combust. Flame 195 (2018) 84–98.

[66] G. Bansal, H.G. Im, S.R. Lee, Autoignition of non-premixed n-heptane/air counterflow subjected to unsteady scalar dissipation rate, Proc. Combust. Inst. 32 I (2009) 1083–1090.

[67] R. Sankaran, H.G. Im, Effects of hydrogen addition on the markstein length and flammability limit of stretched methane/air premixed flames, Combust. Sci. Technol. 178 (2006) 1585–1611.

[68] G. Bansal, H.G. Im, Time scales in unsteady premixed flame extinction with composition fluctuations, Combust. Flame 150 (2007) 404–408.

[69] R. Sankaran, H.G. Im, Dynamic flammability limits of methane/air premixed flames with mixture composition fluctuations, Proc. Combust. Inst. 29 (2002) 77–84.

[70] E.R. Hawkes, J.H. Chen, Comparison of direct numerical simulation of lean premixed methane-air flames with strained laminar flame calculations, Combust. Flame 144 (2006) 112–125.

[71] G. Bansal, H.G. Im, J.K. Bechtold, Flame-flow interactions and flow reversal, Combust. Flame 159 (2012) 1489–1498.

[72] D.M. Valiev, M. Zhu, G. Bansal, H. Kolla, C.K. Law, J.H. Chen, Pulsating instability of externally forced premixed counterflow flame, Combust. Flame 160 (2013) 285–294.

[73] R.J. Kee, F.M. Rupley, J.A. Miller, Chemkin-II: A Fortran Chemical Kinetics Package for the Analysis of Gas-Phase Chemical Kinetics, Report No. SAND89-8009B, Sandia National Laboratories, Livermore, CA, USA, 1991.

[74] R.J. Kee, G. Dixon-Lewis, J. Warnatz, M.E. Coltrin, J.A. Miller, K. Moffat, Harry, A Fortran Computer Code Package for the Evaluation of Gas-Phase, Multicomponent Transport Properties, Sandia National Laboratories, Livermore, CA, USA, 1998.

[75] T. von Karman, On Laminar and Turbulent Friction, NACA Technical Memorandum No.1092, National Advisory Comittee for Aeronautics, Washington, D.C., USA, 1946.

[76] E.M. Sparrow, J.L. Gregg, Mass Transfer, Flow, and Heat Transfer About a Rotating Disk, J. Heat Transfer 82 (1960) 294–302.

[77] G. Dixon-Lewis, T. David, P.H. Gaskell, S. Fukutani, H. Jinno, J.A. Miller, R.J. Kee, M.D. Smooke, N. Peters, E. Effelsberg, J. Warnatz, F. Behrendt, Calculation of the structure and extinction limit of a methane-air counterflow diffusion flame in the forward stagnation region of a porous cylinder, Symp. Combust. 20 (1985) 1893–1904.

[78] R. Zhou, S. Hochgreb, The behaviour of laminar stratified methane/air flames in counterflow, Combust. Flame 160 (2013) 1070–1082.

[79] V. Giovangigli, M.D. Smooke, Extinction of Strained Premixed Laminar Flames with Complex Chemistry, Combust. Sci. Technol. 53 (1987) 23–49.

[80]   R.J. Kee, J.A. Miller, G.H. Evans, G. Dixon-Lewis, A computational model of the structure and extinction of strained, opposed flow, premixed methane-air flames, Symp. Combust. 22 (1989) 1479–1494.

[81]   H. Schlichting, K. Gersten, Boundary-Layer Theory, 8th Revise, Springer-Verlag, Berlin Heidelberg, Germany, 2000.

[82]   N. Bouvet, D. Davidenko, C. Chauveau, L. Pillier, Y. Yoon, On the simulation of laminar strained flames in stagnation flows: 1D and 2D approaches versus experiments, Combust. Flame 161 (2014) 438–452.

[83]   R.J. Kee, G. Dixon-Lewis, J. Warnatz, M. Coltrin, J.A. Miller, A Fortran Computer Code Package for the Evaluation of Gas-Phase Multicomponent Transport Properties, Report No. SAND86-8246, Sandia National Laboratories, Livermore, CA, USA, 1986.

[84]   K.K. Kuo, Principles of Combustion, 2nd ed., John Wiley & Sons, Inc., Hoboken, NJ, USA, 2005.

[85]   R.J. Kee, F.M. Rupley, J.A. Miller, M.E. Coltrin, J.F. Grcar, E. Meeks, H.K. Moffat, A.E. Lutz, G. Dixon-Lewis, M.D. Smooke, J. Warnatz, G.H. Evans, R.S. Larson, R.E. Mitchell, L.R. Petzold, W.C. Reynolds, M. Caracotsios, W.E. Stewart, P. Glarborg, C. Wang, O. Adigun, EQUIL: A Program for Computing Chemical Equilibria, CHEM-KIN Collection, Release 3.6, Reaction Design, Inc., San Diego, CA, 2001.

[86]   L.L. Raja, R.J. Kee, L.R. Petzold, Simulation of the transient, compressible, gas-dynamic behavior of catalytic-combustion ignition in stagnation flows, Symp. Combust. 27 (1998) 2249–2257.

[87]   A. Jameson, S. Yoon, Multigrid Solution of the Euler Equations Using Implicit Schemes, AIAA J. 24 (1986) 1737–1743.

[88]   L.R. Petzold, A description of DASSL: A differential/algebraic system solver, Report No. SAND82-8637, Sandia National Laboratories, Livermore, CA, USA, 1982.

[89]   L. Petzold, Differential/Algebraic Equations are not ODE's, SIAM J. Sci. Stat. Comput. 3 (1982) 367–384.

[90]   S. Li, L. Petzold, Design of new DASPK for sensitivity analysis, Technical Report of Computer Science Department TRCS99-23, University of California, Santa Barbara, CA, USA, 1999.

[91]   J.F. Grcar, The Twopnt Program for Boundary Value Problems, Report No. SAND91-8230, Sandia National Laboratories, Livermore, CA, USA, 1992.

[92]   J.A. Miller, R.J. Kee, C.K. Westbrook, Chemical Kinetics and Combustion Modelling, Annu. Rev. Phys. Chem. 41 (1990) 345–387.

[93]   Y. Ra, Laminar Flame Propagation in a Stratified Charge, Ph.D. Thesis, Massachusetts Institute of Technology, Cambridge, MA, 1999.

[94]   Y.M. Marzouk, The Effect of Flow and Mixture Inhomogeneity on the Dynamics of Strained Flames, Master Thesis, Massachusetts Institute of Technology, Cambridge, MA, 1999.

[95]   Y.M. Marzouk, A.F. Ghoniem, H.N. Najm, Dynamic response of strained premixed flames to equivalence ratio gradients, Proc. Combust. Inst. 28 (2000) 1859–1866.

[96] H.E. Perlee, I. Liebman, M. Zabatakis, Formation and Flammability of Stratified Methane-Air Mixtures, Report of Investigation 6348, U.S. Dept. of the Interior, Bureau of Mines, 1964.

[97] G. a. Karim, P. Tsang, Flame Propagation Through Atmospheres Involving Concentration Gradients Formed by Mass Transfer Phenomena, J. Fluids Eng. 97 (1975) 615–617.

[98] G.A. Karim, H.T. Lam, Ignition and Flame Propagation within Stratified Methane-Air Mixtures Formes by Convective Diffusion, Symp. Combust. 21 (1986) 1909–1915.

[99] D.W. Mikolaitis, The unsteady propagation of premixed flames through nonhomogeneous mixtures and thermal gradients, Combust. Flame 57 (1984) 87–94.

[100] E.J. Bissett, D.L. Reuss, Analysis of a Nonadiabatic Flame Propagating through Gradients of Fuel or Temperature, Symp. Combust. 21 (1986) 531–538.

[101] C.K. Westbrook, Propagation of a flame through a stratified charge combustion chamber, Acta Astronaut. 5 (1978) 1185–1198.

[102] P. Girard, M. Huneau, C. Rabasse, J.C. Leyer, Flame propagation through unconfined and confined hemispherical stratified gaseous mixtures, Symp. Combust. 17 (1979) 1247–1255.

[103] R. Lauvergne, F.N. Egolfopoulos, Unsteady response of C_3H_8/Air laminar premixed flames submitted to mixture composition oscillations, Proc. Combust. Inst. 28 (2000) 1841–1850.

[104] A.P. da Cruz, A.M. Dean, J.M. Grenda, A numerical study of the laminar flame speed of stratified methane/air flames, Proc. Combust. Inst. 28 (2000) 1925–1932.

[105] T. Kang, D.C. Kyritsis, Methane flame propagation in compositionally stratified gases, Combust. Sci. Technol. 177 (2005) 2191–2210.

[106] T. Kang, D.C. Kyritsis, A combined experimental/computational investigation of stratified combustion in methane-air mixtures, Energy Convers. Manag. 48 (2007) 2769–2774.

[107] T. Kang, D.C. Kyritsis, Departure from quasi-homogeneity during laminar flame propagation in lean, compositionally stratified methane-air mixtures, Proc. Combust. Inst. 31 (2007) 1075–1083.

[108] T. Kang, D.C. Kyritsis, Phenomenology of methane flame propagation into compositionally stratified, gradually richer mixtures, Proc. Combust. Inst. 32 (2009) 979–985.

[109] H. Tomita, M.R. Abdul Rahman, S. Miyamae, T. Yokomori, T. Ueda, Flame dynamics of equivalence ratio oscillations in a laminar stagnating lean methane/air premixed flame, Proc. Combust. Inst. 35 (2015) 989–997.

[110] M.R. Abdul Rahman, T. Yokomori, T. Ueda, Model of flame dynamics of laminar premixed flame subject to the low frequency equivalence ratio oscillations, Int. Commun. Heat Mass Transf. 61 (2015) 8–15.

[111] S. Balusamy, A. Cessou, B. Lecordier, Laminar propagation of lean premixed flames ignited in stratified mixture, Combust. Flame 161 (2014) 427–437.

[112] J. Zhang, J. Abraham, A numerical study of laminar flames propagating in stratified

mixtures, Combust. Flame 163 (2016) 461–471.

[113] X. Shi, J.-Y. Chen, Z. Chen, Numerical study of laminar flame speed of fuel-stratified hydrogen/air flames, Combust. Flame 163 (2016) 394–405.

[114] X. Shi, J.-Y. Chen, Numerical analysis and model development for laminar flame speed of stratified methane/air mixtures, Combust. Flame 184 (2017) 233–245.

[115] X. Shi, J.-Y. Chen, Y. Chen, Laminar flame speeds of stratified methane, propane, and n-heptane flames, Combust. Flame 176 (2017) 38–47.

[116] G.P. Smith, D.M. Golden, M. Frenklach, N.W. Moriarty, B. Eiteneer, M. Goldenberg, C.T. Bowman, R.K. Hanson, S. Song, W.C. Gardiner Jr, V. V. Lissianski, Z. Qin, GRI-Mech 3.0, http://www.me.berkeley.edu/gri_mech/, accessed Apr. 12, 2018.

[117] W.P. Jones, R.P. Lindstedt, Global Reaction Schemes for Hydrocarbon Combustion, Combust. Flame 73 (1988) 233–249.

[118] J. Andersen, C.L. Rasmussen, T. Giselsson, P. Glarborg, Global combustion mechanisms for use in CFD modeling under oxy-fuel conditions, Energy and Fuels 23 (2009) 1379–1389.

[119] Y. Wang, W. Han, Z. Chen, Effects of stratification on premixed cool flame propagation and modeling, Combust. Flame 229 (2021) 111394.

[120] X. Wu, P. Moin, Large-activation-energy theory for premixed combustion under the influence of enthalpy fluctuations, J. Fluid Mech. 655 (2010) 3–37.

[121] B. Coriton, M.D. Smooke, A. Gomez, Effect of the composition of the hot product stream in the quasi-steady extinction of strained premixed flames, Combust. Flame 157 (2010) 2155–2164.

[122] J.H. Tien, M. Matalon, On the Burning Velocity of Stretched Flames, Combust. Flame 84 (1991) 238–248.

[123] S.G. Davis, J. Quinard, G. Searby, Markstein Numbers in Counterflow, Methane- and Propane-Air Flames: A Computational Study, Combust. Flame 130 (2002) 123–136.

[124] Z. Zhou, Y. Shoshin, F.E. Hernández-Pérez, J.A. van Oijen, L.P.H. de Goey, Effect of Lewis number on ball-like lean limit flames, Combust. Flame 188 (2018) 77–89.

[125] G. Yu, C.K. Law, C.K. Wu, Laminar Flame Speeds of Hydrocarbon + Air Mixtures with Hydrogen Addition, Combust. Flame 63 (1986) 339–347.

[126] Y. Chen, Premixed flame propagation in a step-stratified charge, Fuel 252 (2019) 524–541.

[127] J.A. Wehrmeyer, Z. Cheng, D.M. Mosbacher, R.W. Pitz, R. Osborne, Opposed Jet Flames of Lean or Rich Premixed Propane-Air Reactants versus Hot Products, Combust. Flame 128 (2002) 232–241.

[128] Q. Tang, H. Liu, M. Li, C. Geng, M. Yao, Multiple optical diagnostics on effect of fuel stratification degree on reactivity controlled compression ignition, Fuel 202 (2017) 688–698.

[129] S. Hemdal, Characterization of stratified fuel distribution and charge mixing in a DISI engine using Rayleigh scattering, Combust. Flame 193 (2018) 218–228.

[130] M. Stöhr, Z. Yin, W. Meier, Interaction between velocity fluctuations and equivalence ratio fluctuations during thermoacoustic oscillations in a partially premixed swirl combustor, Proc. Combust. Inst. 36 (2017) 3907–3915.

[131] Y.C. See, M. Ihme, Large eddy simulation of a partially-premixed gas turbine model combustor, Proc. Combust. Inst. 35 (2015) 1225–1234.

[132] I. Boxx, M. Stöhr, C. Carter, W. Meier, Temporally resolved planar measurements of transient phenomena in a partially pre-mixed swirl flame in a gas turbine model combustor, Combust. Flame 157 (2010) 1510–1525.

[133] W. Meier, X.R. Duan, P. Weigand, Investigations of swirl flames in a gas turbine model combustor: II. Turbulence-chemistry interactions, Combust. Flame 144 (2006) 225–236.

[134] S. Hong, R.L. Speth, S.J. Shanbhogue, A.F. Ghoniem, Examining flow-flame interaction and the characteristic stretch rate in vortex-driven combustion dynamics using PIV and numerical simulation, Combust. Flame 160 (2013) 1381–1397.

[135] Z. Zeng, P. Du, Z. Wang, K. Li, Combustion flow in different advanced vortex combustors with/without vortex generator, Aerosp. Sci. Technol. 86 (2019) 640–649.

[136] M.S. Sweeney, S. Hochgreb, R.S. Barlow, The structure of premixed and stratified low turbulence flames, Combust. Flame 158 (2011) 935–948.

[137] B. Coriton, J.H. Frank, A.G. Hsu, M.D. Smooke, A. Gomez, Effect of quenching of the oxidation layer in highly turbulent counterflow premixed flames, Proc. Combust. Inst. 33 (2011) 1647–1654.

[138] B. Coriton, J.H. Frank, A. Gomez, Effects of strain rate, turbulence, reactant stoichiometry and heat losses on the interaction of turbulent premixed flames with stoichiometric counterflowing combustion products, Combust. Flame 160 (2013) 2442–2456.

[139] B. Coriton, J.H. Frank, A. Gomez, Interaction of turbulent premixed flames with combustion products: Role of stoichiometry, Combust. Flame 170 (2016) 37–52.

[140] C.J. Sung, J.B. Liu, C.K. Law, On the scalar structure of nonequidiffusive premixed flames in counterflow, Combust. Flame 106 (1996) 168–183.

[141] F. Dawood, M. Anda, G.M. Shafiullah, Hydrogen production for energy: An overview, Int. J. Hydrogen Energy 45 (2020) 3847–3869.

[142] H. Nazir, C. Louis, S. Jose, J. Prakash, N. Muthuswamy, M.E.M. Buan, C. Flox, S. Chavan, X. Shi, P. Kauranen, T. Kallio, G. Maia, K. Tammeveski, N. Lymperopoulos, E. Carcadea, E. Veziroglu, A. Iranzo, A.M. Kannan, Is the H_2 economy realizable in the foreseeable future? Part I: H_2 production methods, Int. J. Hydrogen Energy 45 (2020) 13777–13788.

[143] S. Verhelst, Recent progress in the use of hydrogen as a fuel for internal combustion engines, Int. J. Hydrogen Energy 39 (2014) 1071–1085.

[144] I. Dincer, C. Acar, Review and evaluation of hydrogen production methods for better sustainability, Int. J. Hydrogen Energy 40 (2014) 11094–11111.

[145] P. Dimitriou, T. Tsujimura, A review of hydrogen as a compression ignition engine fuel, Int. J. Hydrogen Energy 42 (2017) 24470–24486.

[146] N. Sazali, Emerging technologies by hydrogen: A review, Int. J. Hydrogen Energy 45 (2020) 18753–18771.

[147] C. Tang, Y. Zhang, Z. Huang, Progress in combustion investigations of hydrogen enriched hydrocarbons, Renew. Sustain. Energy Rev. 30 (2014) 195–216.

[148] H.L. Yip, A. Srna, A.C.Y. Yuen, S. Kook, R.A. Taylor, G.H. Yeoh, P.R. Medwell, Q.N. Chan, A review of hydrogen direct injection for internal combustion engines: Towards carbon-free combustion, Appl. Sci. 9 (2019) 1–30.

[149] B. Khandelwal, A. Karakurt, P.R. Sekaran, V. Sethi, R. Singh, Hydrogen powered aircraft: The future of air transport, Prog. Aerosp. Sci. 60 (2013) 45–59.

[150] H.S. Kim, V.K. Arghode, A.K. Gupta, Combustion characteristics of a lean premixed LPG-air combustor, Int. J. Hydrogen Energy 34 (2009) 1045–1053.

[151] R.W. Schefer, Hydrogen enrichment for improved lean flame stability, Int. J. Hydrogen Energy 28 (2003) 1131–1141.

[152] A. Colorado, V. McDonell, Emissions and stability performance of a low-swirl burner operated on simulated biogas fuels in a boiler environment, Appl. Therm. Eng. 130 (2018) 1507–1519.

[153] L. Bartolucci, S. Cordiner, V. Mulone, V. Rocco, Natural Gas Stable Combustion under Ultra-Lean Operating Conditions in Internal Combustion Engines, Energy Procedia 101 (2016) 886–892.

[154] S. Tsuboi, S. Miyokawa, M. Matsuda, T. Yokomori, N. Iida, Influence of spark discharge characteristics on ignition and combustion process and the lean operation limit in a spark ignition engine, Appl. Energy 250 (2019) 617–632.

[155] X. Wen, L. Dressler, A. Dreizler, A. Sadiki, J. Janicka, C. Hasse, Flamelet LES of turbulent premixed/stratified flames with H_2 addition, Combust. Flame 230 (2021) 111428.

[156] D. Cicoria, C.K. Chan, Effects of turbulence and strain rate on hydrogen-enriched high Karlovitz number lean premixed methane flames, Fuel 211 (2018) 754–766.

[157] Z. Chen, P. Dai, S. Chen, A model for the laminar flame speed of binary fuel blends and its application to methane/hydrogen mixtures, Int. J. Hydrogen Energy 37 (2012) 10390–10396.

[158] C.L. Tang, Z.H. Huang, C.K. Law, Determination, correlation, and mechanistic interpretation of effects of hydrogen addition on laminar flame speeds of hydrocarbon-air mixtures, Proc. Combust. Inst. 33 (2011) 921–928.

[159] H. Nazir, N. Muthuswamy, C. Louis, S. Jose, J. Prakash, M.E. Buan, C. Flox, S. Chavan, X. Shi, P. Kauranen, T. Kallio, G. Maia, K. Tammeveski, N. Lymperopoulos, E. Carcadea, E. Veziroglu, A. Iranzo, A.M. Kannan, Is the H_2 economy realizable in the foreseeable future? Part II: H_2 storage, transportation, and distribution, Int. J. Hydrogen Energy 45 (2020) 20693–20708.

[160] C.H. Christensen, T. Johannessen, R.Z. Sorensen, J.K. Norskov, Towards an ammonia-mediated hydrogen economy?, Catal. Today 111 (2006) 140–144.

[161] E. Boateng, A. Chen, Recent advances in nanomaterial-based solid-state hydrogen storage, Mater. Today Adv. 6 (2020) 100022.

[162] S. Rönsch, J. Schneider, S. Matthischke, M. Schlüter, M. Götz, J. Lefebvre, P. Prabhakaran, S. Bajohr, Review on methanation - From fundamentals to current projects, Fuel 166 (2016) 276–296.

[163] M. Thema, T. Weidlich, M. Hörl, A. Bellack, F. Mörs, F. Hackl, M. Kohlmayer, J. Gleich, C. Stabenau, T. Trabold, M. Neubert, F. Ortlo, R. Brotsack, D. Schmack, H. Huber, D. Hafenbradl, J. Karl, M. Sterner, Biological CO2-Methanation: An Approach to Standardization, Energies 12 (2019) 1–32.

[164] S. Giddey, S.P.S. Badwal, C. Munnings, M. Dolan, Ammonia as a Renewable Energy Transportation Media, ACS Sustain. Chem. Eng. 5 (2017) 10231–10239.

[165] A. Valera-Medina, S. Morris, J. Runyon, D.G. Pugh, R. Marsh, P. Beasley, T. Hughes, Ammonia, Methane and Hydrogen for Gas Turbines, Energy Procedia 75 (2015) 118–123.

[166] A. Valera-Medina, R. Marsh, J. Runyon, D. Pugh, P. Beasley, T. Hughes, P. Bowen, Ammonia–methane combustion in tangential swirl burners for gas turbine power generation, Appl. Energy 185 (2017) 1362–1371.

[167] K.D.K.A. Somarathne, A. Hayakawa, H. Kobayashi, Numerical investigation on the combustion characteristics of turbulent premixed ammonia/air flames stabilized by a swirl burner, J. Fluid Sci. Technol. 11 (2016) 1–10.

[168] O. Kurata, N. Iki, T. Matsunuma, T. Inoue, T. Tsujimura, H. Furutani, H. Kobayashi, A. Hayakawa, Performances and emission characteristics of NH_3-air and NH_3-CH_4-air combustion gas-turbine power generations, Proc. Combust. Inst. 36 (2017) 3351–3359.

[169] K.D.K.A. Somarathne, S. Hatakeyama, A. Hayakawa, H. Kobayashi, Numerical study of a low emission gas turbine like combustor for turbulent ammonia/air premixed swirl flames with a secondary air injection at high pressure, Int. J. Hydrogen Energy 42 (2017) 27388–27399.

[170] A. Hayakawa, Y. Arakawa, R. Mimoto, K.D.K.A. Somarathne, T. Kudo, H. Kobayashi, Experimental investigation of stabilization and emission characteristics of ammonia/air premixed flames in a swirl combustor, Int. J. Hydrogen Energy 42 (2017) 14010–14018.

[171] K.D.K.A. Somarathne, S. Colson, A. Hayakawa, H. Kobayashi, Modelling of ammonia/air non-premixed turbulent swirling flames in a gas turbine-like combustor at various pressures, Combust. Theory Model. 22 (2018) 973–997.

[172] O. Kurata, N. Iki, T. Inoue, T. Matsunuma, T. Tsujimura, H. Furutani, M. Kawano, K. Arai, E.C. Okafor, A. Hayakawa, H. Kobayashi, Development of a wide range-operable, rich-lean low-NOx combustor for NH_3 fuel gas-turbine power generation, Proc. Combust. Inst. 37 (2019) 4587–4595.

[173] E.C. Okafor, K.D.K.A. Somarathne, A. Hayakawa, T. Kudo, O. Kurata, N. Iki, H. Kobayashi, Towards the development of an efficient low-NOx ammonia combustor for a micro gas turbine, Proc. Combust. Inst. 37 (2019) 4597–4606.

[174] E.C. Okafor, K.D.K.A. Somarathne, R. Ratthanan, A. Hayakawa, T. Kudo, O. Kurata, N. Iki, T. Tsujimura, H. Furutani, H. Kobayashi, Control of NOx and other emissions in micro gas turbine combustors fuelled with mixtures of methane and ammonia, Combust. Flame 211 (2020) 406–416.

[175] E.C. Okafor, H. Yamashita, A. Hayakawa, K.D.K.A. Somarathne, T. Kudo, T. Tsujimura, M. Uchida, S. Ito, H. Kobayashi, Flame stability and emissions characteristics of liquid ammonia spray co-fired with methane in a single stage swirl combustor, Fuel 287 (2021) 119433.

[176] A.A. Khateeb, T.F. Guiberti, X. Zhu, M. Younes, A. Jamal, W.L. Roberts, Stability limits and NO emissions of technically-premixed ammonia-hydrogen-nitrogen-air swirl flames, Int. J. Hydrogen Energy 45 (2020) 22008–22018.

[177] A.A. Khateeb, T.F. Guiberti, X. Zhu, M. Younes, A. Jamal, W.L. Roberts, Stability limits and exhaust NO performances of ammonia-methane-air swirl flames, Exp. Therm. Fluid Sci. 114 (2020) 110058.

[178] X. Zhu, A.A. Khateeb, T.F. Guiberti, W.L. Roberts, NO and OH* emission characteristics of very-lean to stoichiometric ammonia-hydrogen-air swirl flames, Proc. Combust. Inst. 38 (2021) 5155–5162.

[179] A.A. Khateeb, T.F. Guiberti, G. Wang, W.R. Boyette, M. Younes, A. Jamal, W.L. Roberts, Stability limits and NO emissions of premixed swirl ammonia-air flames enriched with hydrogen or methane at elevated pressures, Int. J. Hydrogen Energy 46 (2021) 11969–11981.

[180] A. Hayakawa, T. Goto, R. Mimoto, T. Kudo, H. Kobayashi, NO formation/reduction mechanisms of ammonia/air premixed flames at various equivalence ratios and pressures, Mech. Eng. J. 2 (2015) 14-00402-14–00402.

[181] G. Ciccarelli, D. Jackson, J. Verreault, Flammability limits of NH_3-H_2-N_2-air mixtures at elevated initial temperatures, Combust. Flame 144 (2006) 53–63.

[182] E.C. Okafor, Y. Naito, S. Colson, A. Ichikawa, T. Kudo, A. Hayakawa, H. Kobayashi, Experimental and numerical study of the laminar burning velocity of CH_4–NH_3–air premixed flames, Combust. Flame 187 (2018) 185–198.

[183] Z. Tian, Y. Li, L. Zhang, P. Glarborg, F. Qi, An experimental and kinetic modeling study of premixed NH_3/CH_4/O_2/Ar flames at low pressure, Combust. Flame 156 (2009) 1413–1426.

[184] R.C. da Rocha, M. Costa, X.S. Bai, Chemical kinetic modelling of ammonia/hydrogen/air ignition, premixed flame propagation and NO emission, Fuel 246 (2019) 24–33.

[185] X. Han, Z. Wang, M. Costa, Z. Sun, Y. He, K. Cen, Experimental and kinetic modeling study of laminar burning velocities of NH_3/air, NH_3/H_2/air, NH_3/CO/air and NH_3/CH_4/air premixed flames, Combust. Flame 206 (2019) 214–226.

[186] P. Glarborg, J.A. Miller, B. Ruscic, S.J. Klippenstein, Modeling nitrogen chemistry in combustion, Prog. Energy Combust. Sci. 67 (2018) 31–68.

[187] K.D.K.A. Somarathne, E. C. Okafor, A. Hayakawa, T. Kudo, O. Kurata, N. Iki, H. Kobayashi, Emission characteristics of turbulent non-premixed ammonia/air and methane/air swirl flames through a rich-lean combustor under various wall thermal boundary conditions at high pressure, Combust. Flame 210 (2019) 247–261.

[188] R.W. Bilger, The Structure of Turbulent Nonpremixed Flames, Symp. Combust. 22 (1988) 475–488.

[189] R.J. Kee, J.F. Grcar, M.D. Smooke, J.A. Miller, E. Meeks, PREMIX : A FORTRAN Program for Modeling Steady Laminar One-Dimensional Premixed Flames, Report No. SAND89-8240, Sandia National Laboratories, Livermore, CA, USA, 1985.

[190] X. Han, Z. Wang, Y. He, Y. Zhu, K. Cen, Experimental and kinetic modeling study of laminar burning velocities of NH_3/syngas/air premixed flames, Combust. Flame 213 (2020) 1–13.

[191] J.A. Miller, C.T. Bowman, Mechanism and modeling of nitrogen chemmistry in combustion, Prog. Energy Combust. Sci. 15 (1989) 287–338.

[192] M.T. Javed, Z. Ahmed, M.A. Ibrahim, N. Irfan, A comparative kinetic study of SNCR process using ammonia, Brazilian J. Chem. Eng. 25 (2008) 109–117.

[193] Z. ur Rahman, X. Wang, J. Zhang, J. Baleta, M. Vujanović, H. Tan, Kinetic study and optimization on SNCR process in pressurized oxy-combustion, J. Energy Inst. 94 (2021) 263–271.

[194] F. Kasuya, P. Glarborg, J.E. Johnsson, K. Dam-Johansen, The thermal DeNOx process: Influence of partial pressures and temperature, Chem. Eng. Sci. 50 (1995) 1455–1466.

[195] Z. min Lu, J. dong Lu, Influences of O_2 concentration on NO reduction and N_2O formation in thermal deNOx process, Combust. Flame 156 (2009) 1303–1315.